AN ABSTRACT OF THE THESIS OF

Teresa King Hagelberg for the degree of Doctor of Philosophy in Oceanography presented on February 3, 1993.

Title: Variability of Late Neogene Eastern Equatorial Pacific Carbonate Sedimentation and Global Ice Volume on Timescales from 10,000 Years to 1 million Years.

Redacted for Privacy

Abstract Approved: _____

Nicklas G. Pisias

Sedimentary sections recovered during the Deep Sea Drilling Project and the Ocean Drilling Program provide the opportunity to study the evolution of Neogene climate at high resolution over time periods spanning millions of years. Two components of the paleoclimatic system, eastern equatorial Pacific carbonate sedimentation and global ice volume, were examined with the common goal of understanding late Neogene climatic variability. Before examining the temporal evolution in detail, stratigraphic continuity of the sedimentary sections was confirmed. Remotely measured sedimentary properties were used to document section continuity between adjacent and overlapping cores at each drill site during ODP Leg 138. This strategy also provided several realizations of the sedimentary process. Multiple realizations of wet bulk density at each of eight drill sites were averaged to produce continuous records having a ~2 cm resolution. Estimates of local sedimentation variability were also developed to confirm that sedimentation rate variations imposed by orbital tuning strategies are within the range of local sedimentation variability that is present.

In the eastern equatorial Pacific, wet bulk density is a proxy indicator of calcium carbonate concentration. Eight records spanning the last 6 million years at a ~1000 year resolution were used to investigate spatial and temporal variations in carbonate sedimentation. Two modes of variability in calcium carbonate concentration and carbonate mass

accumulation were resolved. The spatial pattern of the dominant mode of variability indicates latitudinal control of carbonate sedimentation. Over the past 6 myr, the dominant mode of variability is highly coherent with changes in insolation. The dominant mode of carbonate sedimentation has consistent spatial patterns in the presence of large oceanographic and tectonic boundary condition changes. A primary control from surface oceanographic processes was inferred. The second mode of variability in carbonate sedimentation may be influenced by processes related to dissolution and noncarbonate dilution. Carbonate sedimentation and ice volume variations are linearly related in the Milankovitch band during the past 4 myr.

Evolution of ice volume over the past 2.5 myr was investigated using oxygen isotope records. Third order statistics were used to study the extent of linear relative to nonlinear variations in ice volume. The same statistically significant phase couplings that are present in the time series of solar insolation are also present in the global ice volume record. These results are consistent with a linear response of the climate system to orbital forcing. An evolution in the nature of the phase coupling is seen, with an increase in the asymmetry of the ice volume record over the late Neogene.

Coherence between paleoceanographic records and insolation variations has been used as a measure of time scale accuracy. The effects of age model error and amplitude error on estimates of coherence and bicoherence were investigated. Coherence estimates are more robust to amplitude error and time scale error than bicoherence estimates. A test for time scale error which uses the statistical properties of the bispectrum is not applicable to the problem of time scale accuracy in paleoceanography. However, under the assumption of a linear response of climate to insolation in the Milankovitch band, the high sensitivity of bicoherence estimates suggests that bicoherence may be a more sensitive indicator of age model accuracy.

Variability of Late Neogene Eastern Equatorial Pacific Carbonate Sedimentation and Global Ice Volume on Timescales from 10,000 Years to 1 million Years

by

Teresa King Hagelberg

A THESIS

submitted to

Oregon State University

in partial fulfillment of

the requirements for the

degree of

Doctor of Philosophy

Completed February 3, 1993

Commencement June 1993

APPROVED:

Redacted for Privacy

Professor of Oceanography in charge of major

Redacted for Privacy

Dean of the College of Oceanography

Redacted for Privacy

Dean of the Graduate School

Date Thesis Presented February 3, 1993

Typed by Teresa K. Hagelberg and David Reinert for Teresa King Hagelberg

ACKNOWLEDGMENTS

I've lived in Corvallis for over 6 years now, all the time an Oceanography student so naturally there are lots of people to acknowledge. I want to make sure that I acknowledge EVERYONE who has enriched my life here. Thank you everybody.

First and foremost I would like to thank my advisor, Nick Pisias, for all of his support over the past 6 years. Nick's encouragement has never waivered. I think it is significant that, after 3 years doing my master's degree with Nick, he let me stay on for my Ph.D. Did Nick forsee what the next 3 years would bring? Nick has provided me with a great deal of independence, yet has always been available to help and give advice. I have also been fortunate to have had Alan Mix as a committee member and backup advisor. I am grateful to Alan for 6 years of free advice and feedback. I'd like to thank Rob Holman for being an honorable committee member, and for his patience, listening ability, and insight. Dudley Chelton has enriched my graduate education by giving me the opportunity to sit through his class twice, and has also helped to improve this thesis. Finally, I would like to thank Jerry Heidel from the Vet school for being my Grad. Rep.

Dave Reinert helped in preparing this thesis, making the assembly process much easier for me. Had it not been for David's help, I would be enrolling for Spring Term! For all kinds of miscellaneous help over the years, I am grateful to Sue Pullen.

Several individuals have contributed significantly to my research. In particular, I am grateful to Nick Shackleton. Not only has Nick provided the oxygen isotope records from Sites 677 and 846 which are studied in my thesis, but Nick has developed the age models that I have relied on in every chapter. Working with Nick during ODP Leg 138 and afterward has been an enriching and enjoyable experience. I thank Maureen Raymo and William Ruddiman for providing the isotope records from Site 607 which are studied in Chapter 4. Larry Mayer, Mitch Lyle (FOB), and Andre Berger are also acknowledged for extensive input, advice, and feedback.

ODP Leg 138 scientists and crew require special recognition. It is impossible to single out a few people at the expense of leaving others out, however....Christina Ravelo & Isabella Raffi managed to keep me laughing for 2 solid months at sea (che schifo!), and Margaret Leinen taught Christina & I what we need to know in order to become senior sedimentologists someday. Everyone - Steve Hovan, Ted Moore, Jose Abel-Flores, Shaul Levi, Gary Klinkhammer, Dave Schneider, Kathy Dadey, Mitch Lyle, Edith Vincent, Masao Iwai, John Farrell, Steve Bloomer, Alan Mix, Alan Kemp, Nick Pisias, Nick Shackleton, Larry Mayer, Kevin MacKillop, Jean-Pierre Valet, Laure Meynadier, Tom Janecek, Kay Emeis, Misha Levitan, Dae Kim, Peter Holler, Eric Galimov, Jack Baldauf, Wendy, Gretchen, Bill, Brad .....and the rest of the crew - thanks!

Several people in the nearshore community have been friends, colleagues, and all around great people to work with: (in ADDITION to Rob, of course): Tom Lippomann and Todd Holland have been great officemates. Joan Oltman-Shay was inspirational and an influence on my decision to continue into a Ph.D. program, and I am thankful for her support. Peter Howd helped to keep me IN the Ph.D. program. I'd also like to remember Paul O'Neill from Pandora's early days. Also - Diane, Kathryn, Nathaniel, Cindy, Mark, Christine, and last but not least the geeks (a.k.a. Chuck and Tom. I do appreciate you guys.) For discussions about bispectra during the past 2 years, I am grateful to Tom L. (again!), John Haines, Tom Herbers,, Mike Freilich, and Vinod Chandran.

Most everyone to come through the rad lab has made the past 6 years memorable, including Adrienne Roelofs, Pat Hays, Katy Condon, Kara Nelson, Stacey Moore, Ann Sabin, Sara Harris, Mysti Weber, Chris Harwood, Kathryn Wimmer, and Reza B. Thanks to Joe Ortiz, Jim Watkins, Anne Morey, June Wilson, Bill Rugh, Rainer Zahn, Jorunn, Vegard, and Sabine for significantly enhancing the paleo contingency. Thanks to all of OSU Marine Geology for such a wonderful and congenial atmosphere for the past years: Colliers, Mosers, Christies, Klinkhammers, Andy and Bobbi, Doug (FOB), Randy, Dana,

Jim McManus, Dave Murray. KBVR folks have made the last 24 months here great - especially to Tom C. & Emory C. who made the last months of thesis preparation bearable. Thank you Chris Joy for a fantastic rock rotation. I will miss KBVR. Emory, good luck with Ann. I appreciate EVERYONE at the Beanery and Bombs Away, especially Joel, but also John, Regina, James, Jason, Dan, Pat, Fran, Cher, Shelly, Bob, Travis, Susan (coop) - and everyone who ever gave me free coffee, tea, beer, or food. Much support and encouragement has come from folks far away but close in spirit, especially Cherry, Pete and Liz. Thanks for staying in touch and remembering me.

I can't say enough about my closest OSU friends - especially Leigh and Joel (and Skippy and Spike). Also Sue, Rodney, Jessica, Phil, Anne and Alice & co. - its been great. Along with Carl, y'all are the source of nearly all of my pleasant memories during these past years. Thanks for all the conversations, movies, excursions, and food and drink. I hope that we can all stay in touch. Leigh, I will return to Corvallis when you defend to make sure everything is in order and to take care of your party.

The most important support and encouragement has always come from my family. Regardless of other events, Carl and my parents have always supported my decisions and encouraged me. I will always try to be aware of their love and support. I hope that I can provide the same. So, Carl, Mom, Dad, Catherine, Beth, Tony, Christie, Ray, Ellen, Mike, Karen, Jim - thanks!

OK, I think that just about covers it. Thank you everyone.

TABLE OF CONTENTS

LIST OF FIGURES

LIST OF TABLES

VARIABILITY OF LATE NEOGENE EASTERN EQUATORIAL PACIFIC CARBONATE SEDIMENTATION AND GLOBAL ICE VOLUME ON TIMESCALES FROM 10,000 YEARS TO 1 MILLION YEARS

CHAPTER ONE: GENERAL INTRODUCTION

INTRODUCTION AND OUTLINE

The field of paleoceanography has undergone significant advances during the past 20 years. Many of the scientific advances are due in part to technological developments associated with the Ocean Drilling Program (ODP) and its predecessor, the Deep Sea Drilling Program (DSDP). Earlier work relied almost exclusively on short piston cored sediment records. Thus, a trade off existed between high sedimentation rate cores covering short time periods at high resolution, and low sedimentation rate cores covering long time periods at low resolution. This, and uncertainties in chronology, were primary inhibitors of time series studies in the frequency domain for many years.

As a result of technological advances in drilling and core recovery, scientists are now able to study long, undisturbed geological sections. However, even with advances in sediment recovery associated with Hydraulic Piston Corer and Advanced Piston Corer development, new problems became evident in documenting section continuity. This has led to the strategy of drilling multiple adjacent holes at one site in order to recover undisturbed, continuous sediment sections.

The second significant factor responsible for advances in paleoceanography over the past 20 years, concurrent with technological developments, has been timescale development. Since the initial study of Hays et al. (1976), it has been demonstrated that the time series of changes in the Earth's precession and obliquity can be used as a calibration tool for geologic timescales. Given geological records that are known to be continuous in the depth domain, development of a high resolution time scale is possibly the most

important aspect of any high resolution paleoceanographic time series study. The ability to calibrate time scales at high resolution, combined with the ability to obtain continuous, undisturbed geological sections has put paleoceanographers in a position to study millions of years of climatic change at a resolution comparable to the mixing time of the oceans.

This thesis uses continuous records from DSDP and ODP sections to study the evolution of Neogene climate. Two components of the climate system are studied, the carbonate system of the eastern equatorial Pacific during the past 6 myr, and global ice volume proxies for the past 2.5 myr. These studies are preceded by an introduction to the Milankovitch hypothesis for global climate change, given below. In Chapter 2 the issue of high resolution section continuity for ODP sections from the eastern equatorial Pacific is addressed. In Chapter 3 the spatial and temporal variability of carbonate sedimentation in the eastern equatorial Pacific during the last 6 myr is investigated. In Chapter 4 linear relative to nonlinear interactions in the climate system are studied by examining variability in global ice volume records spanning the past 2.5 myr. Chapter 5 examines the implications of variability in both amplitudes and time scale for the results presented in Chapters 3 and 4.

Chapter Two, titled "Refinement of a High-Resolution, Continuous Sedimentary Section for the Study of Equatorial Pacific Paleoceanography: ODP Leg 138", addresses the continuity of sedimentary sections drilled during ODP Leg 138. Wet bulk density records were used to correlate between adjacent drilled holes at 8 drill sites at centimeter scale resolution. Multiple records of wet bulk density at each site provided multiple realizations of the same sedimentary process. These realizations were averaged to produce a continuous record of wet bulk density at each site. This procedure allowed development of error estimates for measurements present in more than one hole at each drill site, and allowed estimates of local sedimentation variability to be obtained. A primary result was the development of high resolution wet bulk density records which could be used for

investigation of late Neogene eastern equatorial Pacific sedimentation. This study has been submitted to the Scientific Results Volume of Leg 138 of the Ocean Drilling Program. Co-authors are N.G. Pisias, N.J. Shackleton, A. Mix, and S. Harris.

Chapter 3, titled " Spatial and Temporal Variability of Late Neogene Equatorial Pacific Carbonate: ODP Leg 138", has also been submitted to the Scientific Results Volume of Leg 138 of the Ocean Drilling Program. Co-authors of this study are N.G. Pisias, N.J. Shackleton, L.A. Mayer and A.C. Mix. Eight high resolution records of wet bulk density, a carbonate proxy, are used to investigate spatial and temporal variability in eastern equatorial Pacific carbonate sedimentation over the past 6 myr. The role of surface oceanographic processes on carbonate sedimentation relative to the role of deep ocean alkalinity changes is studied. Two modes of variability in carbonate sedimentation are resolved through Empirical Orthogonal Functions (EOFs). The dominant mode of variability in carbonate sedimentation includes a high degree of Milankovitch band variability. The spatial expression of the dominant mode is highly coupled to latitude in the equatorial Pacific, indicating a relationship to equatorial divergence. The relationship of carbonate sedimentation to surface ocean processes is present in each of 3 dominant frequency bands. The second mode of variability does not include as much Milankovitch band variability, and may indicate processes related to both dissolution and surface ocean influence. The second mode of variability is only present through the past 4 myr, suggesting a response to closure of the Isthmus of Panama. Throughout the past 6 myr, and in the presence of large oceanographic and tectonic boundary condition changes, the fundamental spatial pattern of carbonate sedimentation in the eastern equatorial Pacific has remained unchanged. This indicates a process controlling carbonate sedimentation which is very sensitive to surface oceanographic processes, yet relatively insensitive to external boundary condition changes.

Chapter 4, titled "Linear and Nonlinear Couplings between Orbital Forcing and the Marine $\delta^{18}O$ Record during the Late Neogene" was published in Paleoceanography in 1991. N.G. Pisias and S. Elgar are co-authors. Since 1976, a prevailing opinion has been that a linear mechanism forces changes in Pleistocene ice volume via changes in insolation reaching the earth at periods of 41, 23, and 19 kyr (e.g. Hays, et al., 1976; Pisias and Moore, 1981; Imbrie et al., 1984, 1989, 1992). However, the bulk of variability in the marine $\delta^{18}O$ record (an ice volume proxy) is concentrated near 100 kyr. A linear response of the climate system has generally been regarded as insufficient to explain this dominance because variability in insolation at 100 kyr is small, and a nonlinear response has often been invoked. Third order statistics of the $\delta^{18}O$ time series were used to recover the phase information necessary to determine if the 100 kyr cycle is consistent with a nonlinear process. Statistically significant quadratic phase couplings, indicated by bicoherence estimates, were resolved in the time series of insolation, the climatic forcing, and in the time series of $\delta^{18}O$. This analysis suggested that during the late Pleistocene, the dominance of the 100 kyr cycle is consistent with a linear, resonant response to eccentricity forcing. From 2.6 Ma to present, an increase in the asymmetry of the ice volume records was resolved, indicating an evolution in the nature of the climatic phase coupling.

Chapter 5 is titled "Implications of Variability in Sampling and Time Scale for High Resolution Paleoceanographic Studies." Because all paleoceanographic time series studies must assume a correct age model, the variability and effects of time scale error are important. A study by Pisias (1981) examined the assumptions involved in tuning a geologic time scale using time series of orbital changes, but no study has examined variability of cross-spectral estimates to errors in the age model. Because the coherence and phase estimates between a tuned record and insolation are a primary means of calibrating chronologies for the Pleistocene, Pliocene, and even Miocene, it is useful to know the robustness of these estimates to age model noise. In light of the results presented in Chapter 4, it is also important to understand how robust bicoherence estimates are to time scale

variability and amplitude errors. The effects of small scale and large scale time scale variability on coherence and bicoherence estimates were explored using a Monte-Carlo approach with records modeled after the time series from Chapters 3 and 4. In general coherence estimates are highly robust to amplitude and age model noise, while bicoherence estimates are highly sensitive. Because bicoherence estimates are much more sensitive than coherence estimates, bicoherence may be a better indicator of time scale accuracy, given that the record being tuned is linearly responding to insolation changes. This study reinforced the utility of Monte-Carlo simulations with paleoceanographic records. Because record lengths are typically short and thus degrees of freedom low, results from applications of higher order spectra and advanced statistical applications are strengthened with simulations of random data.

MILANKOVITCH THEORY

Of all the theories which have been proposed to explain the Ice Ages of the past 2 myr, only the Milankovitch theory is supported by substantial observations. Berger (1988) and Imbrie and Imbrie (1979) give a detailed description and introduction to the astronomical considerations and geological observations leading to the development of the Milankovitch theory of climate change. Some of the more important developments extending back over the past 150 years are reviewed here.

The concept of a relationship between astronomically induced variations in Earth's insolation and glacial intervals was first proposed by Croll in the late 19th century (Croll, 1875). He determined that the major factors influencing glacial development included the tilt of the Earth's axis, the precession of the equinoxes, and variations in orbital eccentricity, as these parameters influence seasonal and annual insolation patterns. Croll hypothesized that the critical season for conditions favorable to glaciation was Northern Hemisphere winter. Less sunlight would produce more snow, and a positive feedback could be initiated whereby additional snow and increased albedo would lead to glacier development. Croll's hypothesis also predicted an out of phase relationship between Northern and Southern Hemisphere glaciations. In the late 19th century, Croll's theory was discounted because he predicted that the last ice age occurred 80,000 years B.P, which was inconsistent with the estimates of geologists, and meteorologists did not believe that solar insolation alone could be enough.

In 1921, Spitaler rejected Croll's hypothesis, and postulated that long, cool summers and short winters were more conducive to development of glacial conditions (Berger, 1988). This was followed by an extensive exploration of the irradiance curves as a function of latitude and season by Milutin Milankovitch, a Yugoslavian mathematician. Milankovitch theorized that in some time intervals near the summer solstice the insolation near the top of the atmosphere is lower at the equator than at the poles. During these summers, the season is long and cool enough so that snow melt is reduced. A positive

feedback is initiated via an increase in planetary albedo. Milankovitch hypothesized that a minimum in summer Northern Hemisphere insolation at high latitudes was necessary to bring about the onset of glacial periods. Milankovitch's calculations produced a record of the intensity of summer insolation over the past 600,000 years. In his curve (Figure I.1), he identifies low points in the summer insolation as coincident with the occurrence of Ice Ages as identified by geologists. (Milankovitch, 1941).

The dominant orbital elements influencing Milankovitch's insolation curve are orbital eccentricity, obliquity (or tilt), and precession. These three orbital parameters primarily effect the distribution and seasonality of insolation. Eccentricity of the Earth's orbit is the only orbital parameter which directly affects the integrated energy at all latitudes that the Earth receives. Obliquity, the tilt of the Earth's axis relative to vertical, influences the amount of insolation received as a function of latitude. Precessionof the Earth's axis and precession of the equinoxes influence the Earth-Sun distance during any season as well as the length of a season.

The equations describing variations in the Earth's orbital parameters are derived from the equations of celestial mechanics for the eight major planets in the solar system (excluding Pluto) and the sun. For each planet, an approximate solution is achieved by integrating the Lagrange equations for 6 planetary variables, thus a system of 48 differential equations must be solved (Bretagnon, 1984). The six planetary variables, illustrated in

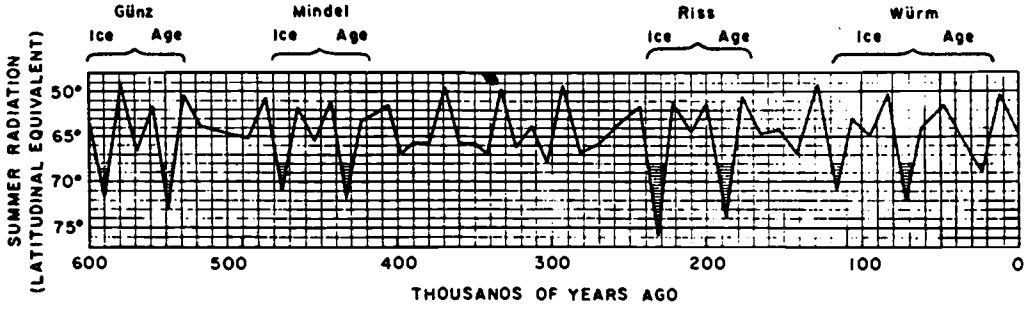

Figure I.1. The Milankovitch radiation curve for 65°N from 600,000 years B.P. to present. Low points that are shaded indicate Milankovitch's identification of reduced insolation with four European ice ages. The vertical axis expresses the insolation change as a function of latitudinal equivalent for 65°N. (From Imbrie and Imbrie, 1979.)

Figure I.2, are: a,λ,k,h,q, and p, where k = e cos ω, h = e sin ω, q= γ cos Ω, p = γ sin Ω, γ= sin i/2, a is the semi-major axis of the planets orbit, λ is the mean longitude of the planet, e the eccentricity of the orbit, ω is the longitude of perihelion as measured from the moving vernal equinox, i is the inclination of the axis, and Ω is the longitude of the node (Bretagnon, 1984, Berger, 1984). The solution for the variations in these orbital parameters is achieved by successive approximation or by series expansion. Several different solutions have been compared by Berger (1984) in order to evaluate the accuracy of the various solutions. Berger formulates the differential equations of the planetary motions as:

$$\frac{d\sigma_{k,n}}{dt} = \sum_{j=1,\, j\neq n}^{8} \sum_{i=1}^{6} f_{i,n}\,(\sigma_{1,n}, \ldots, \sigma_{6,n})\, \frac{\partial R_{j,n}}{\partial \sigma_{i,n}}$$

$$\sigma_{i,n} = \{h,k,p,q,a,l\}_{i,n} \qquad 1 \leq i \leq 6,\ 1 \leq n \leq 9$$

$$R_{j,n} = \Sigma_{r,s,t,u}\, A(a_j,a_n,m_j,m_n)\, e_j^{\,r}\, e_n^{\,s}\, (\sin i_j/2)^{\,t} \cdot (\sin i_n/2)^{\,u} \cos \phi_{j,n}$$

$$\phi_{j,n} = b_1 \lambda_j + b_2 \lambda_n + b_3 \pi_j + b_4 \pi_n + b_5 \Omega_j + b_6 \Omega_n$$

where a, λ, and Ω are as defined above, (h,k) combine eccentricity and the longitude of perihelion; (p,q) combine the inclination of the ecliptic and the longitude of the node (Ω), and σ represents a, λ, h, k, p, and q collectively. π is the longitude of perihelion, r, s, t, and u are integers, and m is the planetary mass. R is the perturbation function. Berger (1984) demonstrated that the most important terms include the plantetary masses and the planetary eccentricities and inclinations. The most recent astronomical solution includes these terms up to the third order (Berger, 1988).

Berger (1988) expresses the insolation parameters of eccentricity, (e), obliquity (ε), and precession (e sin ω) as quasi-periodic functions of time by only retaining the most important higher-order terms from the above equations:

$$e = e_0 + \Sigma_i\, E_i \cos (\lambda_i t + \beta_i)$$

$$e \sin \omega = \Sigma i\, P_i \sin (\alpha_i t + \zeta_i)$$

$$\varepsilon = \varepsilon^* + \Sigma_i\, A_i \cos (f_i t + \delta_i)$$

where the E_i, P_i, and A_i are the amplitudes, λ_i, α_i, and f_i are the frequencies, and β_i, ζ_i, and δ_i are the phases. Contrary to the perception of many geologists, the frequencies associated with Earth's eccentricity, obliquity, and precession are not the single frequencies of 100 kyr, 41 kyr, and in the case of precession, 23 kyr and 19 kyr. Each of these parameters is quasiperiodic. The primary frequencies for these three orbital parameters and the amplitudes are given in Table I.1. The primary periods in the precession band range from 19 kyr to 24 kyr, the primary periods in the obliquity band range from 28 kyr to 54 kyr, and the primary periods in the eccentricity band range from 2 myr to 94 kyr.

Milankovitch's theory, which related variations in these orbital parameters to climate change, was challenged on several fronts. Until the late 1960's it was generally discounted in the U.S. Geological evidence and radiocarbon dating indicated more glacial advances during the last 80,000 years than could be explained by Milankovitch theory. The

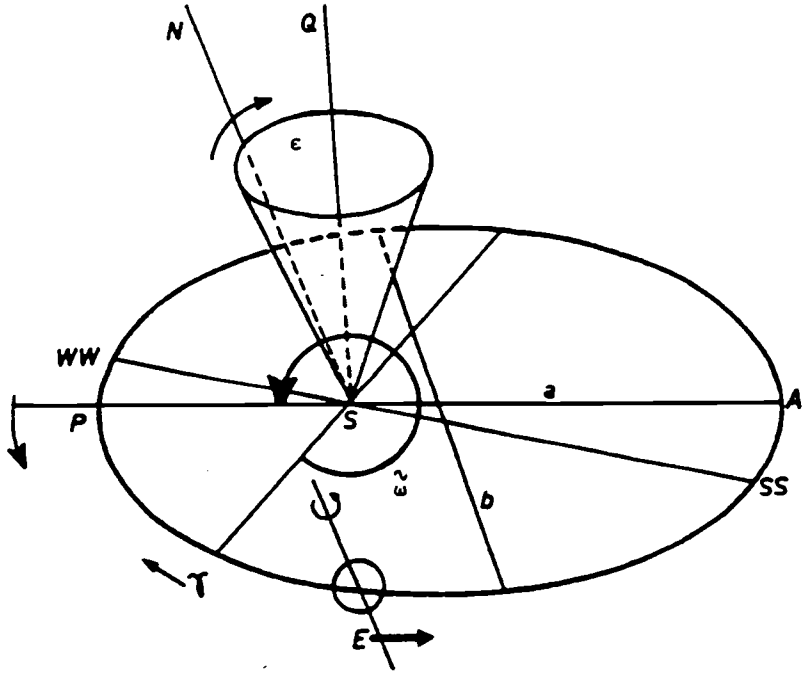

Figure I.2. Elements of the Earth's orbit, as illustrated by Berger (1988). The orbit of the Earth (E), around the Sun (S) is represented by the ellipse. The semimajor axis and semiminor axis are denoted a and b, respectively. WW and SS denote the modern winter and summer solstices, and g denotes the modern vernal equinox. Obliquity, e, is the inclination of the Earth's axis, the angle between the perpendicular (SQ) and the axis of rotation (SN). w is the longitude of perihelion relative to the moving vernal equinox.

accuracy of Milankovitch's astronomical solution was questioned. Finally, climatologists used simple annual mean energy balance models to contend that the climatic response to changes in insolation were too small to explain glacial advances.

During the late 1960's, improvements in radiometric dating, the study of sea level terraces and deep sea sediments led to a reexamination of the Milankovitch hypothesis by Broecker et al. (1968). Better paleoclimatological indices, geological time scale improvements, and improvements in the ability to compute orbital variations led to a general revival of the Milankovitch theory. The strongest evidence in support of the Milankovitch theory came in 1976 when Hays, Imbrie, and Shackleton demonstrated that variations in sea surface temperature, upwelling, and global ice volume all contained concentrations of variance at periods of 19 and 23 kyr (corresponding to precession band variations), 41 kyr (corresponding to obliquity band variations) and 100 kyr (corresponding to eccentricity band variations). Subsequently, Kominz and Pisias (1979) demonstrated significant coherence between ice volume variations as indicated by the proxy indicator $\delta^{18}O$ and paleo-insolation curves at 19 kyr, 23 kyr, and 41 kyr.

Since these studies, numerous lines of evidence from Pleistocene oceanic records have been compiled which support the Milankovitch theory. Recently, a climatic record from land was recovered that also shares similarities with Milankovitch band oscillations (Winograd et al., 1992). In addition, the influence of Milankovitch variations on climate has been extended to Pliocene and Cretaceous periods. This pervasive evidence provides a theoretical framework within which to study paleoclimatic change.

Table I.1. Periods associated with the main terms in the expansions of precession, obliquity, and eccentricity (from Berger, 1988)

Precession		**Obliquity**		**Eccentricity**	
Amplitude	**Period (kyr)**	**Amplitude**	**Period (kyr)**	**Amplitude**	**Period (kyr)**
0.0186080	23.716	-2462.22	41.000	0.011029	412.885
0.0162752	22.428	-857.32	39.730	-0.008733	94.945
-0.0130066	18.976	-629.32	53.615	-0.007493	123.297
0.0098883	19.155	-311.76	28.910	-0.004701	2035.441

CHAPTER TWO

REFINEMENT OF A HIGH-RESOLUTION, CONTINUOUS SEDIMENTARY SECTION FOR THE STUDY OF EQUATORIAL PACIFIC PALEOCEANOGRAPHY: ODP LEG 138

T.K. Hagelberg, N.G. Pisias, N.J. Shackleton, A.C. Mix, S. Harris

ABSTRACT

Ocean Drilling Program Leg 138 was designed to study the late Neogene paleoceanography of the equatorial Pacific at time scales of thousands to millions of years. Crucial to this objective was the acquisition of continuous, high resolution sedimentary records. It is well known that between successive APC (Advanced Piston Corer) cores, portions of the sedimentary sequence are often absent, despite the fact that core recovery is often recorded as 100%. To confirm that a continuous sedimentary sequence was sampled, each of the 11 drill sites was multiple APC cored. At each site, continuously-measured records of magnetic susceptibility, GRAPE (Gamma Ray Attenuation Porosity Evaluator) wet bulk density, and digital color reflectance were used to monitor section recovery. These data were used to construct a composite depth section while on site. This strategy often verified 100% recovery of the complete sedimentary sequence with two or three offset piston cored holes.

In this study these initial efforts are extended to document complete sediment section recovery and to investigate sources of error associated with both sediment density measurements as well as estimation of local sedimentation rate changes. These realizations were fully utilized during post-cruise processing of the GRAPE data. At each Leg 138 site, fine scale correlation (on the order of centimeters) of the GRAPE records was accomplished using the inverse correlation techniques of Martinson et al. (1982). After refining the

interhole correlation, GRAPE records from adjacent holes were "stacked" to produce a less noisy estimate of sediment wet bulk density. The continuity of the stacked GRAPE record can be documented in detail, and confirmed with reflectance and susceptibility records. Moreover, the stacking procedure allows development of error estimates for measurements present in more than one hole. The resulting stacked GRAPE time series have high temporal resolution (less than 1000 years) for the past 5 myr. The continuous framework presented here provides a common depth scale for all holes at each site, facilitating comparison of high resolution data from different holes. Finally, the high resolution mapping of cores from adjacent holes allows determination of the range of variability in sedimentation associated with both true sedimentation variability and the coring process at a given site.

INTRODUCTION

The primary objective of ODP Leg 138 was the acquisition of high resolution records of late Neogene climatic variability from the eastern equatorial Pacific (Mayer, Pisias, et al., 1992). Crucial to meeting this objective was verification that a continuous sedimentary section was recovered at each drill site. Portions of the sedimentary sequence are often missing between two successive Advanced Piston Corer (APC) cores in a single hole. Thus, the only means of meeting the objective of continuous section recovery is the drilling of multiple adjacent holes, offset in depth, at each site. A strategy was developed for Leg 138 to verify section recovery in close to real-time.

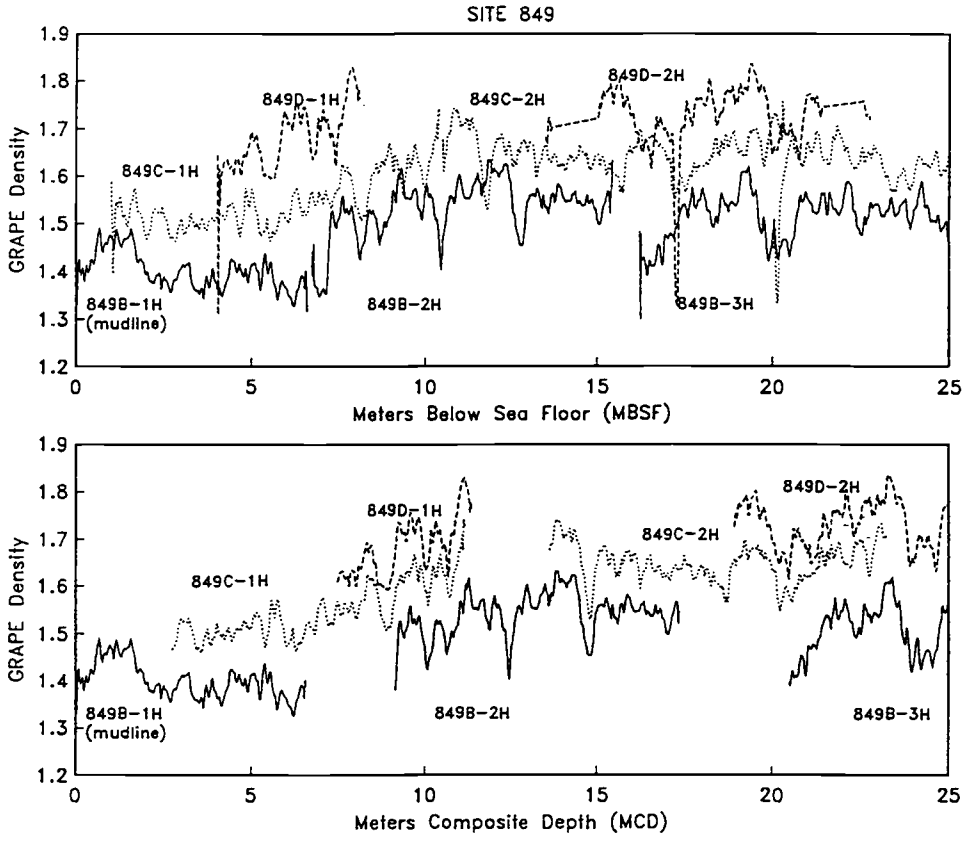

Figure II.1. Composite depth section example (GRAPE only) illustrating how cores are moved along a depth scale to arrive at a maximum correlation between adjacent holes. Top: uncleaned but smoothed GRAPE bulk density from the top 25 meters of Site 849 on the mbsf (meters below seafloor) depth scale. Bottom: Site 849 GRAPE data after cleaning and on the mcd (meters composite depth) scale. Solid line: Hole B; dotted line: Hole C; dashed line: Hole D. GRAPE density values for holes C and D are offset for clarity.

Development of a shipboard composite section involved the use of high resolution, nonintrusively measured sedimentary parameters (Gamma Ray Attenuation Porosity Evaluator or GRAPE, magnetic susceptibility, and digital color reflectance). These parameters were measured in almost every core and could be correlated between adjacent holes at every drilled site. Development of the shipboard composite depth section simply involved a translation of cores along a depth scale, as illustrated in Figure II.1. Depths measured in mbsf (meters below the sea floor) were transformed to a composite depth scale (mcd, meters composite depth) by adding a constant to the mbsf depth for each core (Mayer, Pisias, et al., 1992; Hagelberg et al., 1992).

Developing a composite depth scale by adding a constant to the original depth scale for every core is of only limited value to high resolution paleoceanographic studies. Differential stretching or squeezing within a 9 meter core due to physical disturbance during coring or by natural variations in local sedimentation between adjacent holes were not considered. From the high resolution GRAPE data as well as from core photos (Figure II.2), it is apparent that nonuniform distortion of sediment within a core is prevalent. To build continuous records of climate change from deep sea sediments, it is useful to know the relative level of distortion within a given core as well as between holes, on a scale of centimeters. If the level of depth domain distortion within cores can be quantified, the level of sedimentation rate variability at a single site can be examined.

Post-cruise processing of the GRAPE wet bulk density records from Leg 138 based on these considerations led to a refinement of the composite depth scale. This study documents how fine scale correlation on the order of centimeters was accomplished during post-Leg 138 study. The results are presented in four sections: 1) To introduce the problems which have necessitated composite section development, a historical review of previous strategies of composite depth formation is given, concluding with Leg 138 efforts. 2) The strategy for post-cruise refinement of the Leg 138 composite depth scales is presented. It is demonstrated how the individual GRAPE records in adjacent holes can be "stacked" to

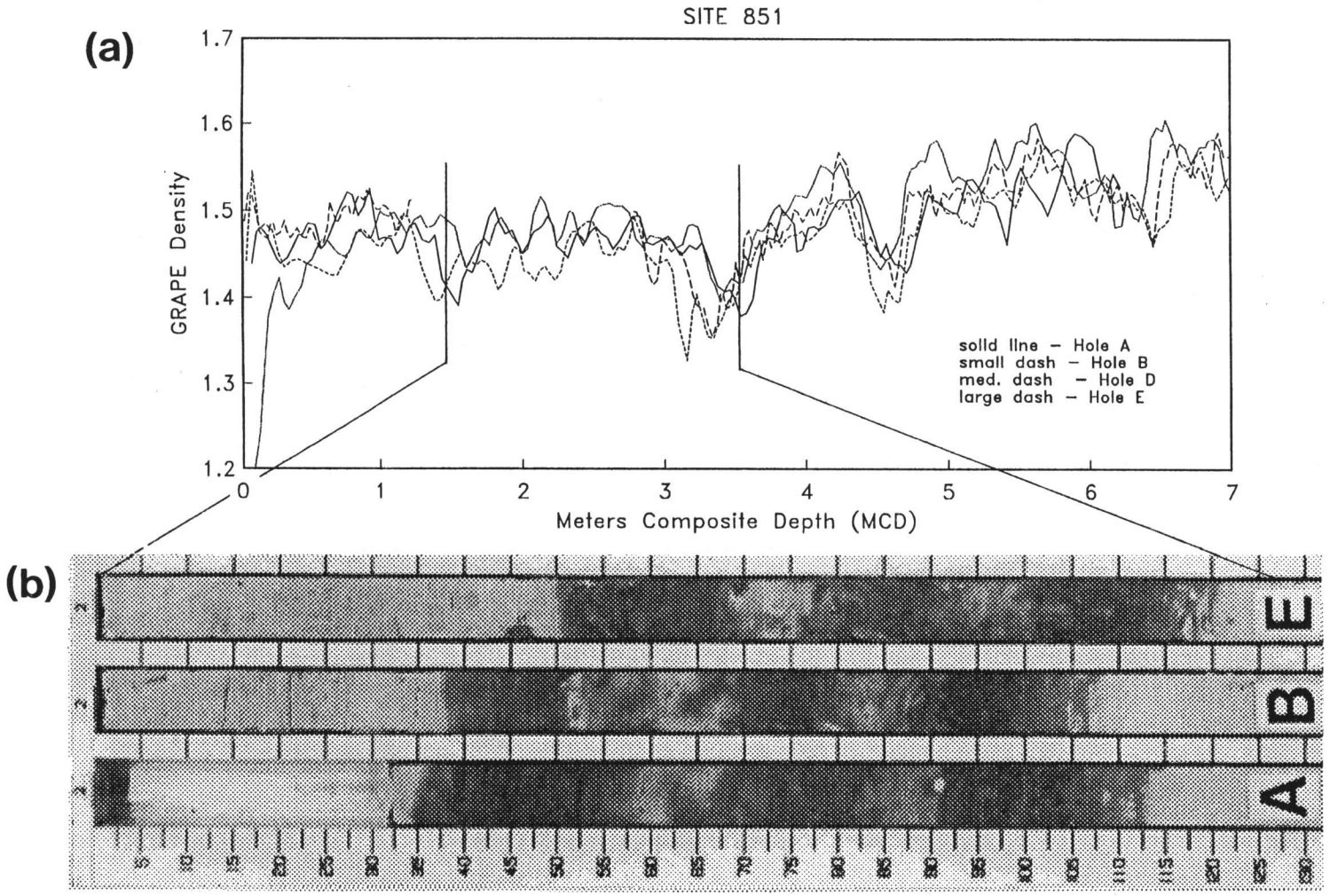

Figure II.2. Cores from 4 adjacent holes in Site 851 indicate distortion on a within cores (<9 meter) basis: (a) Site 851 GRAPE records on the shipboard mcd scale from Holes A (solid line), B (small dash), C (medium dash), and E (large dash). (b) core photos from the same depth interval (1.5 - 3.5 mcd) also illustrate small scale depth variability.

reduce variance in the bulk density estimates. 3) An error analysis on the amplitudes of GRAPE records for sites 846-852 are developed. Error estimates are useful because it is possible to analyze whether within-site as well as between-site differences in GRAPE amplitudes are significant. 4) The extent of within-site variability in depth scale distortion is investigated. Although some of the depth scale distortion in one core relative to another is likely to be induced by the coring process, some of it is likely to be related to the natural variability of sediment composition in a small geographic area. Characterizing this variability has not previously been possible. Variability in core distortion within a small geographic area has implications for sedimentation rate variability, and thus age models developed for those cores. In this last section, the level of distortion required to correlate adjacent holes at high resolution is used to predict sedimentation rate variability which may be anticipated purely as a result of small scale variations in sedimentation.

BACKGROUND

Composite Section Development History

In 1979, Deep Sea Drilling Project Leg 68 was dedicated to the use of the HPC (Hydraulic Piston Corer). This leg marked the beginning of recovery of relatively undisturbed sediment suitable for high resolution paleoceanographic analyses. Leg 68 also marked the beginning of drilling of overlapping holes at one site for the purpose of documenting the recovery of the complete stratigraphic record at a drill site (Prell, et al., 1982). Gardner (1982) and Kent et al. (1982) each constructed composite depth sections for multiple drilled sites 502 and 503 based on carbonate and magneto-stratigraphy. By DSDP Leg 69, Shackleton and Hall (1983) observed coring gaps of "several tens of centimeters" between successive 4.5 meter HPC cores in Site 504. This observation reinforced the need for multiple drilling of offset holes in order to obtain continuous paleoceanographic records. Before the advent of the HPC, however, precise stratigraphic correlation of this nature between adjacent holes could not be considered.

The first drilling leg to explicitly document the difficulties encountered in determining a continuous section was DSDP Leg 86 (Heath et al., 1984). Alignment of lithologic and magnetic boundaries demonstrated intervals of double cored sediment in holes 576 and 576B, and intervals of non-recovery in hole 576B. Heath et al. (1984) estimated from this alignment of cores that about 20% of HPC recovered core may be stratigraphically suspect. Shackleton et al. (1984) noted that biostratigraphic, magnetostratigraphic, and stable isotope events are not observed at the same reported depth (depth below the seafloor) in adjacent holes. These depth discrepancies were addressed by developing a composite depth section. Stable isotope and paleomagnetic stratigraphy were used to adjust sub-bottom depths for each hole at DSDP Site 577.

DSDP Leg 94 marked the beginning of APC (Advanced Piston Corer) use. During this leg considerable attention was given to between hole correlations and total section recovery (Ruddiman et al., 1987). Color variations caused primarily by variations in

%$CaCO_3$ and documented in core photographs were the primary correlation tool between adjacent holes at Sites 607 through 611. Ruddiman et al. (1987) documented in detail section continuity and depth offsets between adjacent holes. For the first time, a detailed discussion of factors leading to core recovery and coring gaps was presented. It was estimated that gaps on the order of 0.5m - 1m are present between successive cores in a given hole. During post-cruise scientific study, Ruddiman et al. (1989) and Raymo et al (1989) used visual core color, %$CaCO_3$, and magnetics to determine a high resolution composite section for sites 607 and 609. Continuous sedimentary sections for Sites 607 and 609 were formed by patching coring gaps from hole A with sediments from hole B.

During Ocean Drilling Program Leg 108 whole core magnetic susceptibility and p-wave velocity measurements taken at 5 cm resolution were used in attempts to correlate between offset holes at Sites 659-665, and Site 667 (Ruddiman, et al., 1988). This study represented a significant advance in documenting sediment section continuity in that it used rapidly acquired, non-intrusive, high resolution sedimentary parameters which are routinely collected during ODP legs. However, at several sites (662-665), magnetic susceptibility signals were too low, and P-wave velocities unreliable; at these sites, a composite section was determined by correlation of %$CaCO_3$ measurements and visual inspection of core color. As in Leg 94, this enabled formation of a continuous sedimentary section by splicing between two holes (e.g., Karlin et al., 1989).

An interhole mapping strategy was applied to Site 677 sediments during ODP Leg 111 (Alexandrovich and Hays, 1989). Tephra layers and biostratigraphic datums were used for initial correlations between Holes 677A and 677B. Subsequent analyses of carbonate and opal at 50 cm sampling intervals were used to correlate between the two holes drilled at Site 677 as well as to nearby DSDP Site 504. Inverse correlation was used to define an optimal mapping function between the records. Similar to the earlier study by Ruddiman et al. (1987), gaps of 1 to 2m were identified between successive cores in each hole. Subsequent higher resolution correlations with oxygen isotope analyses by Shackleton and

Hall (1989) and Shackleton et al. (1990) resulted in a detailed composite section for Site 677. In addition, Shackleton et al. (1990) documented the "growth" of composite section depths downcore. After aligning cores from parallel holes, it was demonstrated that the resulting composite "sample" of the sediment column was approximately 10% longer than the shipboard measured length of section actually cored.

During ODP Leg 114 a composite depth section was generated for Site 704 by using color boundaries and by correlating high resolution measurements of carbonate and opal data from the cores (Froelich et al., 1991). These data were compared to borehole log data to confirm intervals of missing and disturbed sediments. In limited intervals of the record, logging data were successfully correlated to coring records, and intervals of high coring disturbance were identified. A discrepancy between the composite section depths and logging depths was also noted.

Whole-core magnetic susceptibility measurements were used in lithostratigraphic correlation during ODP Leg 115 (Robinson, 1990). Magnetic susceptibility measurements were collected at 3-10 cm intervals in adjacent holes at sites 706, 709, 710, and 711 during Leg 115. A composite section was compiled for these sites. As with previous compositing efforts, gaps between successive cores on the order of 1-2 m were identified.

During ODP Leg 117, magnetic susceptibility measurements were also valuable in constructing stratigraphically complete records extending back 3.2 myr at Sites 721 and 722 (deMenocal et al., 1991, Murray and Prell, 1991). As noted during Leg 111, the complete composite section was approximately 7% longer than the depth of the section below the seafloor measured by the drill string.

Three adjacent holes were used in composite section development for Site 758, ODP Leg 121 (Farrell and Janecek, 1991). As with earlier legs, although APC recovery was 100% to 105%, gaps as large as 2.7 m were revealed between successive cores. Magnetic susceptibility was a primary correlation tool, but $\%CaCO_3$, coarse fraction, and oxygen isotope records were used to construct a composite section. Attempts were made to resolve

depth discrepancies using borehole logs. Although they were not resolved, comparison of logging data to core data was recognized as a means to resolve the discrepancy between ODP measured core depths and the composite section depths which are approximately 10% greater.

The consistent outcome of a "stretched" composite section presents several dilemmas. Section recovery is often documented at greater than 100%, meaning that the length of sediment recovered is greater than the advance of the drill string. However, the composite depth section suggests that only approximately 90% of the true sedimentary sequence is recovered in a single hole. In addition, if composite section lengths are 10% greater than drill string lengths, what is the true depth of the recovered sediment?

Leg 138

The importance of determining continuity of the sedimentary section, as indicated by the above efforts, suggests that composite section development should be a first order priority for paleoceanographic drilling studies. Much of the previous effort in composite section development was carried out post-cruise. During ODP Leg 138, composite section verification became a part of the drilling strategy. This produced two significant advances: First, section recovery was monitored in as close to real time as possible, and composite sections were developed at sea, as discussed below. Borehole logs were also incorporated as a means to resolve differences between drill string measured depths and composite depths. Second, sufficient high resolution data was collected from multiple holes and sites to consider the impact of small scale variability in sedimentation at a given location.

The motivation for concentrating efforts during Leg 138 on GRAPE wet bulk density measurements for interhole and intersite correlation lies in the effectiveness of wet bulk density as a carbonate proxy in the central and eastern equatorial Pacific (Mayer, 1980, 1991). The correlability of carbonate concentration over large regions of the Pacific was first demonstrated over 20 years ago by Hays et al. (1969), and was recently extended to

very broad regions using seismic studies (Mayer et al. 1986). During Leg 138, GRAPE and at least two other high resolution sedimentary parameters, magnetic susceptibility and digital color reflectance (Mix et al., 1992), were used to construct composite depth sections. Advantages of these three sedimentary parameters are that they are all collected nonintrusively, they are measured on every core, and the sampling resolution is 1 - 5 cm. Interactive software was written to examine these data from multiple holes and to develop a composite depth scale while at the drilling site. The sub-bottom depth for each core and each hole at a given site was adjusted in order to maximize the correlation between holes of each sedimentary parameter simultaneously. These adjustments involved an additive constant. In almost all cases this constant was positive which resulted in the depth of each core being slightly deeper in the composite section than its shipboard sub-bottom depth indicated. The effect of this adjustment can be seen by comparing the multiple hole GRAPE data in Figure II.1. The modified depth scale defined by these adjustments is referred to as meters composite depth (mcd). The three different sedimentary parameters often displayed distinctly different variations downcore, and can be considered as independent checks. Thus, confidence in the interhole correlations was derived from cross checking among these three parameters (Figure II.3).

The composite depth section formed at each site was at least 10% longer than the mbsf (meters below sea floor) scale (Hagelberg et al., 1992). As in previous ODP legs, although core recovery often exceeded 100%, less than 90% of the sedimentary sequence was recovered in a given hole. Preliminary shipboard results demonstrated that mbsf depths are closer to logging depths. A simple scaling of composite depths to log depths resulted in a good first order match between logs and core data (e.g., Figure 4 in Hagelberg, et al., 1992). Present work includes the integration of coring data and log data by mapping composite depths to log depths (e.g. Harris, et al., 1993).

Shipboard composite section results for sites 844 - 854 were presented in tabular and graphical form in the initial shipboard reports. From these data, a single spliced record of GRAPE and other parameters was obtained. These results set the stage for detailed post cruise studies and for refinement of the composite depth scale to the order of centimeters, as discussed below.

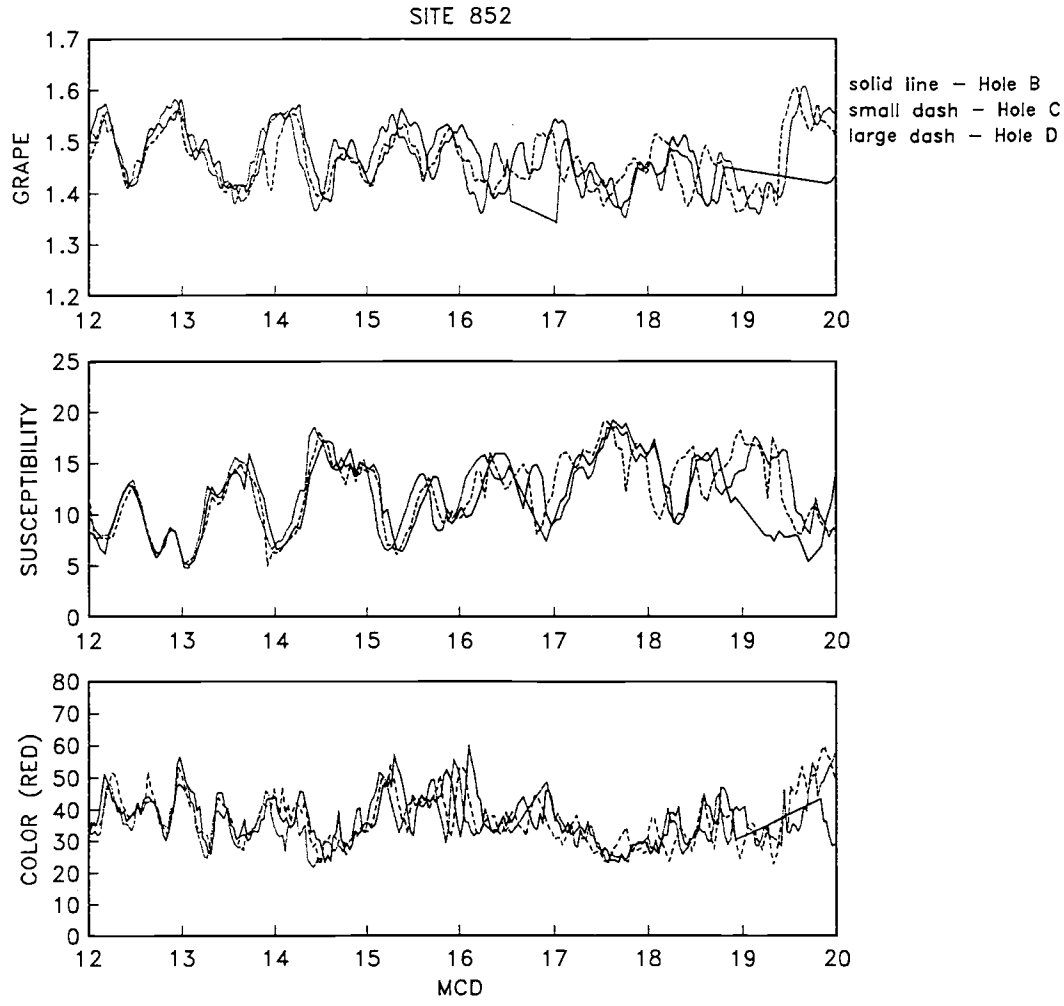

Figure II.3. GRAPE, magnetic susceptibility, and color reflectance records from a portion of Site 852 illustrate the presence of multiple measurements over the same depth interval.

METHODS

The quality of the high resolution multiparameter data collected during Leg 138 and the initial composite depth scale for each site makes this study possible. Note (Figure II.3) that from every Leg 138 site, there are multiple measurements of GRAPE wet bulk density, color, and magnetic susceptibility over much of the drilled section. In previous paleoceanographic studies making use of composite depth sections from adjacent holes, investigators have "spliced" between adjacent holes in order to arrive at a single high resolution record (e.g., Ruddiman et al., 1989, Raymo et al., 1989, Murray and Prell, 1991). Selecting a single hole as a reference, gaps between cores are filled in with data from the adjacent hole or holes. This is often the best approach, as isotopic and geochemical analyses on core data are time consuming, and collecting data from multiple holes is often not possible. With remote measurements such as GRAPE, however, it is possible to use all data from all holes at the same depth in a given site in order to arrive at a single estimate. One can consider each adjacent hole as a separate realization of the same sedimentary process. A less noisy estimate of the true wet bulk density can be accomplished by averaging the measurements. In order to do this, however, a composite depth scale on the order of the sampling interval (a few centimeters) is necessary. Thus, a refinement of the shipboard composite depth scale is required. During post cruise processing of the Leg 138 GRAPE data, such a refinement was accomplished through the use of inverse correlation.

Inverse correlation is a means of objectively correlating a distorted temporal or spatial signal to an undistorted (reference) signal, via some mapping function. The approach developed by Martinson et al. (1982) seeks to define a mapping function based on maximum coherence between the two signals and minimal error. The mapping function takes the form of a Fourier sine series. Inverse correlation has been used to correlate data between adjacent holes and nearby drill sites in previous DSDP and ODP studies (Alexandrovitch and Hays, 1989, de Menocal et al., 1991). It has become a common tool in paleoceanographic time series development (e.g., Martinson et al, 1987).

Although magnetic susceptibility and color reflectance data are equally suitable for high resolution correlation between holes, primary correlations were made using the Leg 138 GRAPE records for several reasons. First, GRAPE data are most easily related to a sedimentary parameter (%$CaCO_3$ in a two component carbonate-opal system). Second, the GRAPE data have a relatively high signal to noise ratio at most sites. Third, of the 3 measured parameters used in composite section development, GRAPE data have the highest sampling resolution. Samples can be collected continuously, and are limited by the width of the gamma ray beam that passes through the sediment core (approximately 1 cm). Finally, a single "shipboard splice" of GRAPE had been assembled for each site by N.J. Shackleton after shipboard composite depth section development. This spliced record, which used GRAPE from multiple holes, could be used as a reference signal for the other holes, as discussed below. While the susceptibility and color reflectance data were not used in the inverse mapping step the data provides a powerful independent check on the correlation defined using the GRAPE data. In a few limited intervals where GRAPE wet bulk density variability was low, susceptibility and color became primary correlation tools, however.

In limited intervals of each core (primarily at the core tops and bottoms), GRAPE data could not be used for composite section refinement due to anomalously low wet bulk densities. There intervals are given in Appendix I. For the purpose of developing a single composite GRAPE record, this was not a concern as the GRAPE data over these intervals were disregarded. In general the intervals of core containing anomalously low densities are disturbed, and are not of interest. However, for the purposes of developing a high resolution depth scale for all of the cored section, color reflectance should be used in these intervals.

GRAPE measurements have much high frequency variability, some of which is noise (see discussion below). To improve the correlation, records were smoothed to a 2 cm resolution using a Gaussian filter. As discussed and illustrated by Martinson et al., (1982), filtering aids recovery of the optimal mapping function by improving the first guess. All of the GRAPE records used in mapping were smoothed beforehand in this manner.

For the leg 138 drill sites, selection of a reference signal for which to map every core ("distorted" signal) is necessarily somewhat arbitrary, as virtually every core can be expected to contain some level of distortion. For each site, the reference signal used was the GRAPE wet bulk density shipboard splice developed by Shackleton. The shipboard splice was subjectively chosen from a qualitative assessment of the amplitude and resolution of the GRAPE records between adjacent holes at each site. During the construction of the spliced record attempts were made to minimize the amount of necessary jumps between adjacent holes in arriving at a single record. An example section from Site 849 is given in Figure II.4. Shipboard splices of GRAPE wet bulk density for sites 844-854 are illustrated in the backpocket figure of the Leg 138 Initial Reports volume (Mayer, Pisias, et al., 1992). The tie points for each splice are given in Table II.1. Because the shipboard splice made use of multiple holes at each site, and because the shipboard splice avoided the use of obviously distorted or disturbed sections of core, this record is the best choice of a *relative* composite reference signal for inverse correlation. Although not all core distortion can be addressed in this manner, all of the multiple hole data can be correlated to a common depth scale. Thus, a *relative* measure of core distortion is available. In a few cases, the section of core chosen as the reference was discovered to be more distorted than the same section in other holes after mapping. Further adjustments relating to distortion of the final stacked record were embedded in time domain chronology adjustments (Shackleton, 1993 in prep).

At Sites 846-852, individual cores in each hole were mapped, in turn, to the corresponding section of the shipboard splice. Note that in some intervals this means that part of a record is mapped to itself. For each core, a mapping function which transforms depth in core in mcd (meters composite depth) to depth in core rmcd (revised meters composite depth) was produced. The number of coefficients used in the mapping function was chosen iteratively. Beginning with 3 Fourier coefficients, additional coefficients were added until the coherence between the reference (splice) and the distorted core signal was maximized, or until a further increase in coherence required an unusually large core distortion. Although inverse correlation is in itself an objective approach to signal correlation, the final step of determining the number of Fourier coefficients to be used in determining an optimal mapping function is subjective. In this study, attempts were made to use the smallest number of Fourier coefficients necessary to obtain maximal coherence, and attempts were made to minimize large changes in the slope of the mapping function. The number of coefficients used in mapping each core ranged from 7 to 47. Figure II.5 gives examples of 2 mapping functions from two Site 847 cores, one where 15 coefficients gives very high coherence, and one where 47 coefficients were used. In both examples the correlation between the initial unmapped core interval and the corresponding interval of the shipboard splice increases noticeably without inducing a large change in the mapping function.

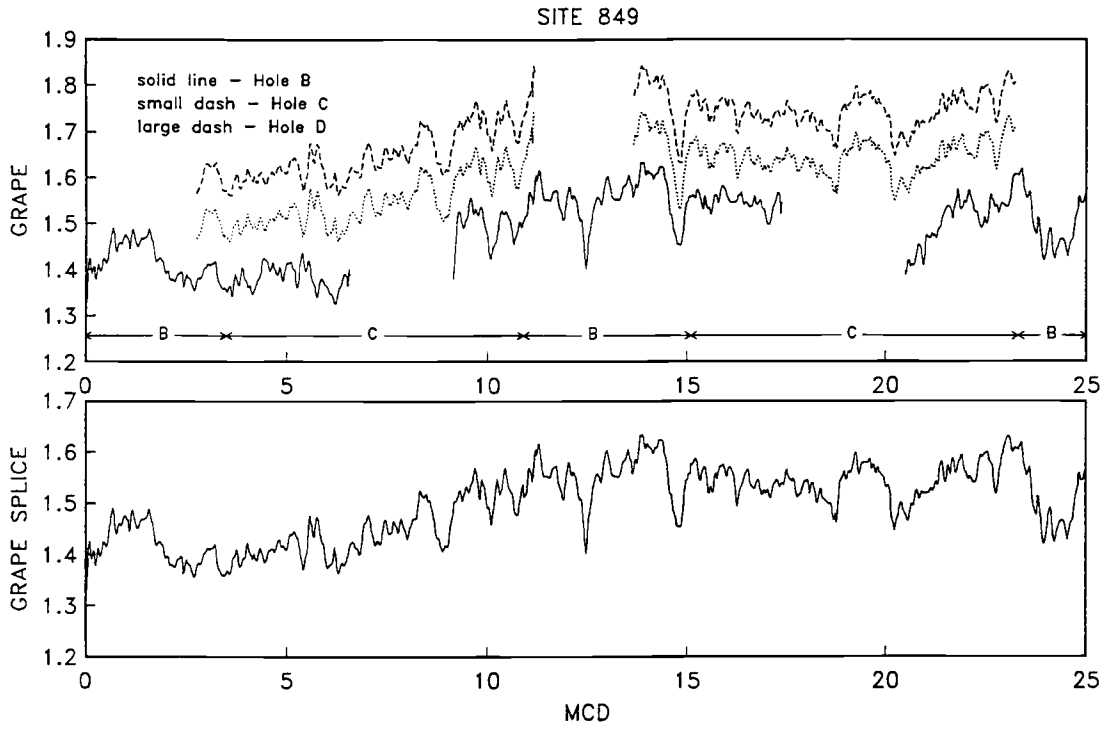

Figure II.4. Development of the "shipboard splice" for the top 25 meters of Site 849. Top: GRAPE density from 3 holes from Site 849 on the composite depth scale (solid line: hole B; dotted line: hole C; dashed line: hole D). The letters at the bottom indicate which hole the shipboard splice was selected from for that depth interval. GRAPE values for holes C and D are offset for clarity. Bottom: The spliced GRAPE record that results from moving between holes as indicated in top panel.

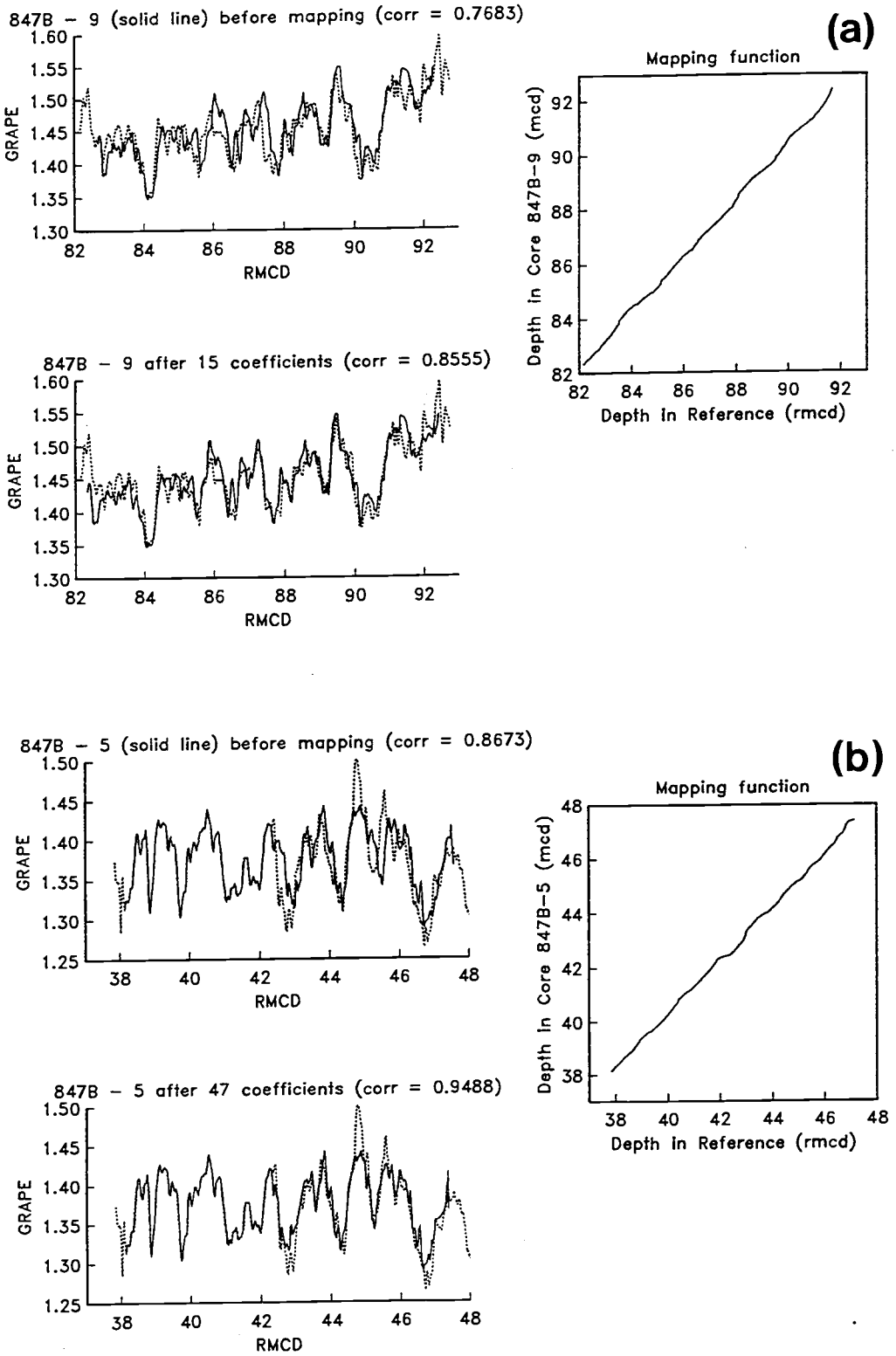

Figure II.5. Examples of before (above) and after (below) inverse correlation from two cores at Site 847. The mapping function between depth in core (mcd) and depth in the shipboard splice (rmcd) is shown at right. A: 15 Fourier coefficients used. B: 47 Fourier coefficients used in inverse correlation.

Table II.1. The tie points used to construct the shipboard splices of GRAPE (Mayer, Pisias, et al., 1992).

Site	844	845		846		847		848	
MCD	**Hole**	**MCD**	**Hole**	**MCD**	**Hole**	**MCD**	**Hole**	**MCD**	**Hole**
0.0	C	0.0	A	0.0	B	0.0	B	0.0	B
4.5	B	6.0	B	4.0	C	5.0	C	1.3	A
14.4	C	9.5	A	10.5	B	8.0	B	11.8	C
18.3	B	27.0	C	16.0	D	14.0	C	16.9	B
21.5	C	29.8	A	23.0	B	21.2	D	24.5	D
29.7	D	36.8	C	27.6	D	24.5	C	27.8	B
38.2	B	40.4	A	32.0	B	32.2	D	35.0	D
43.2	C	49.0	B	35.0	C	38.0	B	36.5	B
52.0	B	50.5	A	42.2	D	42.3	D	43.0	C
55.7	C	58.8	B	45.7	C	46.0	C	47.2	B
62.5	B	60.9	A	53.0	D	52.0	D	53.3	C
65.8	C	69.2	B	56.5	B	55.5	C	57.4	B
70.9	B	72.2	A	58.5	C	64.4	D	64.5	C
76.6	C	79.5	A	64.3	B	69.0	C	69.5	B
83.8	B	82.5	A	67.7	D	75.8	D	76.0	C
86.9	C	90.6	B	76.5	B	81.0	C	81.0	B
93.6	B	95.2	A	80.0	D	84.4	D	87.5	C
96.3	C	101.3	B	85.0	B	90.5	C	92.0	B
104.0	B	108.0	A	89.0	D	96.5	B	98.0	C
110.5	C	111.3	B	95.5	C	100.0	C	101.7	B
115.0	B	115.1	A	98.3	B	107.0	D		
121.4	C	117.1	B	99.0	D	114.0	C		
125.0	B	119.2	A	107.3	C	116.5	D		
126.9	C	123.0	B	111.0	D	122.2	C		
133.9	B	127.5	A	117.0	C	126.5	D		
138.3	C	134.2	B	120.3	D	134.5	C		
146.3	B	136.4	A	128.0	C	138.5	D		
148.5	C	145.0	B	130.5	D	143.8	C		
157.0	B	151.0	A	140.0	C	147.8	B		
159.4	C	156.4	B	142.4	D	155.0	C		
167.1	B	159.3	A	145.8	C	159.2	B		
170.7	C	167.0	B	152.2	B	202.3	C		
176.2	B	174.5	A	155.0	D	204.8	B		
179.1	C	178.1	B	160.0	C				
184.3	B	182.8	A	163.0	B				
190.6	C	188.3	B	165.0	D				
197.6	B	192.0	A	173.0	B				
		197.7	B	176.5	D				
		203.2	A	180.2	C				
		210.3	B	185.2	B				
		214.0	A	188.5	C				
		218.7	B	194.3	B				
		233.5	A	200.0	C				
				206.5	B				
				209.7	D				
				215.3	B				
				224.2	D				
				228.0	B				
				236.5	D				
				240.7	B				
				248.0	D				
				252.0	B				
				260.8	D				
				261.5	B				

Table II.1, ctd.

Site 849		850		851		852		853	
MCD	**Hole**	**MCD**	**Hole**	**MCD**	**Hole**	**MCD**	**Hole**	**MCD**	**Hole**
0	B	0.0	A	0	D	0.0	A	0.0	D
3.5	C	6.4	B	9.3	C	1.1	D	7.5	B
10.9	B	10.4	A	14.5	B	10.4	B	13.0	D
15.1	C	17.0	B	18.2	C	15.0	D	20.0	B
23.3	B	20.8	A	23.7	B	20.5	B	29.2	D
27.2	C	28.2	B	30.0	E	28.6	C	31.1	B
34.4	B	32.3	A	32.3	B	35.7	D	32.6	D
38.9	C	38.0	B	41.2	C	42.0	C	41.8	B
42.7	B	45.0	A	47.0	E	47.0	D	52.3	B
49.2	C	48.2	B	54.0	B	52.0	B	60.6	D
54.5	B	54.0	A	61.8	C	60.2	C	62.7	B
60.4	C	61.0	B	66.8	B	67.8	D	71.0	D
64.1	B	65.0	A	72.8	C	74.5	B		
72.0	C	71.9	B	75.7	B	81.5	C		
75.8	D	74.5	A	83.2	C	90.1	D		
79.8	C	80.4	B	86.4	B	95.2	B		
84.5	D			92.4	C	103.8	D		
88.7	B			99.6	B	106.7	B		
92.3	C			103.8	C	114.2	C		
98.6	B			108.5	B	121.3	4		
103.7	C			115.3	C				
110.1	B			121.6	B				
114.0	C			126.8	C				
116.5	D			132.3	B				
123.4	B			137.5	C				
125.5	D			142.4	B				
128.8	B			147.1	C				
137.0	D			149.9	B				
151.5	B			168.5	E				
157.7	D			174.0	B				
163.0	B			182.6	E				
167.5	D			188.3	B				
175.0	B			194.5	E				
180.5	D			203.5	B				
186.2	B			208.3	E				
192.6	D			217.0	B				
198.5	B			224.5	E				
202.5	D			230.8	B				
208.9	B			236.2	E				
215.0	D			238.0	B				
220.5	B			245.0	E				
225.5	D			252.4	B				
231.0	B			261.1	E				
236.8	D			264.0	B				
243.4	B			272.0	E				
245.4	D			272.0	E				
252.9	B			277.8	B				
257.8	D			284.5	E				
263.5	B			293.3	B				
268.0	D			296.2	E				
270.9	B			301.0	B				
286.7	D			309.8	E				
293.6	B			316.3	B				
297.2	D			320.6	E				

Table II.1, ctd.

Site 849, ctd.

MCD	Hole
304.2	B
307.2	D
315.5	B
317.8	D
326.3	B
329.1	D
336.8	B
338.9	D
345.8	B
350.3	D
357.8	B
361.0	D
367.9	B

Site 851,ctd.

MCD	Hole
329.0	B
339.4	E
340.5	B
350.7	E
358.0	B
362.0	E
368.5	B
373.0	E
380.3	B

Site 854

MCD	Hole
0	C
3.2	B
4.8	C
14.0	B
15.8	C
23.6	B
39.3	C
41.8	B

RESULTS

Approximately the past 5 myr from Sites 846 through 852 was multiple APC cored during Leg 138. Beyond this point, multiple holes are not available at every site for high resolution correlation. For each of 241 cores from multiple holes, a mapping function was calculated using the technique of Martinson et al. (1982). The mapping function was calculated to maximize the correlation between each individual core and the reference GRAPE record. Table II.2 gives the correlation of each core to the reference splice before and after mapping. On average correlations improved from 0.755 (+/- .16) to 0.923 (+/- 0.07). The mapping function defined by the inverse mapping technique allows each depth within a core to be uniquely mapped into the GRAPE reference record. This transformation changes the depth of any sample in mcd (exclusive of those samples that are a part of the reference) to a new depth scale, rmcd. The transformed depths are available on CD-Rom.

To check that the mapping functions defined on the GRAPE data are consistent with the other high resolution data available for the Leg 138 sites, the mapping functions were applied to the corresponding downcore records of magnetic susceptibility and color. The example given in Figure II.6 demonstrates that the improvement in correlation between GRAPE data from three holes at Site 852 after inverse correlation is also seen in susceptibility and color records. Thus, the susceptibility and color reflectance records provide a means of confirming the high resolution correlation based on GRAPE. Checks of the GRAPE-defined mapping function with the susceptibility and color reflectance data revealed that in several parts of the mapping function required revision in order to reconcile all three data sets. As these intervals were rather short in duration (often less than a meter), manual adjustments proved better than inverse correlation in these cases.

After mapping all of the multiple hole GRAPE data to a common depth scale (rmcd), the data from each hole were combined to form a single depth series. Data were averaged by binning the raw data into 2 cm sampling intervals ("raw" data refers to unsmoothed GRAPE data processed shipboard where multiple measurements at a given depth have

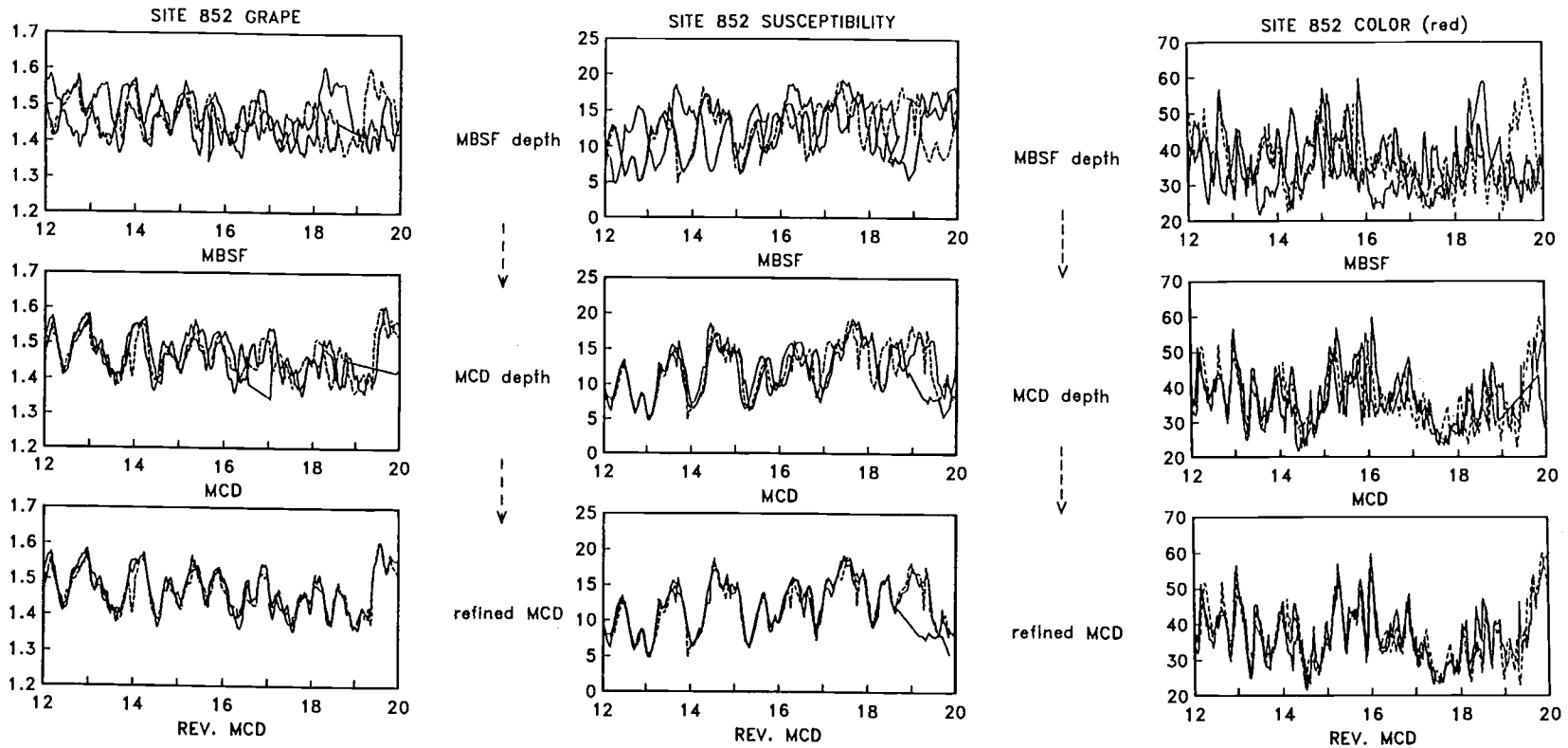

Figure II.6. GRAPE, magnetic susceptibility, and color reflectance data from 3 cores in a portion of Site 852. Top: Records from adjacent holes on the mbsf scale. Middle: the same records on the mcd scale. Bottom: the same records after inverse correlation on the revised composite depth (rmcd) scale.

already been binned and averaged). The average number of measurements in each of these 2 cm intervals for sites 846-852 is listed in Table II.3. Binning of the raw data adds a sharp jittery character to the resulting record. This noise is unrealistic as it is an artifact of the binning, and is not representative of any of the individual hole records. To reduce this effect, the binned data were smoothed using a 6 cm wide gaussian window in the depth domain. Binned and smoothed stacked GRAPE records for Sites 846-852 are shown in Figure II.7.

One can consider each record of GRAPE bulk density (from each hole at a given site) as a separate realization (ensemble) of the same process having uncorrelated errors. Averaging the multiple measurements from the adjacent holes decreases the level of noise in the estimates. The number of measurements in each 2 cm bin are not uniformly distributed in depth (nor in time). The average number of estimates at each site that are combined to increase the signal/noise level are given in Table II.3.

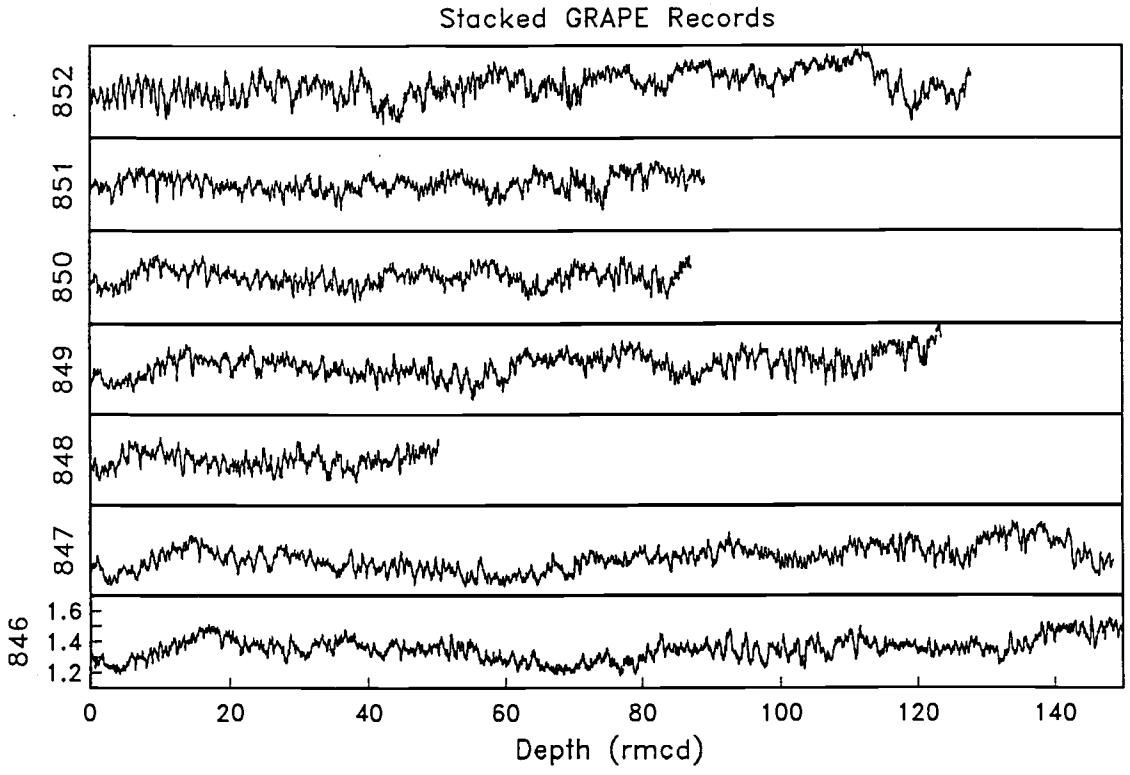

Figure II.7. Stacked GRAPE records from Sites 846-852 after binning, averaging, and smoothing individual hole records that have been correlated the the shipboard splice through inverse correlation.

Table II.2. Correlation of each core to the shipboard splice reference before and after mapping with inverse correlation. The number in parantheses is the number of coefficients used in the mapping function.

SITE 846

CORE	HOLE A		HOLE B		HOLE C		HOLE D	
1	.5764	.7051 (31)	.7534	.8853 (47)	.8549	.9715 (31)	.8122	.8729 (15)
2			.9282	.9669 (31)	.7682	.8799 (31)	.8662	.9778 (7)
3			.6552	.9276 (31)	.7948	.8612 (23)	.8270	.9370 (31)
4			.7281	.9256 (23)	.9544	.9619 (15)	.5427	.8626 (23)
5			.6302	.8100 (15)	.7644	.9628 (31)	.5798	.9229 (23)
6			1.000		.7244	.9306 (31)	.5394	.8723 (31)
7			.6645	.8568 (15)	.6939	.9120 (39)	.7319	.9870 (7)
8			.7270	.8678 (7)	.7707	.9137 (15)	.8068	.9695 (39)
9			.8967	.9383 (15)	.8947	.9518 (31)	.8150	.8555 (7)
10			.7129	.9518 (31)	.9282	.9639 (31)	.9743	.9811 (15)
11			.8163	.9238 (19)	.6985	.9037 (31)	.7977	.9604 (23)
12			.6802	.8333 (11)	.6750	.8803 (23)	.5652	.9710 (23)
13			.8204	.9334 (23)	.8257	.9606 (31)	.9922	.9948 (7)
14			.4701	.6377 (15)	.6398	.8933 (31)	.6538	.8309 (7)
15			.9312	.9764 (17)	.9091	.9870 (31)	.9222	.9880 (23)
16			.4237	.9006 (27)	.8849	.9613 (31)	.8771	.9954 (47)
17			.8812	.9508 (31)	.9041	.9537 (23)	.4440	.9604 (39)
18			.7718	.9702 (23)	.6685	.9620 (23)	.7410	.8892 (15)
19			.6416	.9184 (19)	.9215	.9773 (31)	.3057	.8218 (39)
20			.5732	.8883 (31)	.5129	.8970 (31)	.4713	.9245 (31)
21			.6717	.9056 (7)			.1325	.7281 (23)
22			.9166	.9602 (15)			.6465	.8631 (15)
23			.5778	.8601 (23)			.4808	.8941 (23)
24			.9808	.9831 (7)			.4484	.5360 (7)
25			.9755				.4412	.7088 (7)
26			1.000					

SITE 847

CORE	HOLE A		HOLE B		HOLE C		HOLE D	
1	.8924	.9293 (15)	.9118	.9798 (23)	.8957	.9554 (23)	(NO GRAPE)	
2			.9345	.9823 (23)	.8480	.9920 (47)	.8970	.9367 (31)
3			.8618	.8920 (7)	.8594	.9647 (31)	.8037	.8989 (15)
4			.8123	.9016 (39)	.5532	.8092 (31)	.8425	.9538 (31)
5			.8673	.9488 (47)	.7564	.9703 (50)	.6685	.8903 (31)
6			.7869	.8839 (15)	.8093	.9922 (47)	.8220	.9309 (15)
7			.8061	.9168 (23)	.8590	.9750 (31)	.6648	.9653 (47)
8			.5455	.8473 (31)	.6277	.8925 (23)	.7164	.9360 (23)
9			.7683	.8555 (15)	.9199	.9749 (47)	.8090	.9577 (15)
10			.4147	.8533 (23)	.4300	.8828 (31)	.6148	.7896 (15)
11			.8325	.9258 (23)	.4848	.9393 (47)	.7911	.9728 (47)
12			.8280	.9113 (31)	.6573	.9587 (23)	.4670	.9712 (39)
13			.9569	.9746 (23)	.8460	.9033 (23)	.8790	.9881 (15)
14			.8854	.9595 (15)	.6467	.8485 (15)	.9312	.9814 (39)

SITE 848

CORE	HOLE A		HOLE B		HOLE C		HOLE D	
1	.7562	.9846 (39)	.8548	.9564 (23)	.7430	.8103 (7)	.8478	.9206 (15)
2			.5216	.9463 (31)	.7541	.9667 (31)	.6290	.9096 (23)
3			.5773	.9718 (39)	.8238	.8923 (31)	.6450	.9046 (23)
4			.9037	.9777 (47)	.8316	.9328 (31)	.6459	.9262 (23)
5			.7216	.9879 (39)	.6581	.8220 (23)	.4243	.7573 (15)

Table II.2, ctd.

SITE 849

CORE	HOLE A	HOLE B		HOLE C		HOLE D	
1	(NO GRAPE)	.7700	.9205 (47)	.8676	.9938 (23)	.9218	.9613 (15)
2		.7765	.9656 (47)	.9895	.9944 (47)	.7525	.8446 (15)
3		.7600	.9042 (31)	.8512	.9572 (39)	.7125	.8724 (23)
4		.6061	.8785 (31)	.5232	.9511 (47)	.6829	.8901 (31)
5		.6202	.9660 (47)	.8337	.9557 (31)	.8611	.9256 (23)
6		.9424	.9880 (47)	.9009	.9757 (39)	.8399	.8862 (31)
7		.7434	.9769 (47)	.7224	.9253 (23)	.8459	.9593 (47)
8		.7256	.9534 (23)	.8125	.9770 (31)	.6761	.9557 (31)
9		.9179	.9704 (7)	.9008	.9799 (31)	.7519	.9184 (15)
10		.9175	.9347 (31)	.6598	.9769 (47)	.3183	.9258 (23)
11		.7714	.9594 (15)	.6055	.7614 (31)	.8698	.9911 (47)

SITE 850

CORE	HOLE A		HOLE B	
1	.9413	.9874 (23)	.8161	.9568 (23)
2	.7944	.9450 (15)	.7921	.9488 (23)
3	.4900	.9265 (23)	.4998	.9254 (39)
4	.8221	.9639 (47)	.8323	.9794 (47)
5	.6778	.8252 (23)	.6805	.9350 (47)
6	.9221	.9796 (15)	.9371	.9734 (31)
7	.8091	.9864 (47)	.8375	.9301 (47)
8	.7650	.9756 (47)	.8269	.9797 (47)

SITE 851

CORE	HOLE A		HOLE B		HOLE C		HOLE E	
1	.2952	.6123 (7)	6818	8195 (15)	.3567	.7742 (23)	.7149	.8427 (23)
2			.8810	.9179 (7)	.7551	.9259 (23)	.4377	.8254 (23)
3			.6882	.9265 (39)	.5827	.8833 (31)	.4944	.9132 (47)
4			.8773	.9975 (7)	.7679	.9305 (39)	.7881	.8746 (15)
5			.6331	.8389 (23)	.7670	.8786 (39)	.8085	.9566 (31)
6			.7452	.9720 (23)	.7097	.9558 (47)	.8394	.9215 (23)
7			.8328	.9813 (47)	.8196	.9394 (15)	.8017	.9273 (31)
8			.8476	.9741 (23)	.6362	.9097 (23)	.7112	.9277 (39)

CORE	HOLE D	
1	.9500	.9590 (31)
2	.3526	.8202 (23)

SITE 852

CORE	HOLE A		HOLE B		HOLE C		HOLE D	
1	.9055	.9647 (39)	.7469	.9578 (47)	.6007	.8671 (15)	.9848	.9945 (47)
2			.5145	.9712 (15)	.8312	.9409 (23)	.8827	.9019 (15)
3			.8087	.9909 (31)	.8734	.9314 (23)	.8760	.9672 (47)
4			.8415	.9618 (47)	.9703	.9752 (23)	.9618	.9779 (31)
5			.8324	.9453 (39)	.9659	.9859 (49)	.9618	.9779 (31)
6			.8066	.9914 (15)	.8087	.9439 (47)	.8286	.9186 (15)
7			.8205	.9387 (31)	.8253	.9937 (47)	.9312	.9902 (47)
8			.9079	.9659 (31)	.8132	.8975 (23)	.7660	.8927 (23)
9			.8257	.8819 (31)	.9943	.9944 (7)	.9164	.9670 (47)
10			.9209	.9902 (39)	.7532	.8672 (31)	.9219	.9440 (31)
11			.9589	.9780(23)	.4822	.6413 (23)	.9279	.9664 (23)
12			.6103	.9329 (23)	.9851	.9893 (15)	.8678	.9644 (23)

Table II.3. Average number of measurements in each 2 cm bin for sites 846-853.

Site	Depth Range	Avg. # measurements
846	0-287 mcd	1.90
847	0-148 mcd	2.47
848	0-50 mcd	2.61
849	0-123 mcd	2.25
850	0-87 mcd	1.60
851	0-89 mcd	1.42
852	0-128 mcd	2.87

DISCUSSION

Error Estimation

Given that multiple estimates of GRAPE measurements are available at each depth, investigations into errors associated with these records can be addressed. First, what is the source of measurement error in the amplitudes of GRAPE wet bulk density estimates? Boyce (1976) gave a review of the errors encountered in estimating bulk density from GRAPE. A small error (a maximum of 2%) in wet bulk density determination occurs if the grain density of the lithology under examination is not accurately known. Also, error can result from random gamma-ray emissions, which have been determined to be on the order of 2% (Boyce, 1976). This error is reduced during shipboard processing of GRAPE data, as multiple measurements taken at exactly the same depth (while the Multi-Sensor track pauses to take magnetic susceptibility and P-wave velocity measurements) are averaged to produce the "raw" GRAPE measurements. If the cored material does not completely fill the core liner, the gamma ray passing through the core passes through air, water, or slurry, lowering the resulting bulk density measurement. In addition, the gamma ray beam does not in this case pass through the center of the core. These possible sources of error as well as variation in the thickness of the core liner can influence GRAPE wet bulk density estimates.

There are a number of ways to estimate sampling errors on the resulting interpolated GRAPE estimates. For example, one could consider the errors as a residual deviation of the raw data values from the resulting smoothed estimate. This involves a comparison of raw data to filtered data that is derived from the raw data. On the other hand, one could consider the errors as simply the standard deviation of the data within any one 2 cm bin, independent of the surrounding data. In practice, the differences between the two methods are not significant. The latter method was chosen as it is more directly tied to the scatter

of the raw data within any 2 cm interval. In addition, calculating the standard deviation of the binned data disregards the filtering effects of the Gaussian smoother. Figure II.8 shows 1 standard deviation errors for representative portions of sites 846-852.

There are two significant advantages to having error estimates. First, similar features between the amplitude of GRAPE (carbonate) events at different sites can be quantitatively compared. The primary paleoceanographic objective using the GRAPE data is to study spatial changes in carbonate concentration with respect to latitude and longitude in the eastern equatorial Pacific. With error estimates, it is possible to quantify whether individual events between sites record significant changes in GRAPE (carbonate), or if site to site differences are on the same order as the error at any one site. The second advantage is that one can determine if adjacent features (GRAPE highs and lows) within a given site are significantly different from one another. Error estimates such as this have not been available previously for this kind of geologic data. Both of these determinations are illustrated in the following example.

Shackleton (1992) combined bio- and magneto-stratigraphic events with GRAPE wet bulk density features from the shipboard splices for Sites 846-852 to develop an internally consistent chronostratigraphic framework. A series of GRAPE "events" were identified based on their relation to bio- and magnetostratigraphy, and were correlated to other sites using the GRAPE record. An example event, event "F" was identified as a sharp density maximum that occurs below the Gilbert/Gauss magnetic boundary and near two nannofossil biostratigraphic events, the extinction of *Reticulofenestra pseudoumbilicus* and the upper limit of *Spenolithus abies* (Shackleton et al., 1992). The age of this event is approximately 3.44 Ma. The depth of this event at each site as determined in the shipboard splice is given in Table II.4 (since depths are given from the shipboard splice, mcd=rmcd, depths originally from Shackleton et al. (1992)). Figure II.9 shows the GRAPE density from these depth intervals in the stacked records, with 1 standard deviation errors. Qualitatively, the peaks at Sites 846 and 847 are fairly large relative to the peaks at Sites

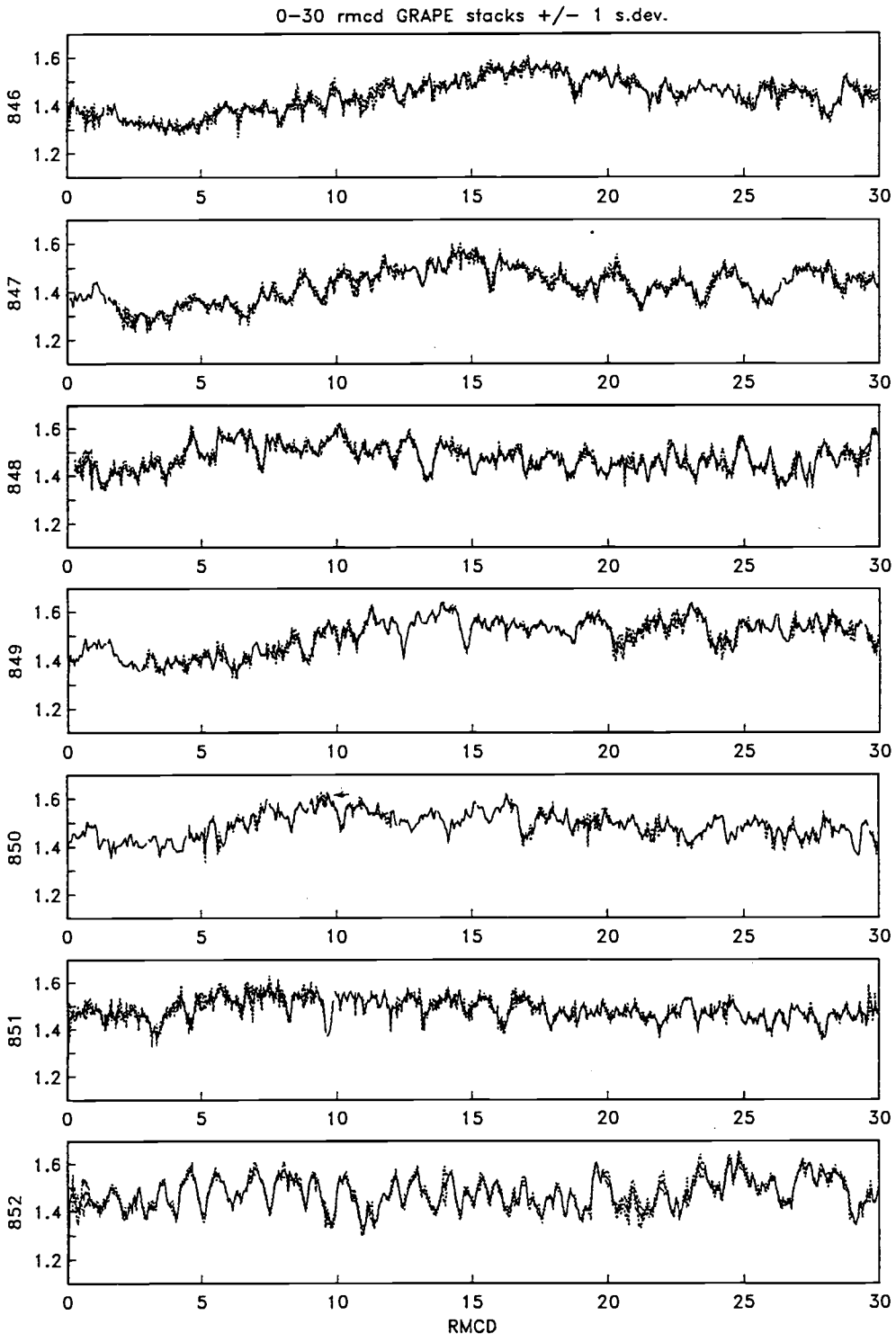

Figure II.8. Stacked GRAPE records from Sites 846 - 852 with +/- 1 standard deviation envelopes (except for intervals where only 1 measurement is present). The 30 meter sections shown are representative for each site.

848 and 850. Since error estimates on the density records have been developed, the significance of these differences can be accomplished through an analysis of variance.

A traditional one-way analysis of variance only yields information on whether a set of samples are statistically different from one another or not, with no information on how the individual samples may differ. A modification of this traditional test known as Bonferroni's method (Rice, 1988) allows a simultaneous comparison between individual pairs of measurements. From the seven sites, there are 21 possible pairwise comparisons. A set of simultaneous 95% confidence intervals for any two pairwise comparisons Y_{i1} and Y_{i2} is

$$(\overline{Y}_{i_1} - \overline{Y}_{i_2}) \pm s_p \frac{t_{18}(.025/21)}{\sqrt{J_i}} \qquad (3)$$

where Y_{i1} and Y_{i2} are the sample means, t is the bonferroni t statistic, s_p is the square root of the pooled variance (=0.0221), and J is the average number of observations in each sample (3). The bonferroni t statistic for a .05 significance level in this case is $t_{18}(0.025/21) = 3.46$. Thus, if any two of the stacked GRAPE estimates from Sites 846 - 852 differ by more than 0.0441, they are significantly different from one another at a .05 level. Using this test, the event F GRAPE maxima in Figure II.9 are significantly different from one another with the exception of 4 pairs of sites: 846/849, 847/849, 847/850, and 848/852. The remaining 17 possible pairwise comparisons are significantly different at a .05 level. Although this is an analysis of only a single isolated GRAPE event, the implication from this example is that most of the spatial differences in carbonate sedimentation from site to site are statistically significant.

As illustrated in Figures II.8 and II.9, it is also possible to determine if adjacent peaks and valleys in the GRAPE records are significantly different from the surrounding features. At GRAPE event F at Site 848, for example, the low amplitude peaks and troughs in the GRAPE record at 36.8 RMCD, are within one standard deviation of each other. This is better illustrated in the portions of GRAPE records in Figure II.8. Many large scale events in the GRAPE records are prominent, but small amplitude variability is often within the

range of the error bars. The implication from these data are that Sites 846 - 852 are characterized by significant within site variability in GRAPE as well as between site variability. Thus, a spatial study of the GRAPE carbonate proxy records from these sites will resolve variations in GRAPE densities which are significant.

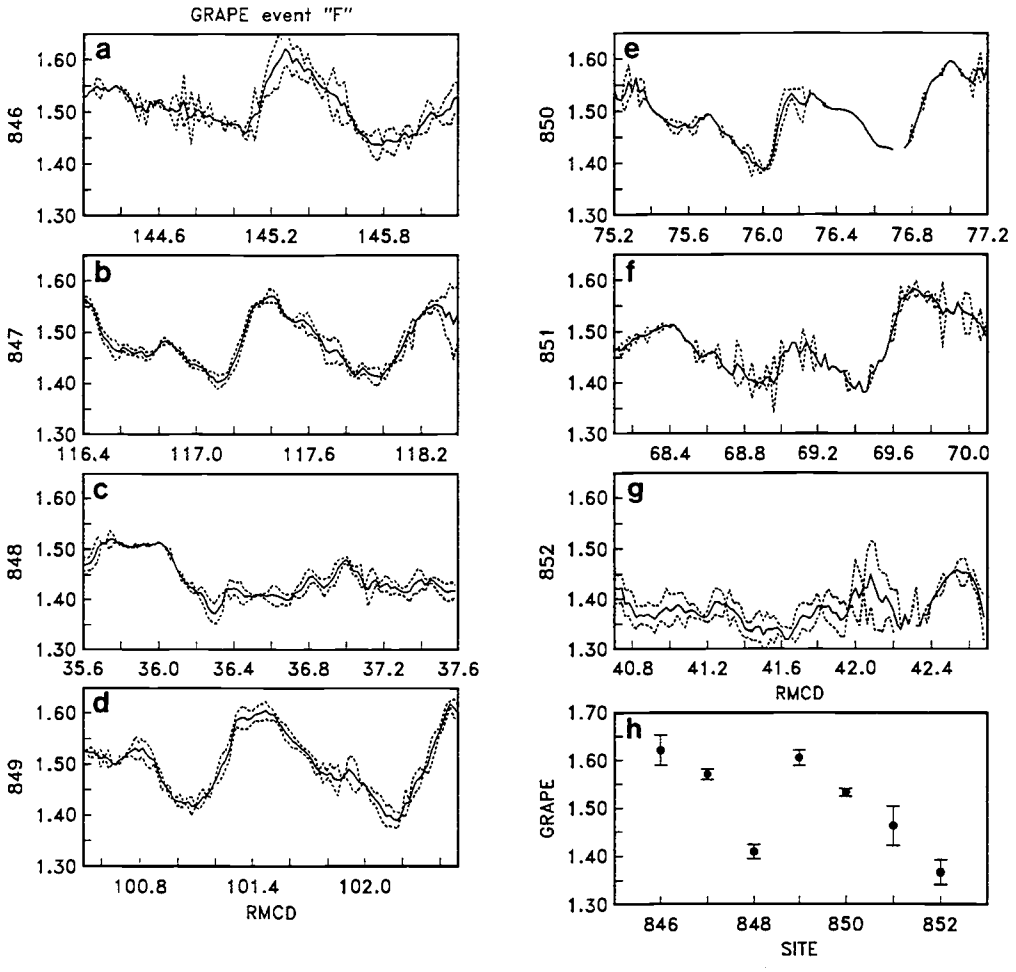

Figure II.9. (a-g) GRAPE event "F" (defined by Shackleton, 1992) at sites 846-852. h: Mean and std. deviation of event F (see Table II.3 for depths).

Depth Scale Variability

As noted by Ruddiman et al. (1986), if core breaks were the only factor preventing recovery of continuous sedimentary sections, it would be straightforward to recover a continuous sedimentary section by drilling two adjacent holes offset in depth. However, the drill string length cannot be used as the only measure of positioning between holes. The cohesive properties of the sediment being cored introduces an additional degree of variability to coring recovery and coring gaps. Sediment with higher water content is likely to be more susceptible to coring disturbance. HPC design has also been suggested as a complicating factor, although no study has considered it explicitly.

Sea state and vessel heave are also possible complicating factors. However, variability in coring gaps estimated from composite depth sections were compared with sea state and vessel heave during Leg 138, with no clear relationship seen (Hagelberg et al., 1992). This suggests that this effect alone is not the only process responsible for the presence of coring gaps.

Somehow in the coring process, the sedimentary section must be expanded if core recovery is documented at 100%, yet the composite section suggests that over 10% of the sequence is missing. Expansion of sediment due to release of gas or due to release of overburden pressure has been suggested as a factor. Consolidation tests suggest that release of overburden pressure may account for up to 50% of offset between composite and mbsf depth (MacKillop et al., 1993). If compaction is a significant process, then this may explain why only a portion of the true sedimentary sequence is recovered. It appears that

Table II.4. Statistics for stacked GRAPE records from sites 846-852 over GRAPE event "F" defined by Shackleton et al. (1992).

Site	Event Depth (rmcd)	GRAPE	N	Std. Dev.
846	145.27	1.621	4	0.031
847	117.41	1.571	5	0.011
848	36.60	1.409	4	0.015
849	101.47	1.605	4	0.016
850	76.16	1.533	2	0.008
851	69.12	1.463	B	0.041
852	41.72	1.367	4	0.025

compaction effects may play a larger role in creating the apparent lack of complete recovery than previously thought. If so, then the remainder of coring variability may be accounted for by random changes in sea state, vessel heave, and other coring artifacts.

Local Variability in Sediment Deposition Rates

It is likely that some of the depth scale variability recorded in GRAPE measurements from hole to hole is related to true heterogeneity in the sediment within a very small geographic area. Adjacent drilled holes are typically separated by 10's of meters. Thus the depth scale variability that is resolved on within-core scales may also provide a measure of the natural variability in sedimentation rates. The inverse mapping methods used above provide for the first time a sufficient data set to examine the impact of this source of variability on geologic records.

Figure II.10 presents the differences between the original composite depth and the revised composite depth for sites 846-852 in histogram form. Only observations that were not included in the shipboard splice (the mapping reference) were included. The changes in depth from mcd to rmcd are roughly equally distributed about the mean, and the majority of measurements required less than a 10 cm change in depth. With the exception of Sites 846 and 848, almost all of the measurements at each hole at each site required changes in depth of less than 30 cm.

How much stretching or squeezing occurs between two successive measurements in one hole relative to another? If this can be determined, it is possible to calculate the relative variability in sedimentation rates on a small scale, from hole to hole at a site. By determining the amount of variation in depth, and thereby sedimentation rates, at small scales at a given site, the range of sedimentation rate changes that would be anticipated to account for this variability can be predicted. This, in turn, can be compared to sedimentation rate changes that are imposed upon the record using timescale refinement strategies such as orbital tuning (e.g. Martinson, et al., 1987).

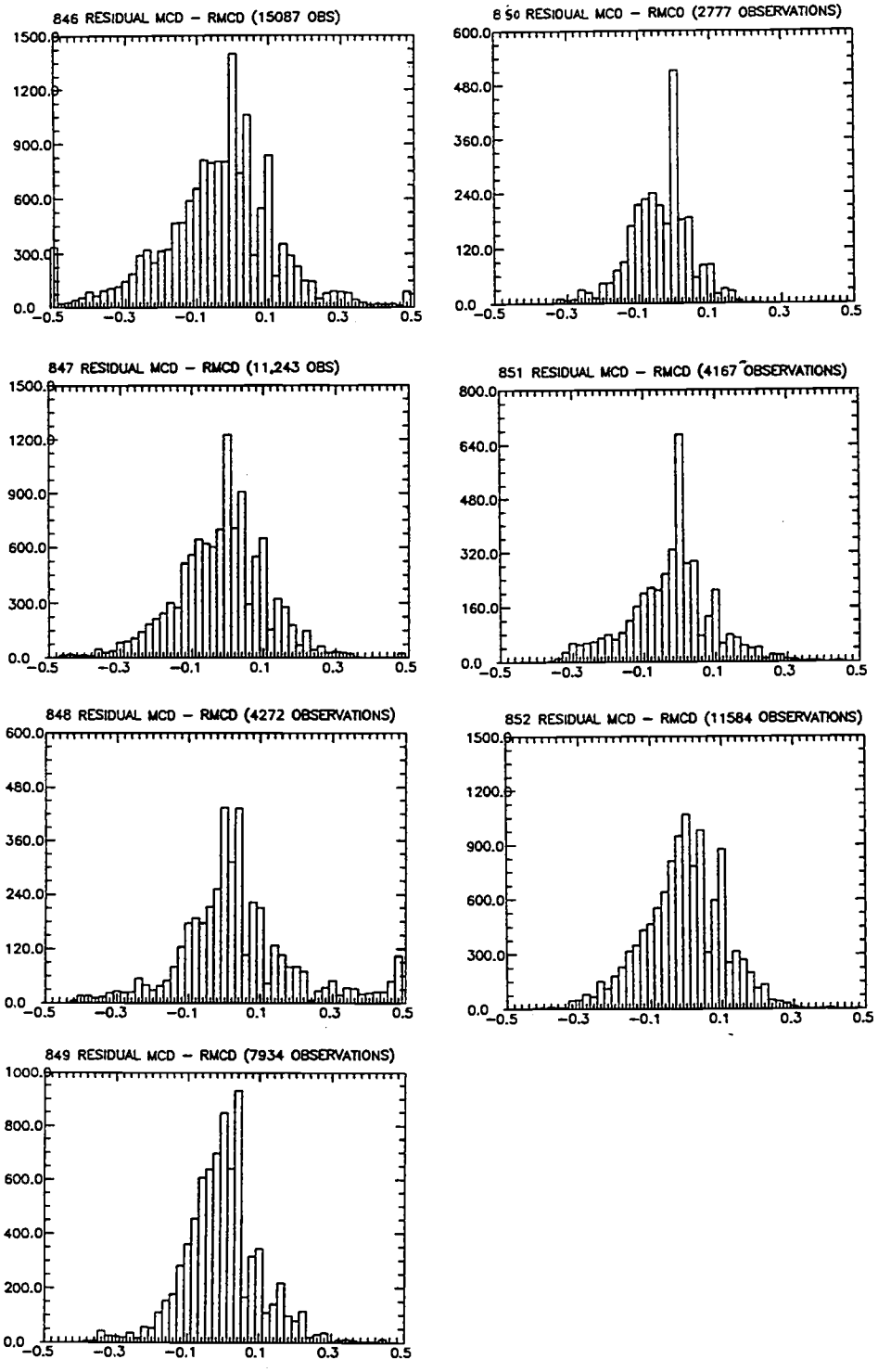

Figure II.10. Differences between mcd and rmcd for each GRAPE measurement correlated to the shipboard splice using inverse correlation, Sites 846-852. These histograms indicate absolute differences between mcd depth and rmcd (intervals that are part of the shipboard splice have been excluded), and indicate that the bulk of changes between mcd and rmcd are 10 cm or less. (x axis is cm, y is # of observations).

For each hole at each mapped site (846 through 852), the differences in mcd between two successive downcore measurements were compared with the corresponding differences in revised mcd for the same pair of observations. As above, only measurements which were not part of the shipboard splice (reference signal) were included. In addition, since the average sampling interval for the GRAPE records was 1-2 cm, only observations which were originally less than 5 cm apart in mcd were included, because the idea is to determine a measure of the relative stretch or squeeze required between two initially adjacent observations. The measure of distortion, D, is calculated as

$$D = \frac{MCD(i) - MCD(i-1)}{RMCD(i) - RMCD(i-1)} \qquad i = 1, 2, 3, \ldots \tag{4}$$

D calculated this way is a measure of the amount of compression between two successive points on the RMCD depth scale relative to the MCD depth scale. Table II.5 gives the distribution of D, the amount of stretch or squeeze, as well as summary statistics for each site. D is plotted as a function of depth for each hole in site 852 in Figure II.11.

As seen in Table II.5, the amount of stretching ($D < 1$) and squeezing ($D > 1$) for each site is similar. For each site, the one standard deviation ranges are approximately $0.67 < D < 1.5$. Thus, the amount of distortion within a given core relative to a reference does not vary significantly from site to site as measured using inverse correlation. This suggests 3 factors: (1) the variation in the amplitudes of depth distortion is independent of sedimentation rate, as sites with a large range in sediment accumulation rates show the same level of distortion. (2) the variation seen in small scale variability may be an artifact of the coring process, because the depth scale changes are so similar from site to site, or (3) the inverse correlation techniques used to correlate a fine scales have an inherent limitation in the number of Fourier coefficients that can be used, so that higher sedimentation rate sites are not correlated as well as lower sedimentation rate sites, and the result is that the amount of distortion appears similar.

It is likely that all three of these factors bear on the level of depth scale variability observed. Factor (3) can be partially ruled out as the number of Fourier coefficients used in inverse correlation rarely was the maximum, and the level of coherence between cores from adjacent holes was similar with both high and low sedimentation rate sites (Table II.2). Factor (2) is difficult to address because the above measures of distortion are relative, that is reference signal itself contains distortion due to coring variability. Although the resolution is lower, core-log integration may allow this factor to be addressed (e.g. Harris et al., 1993). As seen in Figure II.11, although the amplitude of stretching and squeezing necessary to correlate at fine scale between adjacent holes is independent of sedimentation rate, the rate of change of amplitudes downcore is related to fluctuations in sedimentation.

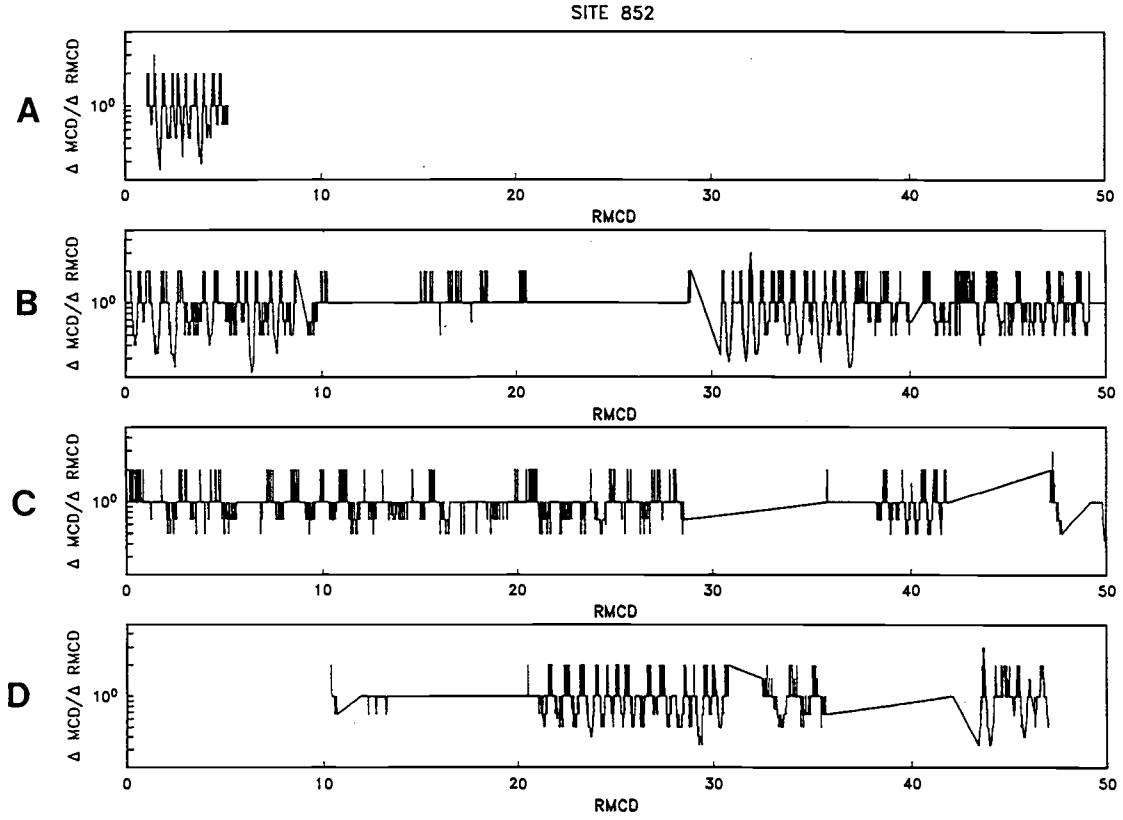

Figure II.11. ***D*** (see text and Table II.4) as a function of rmcd for each hole at Site 852. D=1 indicates no relative stretch or squeeze between a pair of observations going from mcd to rmcd; D > 1 indicates that the pair of observations are closer together on the rmcd scale relative to the mcd scale. D < 1 indicates that the pair of observations must be stretched on the rmcd scale relative to the mcd in order to fit the reference.

If factor (1) is true, then upper and lower limits on deposition rates within a given site can be calculated. Table II.6 gives standard deviation, minimum and maximum sedimentation rates for each of sites 846-852 (in the 0-5 ma range only for 847-852). From Table II.5 and Figure II.11, $D = 2.0$ indicates that successive measurements on the RMCD scale must be compressed 2 times relative to the MCD scale in order to fit the reference. $D = 0.5$ indicates that measurements on the RMCD must be stretched twice as far relative to MCD depths. The bulk of measurements required no change ($D = 1.0$) between successive pairs, indicating relatively constant sedimentation rates measured from adjacent holes. At site 847 for example, for 1375 pairs of observations D fell between 0.5 and 0.7 (50% stretch), and for 1073 pairs D fell between 1.9 and 2.1 (50% compression).

Table II. 5. Frequency distributions of D. (Change in MCD/Change in RMCD) for initailly adjacent GRAPE measurements, sites 846 - 852.

SITE	TOTAL # PAIRS	MEAN	STD. DEV.	RANGE
846	14634	1.15	0.52	0.09 - 4.00
847	10671	1.07	0.40	0.20 - 3.99
848	4084	1.10	0.40	0.25 - 3.00
849	7589	1.05	0.39	0.20 - 3.00
850	2622	1.07	0.41	0.33 - 3.0
851	3760	1.10	0.44	0.20 - 5.00
852	10896	1.10	0.47	0.14 - 3.00

D	#OBSERVATIONS						
	846	**847**	**848**	**849**	**850**	**851**	**852**
0.1 - 0.3	66	27	2	4	0	7	20
0.3 - 0.5	374	200	39	185	78	65	335
0.5 - 0.7	2011	1375	443	1002	337	317	1596
0.7 - 0.9	633	475	183	295	97	556	231
0.9 - 1.1	7692	6873	2651	4997	1666	1733	6608
1.1 - 1.3	0	0	2	2	1	91	2
1.3 - 1.5	522	283	134	187	69	520	178
1.5 - 1.7	521	307	151	187	72	242	242
1.7 - 1.9	0	0	0	0	0	0	0
1.9 - 2.1	2249	1073	463	685	290	158	1565
2.1 - 2.3	0	0	0	0	0	0	0
2.3 - 2.5	1	0	0	0	0	9	0
2.5 - 2.7	2	0	0	0	0	0	0
2.7 - 2.9	0	0	0	0	0	0	0
2.9 - 3.1	292	57	16	45	12	44	119
3.1 - 3.3	0	0	0	0	0	0	0
3.3 - 3.5	0	0	0	0	0	0	0
3.5 - 3.7	0	0	0	0	0	0	0
3.7 - 3.9	0	0	0	0	0	0	0
3.9 - 4.1	A	1	0	0	0	18	0

The end members of sedimentation rate variability induced solely by this interhole variability are illustrated in the following example from Site 847. The highest sedimentation rate recorded at Site 847 (in mcd units, from Leg 138 shipboard chronology) is 66.7 mcd/myr (Table II.6 A). A 50% increase and decrease, respectively, makes the range in sedimentation rate variability 33.5 mcd/myr to 100 mcd/myr. The lowest sedimentation rate recorded at Site 847 is 15.5 mcd/myr (Table II.6 A); a 50% decrease and increase in sedimentation rates make the range 7.75 to 23.25 mcd/myr. The extremes of stretching and squeezing estimated by D for Site 847 are $D = 0.20$ to $D = 3.99$. This translates into a maximum possible sedimentation rate of 335 mcd/myr and a minimum possible sedimentation rate of 3.9 mcd/myr (Table II.6 B). The tuned chronology developed by Shackleton for site 847 (Shackleton, et al., 1992) has a maximum sedimentation rate of 125 mcd/myr and a minimum of 11.9 mcd/myr. These extremes in the tuned timescale are within the level of variability that would be predicted solely on the basis of stretching and squeezing between adjacent holes.

This exercise indicates that the degree of variability present in tuned sedimentation rate models is no greater than the variability induced by the compression and stretching required to map adjacent holes to one another at high resolution. While this does not have direct bearing on determining what the true range of sedimentation rate variability is, large differences in sedimentation rate between the tuned chronologies presented by Shackleton and the shipboard chronology cannot be discounted on this basis, as the range of sedimentation rate variability fits easily within the range of intrasite core distortion.

Table II. 6.
A. Sedimentation rate statistics, Sites 846-852 (from Leg 138 initial reports; 0-5 myr only for sites 847-852). Rates are in mcd/myr.

SITE	MEAN	+/- 1 STD DEV	MIN RATE	MAX RATE
846	33.2	15.0 - 51.5	5.5	61.3
847	36.7	21.7 - 51.7	15.5	66.7
848	12.2	6.3 - 18.1	5.2	21.2
849	41.9	21.5 - 62.3	25.8	75.5
850	33.3	16.3 - 50.3	18.0	64.2
851	26.2	15.8 - 36.6	18.8	48.1
852	14.1	10.3 - 17.9	9.1	20.6

B. Statistics of predicted minimum and maximum sedimentation rates from the data given in A that would be produced by compression and stretching between adjacent cores, as indicated by the values for D given in Table II.5. The standard deviations are calculated by applying the standard deviation of D (Table II.5) to the sedimentation rate standard deviation given in A.

SITE	MEAN	+/- 1 STD DEV	MIN RATE	MAX RATE
846	28.9	8.9 - 81.7	1.4	674.3
847	34.2	14.8 - 77.2	3.9	335.2
848	11.1	4.2 - 25.9	1.7	84.8
849	39.9	14.9 - 94.4	8.6	377.5
850	31.1	11.0 - 76.2	6.0	194.5
851	23.8	10.2 - 55.4	3.8	240.5
852	12.8	6.6 - 28.4	3.0	147.1

C. Range in the maximum/minimum sedimentation rates from the tuned chronology for sites 846-852 (Shackleton et al., in prep). Compare to predicted values from Table II.6 B.

SITE	MEAN	+/- 1 STD DEV	MIN RATE	MAX RATE
846	41.0	25.5 - 56.5	11.4	121.2
847	35.3	19.5 - 51.1	11.9	124.9
848	10.4	5.0 - 15.8	1.9	36.4
849	36.2	11.9 - 60.5	9.0	199.9
850	28.5	7.5 - 49.5	6.9	210.0
851	22.4	10.1 - 34.7	7.9	72.2
852	12.3	7.5 - 17.1	4.8	31.5

CONCLUSIONS

Very high resolution correlations between adjacent holes at sites drilled during Leg 138 are possible. A revised composite depth section accurate to the order of centimeters places data from multiple holes onto a common depth scale. High resolution correlations between holes based on GRAPE bulk density measurements were confirmed by comparing these data to color reflectance and magnetic susceptibility. The measurements in each hole can be stacked to arrive at a less noisy GRAPE estimate for each 2 cm depth at each site. The stacking exercise effectively increases the signal/noise ratio for the resulting sampled time series. A quantitative estimate of error for the GRAPE amplitudes is obtained from the multiple measurements. The high resolution correlations between adjacent holes can be used to assess the amount of distortion required to map 3 adjacent holes to one another. This has implications for small scale sedimentation rate variability at a given site. Changes in sedimentation rate from the tuned chronology of Shackleton (1992) are entirely within the range of variability predicted from correlating among adjacent holes in the depth domain. Finally, the stacking exercise produces a high quality record of GRAPE bulk density which can be used for high resolution paleoceanographic studies.

SPATIAL AND TEMPORAL VARIABILITY OF LATE NEOGENE EQUATORIAL PACIFIC CARBONATE: ODP LEG 138

T.K. Hagelberg, N.G. Pisias, L.A. Mayer, N.J. Shackleton, and A.C. Mix

ABSTRACT

High resolution, continuous records of GRAPE wet bulk density (a carbonate proxy) from ODP Leg 138 provide the opportunity for a detailed study of eastern equatorial Pacific carbonate sedimentation during the last 6 myr. The transect of sites drilled during Leg 138 span both latitude and longitude in the eastern equatorial Pacific from 90°W to 110°W and from 5°S to 10°N. The spatial and temporal variability of carbonate sedimentation in this region is investigated. Two modes of variability are resolved through the use of Empirical Orthogonal Function analysis. In the presence of large tectonic and climatic boundary condition changes over the last 6 myr, the dominant mode of spatial variability in carbonate sedimentation is remarkably constant. The first mode accounts for over 50% of the variance in the data, and is consistent with forcing by equatorial divergence. This mode of variability is dominant in both carbonate concentration and carbonate mass accumulation rate time series. Variability in the first mode is highly coherent with insolation, indicating a strong linear relationship between equatorial pacific carbonate sedimentation and Milankovitch variability. Frequency domain analysis indicates that the coupling to equatorial divergence in carbonate sedimentation is strongest in the precession band (19-23 kyr), and weakest, though still present at lower frequencies. The similar spatial patterns in carbonate sedimentation combined with a consistent relationship to Milankovitch band variability in the presence of other large oceanographic and tectonic changes implies a constant forcing mechanism of carbonate sedimentation throughout the past 6 myr.

The second mode of variability has a consistent spatial pattern of east - west asymmetry over the past 4 myr only; prior to 4 Ma a different mode of spatial variability may be present, possibly suggesting influence by closure of the Isthmus of Panama. Spatial variability in the second mode may be consistent with surface influence from the Peru Current and high latitudes over the past 4 myr. The second mode of variability may also indicate some influence by dissolution or dilution of $\%CaCO_3$. The second mode of variability is not highly coherent with insolation.

Comparison of the modes of carbonate variability to a 4 myr record of benthic $\delta^{18}O$ indicates that both modes of variability in carbonate sedimentation are coherent with $\delta^{18}O$ changes. The first mode of carbonate variability is coherent with site 846/849 $\delta^{18}O$ at the dominant insolation periods during the past 2 myr, and the second mode is coherent att frequencies which are not linearly related to insolation forcing. The relationship between carbonate sedimentation and $\delta^{18}O$ in both modes of carbonate variability suggests that multiple independent modes of variability are operating within the climate system during the late Neogene.

INTRODUCTION AND BACKGROUND

Because the oceanic carbon reservoir is 60 times the size of the atmosphere and it is in direct exchange with the atmosphere, atmospheric CO_2 changes must ultimately be explained by changes in the oceanic carbon cycle (Broecker and Peng, 1982). Ice core evidence indicates that the CO_2 increase at the ends of glacial periods occurs rapidly, on the order of a thousand years. This points to a need to understand the mechanisms controlling the carbon cycle on glacial / interglacial timescales. While ice cores provide a direct measure of changes in atmospheric CO_2, examination of the marine sediment record is necessary to obtain a history beyond that of the last glacial cycle.

Efforts to understand the mechanisms through which the oceanic carbon cycle changes atmospheric CO_2 have led to years of carbon cycle modeling. Recently, Heinze et al. (1991) summarized all previous attempts to explain the oceanic carbon cycle. Hypotheses for glacial-interglacial pCO_2 changes were grouped into 4 categories: 3 different oceanic carbon pumps which are capable of influencing atmospheric CO_2 (a solubility pump, a nutrient pump, and a $CaCO_3$ pump), and changes in the oceanic velocity field and ventilation rates. One example was the hypothesis of Boyle (1988), which required increased ventilation of intermediate waters and a change in the distribution of nutrients. Increased ventilation would send more nutrients into surface waters where increased biological productivity would draw down pCO_2 and transport more TCO_2 into deep waters. An associated increase in $CaCO_3$ dissolution and global alkalinity would amplify the pCO_2 change. Evidence for oceanic carbon pool changes that is needed to evaluate this and other hypotheses is derived from sedimentary $\delta^{13}C$ and $CaCO_3$ records. $\delta^{13}C$ indicates the efficiency of the ocean's biological pump and the nutrient content of deep and surface waters. The $CaCO_3$ concentration in sediments reflects productivity as well as alkalinity changes.

The extent to which $CaCO_3$ sedimentation, especially in equatorial Pacific sediments, has been controlled by production or dissolution has been the subject of debate for over 40 years. Since Arrhenius (1952), studies have investigated the relationship of equatorial Pacific carbonate sedimentation to regional surface processes, global glacial-interglacial changes, and external orbital (Milankovitch) influence (e.g. Hays et al, 1969, Moore et al, 1978, 1982; Farrell and Prell, 1989; Rea et al., 1991). In the equatorial Pacific, large changes in sedimentary calcium carbonate concentration are present on long time scales (millions of years), indicating oceanic boundary condition and geochemical mass budget changes as well as shorter time scales (tens of thousands of years), indicating climatic influence.

On long time scales, changing boundary conditions during the late Cenozoic affect changes in equatorial Pacific sediment composition. van Andel et al. (1975) estimated the initiation of the Equatorial Undercurrent at around 11 - 12 myr ago, when the northward movement of the Australia plate cut off western Pacific - Indian ocean circulation. This development may have caused the onset of a narrow, equatorially symmetric zone of carbonate and opal sedimentation having steep gradients away from the equator. Widespread orogeny in the late Miocene and Pliocene is thought to have had large influence on oceanic alkalinity budgets through increased chemical weathering (Raymo et al., 1988). This uplift may have significantly influenced surface ocean circulation in the equatorial Pacific through associated changes in atmospheric circulation (Ravelo et al., 1992). Prior to closure of the Isthmus of Panama (3-4 ma or earlier), a modeling study suggests that North Atlantic Deep Water production was reduced, carbonate preservation was increased due to less undersaturated Pacific deep waters, and eastern equatorial Pacific surface upwelling was unchanged (Maier-Raimer et al., 1990). Initiation of large scale continental glaciation in the Northern Hemisphere around 2.4 Ma altered oceanic alkalinity and productivity significantly.

van Andel et al. (1975) demonstrated that similar spatial patterns are observed in bulk sediment accumulation rates, carbonate accumulation rates, and carbonate concentration in the central equatorial Pacific throughout the Cenozoic (Figure III.1). A high correlation with latitude reflects the "bulge" of equatorial Pacific productivity. Longitudinal gradients in carbonate accumulation across the central equatorial Pacific (130°-140°W) were relatively small. Their results suggested that over the past 35 million years the equatorial calcite compensation depth (CCD) has fluctuated by only a few hundred meters. This constancy in the depth of the equatorial Pacific CCD requires that large changes in the gradient of $CaCO_3$ dissolution be compensated for by variations in the lysocline depth and variations in carbonate supply from surface waters.

On shorter timescales, regional studies demonstrate that the depth and slope of the lysocline in the central equatorial Pacific has changed dramatically over glacial and interglacial cycles. During the late Pleistocene in the equatorial Pacific, glacial intervals record higher $CaCO_3$ preservation as well as higher accumulation of calcite than interglacial periods (Farrell and Prell, 1989; Berger, 1973). If increased glacial carbonate preservation is produced by changes in deep ocean carbonate ion saturation, the model of Archer (1991a) indicates that a large (20-40 μm) change in the gradient of calcite saturation is required over a fairly small (~100 m) depth interval. On the other hand, if increased glacial $CaCO_3$ preservation is driven by changes in calcite production in surface waters, the gradient in calcite saturation would be relatively homogeneous with depth. To explain glacial increases in carbonate concentration and accumulation through productivity changes, Archer's model requires a doubling of productivity during the last glacial relative to present. This is consistent with independent estimates of glacial surface production in equatorial oceans (e.g. Mix, 1989; Finney et al., 1988;, Prahl et al., 1989; Lyle et al., 1988).

Regardless of whether deep ocean or surface ocean processes are responsible for most of the observed changes in equatorial Pacific carbonate sedimentation on 10,000 - 100,000 year scales, a temporal association with glacial / interglacial changes is evident

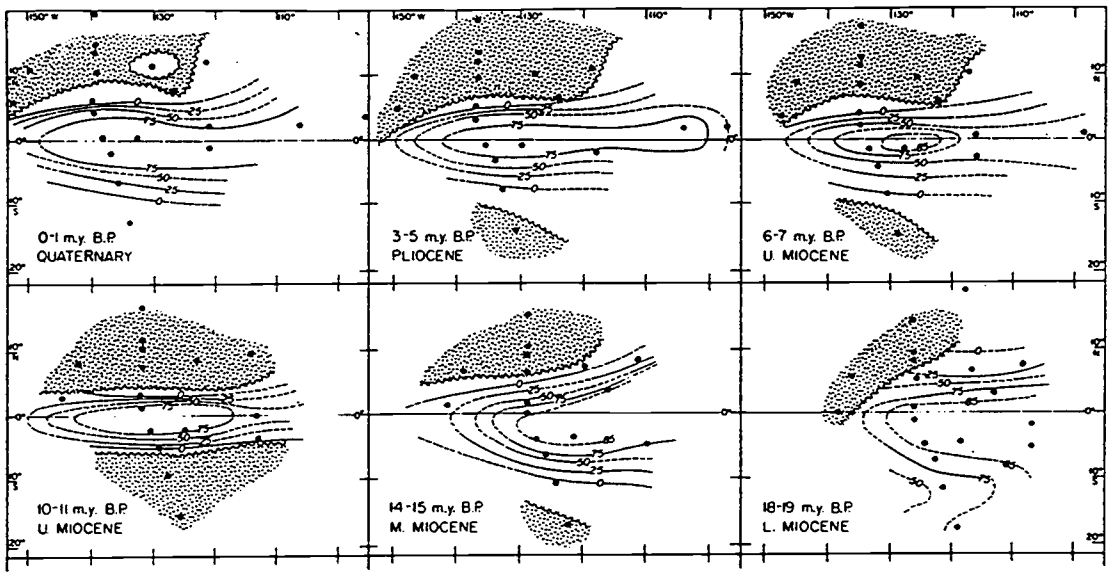

$CaCO_3$ DISTRIBUTION

Contours in percent $CaCO_3$

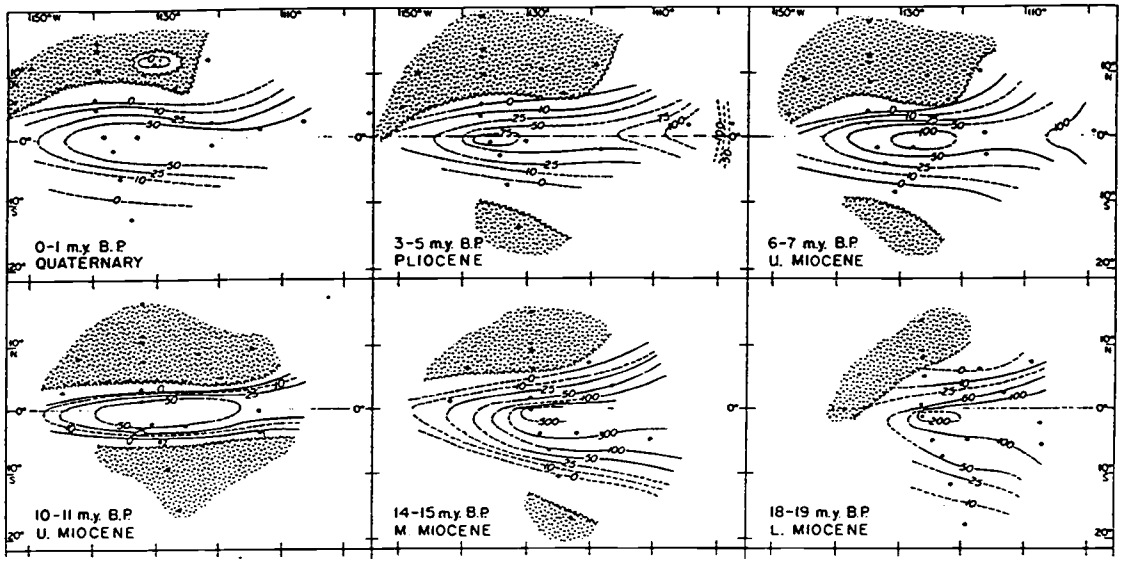

$CaCO_3$ ACCUMULATION RATES

Contours in $g/cm^2/1000$ yr x 100

Figure III.1. Contours of $\%CaCO_3$ (top) and $CaCO_3$ mass accumulation rates (bottom) over the past 19 myr in the equatorial Pacific, from van andel et al., 1975. Note the development of a narrow band of carbonate sedimentation that is resolved over the past 11 myr.

from late Pleistocene sediment records. Moore et al. (1977) were the first to document a 6000-8000 year lag between ice volume and $\%CaCO_3$ in the equatorial Pacific. Farrell and Prell (1989) documented a similar relationship in a reconstruction of late Pleistocene central equatorial Pacific lysocline changes. This lag is due to the response time of oceanic $CO_3^{=}$ in compensating glacial-interglacial TCO_2 changes (Broecker and Peng, 1982). However, in detail the ice volume - carbonate relationship is not straightforward. During the late Pleistocene, some studies have shown carbonate variations to be coherent with ice volume variations (Rea et al., 1991; Farrell and Prell, 1989; Luz and Shackleton, 1975), yet others have indicated either no relationship or a complex one (e.g. Moore et al, 1982; Pisias and Rea, 1988, Lyle et al., 1988). Spatial variability in carbonate sedimentation is significant (Murray, 1987; Farrell and Prell, 1989, 1991); this variability probably contributes to the different conclusions reached by studies which focus on selected locations.

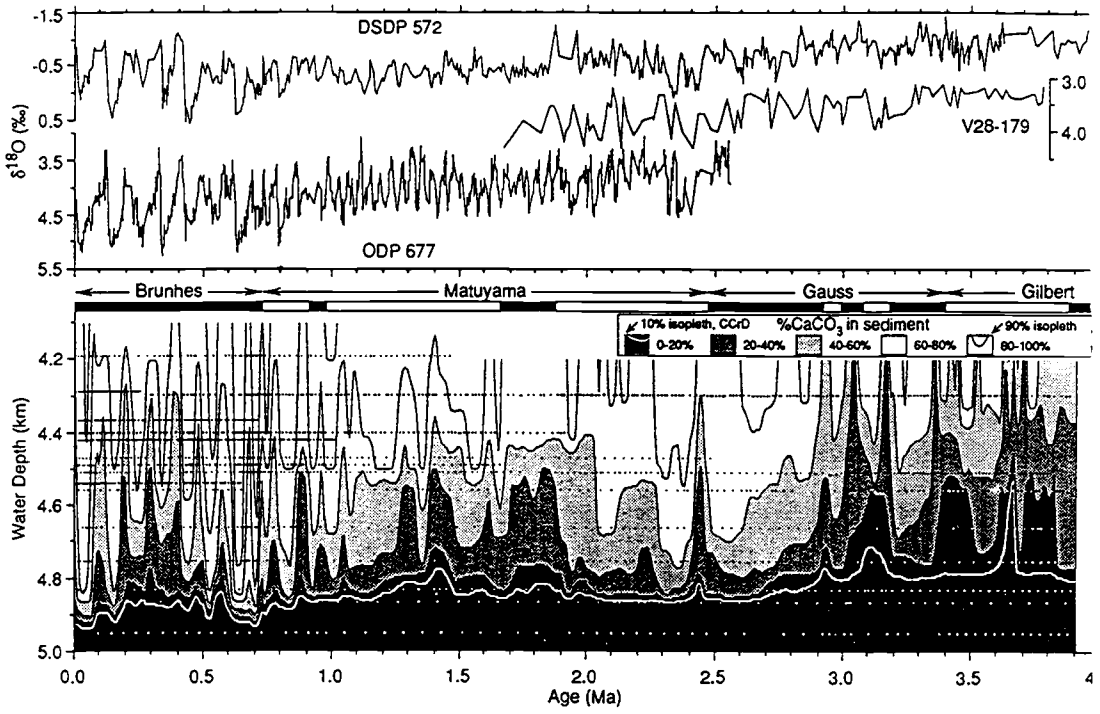

Figure III.2. Contours of $\%CaCO_3$ in the central equatorial Pacific as a function of water depth and time over the past 4 myr, from Farrell and Prell (1991). The evolution in carbonate concentration variations can be compared with fluctuations in $\delta^{18}O$, given at the top of the plot.

Time series studies spanning intervals beyond the late Pleistocene indicate a complex relationship between equatorial Pacific carbonate and ice volume. For example, Pisias and Prell (1985) found variability concentrated at 35 kyr and 60 kyr in carbonate records from equatorial Pacific DSDP Site 572 from 4-6 ma. A comparison of compiled records of carbonate variability spanning the past 4 myr to ice volume records by Farrell and Prell (1991) (Figure III.2) suggests that the relationship between equatorial Pacific lysocline fluctuations and ice volume is not straightforward. It is well known that a change in the amplitude of the variability of global ice volume records ($\delta^{18}O$) from primarily 41 kyr oscillations to 100 kyr oscillations occurred near 1 Ma (Ruddiman et al, 1988; Raymo et al, 1988; Pisias and Moore, 1981). No similar change in the amplitude of $\%CaCO_3$ variability is evident from the data in Figure III.2. However, low sedimentation rates and uncertainties in chronology have made it difficult to determine how strongly $CaCO_3$ and $\delta^{18}O$ covary over the past 4 myr in the equatorial Pacific. The long records of equatorial Pacific $CaCO_3$ and global ice volume compared by Farrell and Prell suggest that the relationships seen in the late Pleistocene were not present during the early Pleistocene and Pliocene. Analyses of high resolution carbonate records from this region are necessary to better establish these relationships.

RESEARCH STRATEGY

The following generalities can be made from the above discussion: 1) Despite many studies, the relationship between equatorial Pacific carbonate sedimentation and global climate changes over the past several million years is not well defined. Strong spatial variability is a likely contributing factor. 2) The debate over production versus dissolution as a control on eastern equatorial Pacific carbonate sedimentation is not resolved. 3) Previous studies were limited to data sets restricted in either spatial coverage or temporal resolution.

The suite of sites sampled by Leg 138 of the Ocean Drilling Program provide a data set to solve these problems. As demonstrated in the next section, these records provide (1) high spatial coverage of a very dynamic region; (2) high temporal sampling resolution (order of 1000-2000 year); (3) long temporal coverage (> 6 myr); (4) an internally consistent chronology; (5) high quality proxy records.

The two longitudinal transects of sites drilled during Leg 138 cross the high productivity region of the equatorial Pacific and sample the major surface currents in this region (Figure III.3). The site locations allow comparison of latitudinal and (to a limited extent) longitudinal gradients of this system. The latitudinal and longitudinal positions of the drilled sites have changed by no more than 0.5^{o} latitude and 4^{o} longitude over the past 6 myr due to northward movement of the Pacific Plate (Pisias et al., 1993). The sites are at water depths within the lysocline, estimated at around 3200m (Parker and Berger, 1971; Adelseck and Anderson, 1978), and above the calcite saturation horizon, estimated at around 4000 m (Broecker and Peng, 1982) (Table III.1). While data are located at different depths, there is not a strong depth - latitude correlation which would complicate determining if changes in carbonate were due to changes in productivity or to changes in lysocline depth (Figure III.4 and Table III.1). Although the depths of these sites are shallower than

the sites studied by Farrell and Prell (1991; Figure III.2), because the equatorial Pacific lysocline shoals to the east, the two sets of sites can be compared with respect to upper lysocline fluctuations.

This study uses the array of Leg 138 sites to determine if effects on carbonate sedimentation due to surface ocean processes, which will be more regional in nature, can be discriminated from effects due to changes in deep ocean chemistry, which will be more uniform in nature. Carbonate proxy records from GRAPE (Gamma Ray Attenuation Evaluator; Boyce, 1976) wet bulk density measurements at Sites 846 - 853 are analyzed. Site 844, located in the Costa Rica Dome, and Site 845, located in the Guatemala Basin, represent different oceanographic environments and are dominantly siliceous clay during much of the late Neogene, and are thus not studied here. The continuity of the records from sites 846-853 can be documented in detail over the last 6 million years. Time series of

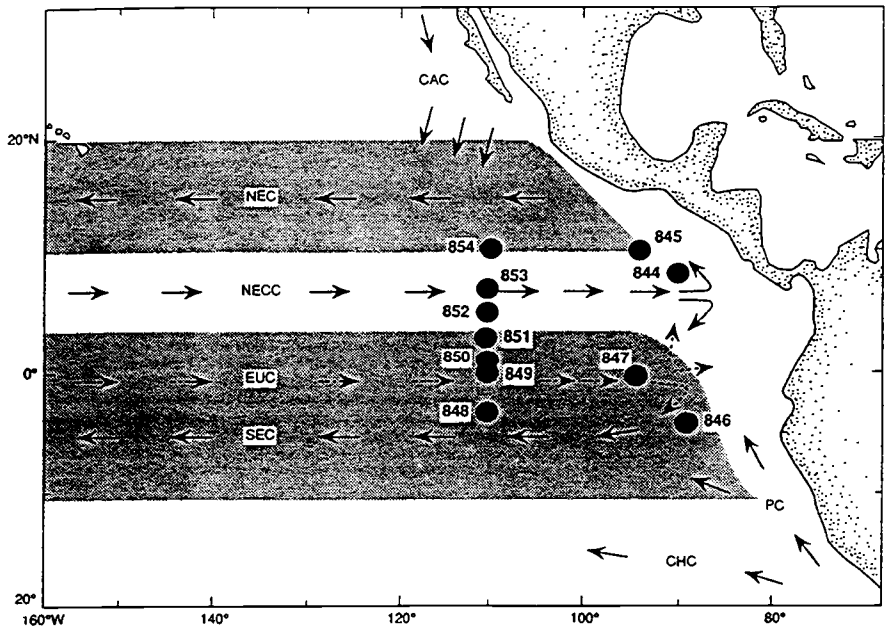

Figure III.3. Present day location of Leg 138 sites 844 - 845, superimposed on a schematic of the general circulation of the eastern equatorial Pacific. The solid arrows indicate surface currents, and the dashed arrow indicates the Equatorial Undercurrent (EUC). The shaded regions illustrated the latitudinal extent of the SEC (South Equatorial Current) and the NEC (North Equatorial Current). NECC is the North Equatorial Countercurrent, CAC is the California Current, CHC is the Chile Current, and PC is the Peru Current.

GRAPE wet bulk density predicted carbonate concentrations and mass accumulation rates are determined using the orbitally calibrated chronology of Shackleton et al. (1993). Uncorrelated modes of spatial variability within the carbonate records are resolved using Empirical Orthogonal Function (EOF) analysis. Linear relationships between solar insolation and carbonate variability are explored through the use of cross-spectral analyses. The temporal evolution of carbonate sedimentation is studied in 1 myr time steps. Analysis of individual frequency bands provides additional information on processes responsible for carbonate variability. These results are all related to sedimentary carbonate concentration (%), which is influenced by dilution from opal and nonbiogenic material. Carbonate concentration is not the most sensitive indicator of carbonate dissolution (Heath and Culberson, 1970). To investigate variability of carbonate sedimentation independent of opal fluctuations, estimates of carbonate mass fluxes are necessary. Spatial and temporal variability of the carbonate mass accumulation time series are examined in the same manner as the $\%CaCO_3$ records. Finally, these results are used to examine interactions between carbonate sedimentation and global ice volume variations over the past 4 myr.

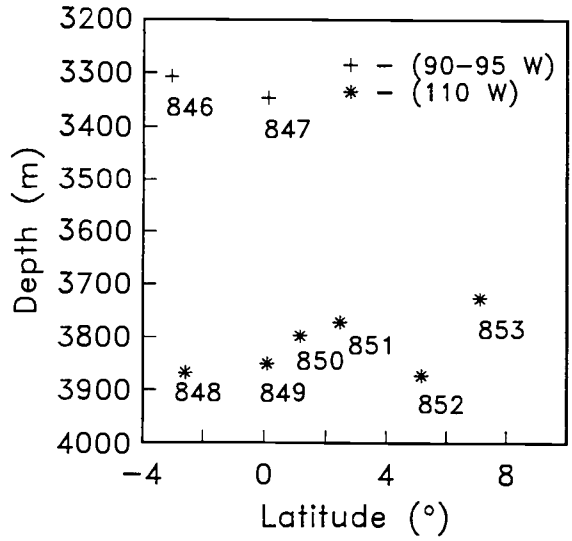

Figure III.4. Sites 846 through 853 vs present day water depth. A large difference in depth occurs between the eastern transect (crosses) and western transect sites (asterisks), and very small differences are seen among the western transect sites. There is no strong depth-latitude correlation.

Table III.1. Present locations and water depths of leg 138 sites 846 - 853

SITE	LATITUDE	LONGITUDE (W)	DEPTH (M)
846	3.05 S	90.49	3307
847	0.11 N	95.19	3346
848	2.59 S	110.28	3867
849	0.10 N	110.31	3850
850	1.17 N	110.31	3797
851	2.46 N	110.34	3772
852	5.17 N	110.04	3872
853	7.12 N	109.45	3726

METHODS

Continuous Records

Each of the 11 Leg 138 drill sites was multiple APC cored in an effort to document recovery of a continuous sedimentary sequence. At each site, records of magnetic susceptibility, GRAPE wet bulk density, and sediment color reflectance were used to monitor section recovery and to construct a composite depth section (Hagelberg et al, 1992; Mayer, Pisias, et al., 1992).

Multiple measurements of GRAPE and other sedimentary parameters on adjacent holes provide multiple realizations of the same sedimentary process at every site. The GRAPE records from each hole at Sites 846 - 852 were 'stacked' to provide a statistically robust and less noisy estimate of sediment bulk density (Hagelberg et al., 1993). The average sampling interval of the stacked, smoothed GRAPE records is 2 cm (Figure III.5). The temporal resolution of the records is on the order of 1000 yr.

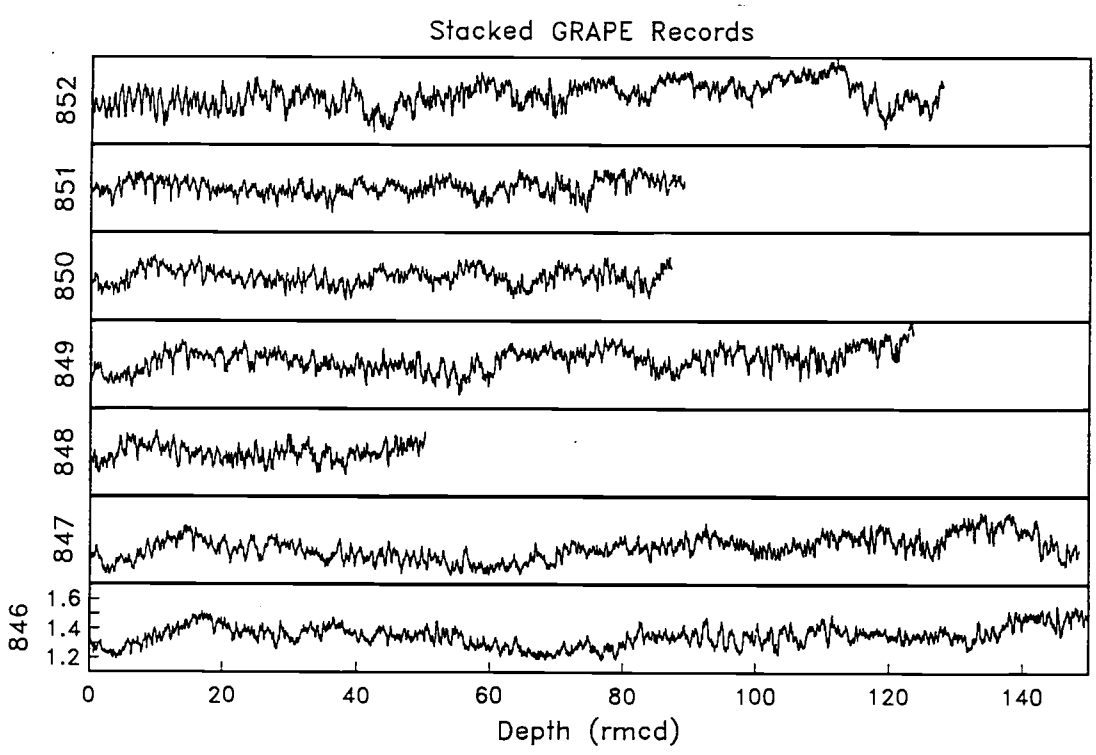

Figure III.5. Stacked GRAPE wet bulk density records from Sites 846-852. The y-axis scale is given in the bottom panel.

GRAPE as a Carbonate Proxy

Sample resolution has traditionally been a problem in studying pre-Pleistocene spatial and temporal climatic variability at high resolution because of time and cost restrictions. This problem is overcome with the Leg 138 $CaCO_3$ proxy records which are derived from GRAPE (Gamma Ray Attenuation Porosity Evaluator) bulk density at near continuous resolution at all sites.

GRAPE was developed in 1965 for Marathon Oil Co., and has been used to measure sediment bulk density on deep sea sediments since DSDP Leg 1, with digital equipment on board since Leg 33 (Schlanger et al., 1976). As sediment cores move between a gamma ray source and a detector system, gamma rays passing through the core are attenuated according to the following relation:

$$I = I_0 \exp^{(-\mu d \rho)} \quad (1)$$

where I_o = the source intensity, I = the attenuated intensity, μ = the mass attenuation coefficient which is mineral-dependent, d = the diameter of the sample, and ρ = the wet bulk density of the material. Assuming that I, I_o, μ, and d are known, this provides an accurate estimate of sediment wet bulk density. GRAPE measurements are limited by the 0.7 cm width of the gamma ray beam. When the Multi-Sensor track is in motion, the resolution of measurements is on the order of 1 cm (Boyce, 1976).

Due to the composition of equatorial Pacific sediments, bulk density is a good predictor of carbonate in this region (Mayer, 1991; Herbert and Mayer, 1991). Equatorial Pacific sediments are primarily composed of two components, biogenic calcite and opal. Wet bulk density measurements record two primary differences between carbonate and opal, their grain densities and their packing properties. The relationship between sediment composition and density and other physical properties led to development of an empirical relationship that predicts carbonate on this basis (Mayer, 1979, 1991). After corrections are made to account for porosity rebound and depth, the following equation is used to predict % carbonate at Sites 846-853:

$$\%CaCO_3 = -835.52 + 1112.69\rho - 332.54\rho^2 \qquad (2)$$

The second term in (2) reflects the linear grain-density relationship, and the last term reflects the nonlinear packing factor. Herbert and Mayer (1991) demonstrated that the sensitivity of sedimentary wet bulk density to $\%CaCO_3$ is controlled by the high porosity of the non-carbonate (opal) fraction. Thus, although biogenic opal has a lower grain density than carbonate (2.1-2.3 g/cm^3 as compared to 2.6-2.7 g/cm^3; Mayer, 1979) differences in porosity are most important.

Stacked GRAPE records developed from the adjacent holes at each site (Hagelberg et al., 1993; Figure III.5) and a spliced record from Site 853 were used to predict % carbonate following modified procedures of Mayer (1991). The effectiveness of GRAPE as a predictor of $\%CaCO_3$ is indicated by the scatterplots and depth series plots in Figure III.6, which compare shipboard $\%CaCO_3$ measurements to predicted values from corresponding holes from sites 846 - 853. The sample cross correlation, or model skill, which gives the fraction of variance explained by the predictive model is given for each site in Table III.2. (This calculation assumes that the measured $\%CaCO_3$ values have no error.) At each site, the correlation is significant at a 0.99 level. Root mean square error ranges from 5.3 Site 853 to 10.2 at Site 846. With the exception of the porosity rebound corrections which are site specific, the above equation is used to predict carbonate at each Leg 138 site. This general equation is the same equation used by Mayer (1991) to predict carbonate at DSDP Site 573. Current efforts include a site-specific refinement of the predictive equation.

Chronology

The correlability of GRAPE records over the Leg 138 sites significantly contributed to development of an internally consistent chronostratigraphic framework for Leg 138 Sites during the leg (Shackleton et al., 1992). A series of events identified primarily on the basis

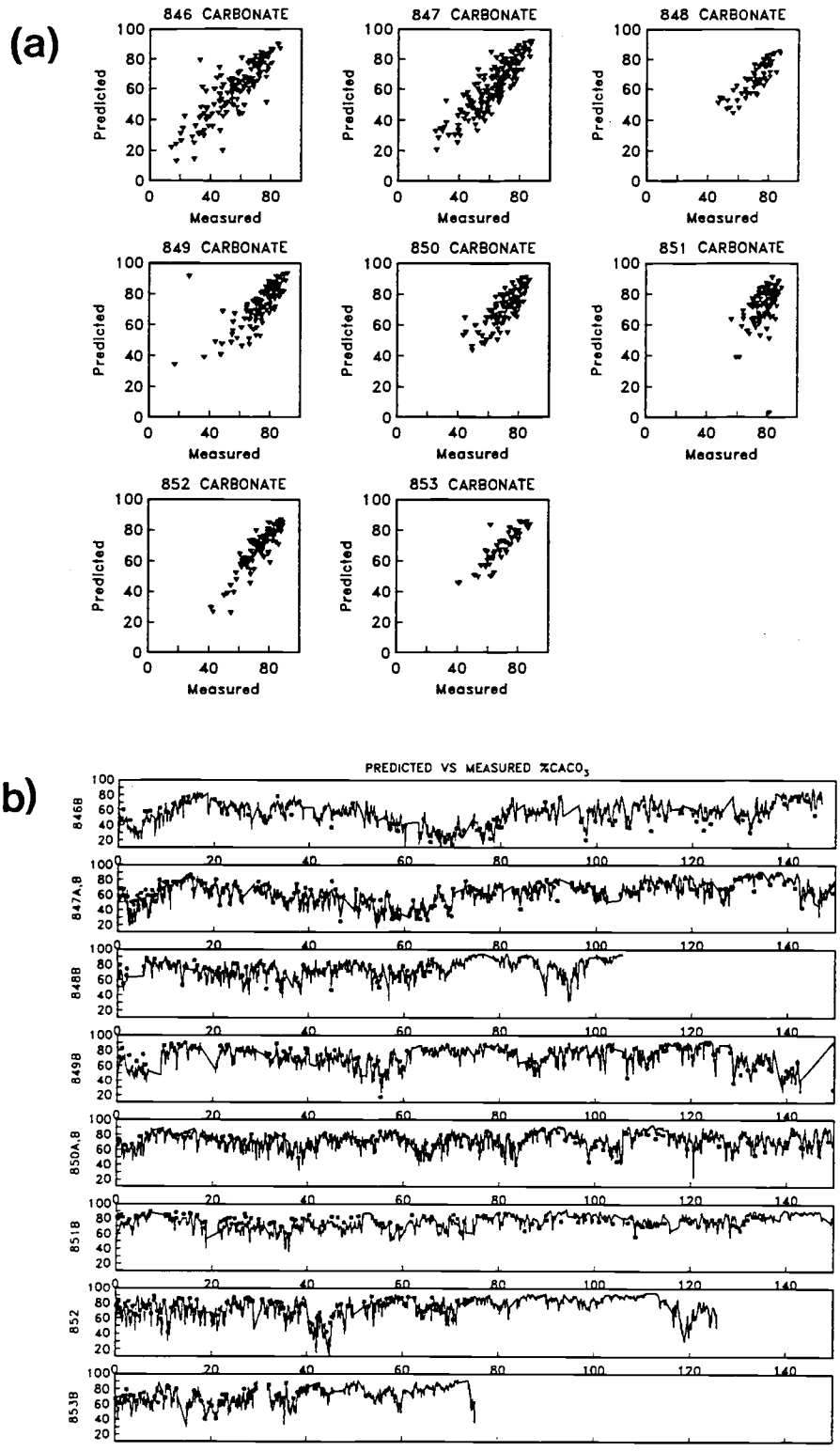

Figure III.6. (a) Scatter plots of predicted vs measured $\%CaCO_3$ from the top 6 myr of Sites 846 - 853. (b) Depth series plots of predicted (solid lines) and measured (squares) $\%CaCO_3$ in holes from sites 846 - 853.

of biostratigraphy and magnetostratigraphy were related to patterns in the GRAPE bulk density records. Although the stratigraphic events could not be identified by magnetostratigraphy or biostratigraphy alone at every site, correlations between the GRAPE bulk density records were used to identify these events at every site.

The assumption that correlable events in the GRAPE records at all sites are entirely in-phase is necessary in order to correlate the records at high resolution. This assumption has major bearing on the results of studying time-varying spatial variability in the carbonate records. The assumption that there is no phase difference between events in the GRAPE records can only be tested with independent parameters from the same sites which can be expected to contain spatially in-phase events. For instance, measurements of benthic $\delta^{18}O$ can be expected to fluctuate entirely in phase across the Leg 138 study area; they can provide a means of testing the assumption that the GRAPE events are in phase. In the absence of data from all sites suggesting otherwise, the assumption of an in-phase response must be followed.

During post-Leg 138 study, it was demonstrated by Shackleton et al. (1992, 1993) that even finer stratigraphic resolution is possible if the assumptions of an orbitally driven system are considered. Variance present in the GRAPE bulk density records from Sites 846 through 853 falls in the Milankovitch band (Pisias et al, 1992). This was used as evidence

---

Table III.2. Statistics for predicted values of $\%CaCO_3$ compared to measured values, sites 846-853. The model skill gives the fraction of variance explained by the two parameter model given in (2). CRIT.VAL. is the 0.99 level for significant skill. RMS is the root mean square error.

		MEASURED $\%CaCO_3$		PREDICTED $\%CaCO_3$				
SITE	**N**	**MEAN**	**STD.DEV.**	**MEAN**	**STD.DEV.**	**SKILL**	**CRIT.VAL**	**RMS**
846	166	57.7	16.2	61.9	17.2	0.85	0.24	8.85
847	227	63.1	13.6	62.7	15.4	0.87	0.20	7.61
848	69	72.0	9.6	68.3	10.5	0.83	0.36	5.69
849	154	74.7	11.4	74.9	12.3	0.74	0.24	8.21
850	128	71.5	9.6	72.2	10.9	0.78	0.27	6.71
851	123	77.8	6.5	73.1	11.6	0.47	0.27	10.2
852	121	74.2	9.8	69.4	12.7	0.90	0.28	5.50
853	59	69.4	10.5	69.3	10.7	0.86	0.39	5.32

for a primary response of these records to variations in the earth's insolation. Variations in GRAPE were correlated to 65°N solar insolation (as determined by Berger and Loutre, 1988) to develop a chronology which is both internally consistent and astronomically calibrated over the past 6 myr (Shackleton et al., 1992, 1993). Because no *a priori* model was available that predicts appropriate time constants for the response of equatorial Pacific carbonate to orbital forcing, zero phase between insolation and GRAPE was assumed. The time series of predicted $\%CaCO_3$ from sites 846-853 on the resulting astronomically calibrated chronology for the interval from 0-6 myr are given in Figure III.7.

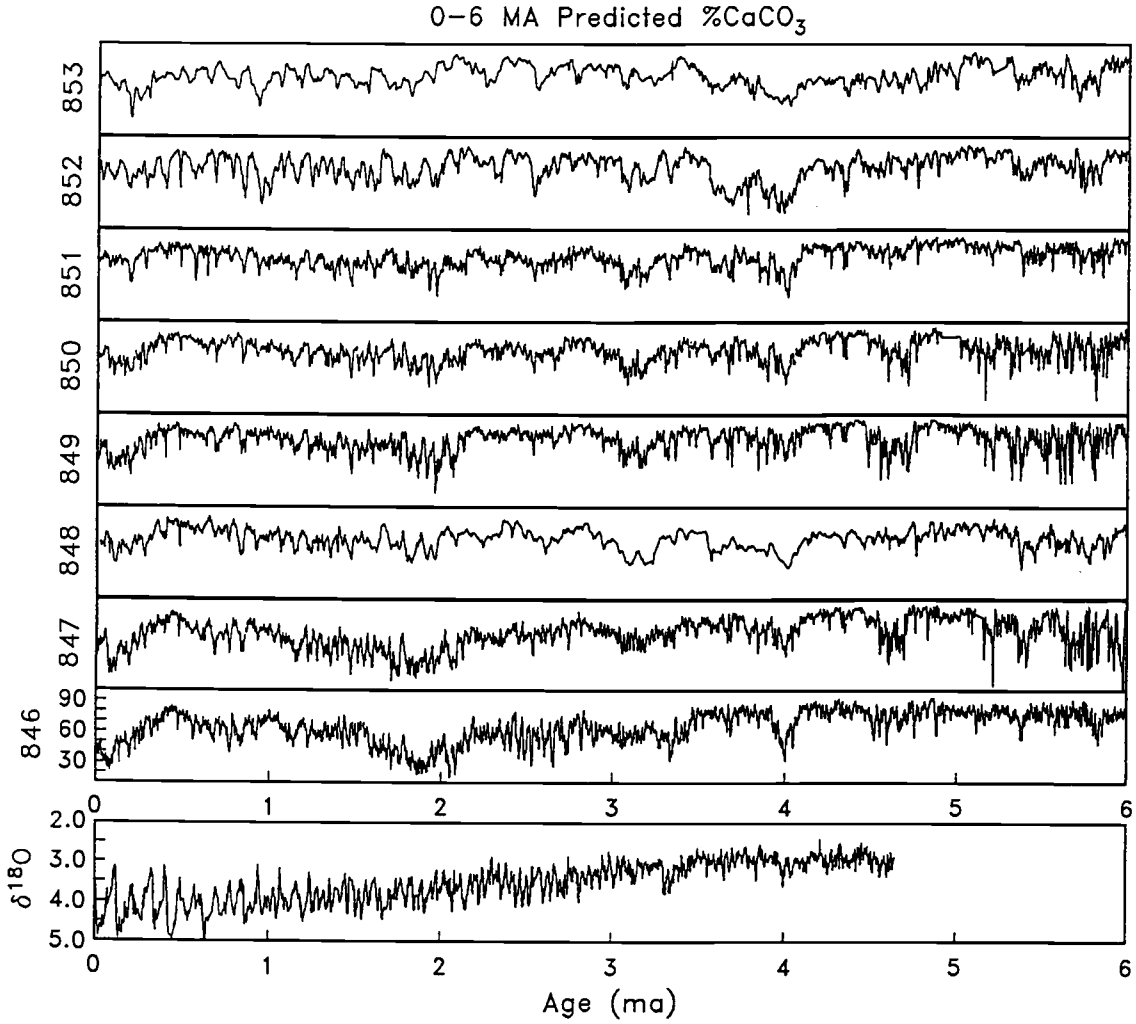

Figure III.7. (top): 6 myr records of predicted $\%CaCO_3$ for sites 846 - 853. The y-axis scale is indicated for site 846. (bottom): Spliced benthic $\delta^{18}O$ record from site 849 (Mix, et al., 1993) and site 846 (Shackleton, et al., 1993).

Mass Accumulation Rates

Although a great deal of information can be gained from the study of $\%CaCO_3$ records alone, it is not always a valid assumption that $\%CaCO_3$ is an accurate indicator of calcite burial. Dilution by biogenic opal and other sedimentary components can influence carbonate concentration in sediments. Farrell and Prell (1989,1991) assumed that opal sedimentation in the central equatorial Pacific was sufficiently negligible such that $\%CaCO_3$ could be used as an approximation of carbonate mass burial. In the eastern tropical Pacific however, opal is often a significant sedimentary component. In this study, carbonate mass accumulation rates are estimated in order to objectively evaluate the role of carbonate sedimentation, and for comparison to spatial variability in the records of $\%CaCO_3$.

Table III.3. A. Grain density statistics, sites 846 -853

SITE	N	MEAN	STD. DEV.
846	398	2.50	0.12
847	375	2.54	0.10
848	115	2.59	0.08
849	317	2.59	0.07
850	260	2.60	0.07
851	248	2.63	0.07
852	135	2.72	0.05
853	75	2.73	0.05

B. Statistics for predicted values of dry bulk density compared to measured values, sites 846-853. The model skill gives the fraction of variance explained by the two parameter model given in (2). CRIT.VAL. is the 0.99 level for significant skill. RMS is the root mean square error.

	MEASURED DRY BULK DENSITY			PREDICTED DRY BULK DENSITY				
SITE	N	MEAN	STD.DEV.	MEAN	STD.DEV.	SKILL	CRIT.VAL	RMS
846	398	0.59	0.14	0.59	0.14	0.90	0.15	.059
847	375	0.55	0.15	0.54	0.14	0.91	0.16	.059
848	115	0.57	0.09	0.58	0.09	0.83	0.28	.049
849	317	0.67	0.13	0.65	0.12	0.83	0.17	.066
850	260	0.63	0.12	0.61	0.11	0.83	0.19	.059
851	248	0.63	0.10	0.62	0.10	0.89	0.19	.045
852	135	0.58	0.12	0.57	0.11	0.86	0.26	.054
853	74	0.52	0.09	0.55	0.09	0.71	0.35	.063

Calculation of mass accumulation rates incorporates several sources of error. Carbonate concentration, which is estimated from GRAPE here, is subject to error. Standard errors in carbonate prediction were estimated in the preceding section (Table III.2) and are on the order of 7%. Second, the dry bulk density of the sediment must be known. Third, a highly constrained chronology is required for sedimentation rate determination. The cumulative errors in estimating these three parameters limits the use of mass accumulation rates.

During Leg 138, wet bulk density, dry bulk density, porosity, and grain density estimates were derived from measurements of wet and dry sediment weights and sediment dry volume following the procedures of Boyce (1976). These estimates were made at 75 cm intervals on the same samples as shipboard $\%CaCO_3$ measurements. High resolution

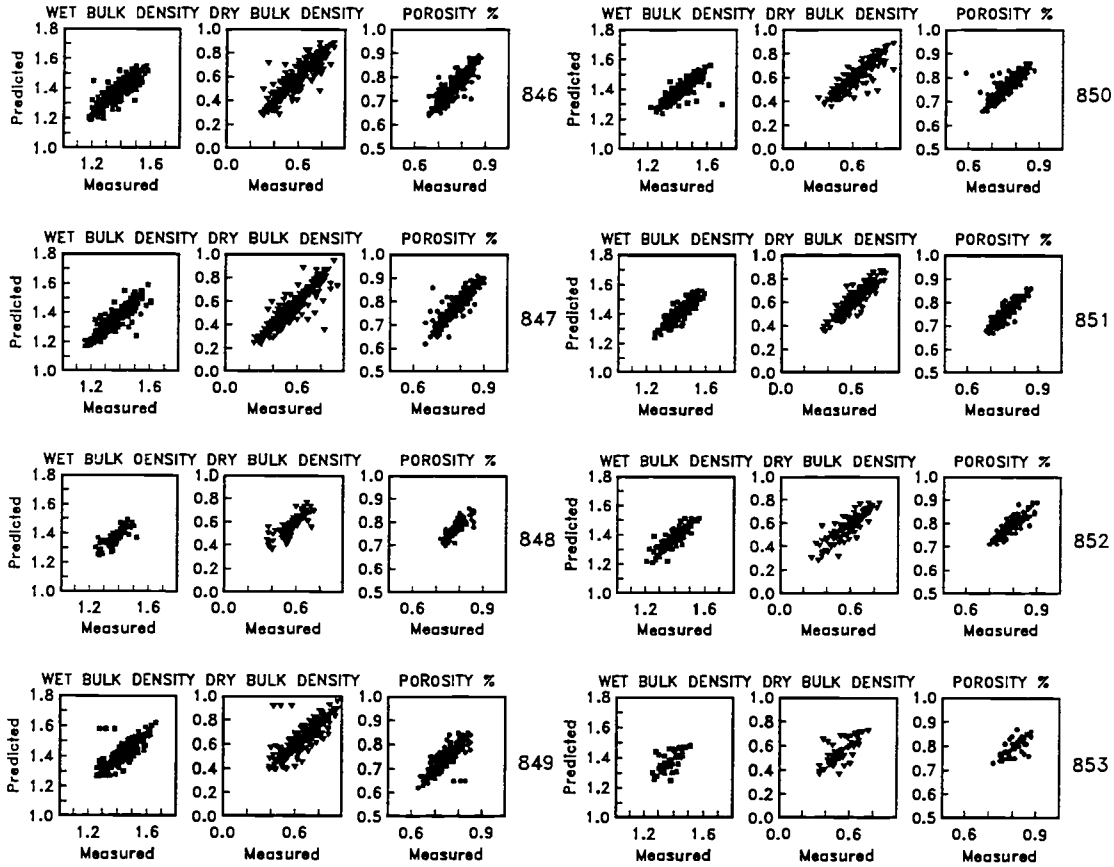

Figure III.8. Scatter plots of predicted vs measured wet bulk density (squares), dry bulk density (triangles) and porosity (circles) for sites 846 - 853. The y-axis scale is given in the bottom panel.

estimates of dry bulk density are possible if dry bulk density can be determined from GRAPE wet bulk density. Sedimentary dry bulk density, by definition, is the density of sediment after the salts and water filling the pore space have been removed. If the porosity of the sediment are known, dry bulk density is estimated from the following relation:

dry bulk density = wet bulk density - 1.025 x porosity.

Porosity can be estimated if the wet bulk density and the grain density of the sediment are known:

porosity = (grain density - wet bulk density)/(grain density - fluid density).

Thus, given an estimate of the sediment grain density, it is possible to estimate sedimentary dry bulk density from GRAPE.

Typical grain densities for biogenic sediments are on the order of 2.6 g/cc (Boyce, 1976). Statistics for sediment grain densities derived from the physical property measurements are given for each site in Table III.3. At any given site, the grain density is uniform. However, there are significant differences between individual sites, as mean grain densities

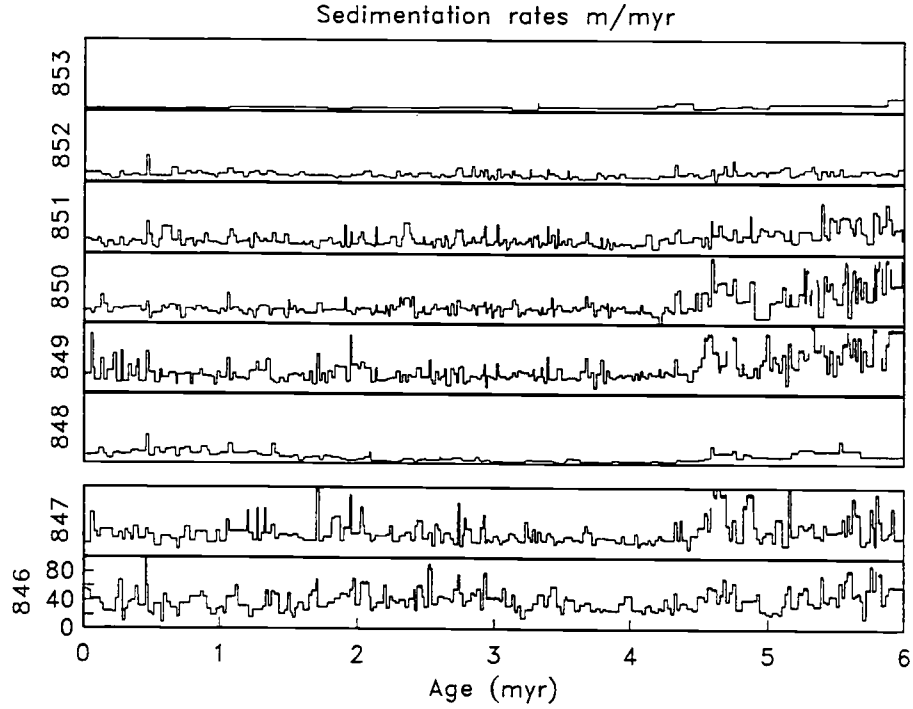

Figure III.9. Sedimentation rates for sites 846 - 853, 0-6 myr, from the Shackleton et al. (1993) age model.

range from 2.5 g/cc at site 846 to 2.7 g/cc at site 853. Using these estimates of grain density, GRAPE predictions of wet bulk density, dry bulk density, and porosity are compared to measured values for each site (Figure III.8 and Table III.3). The correlation between GRAPE-predicted and estimated values is significant at a .99 level for each site. Root mean square error ranges from 0.045 to 0.066, on the order of 8%.

Sedimentation rate estimates in this study are derived directly from tie points in the astronomically calibrated chronology of Shackleton et al. (1993). Average spacing of age control points is 26-30 kyr with two exceptions. Sites 848 and 853 have much lower sedimentation rates, and it was not possible to directly transfer the high resolution chronology to these sites. The sedimentation rates for sites 846-853 derived from this age model shown are in Figure III.9. Estimates of errors in the sedimentation rates are difficult

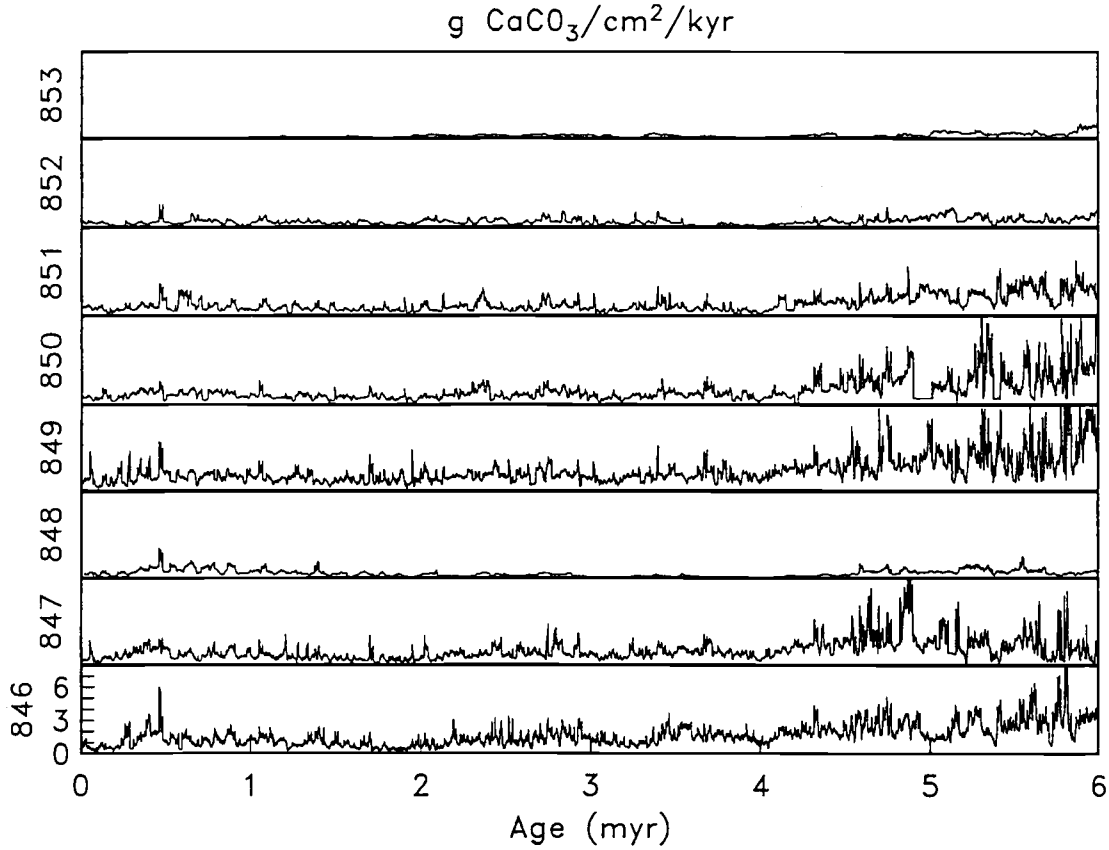

Figure III.10. $CaCO_3$ mass accumulation rates, 0-6 myr for sites 846 - 853. See text for description of how calculated. Y-axis is given in the bottom panel.

to obtain. However, comparison of the tuned chronology with variations typically seen between adjacent holes (Hagelberg et al., 1993) suggests that variability in sedimentation rates on the order of 15% are typical.

Carbonate mass accumulation rates are calculated according to the following relation: MAR ($g/cm^2/kyr$) = $\%CaCO_3$ * DBD (g/cm^3) * sedimentation rate (cm/kyr) Assuming the three sources of error estimated above are uncorrelated, the total error on these estimates is around 7% + 8% + 15% = 30%. This is a very rough approximation, but it serves to indicate the higher error introduced into MAR estimates. Estimates of carbonate MAR for Sites 846 - 853 for the interval 0-6 myr are given in Figure III.10.

EOF Analysis

Each record from Sites 846 through 853 displays some level of variability which is common to all of the sites, as well as variability which is unique to that site. The common variability was used by Shackleton et al. (1992) as a means to correlate bio- and magnetostratigraphic events between sites, as described above. A goal of this study is to quantitatively partition patterns of variability in equatorial Pacific carbonate sedimentation.

The numerical approach used to partition the 8 time series from sites 846-853 into a smaller set of spatial and temporal patterns is known as Empirical Orthogonal Function (EOF) analysis. EOF analysis is a means of representing a spatial array of time series by a finite number of independent (orthogonal) spatial modes of variability and weighted amplitude time series of these modes. In equation form,

$$x_m(t) = \sum_{k=1}^{M} a_k(t) F_k(m) \qquad (3)$$

where t is the time index 0,1,2,...N for observations at M locations ($m = 1,...M$) (in this study, $M = 8$). The M time series are decomposed into a set of orthogonal functions (EOFs) $F_k(m)$, where k is the mode number, multiplied by the amplitude of that mode at time t, $a_k(t)$. The

simplification is that a small number of EOFs describe most of the variability in a data set more efficiently than any other representation. In this study, variability within the arrays of $\%CaCO_3$ and carbonate mass flux records from sites 846 -853 are studied. The EOFS are determined from the data covariance matrix.

Spectral Analysis

Power spectra and cross-spectra and of the amplitude time series from the EOF analyses indicate the frequency distribution of variance of each EOF as well as the extent to which each EOF is coherent with Milankovitch band variability. Power spectral and cross spectral estimates were made using the Blackman-Tukey lagged auto- (or cross-) covariance method (Jenkins and Watts, 1968). Sampling intervals were 1000 yr. For analyses of the entire 6 myr records, 600 lags of the auto and cross-covariance and a cosine taper window were used for smoothed estimates having at least 27 degrees of freedom. For analyses of 1 myr intervals, 400 lags of the auto or cross covariance were used for smoothed estimates having at least 7 degrees of freedom.

RESULTS AND DISCUSSION

General Patterns of Carbonate Variability, 0-6 ma

Figures III.11 and III.12 show the patterns of sedimentary carbonate concentration given in Figure III.7 as functions of water depth and latitude (for the 110°W transect) over the past 4 myr. If all other factors affecting carbonate concentration are held constant, a relationship between increased water depth and decreased $\%CaCO_3$ would be expected through the effect of pressure on the solubility of calcite. Although the depth range covered is limited (Table III.1 and Figure III.4), depth does not appear to be a significant factor controlling $\%CaCO_3$ (Figure III.11). This suggests that processes such as dilution by noncarbonate sedimentary components and / or productivity, are more important than dissolution in determining $\%CaCO_3$.

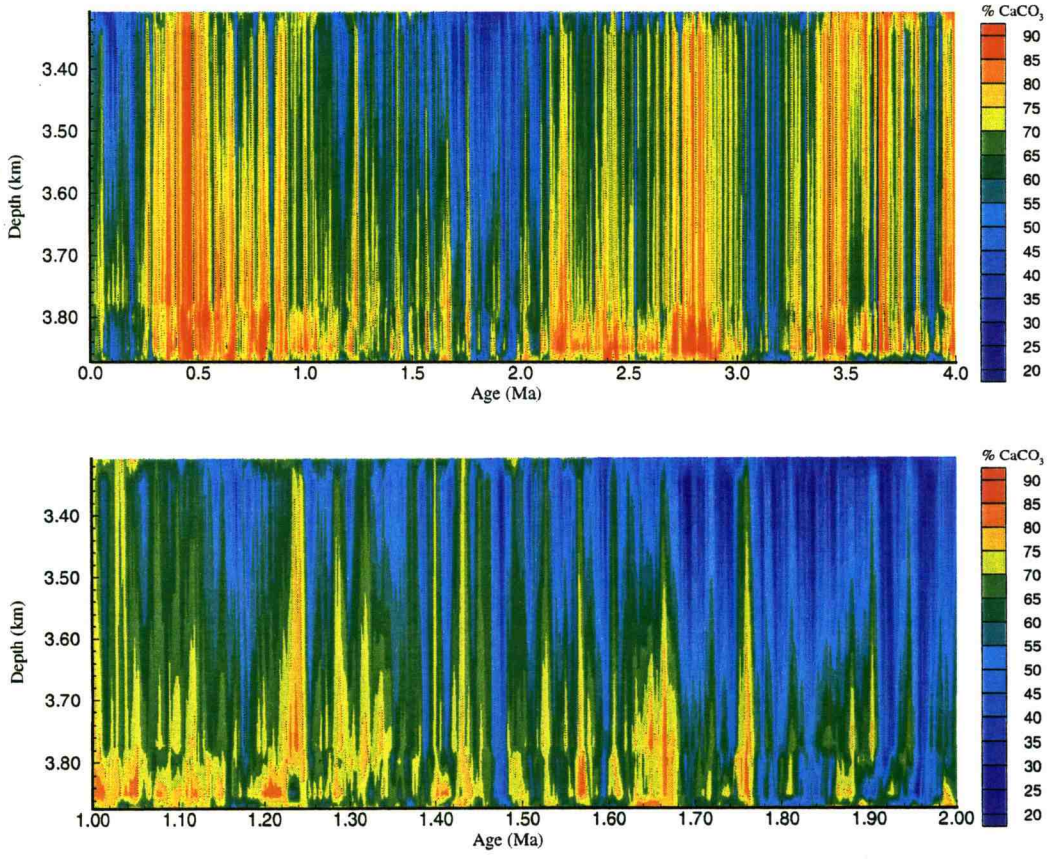

Figure III.11. Contours of predicted $\%CaCO_3$ as a function of depth and time for 0-4 myr. The scale is given to the right. The bottom panel is an expanded view of the interval from 1 - 2 ma.

The extent to which $\%CaCO_3$ variability is coupled to latitude can be inferred from Figure III.12. Although oscillations in $\%CaCO_3$ that are common to all sites are the dominant feature, latitudinal control on $\%CaCO_3$ is evident. The relatively low frequency variability in oscillations common to all sites evident in the top panel of Figure III.12 may suggest dissolution controls on carbonate sedimentation, as all sites appear to be affected similarly. However, variability which is latitudinally controlled appears to be present at all timescales, suggesting that surface ocean processes are significant. The surface water controls on carbonate concentration include dilution by noncarbonate material, carbonate productivity, or a combination of two, as in Lyle et al. (1988). It can generally be concluded from Figures III.11 and III.12 that multiple processes are important in determining the space-time variability of equatorial Pacific carbonate sedimentation. The best way to

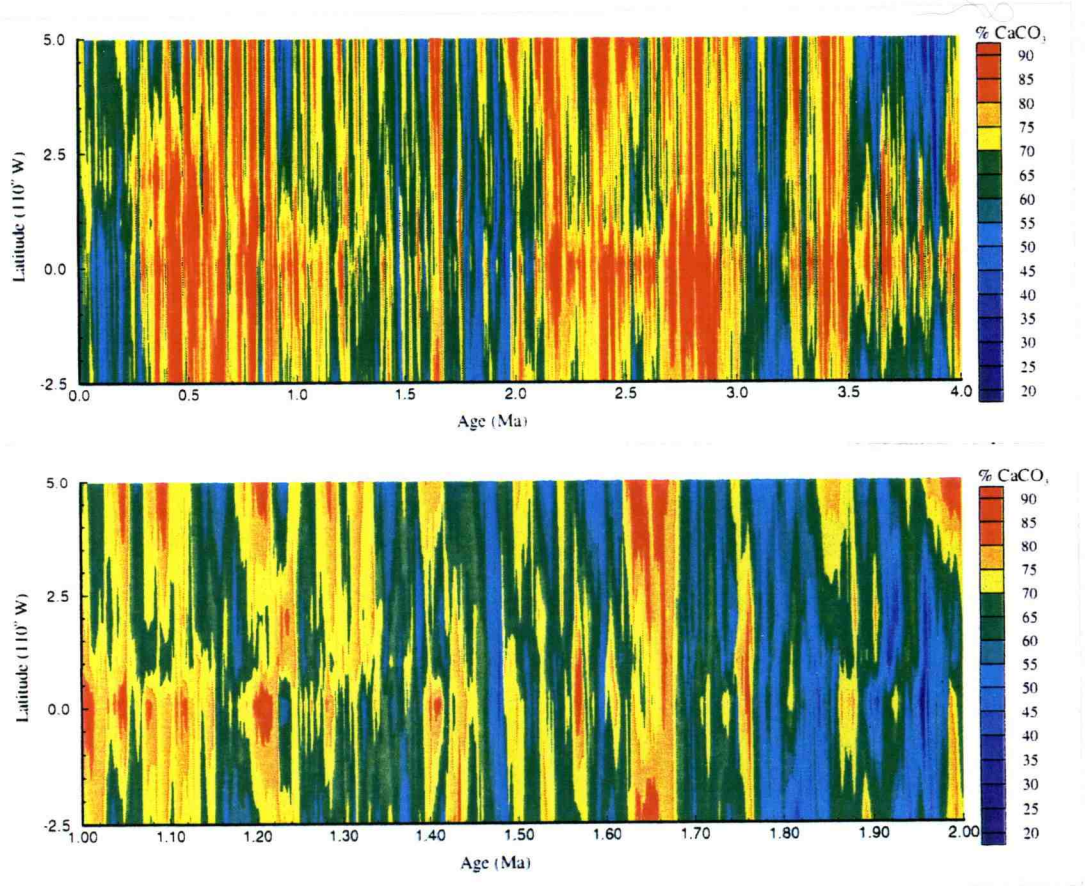

Figure III.12. Contours of predicted $\%CaCO_3$ for 110°W transect sites 848 - 852 as a function of time and latitude for 0-4 ma. The scale is given to the right. The bottom panel is an expanded view of the interval from 1 - 2 ma.

quantify the temporal variations of these processes is with one time series describing each independent mode of variation. This is done in the remainder of this study using EOF analysis.

An EOF analysis of the entire 0-6 myr records for Sites 846-853 resolves two modes of variability which together explain 77% of the total variance. The spatial patterns of these two modes are given in map form in Figure III.13, and the amplitude time series of the two spatial modes are in Figure III.14. Table III.4a gives loadings of the two EOFs.

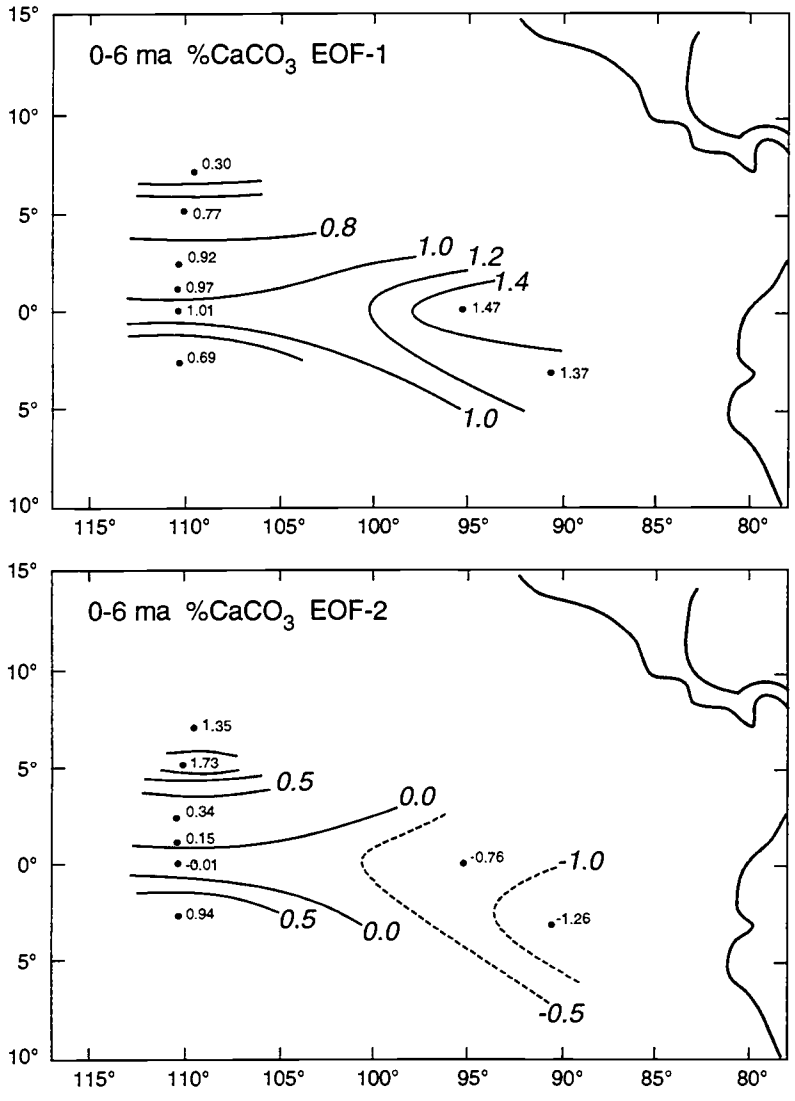

Figure III.13. EOF-1 (top) and EOF-2 (bottom) of $\%CaCO_3$, 0-6 myr. Values contoured are the loadings for each EOF (elements of the eigenvector), normalized by the length of the eigenvector so that the average loading is 1.0.

The first EOF of the 0-6 myr %$CaCO_3$ data accounts for 56% of the total variance (Table III.4a). The spatial map of EOF-1 (Figure III.13a) is characterized by high loading at eastern transect sites 846 and 847. On the western transect, the highest loading is at equatorial site 849, with loadings decreasing away from the equator. The pattern of coupling to the equator suggests that this dominant mode of %$CaCO_3$ variability may be related to equatorial divergence.

The amplitude time series (Figure III.14a) and power spectrum (Figure III.15a) of EOF-1 indicate dominance by a combination of low frequency (200 - 250 kyr) and higher frequency Milankovitch band oscillations. Very high coherence is present between insolation at 65°N (Berger and Loutre, 1988) and EOF-1 at periods of 41 kyr, 23 kyr, and 19 kyr (Figure III.15a and Table III.4b). 65°N insolation and EOF-1 are in phase where

---

Table III.4 A. The first two EOFs, 0-6 Ma %$CaCO_3$

SITE	**EOF 1**	**EOF 2**
846	1.37	-1.26
847	1.47	-0.76
848	0.69	0.94
849	1.01	-0.01
850	0.97	0.15
851	0.92	0.34
852	0.77	1.73
853	0.30	1.35
EIGENVALUE:	643.2	225.6
% VARIANCE:	56.2	19.4

B. Results of cross-spectral analyses between 65°N insolation and EOFs 1 and 2 , 0-6 ma %$CaCO_3$. Positive phase indicates that insolation leads the EOF.

	PERIOD (ky)	**COH.**	**PHASE (deg)**		**PERIOD (ky)**	**COH.**	**PHASE (deg)**
EOF-1	125	0.48	-176 +/- 26	EOF-2	100	0.41	-141 +/- 30
	41	0.89	3 +/- 8		67	0.54	-51 +/- 22
	23.8	0.93	-10 +/- 6		53	0.41	-48 +/- 30
	22.2	0.93	-12 +/- 6		36	0.54	-65 +/- 22
	19	0.95	-5 +/- 5		32	0.47	-40 +/- 26
	15	0.55	15 +/- 22		23	0.47	143 +/- 26
	13	0.49	39 +/- 25		19	0.56	170 +/- 21
	11	0.49	3 +/- 25		17	0.51	130 +/- 24
	10	0.75	7 +/- 13		13	0.44	-90 +/- 28
					12	0.60	-25 +/- 19
					11	0.53	-100 +/- 23

coherent, with the exception of at 100 kyr, where phase is close to -180° (176 +/- 26 degrees, or a 61 year lead of EOF-1). While the coherence at 41 kyr, 23 kyr, and 19 kyr is significant at both a 0.80 (coherence = 0.37) and 0.90 (coherence = 0.66) level, coherence between EOF-1 and insolation at 100 kyr is not significant at a .90 level. Although the presence of astronomical forcing at 100 kyr suggests that the observation of coherence at this frequency may be significant, the low coherence should be regarded with caution. Near zero phase at the dominant insolation frequencies reflects the orbital calibration of the chronology.

The spatial map for EOF-2 of the entire data set accounts for over 19% of the total variance. The highest loadings are off - equator on the 110°W transect, at sites 848, 852, and 853, and at eastern transect sites 846 and 847, where loadings are of the opposite sign (Figure III.13b). The western transect equatorial sites have minimum loading. EOF-2 appears to represent a mode of variability having both north-south and east-west asymmetry, with most of the variability explained by off-equatorial and eastern boundary sites.

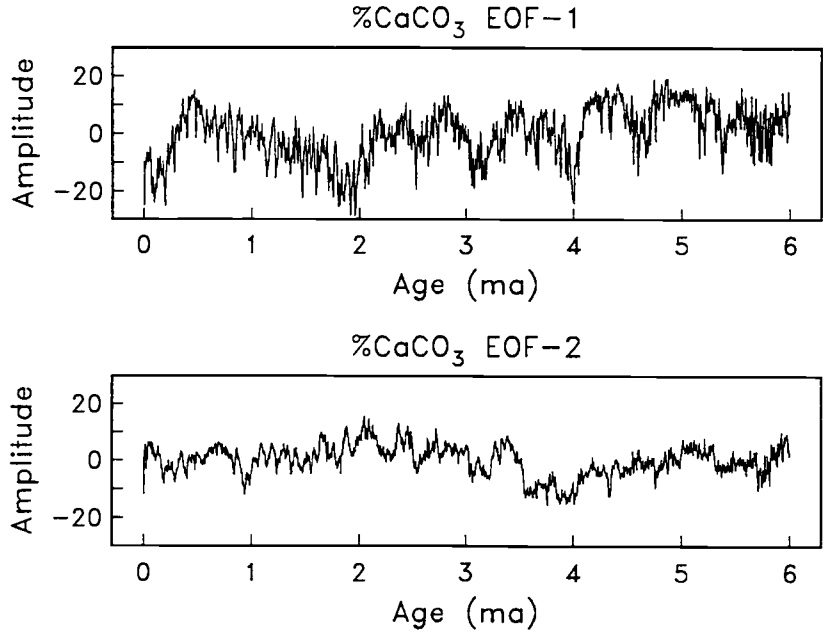

Figure III.14. Amplitude time series of EOF-1 (top) and EOF-2 (bottom) of 0-6 myr $\%CaCO_3$.

Variance in the amplitude time series of EOF-2 (Figure III.14b) is dominated by low frequencies which are not as coherent with insolation variations as EOF-1, although significant (.80 level) coherence is present at some Milankovitch frequencies (Figure III.15b; Table III.3b). At a .90 level, however, none of the frequencies in the EOF-2 time series are coherent with insolation. In the precession band where insolation and EOF-1 are also coherent, insolation and EOF-2 have a phase close to 180° (143 +/- 26 for 23 kyr, and 170 +/- 21 for 19 kyr, or 9 kyr for both). If real, this separation of Milankovitch band variability into two modes implies that multiple processes are operating at the same frequencies. However, as is the case with the 100 kyr oscillations in EOF-1, the lower coherence between EOF-2 and insolation should be regarded with caution.

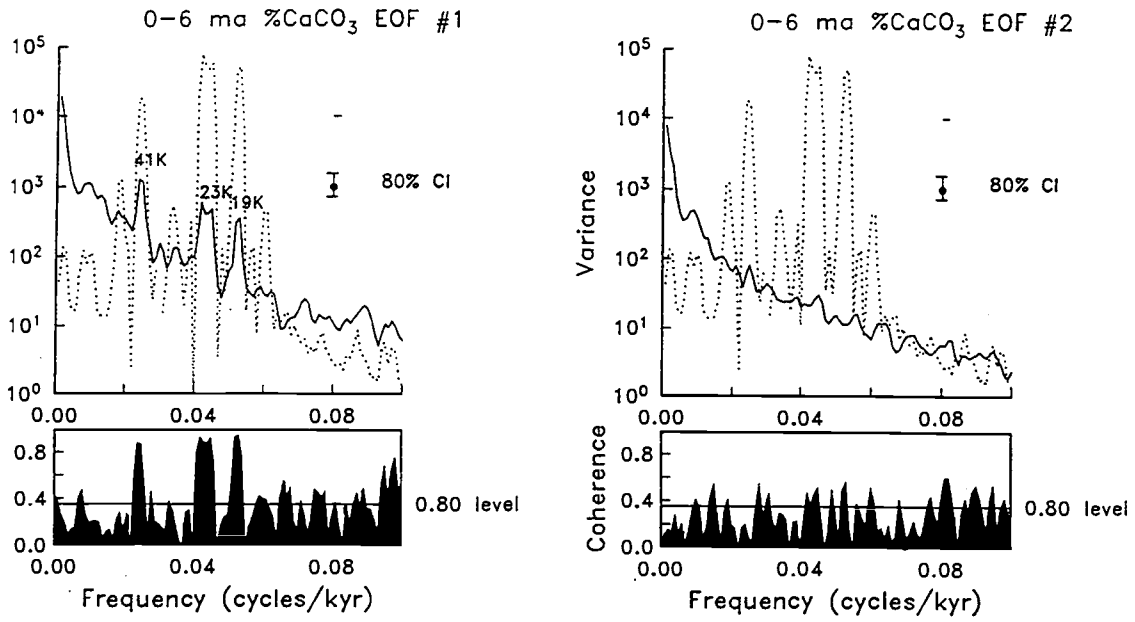

Figure III.15. Power spectra and coherence spectra for EOF-1 (left) and EOF-2 (right), respectively and 65°N insolation (Berger and Loutre, 1988), for the 0-6 myr amplitude time series given in Figure III. 14. The solid line indicates the EOF power spectra, the dotted line is the insolation power spectrum. 80% confidence limits and the bandwidth on the spectra are illustrated in the top panel. The horizontal line in the bottom panel indicates the .80 significance level for coherence.

Evolution of %$CaCO_3$ Variability

As discussed in the Introduction, large changes in both climatic and tectonic boundary conditions have occurred over the past 6 myr. For example, a change in the nature of ice volume variability occurred near 1 ma (Pisias and Moore, 1981; Ruddiman et al., 1989; Raymo et al., 1989) and near 2.4 ma with the onset of major Northern Hemisphere ice sheets (Figure III.7). Large changes in carbonate and bulk sedimentation rates occurred at all sites from 6 ma to 4.7 ma (Mayer, Pisias, et al., 1992; Figure III.7). It is not understood

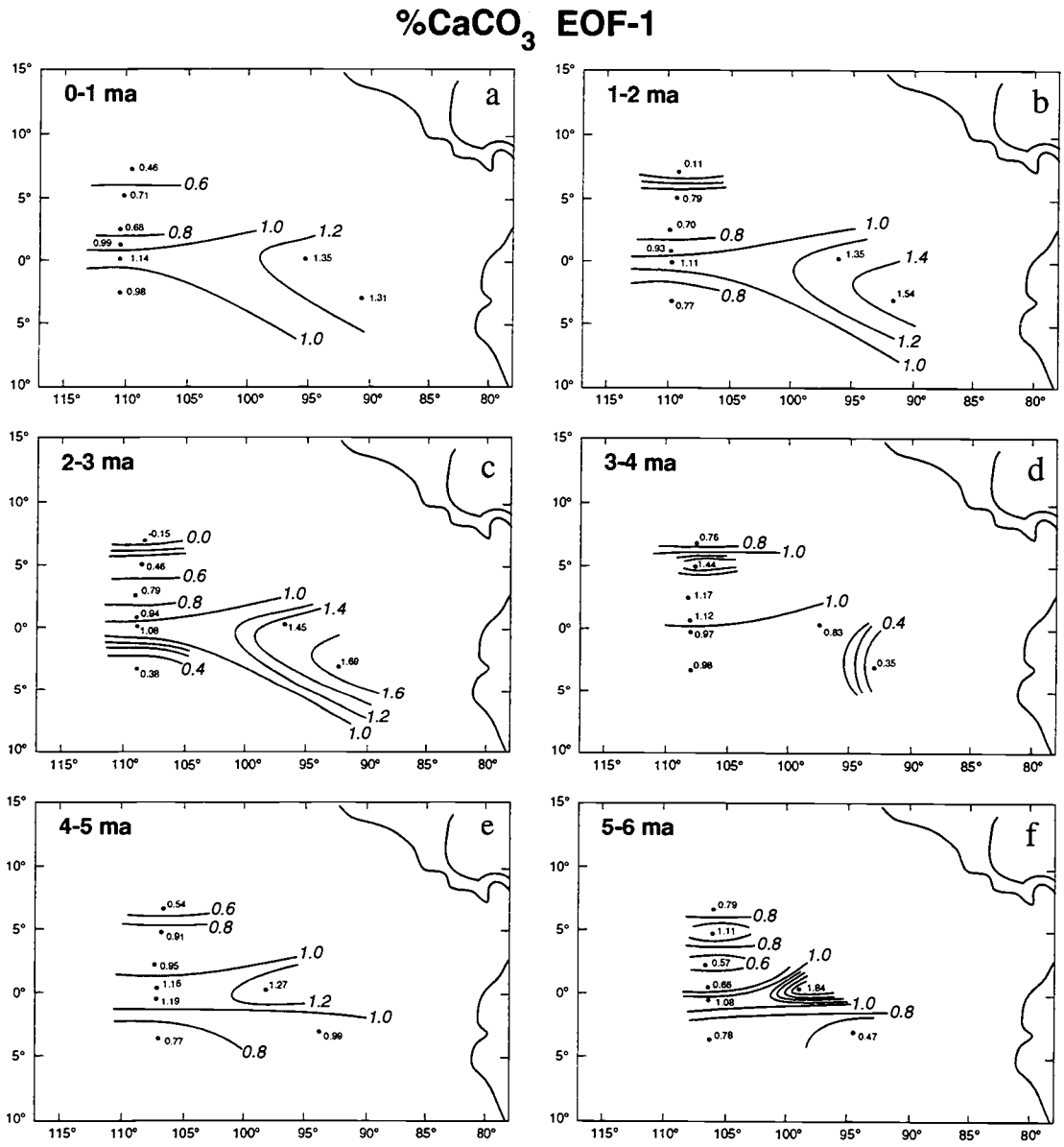

Figure III.16. (a-f): EOF-1 of %$CaCO_3$ in 1 myr time slices, 0 to 6 myr.

how these changes have influenced the modes of variability in equatorial Pacific $\%CaCO_3$. Evolutive spectra also suggest an evolution in $\%CaCO_3$ variability having a transition near 1 ma (Mayer, et al., 1992). Thus, the evolution of the modes of variability which characterize carbonate sedimentation is investigated by performing separate EOF analyses on successive 1 myr time intervals.

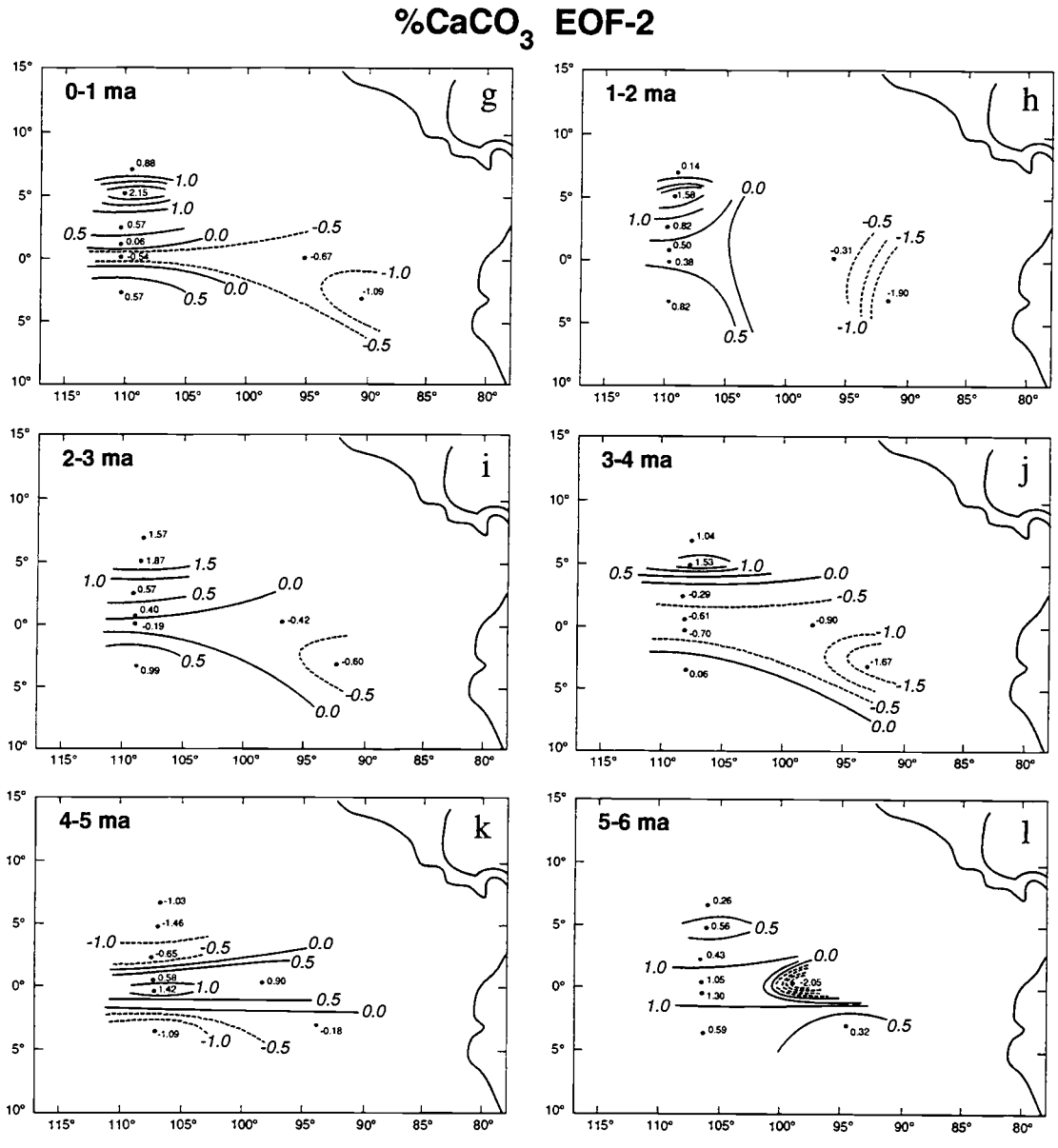

Figure III.16. (g-l): EOF-2 of $\%CaCO_3$ in 1 myr time slices.

The spatial maps of the two dominant EOFs for each time slice are shown in Figure III.16, and the EOFs are given in Table III.5. The Leg 138 sites in each spatial map have been backtracked and are located at approximate paleolatitudes, according to the rotation of Cox and Engebretson (1985). In each time interval two modes dominate. The total

Table III.5. The first two EOFS, 1 Myr time slices $\%CaCO_3$

0-1 MA			**1-2 MA**		
SITE	**EOF 1**	**EOF 2**	**SITE**	**EOF 1**	**EOF 2**
846	1.31	-1.09	846	1.54	-1.90
847	1.35	-0.67	847	1.35	-0.31
848	0.98	0.57	848	0.77	0.82
849	1.14	-0.54	849	1.11	0.38
850	0.99	0.06	850	0.93	0.50
851	0.68	0.57	851	0.70	0.82
852	0.71	2.15	852	0.79	1.58
853	0.46	0.88	853	0.11	0.14
EIGENVALUE:	634.9	129.0	EIGENVALUE:	450.1	113.8
% VARIANCE:	66.0	13.4	% VARIANCE:	59.1	14.9
2-3 MA			**3-4 MA**		
SITE	**EOF 1**	**EOF 2**	**SITE**	**EOF 1**	**EOF 2**
846	1.69	-0.59	846	0.35	-1.67
847	1.45	-0.42	847	0.83	-0.90
848	0.38	0.99	848	0.98	0.06
849	1.08	-0.19	849	0.97	-0.70
850	0.94	0.40	850	1.12	-0.61
851	0.79	0.57	851	1.17	-0.29
852	0.46	1.87	852	1.44	1.53
853	-0.15	1.57	853	0.76	1.04
EIGENVALUE:	294.4	117.9	EIGENVALUE:	502.2	310.1
% VARIANCE:	54.0	21.6	% VARIANCE:	51.2	31.6
4-5 MA			**5-6 MA**		
SITE	**EOF 1**	**EOF 2**	**SITE**	**EOF 1**	**EOF 2**
846	0.99	-0.18	846	0.47	0.32
847	1.27	0.90	847	1.84	-2.05
848	0.77	-1.09	848	0.78	0.59
849	1.19	1.42	849	1.08	1.30
850	1.16	0.58	850	0.66	1.05
851	0.95	-0.65	851	0.57	0.43
852	0.91	-1.46	852	1.11	0.56
853	0.54	-1.03	853	0.79	0.26
EIGENVALUE:	483.0	131.0	EIGENVALUE:	370.5	170.6
% VARIANCE:	64.4	17.5	% VARIANCE:	43.5	20.0

amount of variance explained by these two modes is consistent, with EOF-1 representing from 43% to 66%, and EOF-2 representing from 13% to 32% of the overall variance. In only one time interval, from 5-6 myr, is the variance in the 3rd EOF (not shown) greater than 10%.

With the exception of site 852, which has a high loading from 3-4 ma and 5-6 ma, the spatial pattern of EOF-1 in each time slice has a high degree of coupling to the equator. As with the results from 0-6 ma, the spatial pattern of EOF-1 in each interval suggests an influence of surface ocean processes on variations in $\%CaCO_3$ concentration. The influence of dissolution relative to carbonate productivity in determining these patterns is discussed below.

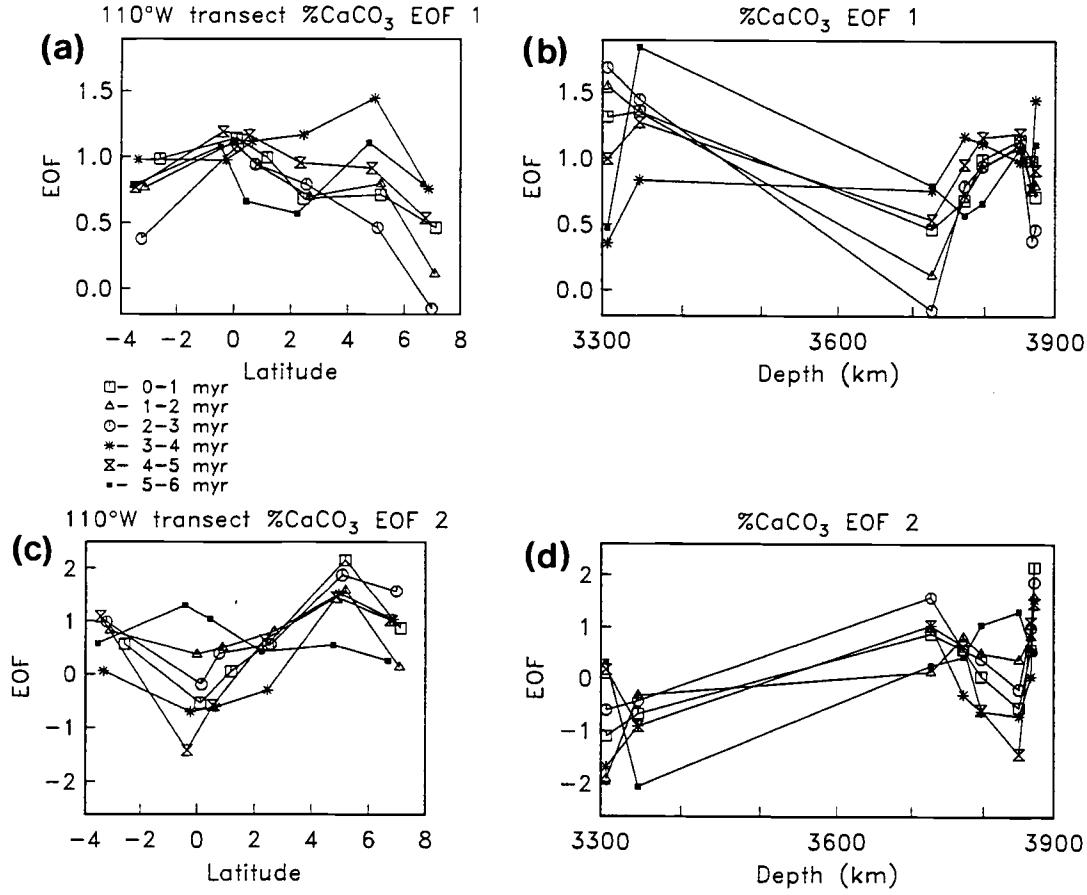

Figure III.17. (a): $\%CaCO_3$ 1 myr time slice EOF-1 loadings on the 110°W transect. (b): EOF-1 loadings for each time slice as a function of present water depth. (c): EOF-2 loadings on the 110°W transect. (d): EOF-2 loadings as a function of water depth. Note that for EOF-2, the 4-5 ma interval is inverted (mulitplied by -1).

Latitudinal gradients across the 110°W transect are given in Figure III.17a. High loadings in EOF-1 occur at the equator with a secondary peak at 4-5°N (Site 852). The relationship between modern water depth and the EOFs for each time slice is illustrated in Figure III.17b. This can be compared to Figure III.11 to evaluate the possible influence of dissolution in influencing the spatial patterns. Although relationships are difficult to resolve because of close depth spacing of sites 848, 849, and 852, the loadings of EOF-1 do not show a correlation with depth.

The spatial pattern of EOF-2 has similar features in the time intervals from 0-1 to 3-4 ma. Like the 0-6 ma analysis (Figure III.13b), a pattern of out of phase (opposite sign) east-west loadings is present, with the equatorial sites 849 and 850 having minimum importance. Highest positive loadings are at Site 852, and highest negative loadings are at Site 846 (Figure III.16 g-l). Prior to 3-4 ma a different spatial pattern is present. The interval from 4-5 ma, while showing a high loading at Site 852, does not display the east-west asymmetry that is seen in the interval from 0-4 ma. From 5-6 ma the spatial pattern of EOF-2 does not appear to have any similarities with the later time intervals. These similarities and differences are also evident in Figure III.17 c-d, which shows latitudinal and depth gradients for EOF-2. Some correlation between water depth and EOF-2 loadings may be evident, particularly between the eastern and western transects.

The change in the spatial pattern of EOF-2 between 3-4 ma and 4-5 ma could be related to changes associated with closure of the Panamanian Isthmus. This interpretation is highly dependent on the EOF loading at site 847, and thus should be taken cautiously until additional eastern equatorial Pacific records are available. However, Figure III17 c also indicates that the spatial pattern of EOF-2 on the 110°W transect is different from 5-6 ma than in later periods. This difference is not dependent on site 847. Thus, while spatial patterns in EOF-2 may indicate a response of carbonate sedimentation to a change in oceanographic boundary conditions between 4 and 6 ma, but additional investigation is necessary.

The amplitude time series for EOF-1 and EOF-2 for each 1 myr time slice are given in Figure III.18 (a-f). The power spectrum of each amplitude time series and coherence with insolation is given in Figure III.19. In general, the power spectra of the EOF-1 time series have more distinct concentrations of variance than the EOF-2 time series. Coherence with orbital insolation (41 kyr, 23 kyr, 19 kyr) is extremely high for EOF 1 in each time interval (Figure III.19 and Table III.6), and is significant at a .80 level (coherence = 0.67) as well as a .90 level (coherence = 0.88). The strong linear relationships indicate that the dominant variability in the $\%CaCO_3$ record over the past 6 myr includes Milankovitch variability. EOF-2 has significant (.80 level) coherence with precession band (23 kyr and 19 kyr) variations in each time slice with the exception of the interval from 1-2 ma. As with EOF-1 from the 0-6 myr analysis, near zero phase between 65°N insolation and EOF-1 reflects the constraint imposed by the orbital calibration of the time scale. Where coherence between EOF-2 and insolation is significant, the phase indicates that two processes are operating at the same Milankovitch frequencies with different time constants, or that two processes are operating, each of which has a different relationship to insolation. In general, EOF-2 contains variability that is not as strongly correlated with insolation as EOF-1. Most of the coherence observed between EOF-2 and insolation is not coherent at a .90 level, and occurs at "non-Milankovitch" frequencies. Thus, most of the variability in EOF-2 is not linearly related to insolation.

Carbonate Mass Accumulation Evolution

Before any inference is made with respect to the role of carbonate production relative to carbonate dissolution in driving the spatial patterns that are resolved, the role of dilution must be considered. Is the carbonate concentration record reflecting dilution by noncarbonate sedimentary components (primarily biogenic opal) more than processes related to carbonate sedimentation? This question can be addressed by analysis of carbonate mass accumulation rates. Although carbonate mass accumulation rates have

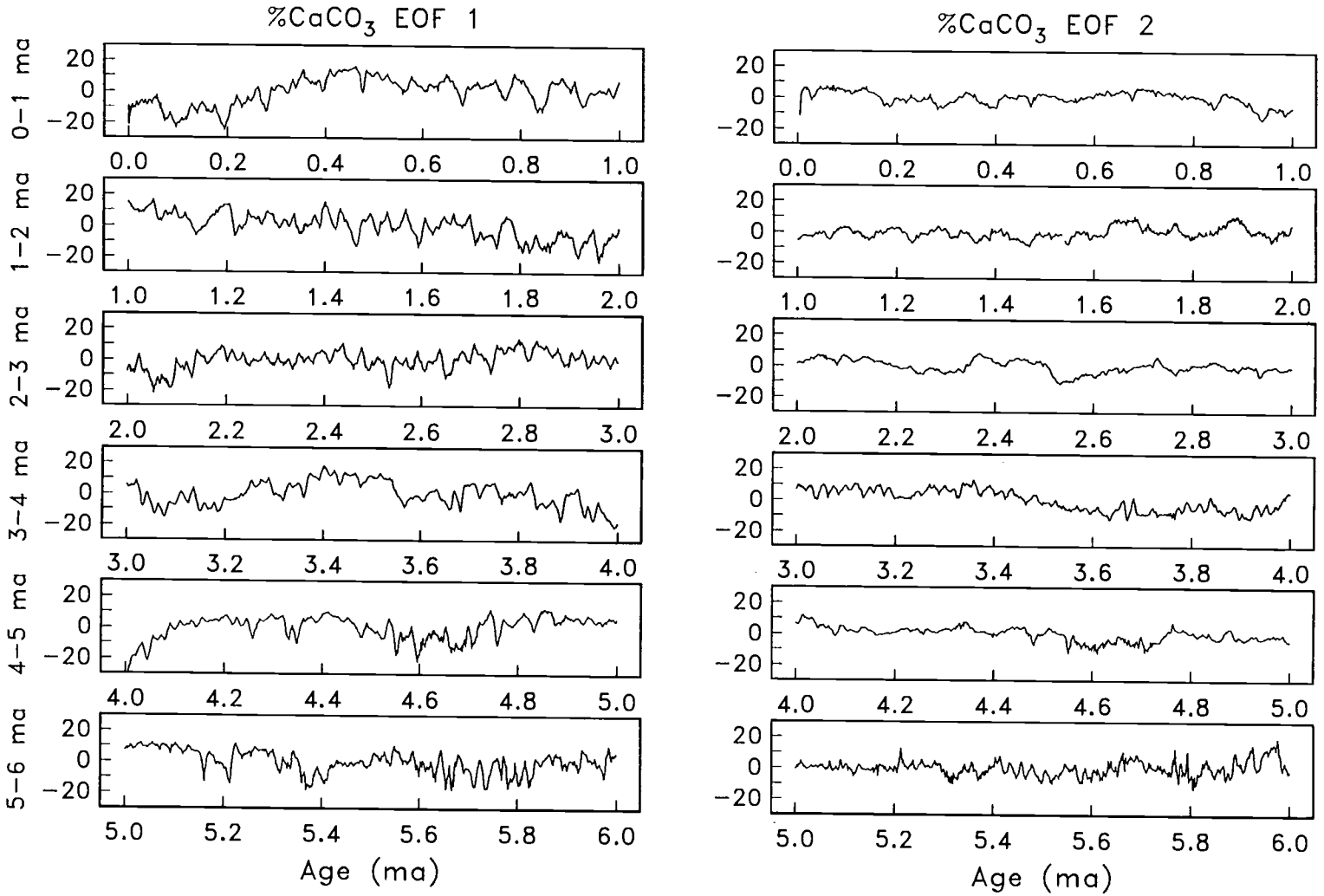

Figure III.18. Amplitude time series of EOF-1 (left) and EOF-2 (right) of 1 myr time slice %$CaCO_3$ EOFs.

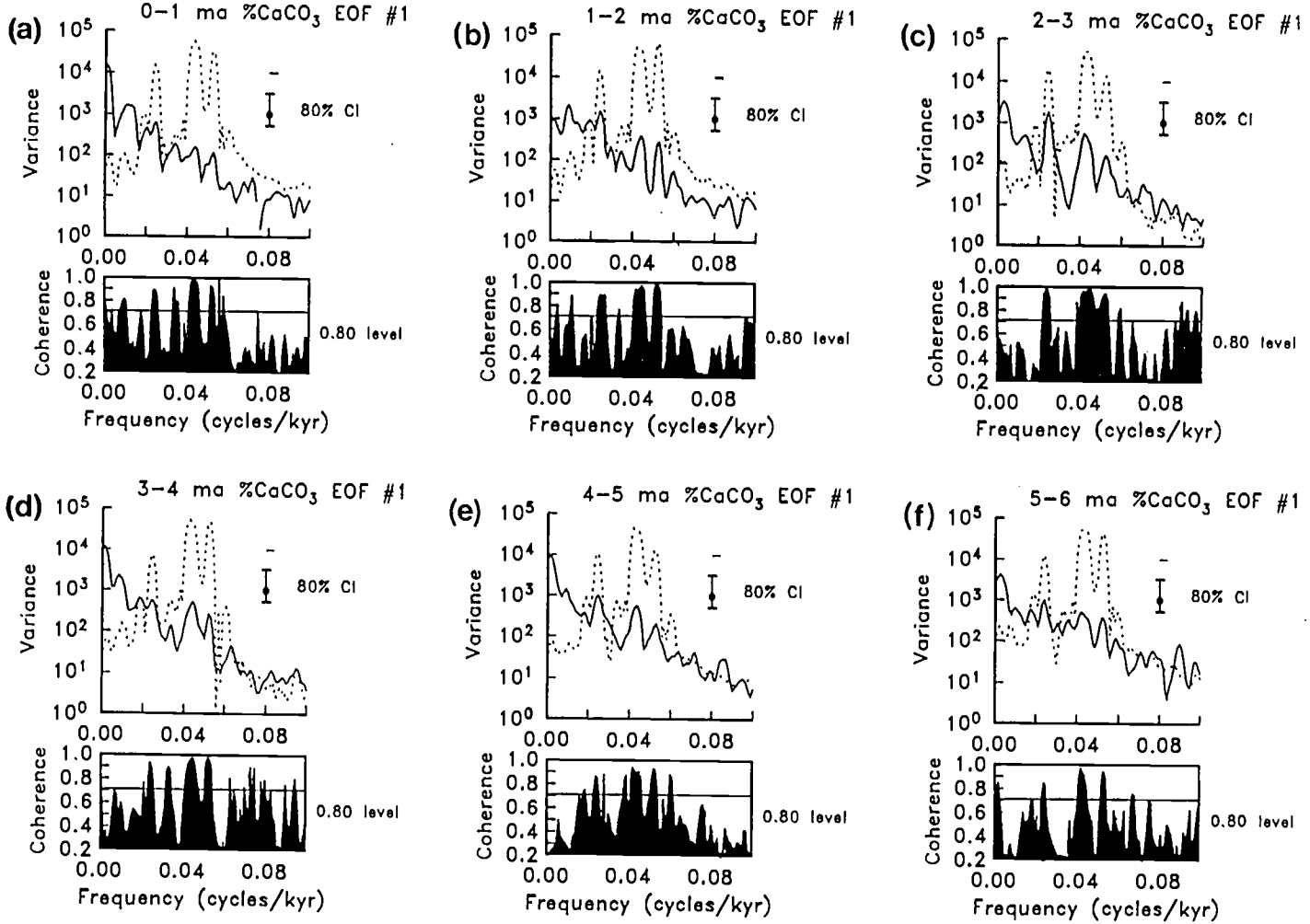

Figure III.19. (a-f): Power spectra and coherence spectra for EOF-1 and 65°N insolation, for the 1 myr time slice amplitude time series given in Figure III.18. Symbols are as described in the caption for Figure III.15.

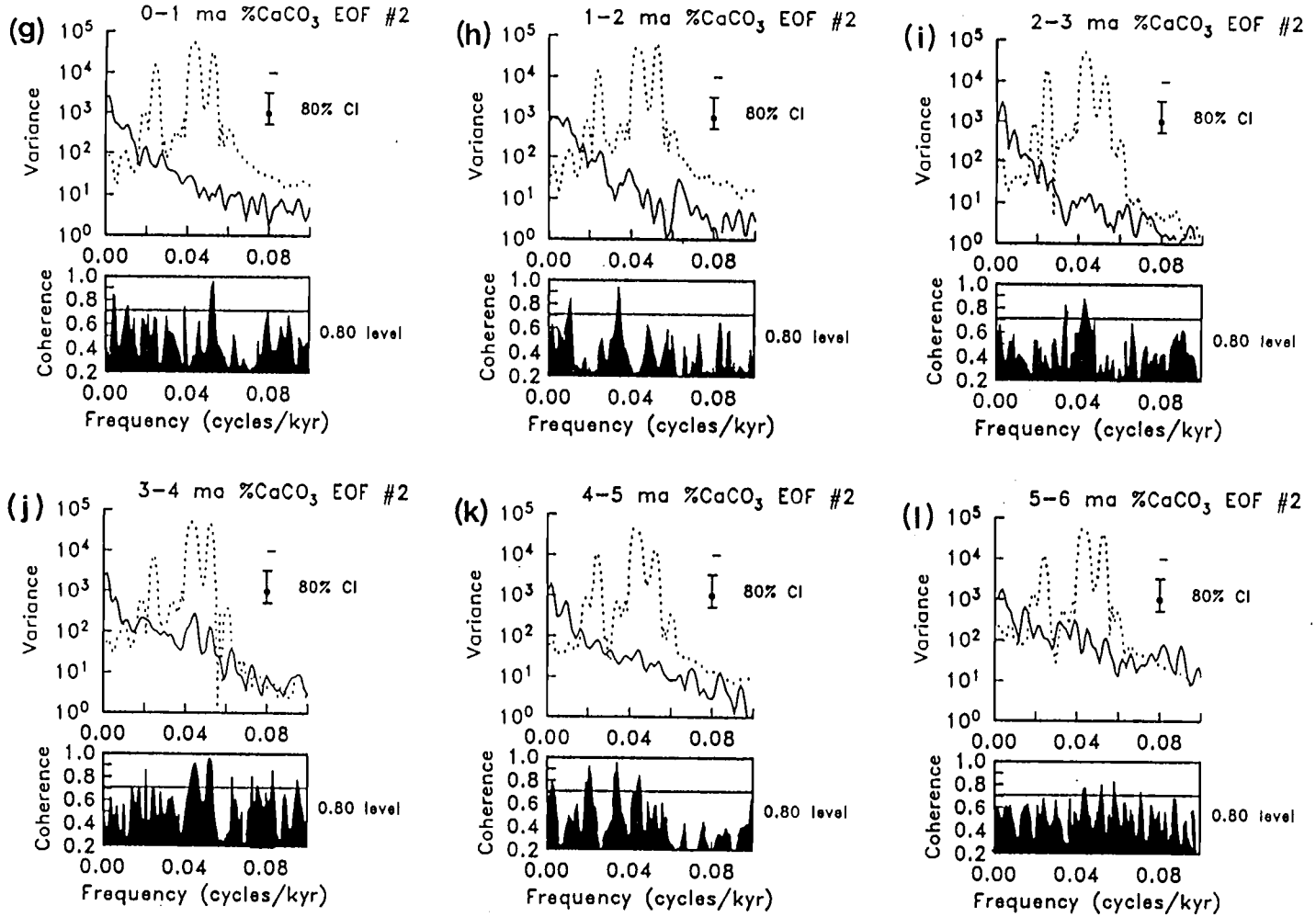

Figure III.19. (g-l): Power spectra and coherence spectra for EOF-2 and 65°N insolation for the amplitude time series given in Figure III.18. Symbols are as described in the caption for Figure III.15.

Table III.6. Summary of cross spectral results between 65°N Insolation and %$CaCO_3$ EOFs 1 and 2. Coherence and phase for periods having significant (.80 level) coherence. Positive phase indicates that insolation leads the EOF.

0-1 MA

	PERIOD (ky)	COH.	PHASE (deg)		PERIOD (ky)	COH.	PHASE
EOF-1	100	0.81	-117 +/- 22	EOF-2	250	0.84	-169 +/- 20
	41	0.89	17 +/- 16		91	0.74	-90 +/- 26
	29	0.91	164 +/- 14		26	0.74	-90 +/- 26
	23	0.98	-1 +/- 6		19	0.94	126 +/- 11
	19	0.93	-9 +/- 13				
	18	0.99	-127 +/- 5				

1-2 MA

	PERIOD (ky)	COH.	PHASE (deg)		PERIOD (ky)	COH.	PHASE
EOF-1	250	0.79	102 +/- 24	EOF-2	91	0.83	-108 +/- 20
	91	0.88	-110 +/- 17		29	0.92	129 +/- 13
	40	0.89	3 +/- 16				
	23	0.97	-12 +/- 8				
	19	0.98	-7 +/- 7				
	10	0.72	-25 +/- 28				

2-3 MA

	PERIOD (ky)	COH.	PHASE (deg)		PERIOD (ky)	COH.	PHASE
EOF-1	41	0.97	-12 +/- 7	EOF-2	29	0.82	-165 +/- 21
	26	0.86	-88 +/- 18		23	0.87	15 +/- 18
	22	0.98	-3 +/- 6				
	19	0.94	2 +/- 11				
	17	0.81	12 +/- 22				
	11	0.81	118 +/- 22				

3-4 MA

	PERIOD (ky)	COH.	PHASE (deg)		PERIOD (ky)	COH.	PHASE
EOF-1	41	0.93	21 +/- 12	EOF-2	48	0.85	158 +/- 19
	30	0.89	1 +/- 15		22	0.92	159 +/- 13
	22	0.98	-21 +/- 7		19	0.96	179 +/- 9
	19	0.97	-7 +/- 7		16	0.80	-126 +/- 23
	16	0.81	59 +/- 22		14	0.81	-92 +/- 22
	11	0.80	43 +/- 23		12	0.86	-93 +/- 18

4-5 MA

	PERIOD (ky)	COH.	PHASE (deg)		PERIOD (ky)	COH.	PHASE
EOF-1	53	0.74	-61 +/- 26	EOF-2	333	0.78	-173 +/- 24
	41	0.86	-16 +/- 18		53	0.78	-69 +/- 24
	36	0.87	140 +/- 17		29	0.94	4 +/- 11
	23	0.93	0 +/- 12		22	0.83	-13 +/- 20
	19	0.93	-2 +/- 13				
	17	0.88	59 +/- 17				

5-6 MA

	PERIOD (ky)	COH.	PHASE (deg)		PERIOD (ky)	COH.	PHASE
EOF-1	53	0.71	-111 +/- 29	EOF-2	23	0.77	-35 +/- 25
	41	0.84	-23 +/- 20		19	0.79	2 +/- 23
	23	0.97	-27 +/- 8		17	0.82	137 +/- 21
	19	0.94	-8 +/- 11				
	15	0.75	30 +/- 26				

higher error and lower temporal resolution than $\%CaCO_3$ time series, if spatial patterns similar to the carbonate concentration EOFs are present, then dilution can be ruled out as the primary cause of the $\%CaCO_3$ spatial variability.

The same set of EOF analyses that were done on $\%CaCO_3$ were performed using the carbonate mass accumulation rate time series (Figure III.9). Individual 1 myr time intervals were examined. As with $\%CaCO_3$ data, in each time slice 64% to 79% of the

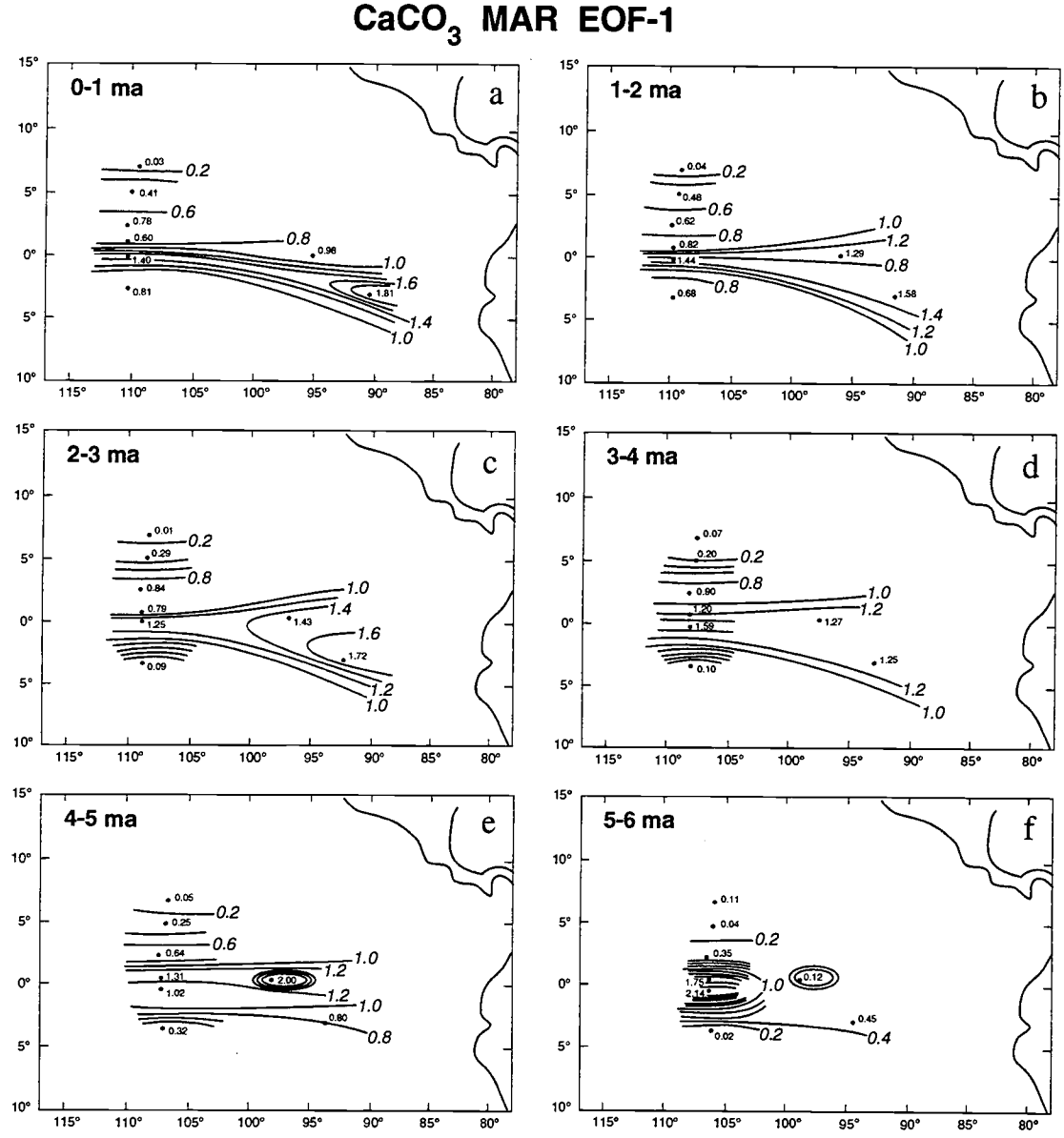

Figure III.20. (a-f): EOF-1 of $CaCO_3$ mass accumulation rate time series (Figure III.10) in 1 myr time slices, 0 to 6 myr.

variance can be explained by the first two EOFS. EOF results are summarized in Table III.7, and spatial maps for each 1 myr interval are given in Figure III.20. The carbonate mass flux EOFs confirm the inferences drawn from the $\%CaCO_3$ results, as discussed below.

From the spatial patterns resolved with the $CaCO_3$ mass accumulation rate data, it can be concluded that over the past 5 myr, the $\%CaCO_3$ pattern resolved reflects mass fluxes of carbonate rather than only dilution. A strong coupling to the equator in the first EOF for

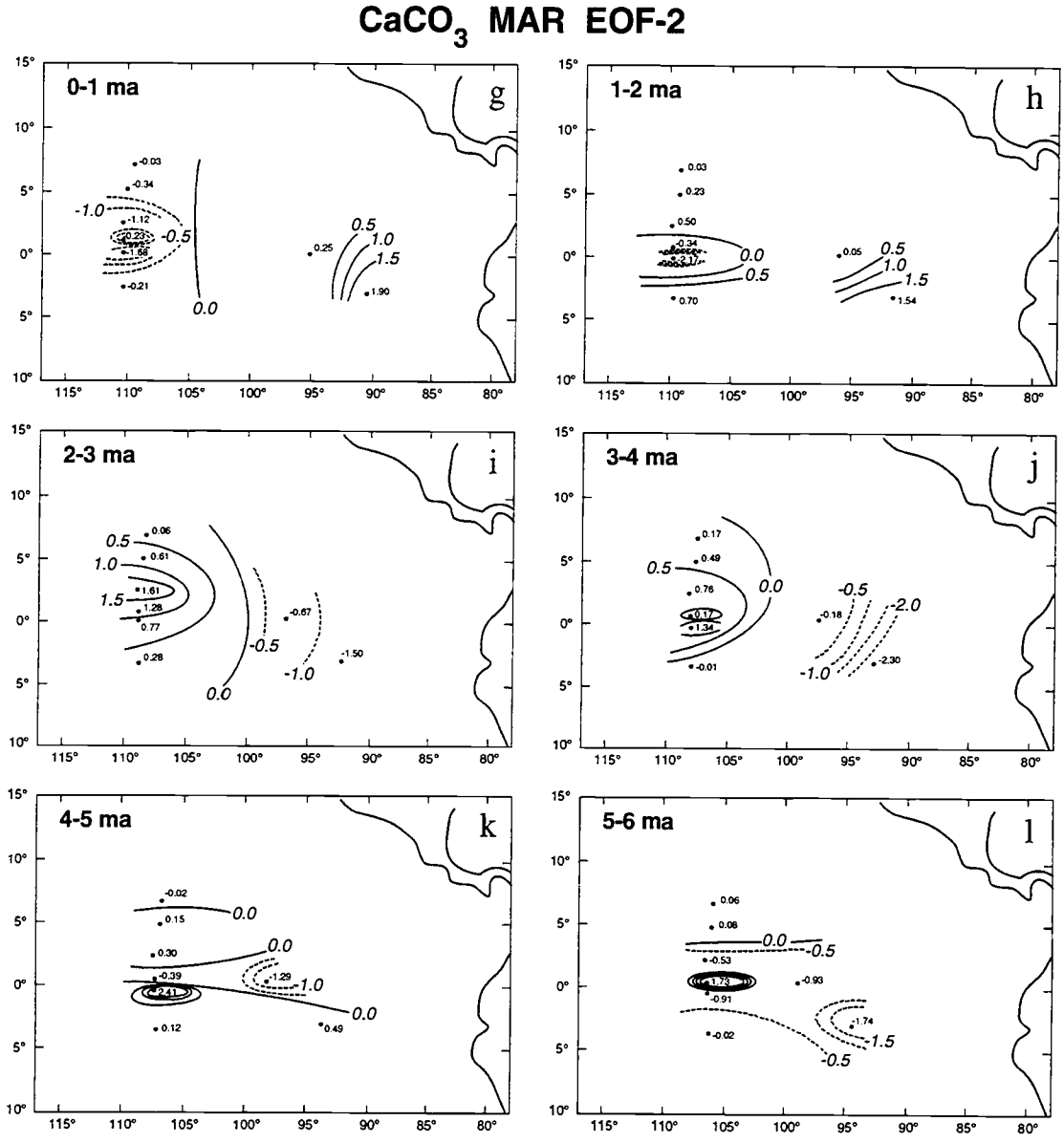

Figure III.20 g-l. EOF-2 of $CaCO_3$ mass accumulation rates.

every time slice is present. This indicates the domination of surface water influence on carbonate sedimentation. While in some short intervals of sites 846-853 low carbonate concentration is indeed a result of dilution by noncarbonate, for example time intervals dominated by monospecific diatom ooze (Kemp and Baldauf, 1993), these intervals are not

---

Table III.7. The first two EOFs, 1 Myr time slices of $CaCO_3$ MAR

0-1 MA			**1-2 MA**		
SITE	**EOF 1**	**EOF 2**	**SITE**	**EOF 1**	**EOF 2**
846	1.81	1.09	846	1.58	1.54
847	0.98	0.25	847	1.29	0.05
848	0.81	-0.21	848	0.68	0.70
849	1.40	-1.68	849	1.44	-2.17
850	0.60	-0.23	850	0.82	-0.34
851	0.78	-1.12	851	0.62	0.50
852	0.41	-0.34	852	0.48	0.23
853	0.03	-0.03	853	0.04	0.03
EIGENVALUE:	1.03	0.19	EIGENVALUE:	0.37	0.16
% VARIANCE:	62.3	11.5	% VARIANCE:	51.0	22.3
2-3 MA			**3-4 MA**		
SITE	**EOF 1**	**EOF 2**	**SITE**	**EOF 1**	**EOF 2**
846	1.72	-1.50	846	1.25	-2.30
847	1.43	-0.67	847	1.27	-0.18
848	0.09	0.28	848	0.10	-0.01
849	1.25	0.77	849	1.59	1.34
850	0.79	1.28	850	1.20	0.17
851	0.84	1.61	851	0.90	0.76
852	0.29	0.61	852	0.20	0.49
853	0.01	0.06	853	0.07	0.17
EIGENVALUE:	0.53	0.22	EIGENVALUE:	0.55	0.26
% VARIANCE:	44.6	18.9	% VARIANCE:	47.8	22.5
4-5 MA			**5-6 MA**		
SITE	**EOF 1**	**EOF 2**	**SITE**	**EOF 1**	**EOF 2**
846	0.80	0.49	846	0.45	-1.74
847	2.00	-1.29	847	0.12	-0.93
848	0.32	0.12	848	0.02	-0.02
849	1.02	2.41	849	2.14	-0.91
850	1.31	-0.39	850	1.75	1.73
851	0.64	0.30	851	0.35	-0.53
852	0.25	0.15	852	0.04	0.08
853	0.05	-0.02	853	0.11	0.06
EIGENVALUE:	3.02	1.13	EIGENVALUE:	5.04	1.85
% VARIANCE:	57.6	21.5	% VARIANCE:	50.8	18.6

representative of the dominant variability over all records. The EOF analyses represent the time integrated modes of variability for each time slice. Thus, although dilution may play some role in influencing %$CaCO_3$ variability, and it may be reflected in EOF-2 of carbonate concentration (see below), it is not the dominant process with the possible exception of the 5-6 Ma interval. The second EOF for the carbonate mass accumulation rates displays strong east-west asymmetry. The spatial pattern is not similar to the second EOF for the %$CaCO_3$ data, suggesting that they are reflecting different oceanographic processes.

The EOF loadings across the 110°W transect (Figure III.21) highlight the strong coupling to the equator in EOF-1. An evolution in gradients is clearly evident, being highest from 5-6 ma. This gradient change parallels variations in sediment thickness (and thus

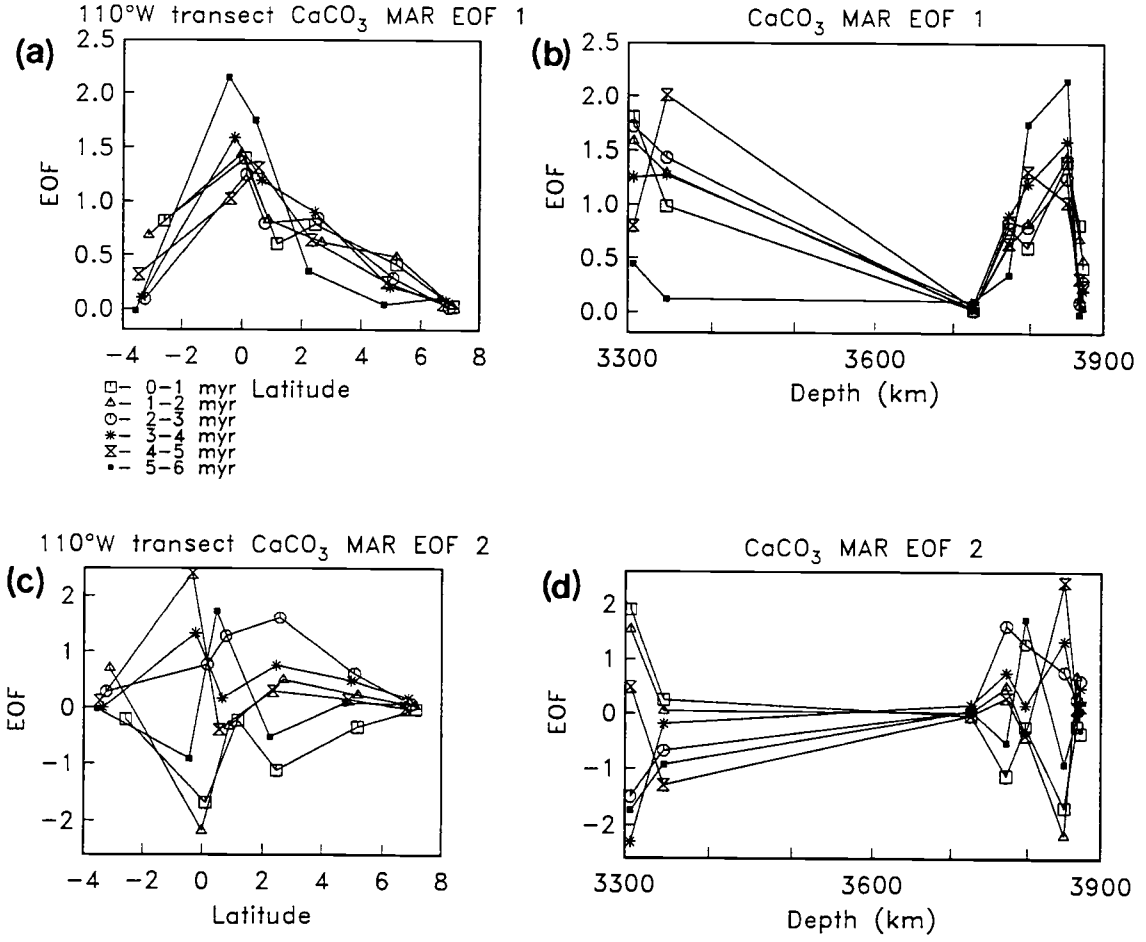

Figure III.21 (a): $CaCO_3$ mass accumulation rate 1 myr time slice EOF-1 loadings on the 110°W transect. (b): EOF-1 loadings for each time slice as a function of present water depth. (c):EOF-2 loadings on the 110°W transect. (d): EOF-2 loadings as a function of water depth.

sedimentation rates) over this time interval. However, a normalized sedimentation rate comparison between sites has indicated that attenuation of records at the lower sedimentation rate sites (848, 852, and 853) is not the same for a given sedimentation rate (Pisias, et al., 1992). Thus, one can conclude that the equatorial pattern displayed by the first EOF is not entirely a function of sedimentation rate. The latitudinal transect for EOF-2 of the carbonate accumulation rate data does not indicate a clear relationship. Neither EOF-1 nor EOF-2 of the carbonate mass accumulation rates appear to have a correlation with water depth (Figure III.21).

The amplitude time series of the carbonate mass flux EOFs are in Figure III.22. Note that the frequency resolution of MAR time series is limited by the resolution of the sedimentation rates of the records. For all sites except 848 and 853, the sedimentation rate resolution is on the order of 20-30 kyr. Site 853 has a sedimentation rate resolution on the order of 200 kyr. If this is taken as the limiting factor, then spectral analyses are not appropriate for the carbonate MAR EOFs. Even so, cross-spectral analyses similar to those performed above with the $\%CaCO_3$ EOFs (not shown) indicated high coherence between EOF-1 and 65°N insolation, and less coherence and Milankovitch band variability in EOF-2.

Comparisons between EOF-1 and EOF-2, respectively, of the $\%CaCO_3$ and $CaCO_3$ MAR records indicate that from 0 to 5 Ma, EOF-1 of carbonate concentration and carbonate flux are positively correlated with cross correlations ranging from 0.38 (4-5 Ma) to 0.72 (1-2 Ma). From 5-6 ma, the cross correlation is close to zero. In the frequency domain, the two EOFs are coherent with one another (often greater than .95) at a broad range of frequencies. Thus, it is reasonable to conclude that the EOF-1 of carbonate mass flux and carbonate concentration are reflecting the same fundamental oceanographic process. EOF-2 of $\%CaCO_3$ and $CaCO_3$ mass flux are highly negatively correlated for the 0-1 Ma interval; from 1-6 Myr the correlation between the two is positive and less than 0.46. With the exception of 0-1 Ma, most variance is not coherent between the two EOFs. The spatial maps

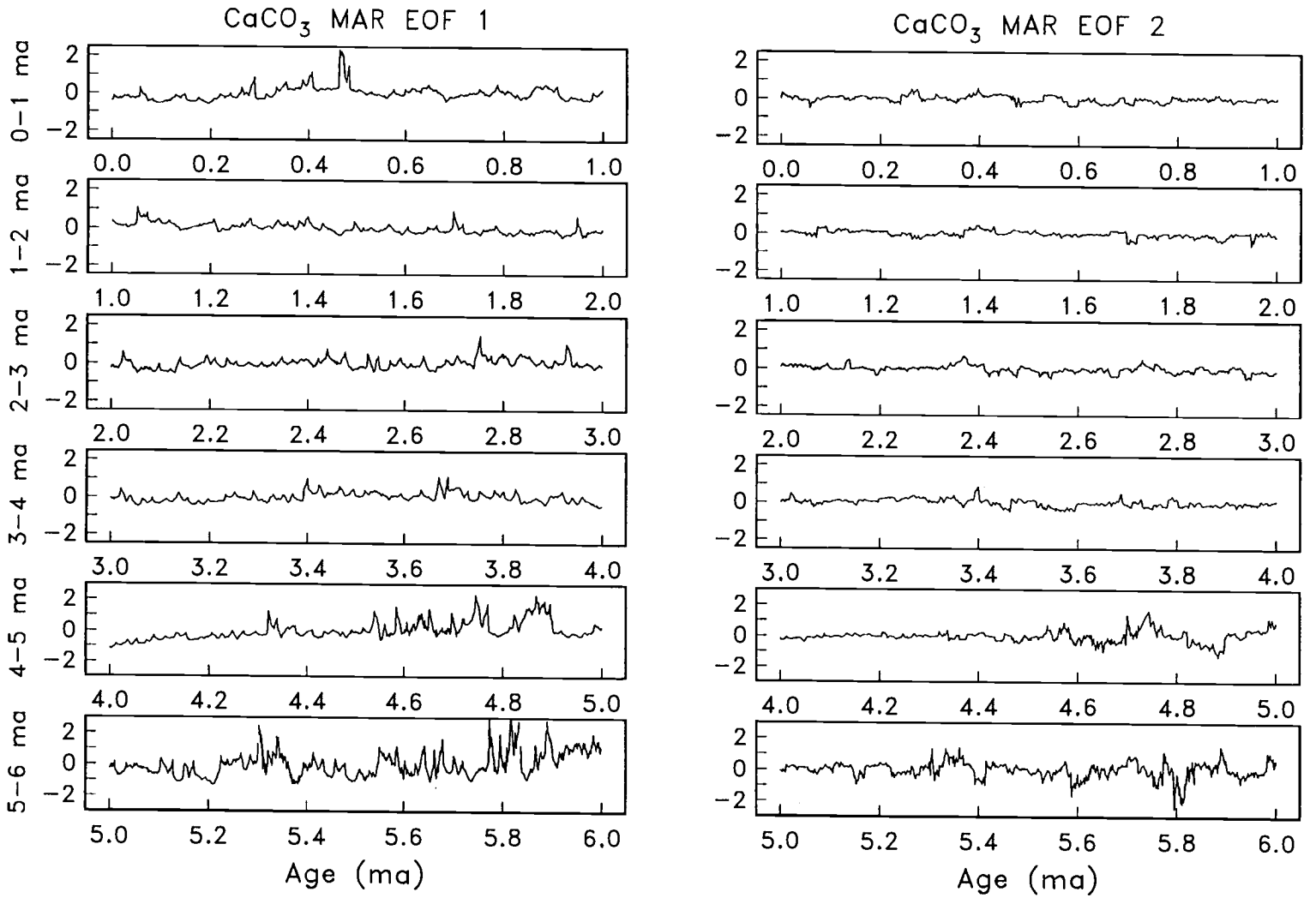

Figure III.22. Amplitude time series of EOF-1 (left) and EOF-2 (right) of 1 myr time slice $CaCO_3$ mass accumulation rate EOFs. Note that the scale for the 4-5 ma and 5-6 ma intervals is different from the later intervals.

of the EOF-2s also differ. Thus, it is unlikely that EOF-2 of $\%CaCO_3$ and $CaCO_3$ MAR reflect the same process. While the EOF-2 of $CaCO_3$ concentration may be influenced by dilution processes, the EOF-2 of carbonate mass flux indicates another process operating in the carbonate system.

Frequency Domain Analyses

The observation that much of the variability represented in EOF-1 is strongly coherent with solar insolation raises the question whether each frequency band has the same spatial structure. The analyses presented above consider all frequencies of the time series together in each record, empirically determining the independent modes of variability. As demonstrated by Imbrie et al. (1992), the processes controlling climatic variations operate differently in the primary Milankovitch frequency bands. It is physically meaningful to examine three of the dominant frequency bands of the carbonate time series separately. For instance, the 23-19 kyr band associated with precession variations may have a different spatial representation than the 41 kyr band associated with orbital obliquity. Similarly, the low frequency band which does not have much variance in solar insolation, is where much of the variance in carbonate variability is concentrated.

To investigate the $\%CaCO_3$ time series in this manner, the records were lowpass and bandpass filtered to isolate three groups of frequencies: frequencies lower than 45 kyr (low pass), frequencies from 45-35 kyr (tilt band), and frequencies from 25-18 kyr (precession band). The "low pass" filter used a cosine taper having a half-amplitude at 0.016 cycles/kyr (62.5 kyr). Energy at frequencies higher than 45 cycles/kyr is excluded. The tilt band filter was centered on 0.024 cycles/kyr (41 kyr), and had a bandwidth of 0.02 cycles/kyr (71 kyr to 29 kyr). The precession band filter was centered at 0.048 cycles/kyr (20.8 kyr) and had a bandwidth of 0.03 cycles/kyr (30 kyr to 16 kyr).

Table III.8. Frequency domain EOF 1 : Lowpass filtered case (frequencies lower than 1/45 Kyr), tilt band case (frequencies between 1/70 Kyr and 1/29 Kyr), and precession band case (1/30 Kyr to 1/16 Kyr). Percent variance indicates the amount of variance in that frequency band.

0-1 MA

SITE	LOWPASS	TILT	PRECESSION
846	1.11	1.08	1.51
847	1.29	1.43	1.02
848	1.09	0.97	0.74
849	1.12	0.58	1.03
850	1.01	1.02	1.21
851	0.69	1.12	0.95
852	0.79	1.05	0.84
853	0.72	0.32	0.12

EIGENVALUE: 470.6 29.4 13.3
% VARIANCE: 69.1 14.9 55.7

1-2 MA

SITE	LOWPASS	TILT	PRECESSION
846	1.75	0.91	1.25
847	1.30	1.55	1.56
848	0.80	0.74	0.38
849	0.99	1.13	1.30
850	0.82	1.13	0.96
851	0.61	0.65	1.01
852	0.76	1.11	0.45
853	0.12	-0.02	0.01

EIGENVALUE: 326.3 57.3 22.9
% VARIANCE: 62.6 67.7 65.4

2-3 MA

SITE	LOWPASS	TILT	PRECESSION
846	1.46	2.19	1.49
847	1.54	1.15	1.35
848	0.41	0.26	0.25
849	1.24	0.57	1.05
850	0.98	0.83	1.12
851	0.79	0.64	1.12
852	0.32	0.62	0.49
853	-0.29	0.06	0.14

EIGENVALUE: 200.0 52.7 29.9
% VARIANCE: 52.8 82.2 77.5

3-4 MA

SITE	LOWPASS	TILT	PRECESSION
846	0.03	1.11	0.90
847	0.59	1.04	1.42
848	1.09	0.30	0.05
849	0.72	1.41	1.47
850	0.91	1.20	1.30
851	1.04	1.15	1.08
852	1.72	0.90	0.38
853	1.02	0.11	0.03

EIGENVALUE: 433.0 27.3 47.9
% VARIANCE: 54.1 70.4 77.5

4-5 MA

SITE	LOWPASS	TILT	PRECESSION
846	0.91	1.42	1.14
847	1.26	0.69	1.57
848	0.85	0.48	0.09
849	1.12	1.50	1.29
850	1.19	0.82	1.15
851	0.95	0.95	0.85
852	0.93	1.18	0.72
853	0.61	0.19	0.00

EIGENVALUE: 397.5 35.9 30.8
% VARIANCE: 70.7 70.4 67.9

5-6 MA

SITE	LOWPASS	TILT	PRECESSION
846	0.40	0.23	0.77
847	1.60	1.65	1.49
848	1.07	0.32	0.03
849	0.77	1.31	1.56
850	0.33	1.16	1.41
851	0.56	0.42	0.66
852	1.27	1.33	0.53
853	1.22	-0.30	0.16

EIGENVALUE: 283.4 42.9 58.7
% VARIANCE: 60.3 59.0 61.2

The results for the first EOF of each of these analyses are shown in Figures III.23-III.26 and are summarized in Table III.8. In each individual frequency band, EOF-2 represented less of the total variance, and is thus not considered here. The spatial patterns of the first EOF of the lowpass carbonate time series from 0-6 Ma are similar to the unfiltered EOFs. A high loading at site 852 relative to sites 851 and 853 is present from 0-2 Ma and from 5-6 Ma (Figure III.23). Loadings are fairly evenly distributed among the 8 sites relative to previous analyses, especially in the intervals 0-1 Ma and 4-5 Ma. With

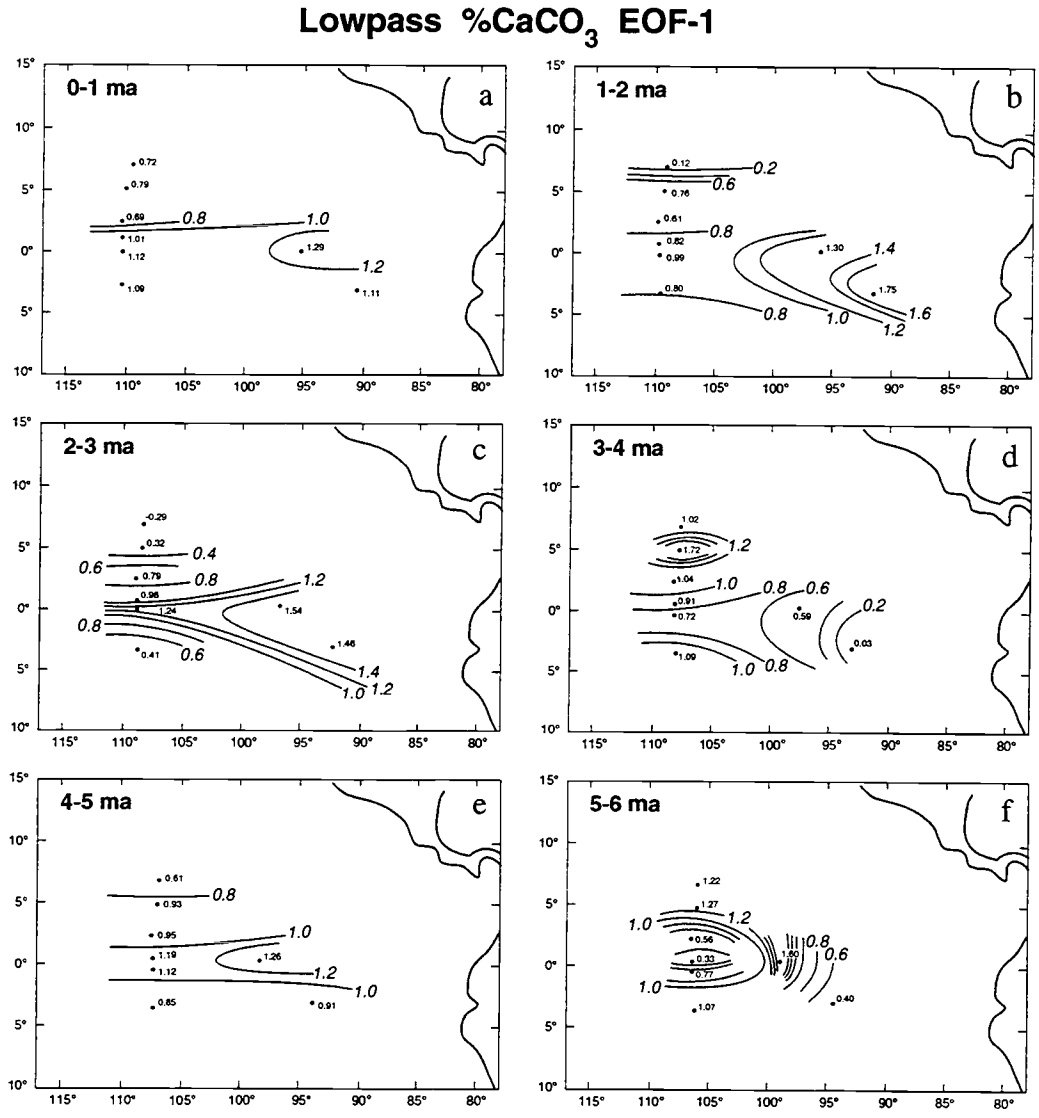

Figure III. 23. (a-f): EOF-1 of the lowpass filtered $\%CaCO_3$ time series in 1 myr time slices, 0 to 6 myr.

the exception of 3-4 Ma and 5-6 Ma, the maximum loading is at the equator (Figure III.24a). Loadings as a function of depth (Figure III.24b) are relatively constant and do not display a strong correlation.

The spatial patterns of the first EOF in the tilt band have a spatial pattern with high loadings on the equator and at site 852 at 6°N. (Figure III.25). Comparison to the low pass results indicates a higher coupling to the equator in this band than in the low frequency band, but only slightly so. Equatorial sites 849 and 850 on the 110°W transect have higher loadings relative to the other sites, and unlike the lowpass filtered records, the latitudinal

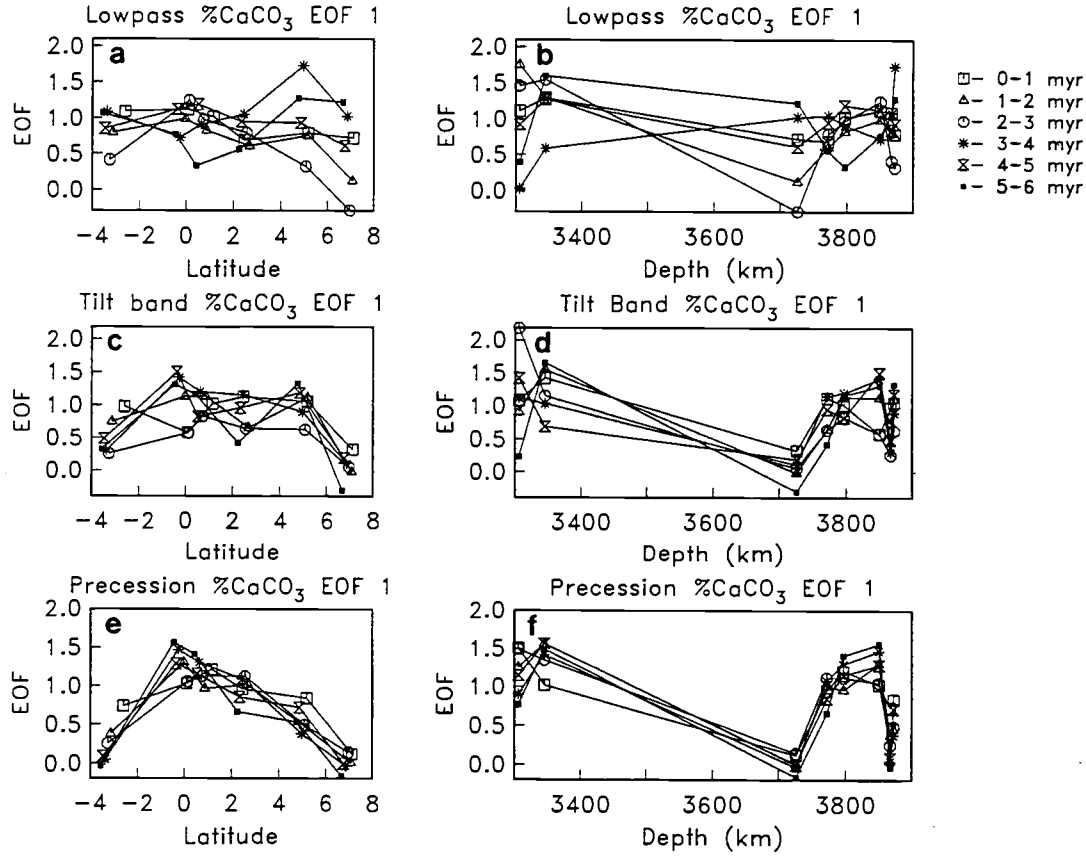

Figure III.24. (a): EOF-1 loadings of lowpass filtered $\%CaCO_3$ time slices on the 110°W transect. (b): Lowpass EOF-1 loadings for each time slice as a function of present water depth. (c): Tilt band $\%CaCO_3$ EOF-1 loadings on the 110°W transect. (d): Tilt band EOF-1 loadings as a function of water depth. (e): Precession band $\%CaCO_3$ EOF-1 loadings on the 110°W transect. (f): Precession band EOF-1 loadings as a function of water depth.

transect (Figure III.24c) clearly resolves a two peaked structure with a primary peak at the equator and a secondary peak near 6°N (Site 852). No strong correlation between loadings and water depth is seen (Figure III.24d).

In the precession band (Figure III.26), highest coupling to the equator with strong gradients away from the equator is present. Variance at site 852 is diminished relative to previous analyses. In every time interval in the tilt band, a high loading at site 852 relative

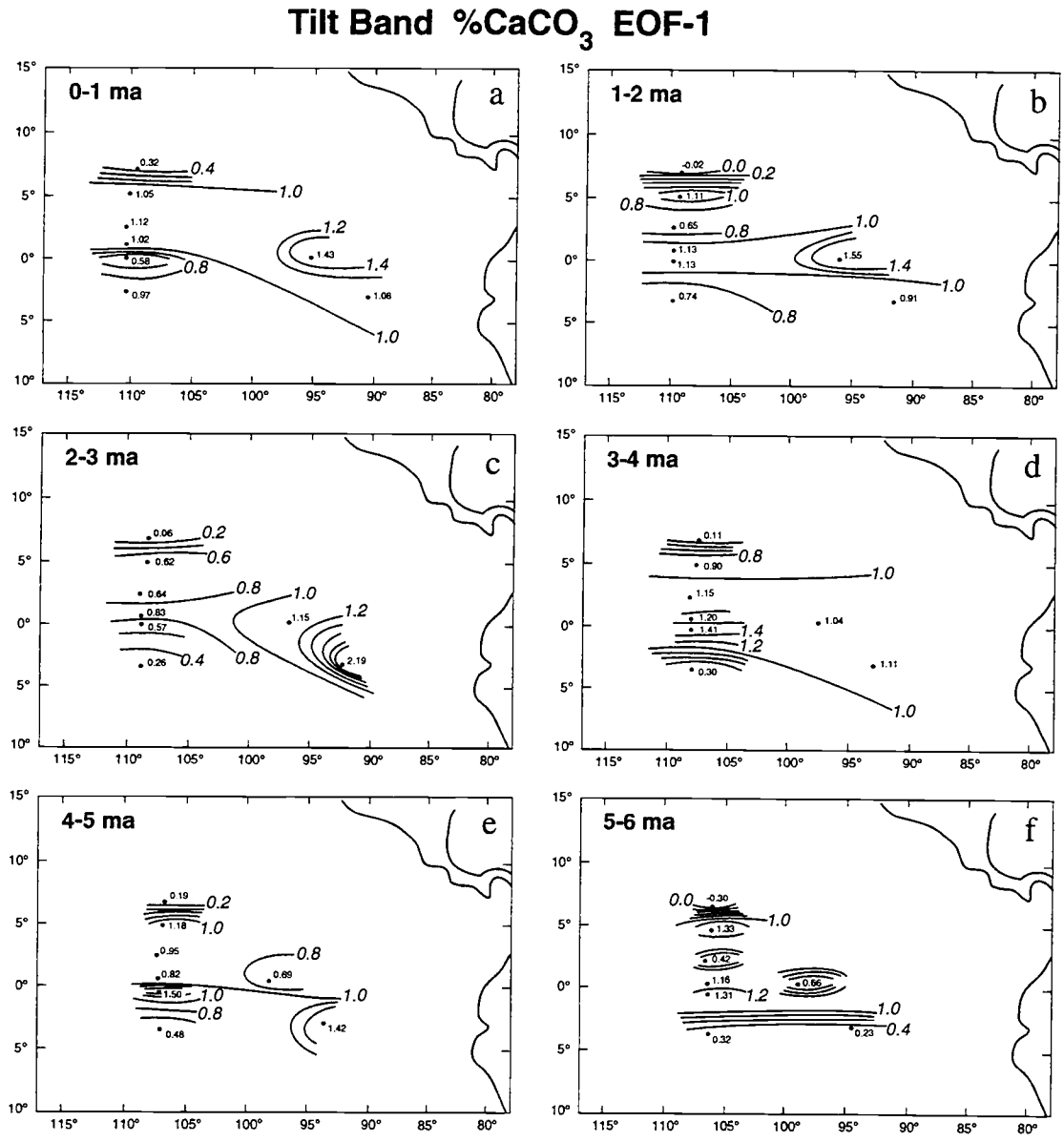

Figure III.25. (a-f): EOF-1 of the tilt band $\%CaCO_3$ time series (see text) in 1 myr time slices, 0 to 6 myr.

to sites 851 and 853 were seen, whereas in the precession band, in every time interval the site 852 loadings fall between the 851 and 853 loadings (Figure III.24c,e). Although error estimates for the EOF loadings are necessary in order to determine if these differences are significant, the consistency of this pattern in every time slice is striking. A general decrease in cross-equatorial gradients is seen from 5-6 ma to 0-1 ma (Figure III.24e). As with the lower frequencies, depth does not appear to be a significant influence on EOF loadings (Figure III.24f).

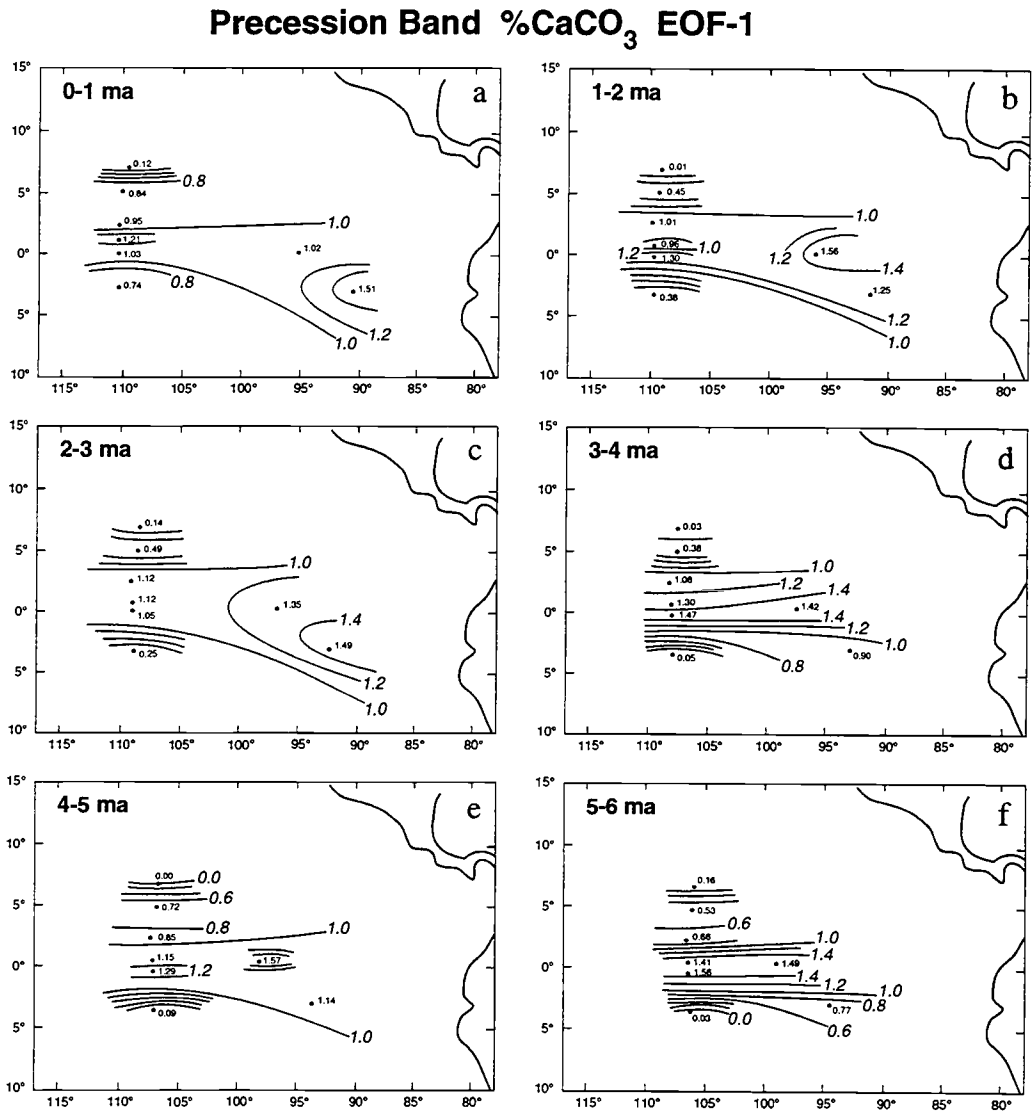

Figure III.26. (a-f): EOF-1 of the precession band $\%CaCO_3$ time series (see text) in 1 myr time slices, 0 to 6 myr.

These frequency band analyses confirm that the mechanisms responsible for variability in carbonate concentration are operating on different timescales. The coupling to the equator that is seen in the entire data set appears highest in the precession band. The high loadings at site 852 in the unfiltered data set primarily reflect processes that are operating at lower frequencies. These results are consistent with astronomical considerations. Precession is a primary influence on insolation at low latitudes, while obliquity variations (the 41kyr band) do not directly affect seasonal surface insolation at the equator (Berger, 1978). Consistent with this, variability in the precession band appears to be associated only with equatorial divergence, while variability in the tilt band may reflect more influence from higher latitudes and the NECC. Variability at lower frequencies is not as tightly coupled to surface ocean processes as the higher frequencies.

Implications

Inference as to the relative importance of carbonate production relative to carbonate dissolution can be drawn from the above information. Taken at face value, the EOF patterns that are resolved above indicate a strong influence by surface ocean processes on eastern equatorial Pacific carbonate sedimentation. In every analysis, the equator is the focus of most of the variability in EOF-1, suggesting a relation to equatorial divergence and thus carbonate productivity. In the $\%CaCO_3$ EOFs alone, the possibility of opal dilution cannot be ruled out. However, the results from EOF analysis of predicted carbonate mass accumulation rate time series exclude the possibility that the equatorial signal resolved in EOF-1 is purely associated with dilution. EOF-1 includes variability highly coherent with insolation variations. Frequency domain analyses suggest a coupling to surface ocean processes at several frequencies. Latitudinal control appears stronger in the tilt and precession bands than in the low frequency band.

One independent line of evidence supports changes in carbonate productivity as the primary factor controlling carbonate sedimentation. Radiolarian faunal data from intervals containing high carbonate concentrations and low carbonate concentrations were studied by Pisias et al. (1993). Radiolarians associated with increased productivity and stronger equatorial divergence correlate with decreased $\%CaCO_3$, while radiolarians associated with warmer, tropical waters correlate with increased $\%CaCO_3$. As carbonate concentration and carbonate mass flux are positively correlated, this indicates that increased opaline productivity coincides with decreased carbonate production in the equatorial Pacific, and vice versa. This is consistent with results from the late Pleistocene. Lyle et al. (1988) postulated that oscillations in production of two planktonic communities dominate in equatorial Pacific surface waters, one community of both opal and calcite-secreting plankton, and one entirely opal. The carbonate fluctuations in the cores studied by Lyle et al. (1988) were demonstrated to primarily related to changes in carbonate flux out of the water column, rather than carbonate dissolution.

The results of Pisias et al (1993) also suggest that the fundamental relationship between radiolarian faunas and carbonate flux and equatorial surface circulation is constant in the presence of other large scale oceanographic changes. If dissolution were primary, the deep water mass reorganizations associated with closure of Panama and the onset of Northern Hemisphere glaciation could be expected to be reflected in carbonate variability. The modeling study of Maier-Raimer et al. (1990) found no change in the strength of equatorial divergence associated with closure of the Isthmus of Panama. Similarly, Hays et al. (1989) did not see a decrease in equatorial divergence associated with this event. These results are consistent with the results implied by the spatial patterns of EOF-1. However, the spatial pattern of EOF-2 may reflect external boundary condition changes rather than only surface ocean processes

Could changes in carbonate saturation state and associated carbonate dissolution be responsible for the variability resolved above? Although the EOF analyses strongly suggest that surface ocean processes are primary, could a dissolution signal be embedded? In order to answer this, carbonate dissolution related to changes in deep ocean alkalinity must be considered as well as dissolution related to organic carbon oxidation, a byproduct of increased productivity. Each of these dissolution processes is discussed below. In addition, comparison to other dissolution indicators is necessary.

If dissolution due to global oceanic chemistry changes is the primary forcing of equatorial Pacific $CaCO_3$ sedimentation, a pattern of variability similar to modern productivity gradients would not be expected. Five of the sites studied above (848 - 852) fall within a 100 m range. If dissolution were primary and all other factors were held constant, these 5 sites would respond similarly to changes in corrosiveness of the overlying waters, and they would have approximately the same variance. However, variability over these sites is significant on time scales up to 20,000 years. The results of Archer's model (Archer, 1991a) predicts that to account for central equatorial Pacific $CaCO_3$ patterns by ocean chemistry changes, a very large gradient in carbonate saturation is required over a 200m depth interval, which is unlikely given the relative homogeneity of the present day gradient (Archer, 1991a).

If dissolution owing to global ocean chemistry variation is dominant, a correlation between water depth and carbonate sedimentation would be present. Because all of the sites are within the upper lysocline, records at deeper water depths would be expected to have more variability than the shallowest sites. The transects of EOF loadings over depth (Figures III.17b, III.21b, and III.24b,d,f) indicate that the opposite is true for EOF-1. Sites 846 and 847, which are the shallowest sites, have on average higher loadings in EOF-1 for $\%CaCO_3$ and $CaCO_3$ MAR than sites 848-853, which are over 400 m deeper. In some cases, such as the low frequency band EOF loadings for $\%CaCO_3$, no relationship with depth can be determined. The only instance where a positive correlation between EOF loadings and

depth is seen is in $\%CaCO_3$ EOF-2. Thus, carbonate dissolution must be considered as a possible dominant factor determining the spatial pattern of EOF-2, and as one of several factors controlling EOF-1 of the low frequency band.

It is possible that variability in carbonate sedimentation at low frequencies is related to carbonate dissolution. Evidence for this lies in the slightly lower gradients with latitude resolved in the low frequency EOFs relative to the tilt band and precession band EOFs, and the low spatial variability from 0-1, 1-2, and 4-5 ma (Figures III.23 and III.24). If this is the case, then influence from dissolution is embedded in the spatial variability of EOF-1 of $\%CaCO_3$, because low frequency variance is dominant in all of the $\%CaCO_3$ records, and EOF-1 accounts for over 50% of the total variance. Additional evidence for this comes from comparisons of EOF-1 with benthic $\delta^{18}O$ (see below). However, with the exception of the time intervals from 3-4 ma and 5-6 ma, the lowpass filtered $\%CaCO_3$ EOFs show a correlation with latitude, and the highest loadings are focused on the equator. Thus, even at low frequencies, surface oceanographic processes exert influence on carbonate sedimentation.

If dissolution is a primary component affecting all Leg 138 sites to the same degree, an attenuation as a function of carbonate sedimentation rate can be expected. If all other factors affecting carbonate sedimentation are held constant except for carbonate sedimentation rates, the higher sedimentation rate sites will show less of a response to the same amount of changes in dissolution. This effect was modeled by Pisias and Prell (1985), using carbonate records from DSDP Leg 85 sites. At the Leg 138 sites, the maximum carbonate accumulation rates are at the equatorial sites, and the minimum carbonate accumulation rates are located away from the equator (Sites 848, 852, and 853). Following the above logic, one could expect dissolution to exert a stronger control on the variability in sites 848, 852, and 853 relative to equatorial sites 849, 850, and 851. This is consistent with the spatial pattern on the 110°W transect observed in EOF-2, and thus is another line of evidence supporting EOF-2 as an indicator of carbonate dissolution.

One line of evidence that argues against dissolution as a primary factor driving the carbonate fluctuations is the comparison to dissolution indices. If dissolution is significant, a correlation between carbonate variability and dissolution indices might be evident. Dissolution indices as estimated from foraminiferal fragmentation data have been generated for Site 847 (Murray, et al., 1993) and Site 846 (Le et al., 1993). Sites 846 and 847 have very high loadings in EOFs 1 and 2 for $\%CaCO_3$ and $CaCO_3$ MAR, but no clear relationship is evident in comparison of these records to fragmentation data. In some instances, carbonate and fragmentation indices appear to be positively correlated, and in other instances, a negative correlation is evident. The resulting correlation coefficient between carbonate concentration, carbonate mass accumulation, and the carbonate EOFs with fragmentation records is close to zero. This result may indicate that fragmentation indices are not the best indicators of carbonate loss due to dissolution.

How important is the role of carbonate dissolution driven by organic carbon respiration? Equatorial sites located in regions of higher productivity would lie under waters more undersaturated in $CO3^{=}$ than sites off of the equator where production is lower. Accordingly, lower $CO3^{=}$ concentration is documented beneath the equator in the eastern Pacific (Broecker and Peng, 1982, p.77). If this type of dissolution is a primary control on carbonate sedimentation, then most variability could be expected to be coupled to equatorial divergence, where productivity is highest. Archer (1991b) modeled the effect of variations of organic carbon degradation on lysocline shape. For the last glacial maximum Archer (1991a) determined that the increase in carbonate accumulation observed by Farrell and Prell (1989) in the central equatorial Pacific can in theory be generated by decreasing the ratio of organic carbon to calcite and thus diminishing respiration-driven dissolution. However, organic carbon accumulation in the equatorial Pacific coincides with higher carbonate accumulation during the Pleistocene at Site 846 (Doose et al., 1993), and in other studies (Pederson, 1983, Lyle et al., 1988). By extension to the late Neogene,

this rules out organic carbon respiration as a primary factor. However, modeling of the ratio of organic carbon to calcite flux will help determine if this process can be dominant in determining the spatial pattern resolved here.

If both global deep ocean chemistry changes and organic carbon-induced dissolution are considered together, then it becomes clear why resolving a single dissolution mode is difficult. One dissolution process would be coupled to water depth, and the other process would be coupled to the surface productivity, all other factors held constant. In addition, while high productivity may lead to increased dissolution in one region of the equatorial Pacific, the increase in rain rate of material could lead to increased preservation in another region. As noted by Archer (1991b), the competition of these two effects may make resolution of either one of them difficult, especially if they are operating on the same timescales.

As noted previously, the spatial distribution of $\%CaCO_3$ EOF-2 may suggest a relationship to these multiple carbonate dissolution processes. For instance, if high oceanic productivity at the eastern boundary is associated with high loadings of EOF-2 on the eastern transect, this may indicate high dissolution induced by organic carbon. The same high productivity might lead to decreased dissolution at off-equator sites on the 110°W transect because of increased chances for burial of carbonate. This would explain the out of phase relationship between eastern and western sites. Although amplitude time series of EOF-2 are also not correlated to foraminiferal fragmentation data, there is evidence for a correlation with water depth (Figure III.17d). On the 110°W transect, the loadings of EOF-2 are consistent with influence from dissolution. However, the lack of a relationship to the fragmentation indicies remains puzzling.

A similar argument can be made regarding the role of noncarbonate dilution in controlling the spatial pattern of $\%CaCO_3$ EOF-2. As the spatial pattern of EOF-2 in $\%CaCO_3$ is different than the spatial pattern of EOF-2 of the mass accumulation rate data, the carbonate concentration data are obviously recording a different process. The spatial

pattern of $\%CaCO_3$ EOF-2 could be indicating dilution related to opal production in the eastern transect sites, while indicating dilution related to carbonate dissolution in the off-equator sites on the western transect. This possibility can be tested with records of opal and noncarbonate, non-opal accumulation and with opaline faunal counts such as that of Pisias et al. (1993).

Table III.9. Summary of cross spectral results between site 846/849 benthic $\delta^{18}O$ and $\%CaCO_3$ EOFs 1 and 2. Coherence and phase for periods having significant (.80 level) coherence. $\delta^{18}O$ data from Shackleton et al (1993; 846) and Mix et al (1993; 849). Positive phase indicates that $\delta^{18}O$ leads.

0-1 MA

	PERIOD (ky)	COH.	PHASE (deg)		PERIOD (ky)	COH.	PHASE
EOF-1	142	0.80	124 +/- 22	EOF-2	83	0.89	73 +/- 16
	100	0.83	48 +/- 20		36	0.94	72 +/- 11
	71	0.86	31 +/- 18		14	0.70	59 +/- 29
	41	0.94	105 +/- 11				
	24	0.78	133 +/- 24				

1-2 MA

	PERIOD (ky)	COH.	PHASE (deg)		PERIOD (ky)	COH.	PHASE
EOF-1	111	0.90	56 +/- 14	EOF-2	333	0.83	-15 +/- 20
	77	0.87	53 +/- 18		111	0.94	61 +/- 11
	43	0.74	156 +/- 27		48	0.73	111 +/- 28
	20	0.81	0 +/- 22		20	0.78	-60 +/- 24
					19	0.84	123 +/- 20

2-3 MA

	PERIOD (ky)	COH.	PHASE (deg)		PERIOD (ky)	COH.	PHASE
EOF-1	40	0.87	124 +/- 17	EOF-2	250	0.90	60 +/- 15
	24	0.86	134 +/- 18		125	0.86	20 +/- 18
	19	0.84	-69 +/- 20		48	0.76	62 +/- 25
	18	0.79	156 +/- 23		31	0.83	77 +/- 21
	14	0.85	-132 +/- 19		26	0.82	-164 +/- 22
					14	0.94	46 +/- 11

3-4 MA

	PERIOD (ky)	COH.	PHASE (deg)		PERIOD (ky)	COH.	PHASE
EOF-1	53	0.80	-166 +/- 22	EOF-2	167	0.83	23 +/- 20
	38	0.87	139 +/- 17		50	0.87	15 +/- 17
	24	0.75	-159 +/- 26		40	0.89	-36 +/- 15
	20	0.74	-119 +/- 27		32	0.93	-13 +/- 13
	14	0.80	158 +/- 23		22	0.77	39 +/- 25
					16	0.79	22 +/- 23

4-4.6 MA

	PERIOD (ky)	COH.	PHASE (deg)		PERIOD (ky)	COH.	PHASE
EOF-1	333	0.91	-160 +/- 12	EOF-2	21	0.72	-66 +/- 24
	42	0.86	174 +/- 15		13	0.83	-48 +/- 17
	18	0.75	158 +/- 22				
	14	0.81	-57 +/- 18				

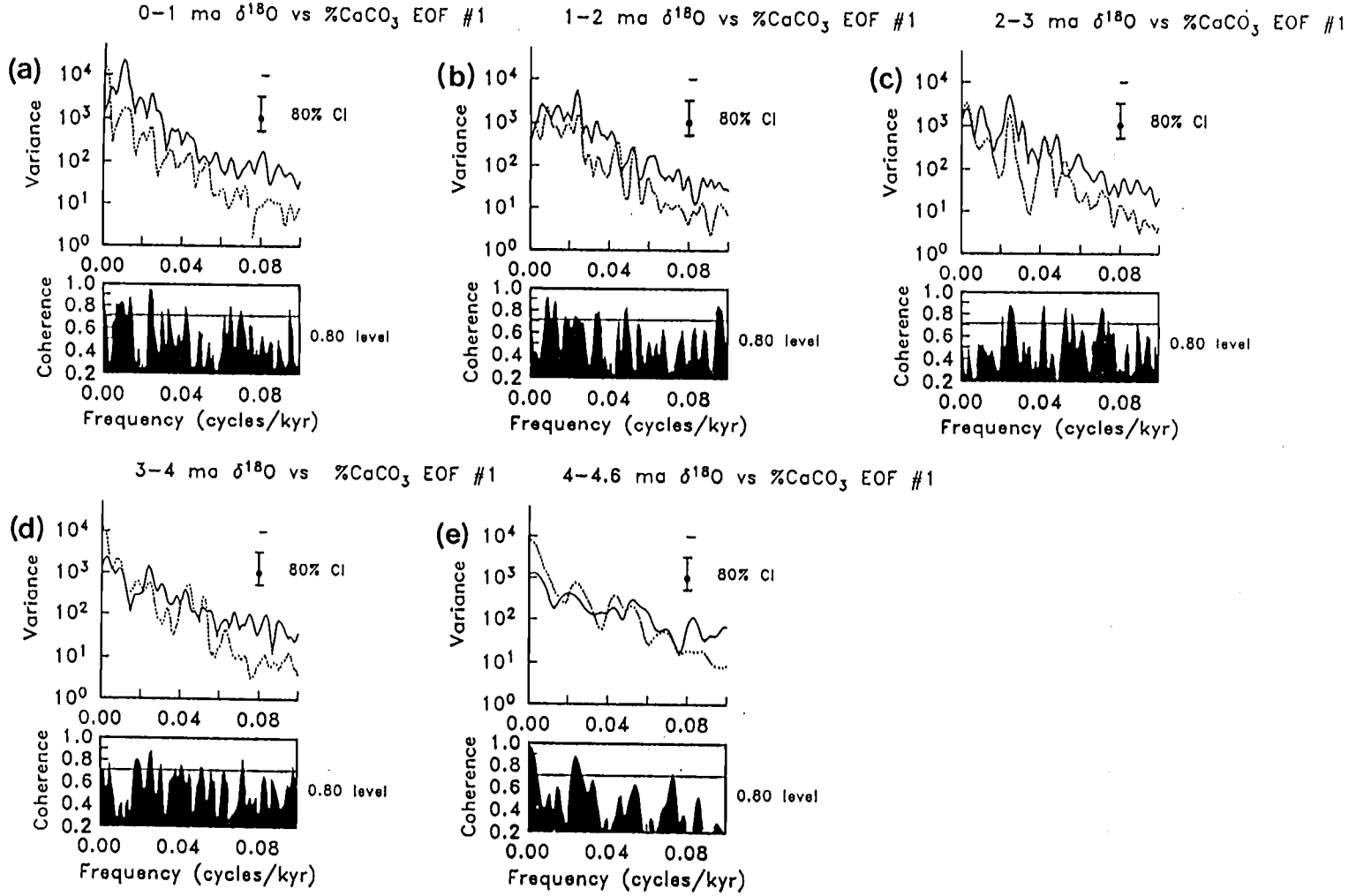

Figure III.27. (a-e): Power spectra and coherence spectra for oxygen isotopes and $\%CaCO_3$ EOF-1, for the 1 myr time slice amplitude time series given in Figure III.18. The solid line indicates the EOF power spectra, the dotted line is the insolation power spectrum. Symbols are as described in the caption for Figure III.15.

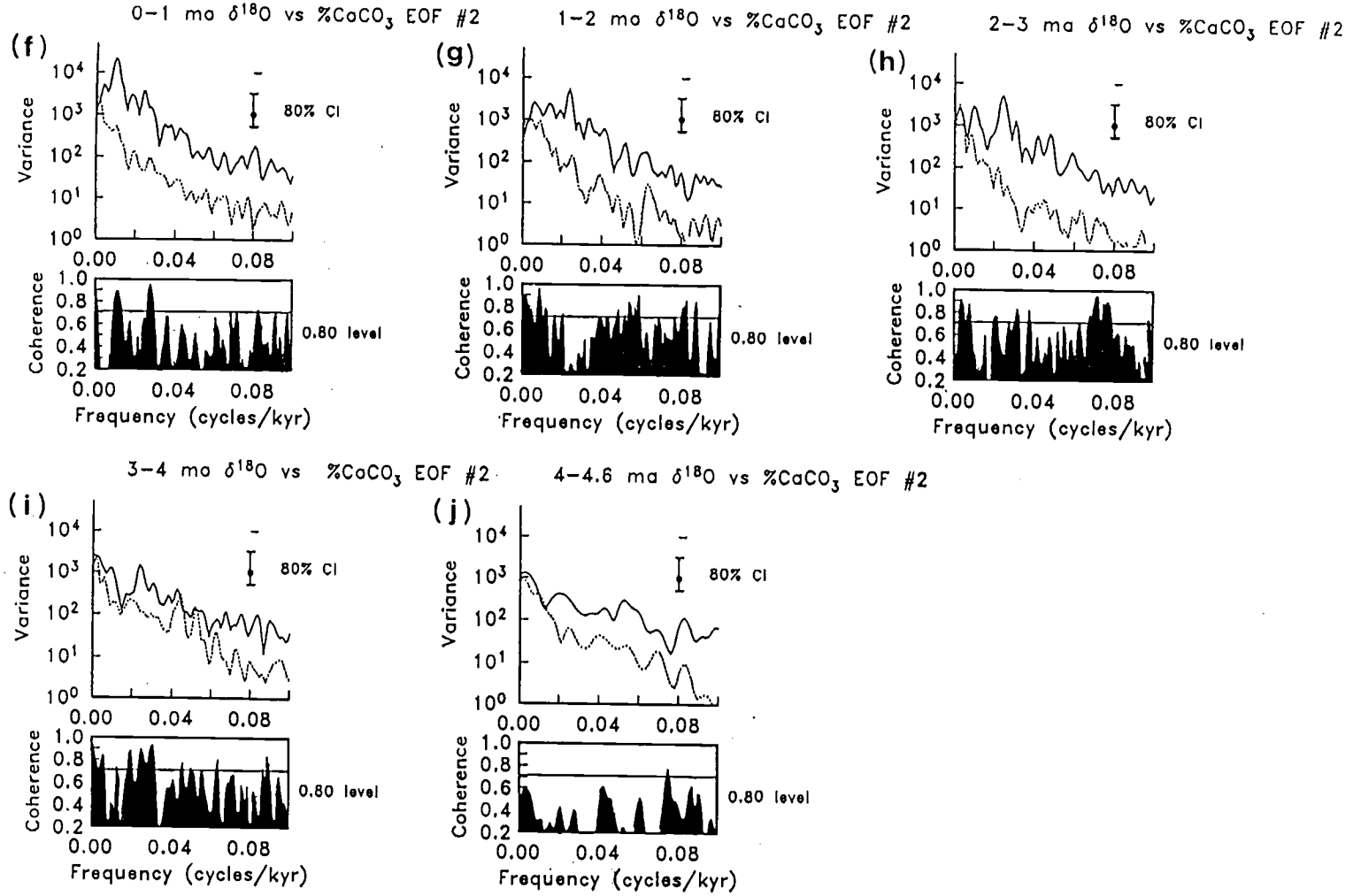

Figure III.27. (f-j): Power spectra and coherence spectra for oxygen isotopes and EOF-2 for the amplitude time series given in Figure III.18. Symbols are as described in the caption for Figure III.15.

The temporal evolution of EOF-2 must also be considered. One modeling study (Maier-Raimer et al., 1990) suggests that the closure of the Isthmus around 3-4 ma was related to significant changes in the intensity of deep ocean circulation. Experiments run with a tropical ocean model coupled to pre-Himalayan uplift GCM wind fields suggest a strong association of north-south wind fields to tropical ocean circulation (Ravelo et al, 1992). The spatial pattern of EOF-2 may indicate a response of carbonate sedimentation to these boundary condition changes, and thus could indiate some surface ocean control on EOF-2.

Carbonate and Ice Volume

The relationships of the carbonate EOFs to ice volume over the past 4.5 myr are now considered. Previous studies (e.g. Farrell and Prell, 1991) suggest that the relationship between carbonate and ice volume seen over the late Pleistocene was not present during the Pliocene and early Pleistocene. A comparison between benthic $\delta^{18}O$ and the carbonate concentration EOFs help to clarify this relationship. Comparisons were made between the spliced 849/846 $\delta^{18}O$ record shown in Figure III7a (4.6 myr record of Mix et al., 1993 and Shackleton et al., 1993) and $\%CaCO_3$ EOFs 1 and 2 for each 1 myr time slice. (Comparisons were also made between $\delta^{18}O$ and $CaCO_3$ MAR EOFs but are not shown. The results are consistent with the $\%CaCO_3$ results). Overall $\delta^{18}O$ and $\%CaCO_3$ EOFs 1 and 2 respectively are not highly correlated in any time slice. Correlation coefficients are no higher than 0.23. Heavy isotopes (glacial) are correlated with higher EOF loadings (higher carbonate) for EOF-1, and with negative EOF loadings for EOF-2. Although overall correlation is low, correlation is high in some frequency bands. Cross spectral comparisons are given in Figure III.27 and summarized in Table III.9.

Coherence between EOF-1 and $\delta^{18}O$ at 41, 23, and 19 kyr over the past 4 myr (Figure III.27 and Table III.9) is significant only at a .80 (coherence = 0.67) level. At a .90 level (coherence= 0.88), coherence between EOF-1 and $\delta^{18}O$ is only significant from 0-1

ma at 41 kyr. . From 0-2 ma, coherence in the 100 kyr band is 0.83 - 0.90, with a phase lag of EOF-1 of 13-17 kyr. These results indicate that carbonate and ice volume variability are coupled at low frequencies during at least the past 2 myr. As documented in the late Pleistocene (e.g. Moore et al., 1977), an 8 to 12 kyr phase lag occurs between $\delta^{18}O$ and equatorial Pacific carbonate sedimentation at 41kyr and precession frequencies.

EOF-2 displays high coherence in the 100 kyr band of $\delta^{18}O$ from 0-2 myr which is significant at a 0.90 level (0.89 to 0.94; Figure III.27), with a phase lag of 18-19 kyr. Coherence between EOF-2 and $\delta^{18}O$ is also high at 36 kyr, where there is significant non-Milankovitch band variability in both records. This suggests that the variability in the climate system which is not linearly related to solar insolation is not only present in $\delta^{18}O$ records, but it is also present in the carbonate system and it is resolved in the EOF analysis. This result underscores the effectiveness of EOF analysis as a technique for resolving uncorrelated modes of variability. The non-Milankovitch band climatic variability which is present and coherent in both $\delta^{18}O$ and in the carbonate system may indicate nonlinear interactions in the climate system. Present work includes a further study of these interactions.

CONCLUSIONS

(1) Spatial patterns in sediment composition in the eastern equatorial Pacific exhibit variability common to all of Leg 138 Sites 846-853, as well as variability that is associated with latitude. Large variability is present over the past 6 myr on timescales from 1 myr to less than 10,000 yr. The spatial patterns are remarkably consistent over the past 6 myr. Although differences between individual time slices are evident, the fundamental spatial pattern that represents the bulk of the variability in the carbonate system is consistent over time periods in which large boundary condition changes take place. This implies a constant forcing mechanism of variability in carbonate sedimentation over the past 6 myr.

(2) Two independent modes of variability account for over 70% of the variance in carbonate concentration and carbonate accumulation records over the past 6 myr. The first mode, EOF-1, is coupled to the equator and is coherent with insolation changes. This pattern of variability appears to be associated with surface ocean processes. The second mode of variability in carbonate sedimentation may be associated with carbonate dissolution over the past 4 myr. Coherence between carbonate EOF-2 and insolation is low.

(3) Variability in carbonate sedimentation differs as a function of frequency, but in the precession band, the tilt band, and the low frequency band, a coupling to surface ocean processes can be inferred. Precession band variability displays the highest coupling to the equator, tilt band variability indicates a stronger role of site 852 at 6°N, and variability in carbonate sedimentation at low frequencies displays the least coupling to equatorial processes.

(4) A correlation of the loadings of EOF-1 of carbonate concentration and mass accumulation with latitude implies a strong linkage of carbonate sedimentation to surface ocean processes. The lack of a correlation between EOF-1 loadings and depth suggests that global alkalinity induced dissolution is not dominant. The loadings of EOF-2 do indicate a relationship with water depth, suggesting that dissolution may play a role in forcing this mode of variability.

(5) Benthic $\delta^{18}O$ and carbonate are positively correlated throughout the past 4 myr, with increased carbonate associated with positive (heavy) $\delta^{18}O$. Over the past 4 myr, the dominant mode of variability in carbonate concentration (EOF-1) is coherent with Site 849/846 $\delta^{18}O$ at 41kyr, 23kyr, and 19 kyr. The second independent mode of carbonate variability (EOF-2) is coherent with $\delta^{18}O$ at non-Milankovitch frequencies from 0-2 ma. The two independent modes of variability observed in the carbonate system each have linearly relationships to $\delta^{18}O$, but at different frequencies and/or phases. This implies strong linkages with ice volume variability in *both* modes of carbonate variability. It also suggests that multiple *independent* modes of variability are operating within the climate system, affecting equatorial Pacific carbonate and benthic oxygen isotopes.

(6) Modeling of dissolution and dilution processes combined with EOF analyses, and comparison to faunal and isotopic indicators from Leg 138 sites can provide additional constraints to the oceanographic interpretations from the EOFs presented here. Parameters indicating surface ocean processes such as radiolarian and foraminiferal census data will be of use in determining the phase of the carbonate response with respect to insolation. Parameters which represent spatially coherent deep ocean changes such as benthic isotopes will constrain the spatial variance in the phase of the carbonate response.

CHAPTER FOUR

LINEAR AND NONLINEAR COUPLINGS BETWEEN ORBITAL FORCING AND THE MARINE $\delta^{18}O$ RECORD DURING THE LATE NEOGENE

T. Hagelberg, N. Pisias, S. Elgar

ABSTRACT

Previous investigations of the response of Plio-Pleistocene climatic records to long-term, orbitally induced changes in radiation have considered a linear response of climate. While the second-order statistics of power spectra and cross spectra provide necessary information on linear processes, insight into the nonlinear characteristics of Pliocene and Pleistocene climate is not provided by these statistical quantities. Second-order statistics do not contain the phase information necessary to investigate nonlinear, phase-coupled processes. Such information is provided by higher-order statistical quantities. In particular, bispectral analysis indicates that nonlinear couplings are present in the climatic (radiative) forcing at the Milankovitch frequencies. Through a linear transfer, this forcing produces similar nonlinear couplings in deep-sea sedimentary oxygen isotope records (ODP site 677 and DSDP site 607) from 1.0 to 0 Ma during the late Neogene. This analysis suggests that during the late Pleistocene, the dominance of the 100,000 year cycle in the climate record is consistent with a linear, resonant response to eccentricity forcing. In the period from 2.6 to 1.0 Ma, a change in the nature of the climatic response to orbital forcing is indicated, as phase couplings present in the isotopic time series are not similar to the phase couplings present in the insolation forcing. Third-order moments (skewness and asymmetry) are used to quantify the shape of the climatic response. From 2.6 Ma to present, an increase in the asymmetry (sawtoothness) of the oxygen isotopic records is accompanied

by a corresponding decrease in the skewness (peakedness) of the records. This indicates an evolution in the nature of the phase coupling within the climate system. These results may provide important constraints useful in development of models of paleoclimate.

INTRODUCTION

Since the pioneering work of Hays et al. [1976], researchers have successfully identified a linear response of Plio-Pleistocene climate to orbital forcing [e.g., Pisias and Moore, 1981; Imbrie et al., 1984, 1989; Raymo et al., 1989; Ruddiman et al., 1989], supporting the Milankovitch hypothesis of climate change. Empirical evidence in support of this hypothesis is strengthened by observations of high coherence and relatively constant phase between the climatic forcing (orbital tilt and precession) and the response (global ice volume) at periods of 41, 23 and 19 kyr. These results suggest a linear relationship between ice sheet growth and decay and orbitally induced changes in the distribution of solar radiation.

A linear response of the climate system to solar insolation changes can account for much of the variance in the obliquity (41 kyr) and precession (23-19 kyr) bands of the paleoclimate spectrum, but it is generally thought to be insufficient to explain the dominance of the 100 kyr cycle during the Pleistocene [Imbrie et al., 1989 and references therein]. Efforts to explain the dominance of 100 kyr power in the paleoclimate record have produced a range of results, as discussed below.

Studies which contend that a linear response cannot explain the 100 kyr cycle in the paleoclimatic record often argue that insolation forcing in the 100 kyr eccentricity band is too small to produce the observed response or that it is altogether nonexistent [e.g., Imbrie et al., 1989; Birchfield and Weertman, 1978]. Although the direct influence of eccentricity on insolation is small (of the order of 0.1% [Berger, 1977]), eccentricity is the only orbital parameter that influences the total amount of radiation the Earth receives annually [Berger, 1989]. In addition, eccentricity variations are observed to correlate positively with changes in estimated summer temperature [Berger, 1978a, Hays et al., 1976]. It is still unknown whether the paleoclimatic spectral peak at 100 kyr is produced from (1) a linear response to eccentricity or (2) a nonlinear interaction between two precession band oscillations

which transfers energy to the 100 kyr band. To investigate this problem, the relative proportions of variance in the paleoclimatic record that are related to a linear response to eccentricity and to a nonlinear response to precessional forcing must be determined.

Paleoclimate research in this area has proceeded along two similar avenues. On one hand, analyses of geologic data provide fundamental observations of how climate has varied over the past several million years. Successful, extensive strategies have been developed to examine records within a consistent chronologic framework and in a systematic manner [e.g., Imbrie et al., 1989]. On the other hand, models have been developed which seek to describe the physics governing these changes with varying degrees of complexity (see the summary by Saltzman [1985, and references therein]). Deterministic models describing dynamics of the "slow response" of climate system evolution are divided into two groups by Saltzman [1985]: (1) quasi-deductive models, based on prognostic equations for specific processes [e.g., Birchfield and Weertman, 1978; Birchfield and Grumbine, 1985; Le Treut and Ghil, 1983; Oerlemans, 1982; Pollard, 1983; Peltier, 1982] and (2) inductive models, which attempt to construct a dynamical system of equations, based on known physical feedbacks, from which reasonable paleoclimatic output can be produced [e.g., Imbrie and Imbrie, 1980; Saltzman and Sutera, 1984; Saltzman et al., 1984; Maasch and Saltzman, 1990]. Several models (of both types) invoke a nonlinear response of the climate system to ice sheet formation to explain the 100 kyr cycle [Le Treut and Ghil, 1983; Imbrie and Imbrie, 1980; Wigley, 1976; Birchfield and Weertman, 1978; Sneider, 1985]. Other models explain this cycle as a free oscillation of the climate system, whose phase is set by weak eccentricity forcing [Saltzman and Sutera, 1984; Saltzman et al., 1984]. Finally, a few models incorporate stochastic effects [Hasselman, 1976; Matteucci, 1989].

Thus a wide range of classes of models exist, all of which seek to explain the same phenomenon (Pleistocene climate). A general test of each model is its ability to reproduce characteristics that are present within the data, as well as its ability to predict characteristics

which have not yet been (or cannot be) determined from data. To first order, every model reproduces some feature or features of the paleoclimatic record, most commonly its power spectrum (a second-order statistic). Insights into the higher-order statistics of the data can provide additional constraints or tests for evaluating the models.

Although some observations suggest a nonlinear response of the paleoclimate system to orbital forcing, this response has not been quantified, in part because the power spectrum does not contain phase information. Power spectral analyses are incapable of detecting the phase coupling which characterizes a nonlinear interaction. Similarly, the cross spectrum contains phase information between only two records at a given frequency and is therefore capable of resolving only a linear relationship. Both the power spectrum and cross spectrum are derived from covariance, a second-order statistical quantity. The presence of quadratic nonlinear interactions between oscillations of different frequencies can be addressed most effectively through the use of the bispectrum, a third-order statistical quantity.

In this study, bispectra of the time series of orbitally induced insolation changes and time series of the oxygen isotopic proxy of global ice volume (from ODP site 677 and DSDP site 607) are presented. Cross spectra and bispectra are used to show that both the radiative forcing and the climatic response contain nonlinearly coupled components, but the interaction between the insolation forcing and response is primarily linear. The analysis suggests that the 100 kyr power observed in the paleoclimatic record is consistent with a linear, resonant response to insolation forcing.

First, a brief introduction to bispectral analysis, including a simple example, is presented. Next, the bispectrum of the calculated record of radiative forcing as well as three Plio-Pleistocene records of global ice volume ($\delta^{18}O$) are presented. The time period from 1.0 to 0 Ma, where 100 kyr power is very high, is compared to the period from 2.6 to 1.0

Ma, where 100 kyr power is lower. Higher-order moments (skewness and asymmetry) are shown to provide quantitative insights into features of these records. Finally, the implications of these results for paleoclimate model development are examined.

BACKGROUND

Bispectral techniques have been in use for over 25 years [Hasselman et al., 1963] (see also the review by Nikias and Raghuveer [1987]). Because this is the first application of these techniques to paleoclimatic time series, a brief summary and an example of its application are presented.

The bispectrum is formally defined as the double Fourier transform of the third-order autocorrelation of a time series [Hasselman et al., 1963]. While the power spectrum describes the distribution of variance (the second central moment) as a function of frequency, the bispectrum describes the distribution of the third moment as a function of bi-frequency. For a discretely sampled time series x(t) with complex Fourier coefficients at frequency f_j given by X(f_j), the power spectrum is

$$P(f_j) = \left\langle X(f_j) X^*(f_j) \right\rangle \tag{1}$$

where the angled brackets indicate expected value (mean) and the asterisk indicates complex conjugate. Similarly, the bispectrum is given by [Haubrich, 1965; Kim and Powers, 1979]:

$$B(f_j, f_k) = \left\langle X(f_j) X(f_k) X^*(f_j + f_k) \right\rangle \tag{2}$$

If there is energy (variance) at frequency f_j, then P(f_j) is nonzero. The bispectrum, however, is zero at the bi-frequency f_j,f_k, when the modes f_j,f_k, and f_{j+k} are independent of one another, even if energy is present at these frequencies. For independent oscillations, the phases are random relative to each other, yielding a zero bispectrum upon averaging over many realizations. In theory, the bispectrum is nonzero only if these three modes are quadratically coupled, meaning that their phases are nonlinearly coupled to one another.

Like the cross spectrum, which provides coherence and phase information, the complex-valued bispectrum is often cast in terms of its normalized magnitude, the bicoherence, and its phase, the biphase (denoted $b(f_j, f_k)$ and ß(f_j, f_k), respectively). The

squared value of bicoherence, $b^2(f_j, f_k)$, represents the fraction of power at frequency $f_j + f_k = f_{j+k}$ owing to quadratic (nonlinear) interactions of the three modes [Kim and Powers, 1979]. Analogous to the linear coherence spectrum, the bicoherence spectrum is normalized such that $0 < b < 1$ [Kim and Powers, 1979]. The biphase is analogous to the phase of the cross spectrum, and ranges between $-\pi$ and π.

A simple example demonstrates the effect of nonlinear phase coupling on both the shape of a time series and the detection of phase coupling by the bispectrum. Let the time series $x(t)$ be composed of three cosines and a low-amplitude Gaussian noise component:

$$x(t) = \cos(2\pi f_1 t+\phi_1) + \cos(2\pi f_2 t+\phi_2) + \cos(2\pi f_3 t+\phi_3) + \text{noise} \quad (3)$$

where f_i is the frequency and ϕ_i is the phase of each cosine.

The frequencies of these cosines are chosen to be $f_1 = 0.010$, $f_2 = 0.043$, and $f_3 = f_1 + f_2 = 0.053$ for ease in comparison of this simulated record with late Pleistocene $\delta^{18}O$ time series, which show power spectral peaks at these frequencies in cycles/thousand years. Three different cases are examined. In the first case (case 1), ϕ_1, ϕ_2, and ϕ_3 are all random variables uniformly distributed over $(0, 2\pi]$. This case represents a linear (Gaussian) system where there is no nonlinear phase coupling. The phases of each oscillation are random relative to one another when averaged over many realizations. In the second case (case 2), ϕ_1 and ϕ_2 are uniform random variables, but $\phi_3 = \phi_1 + \phi_2$, and thus f_1, f_2, and f_3 are now phase coupled. The relationship between the three modes is no longer random. Similarly, in the last case (case 3), ϕ_1 and ϕ_2 are uniform random variables, but $\phi_3 = \phi_1 + \phi_2 + \pi/2$ (the choice of ϕ_3 in cases 2 and 3 results in biphases of 0° and 90°, and waveforms with maximum skewness and asymmetry, respectively, as discussed below). For each case examined, sixteen 256-point realizations were made, resulting in a 4096-point record.

Portions of each time series and the corresponding power spectrum for each case are shown in Figures IV.1 and IV.2, respectively. In each case, the power spectra show concentrations of variance at frequencies f_1, f_2, and f_3 with random fluctuations at other

frequencies resulting from the noise. Even though the time series for each case look different, the power spectra are identical. This is because the power spectrum is phase independent and the three cases differ only in their phase relationships.

Figure IV. 3 shows the bicoherence spectra for cases 1, 2, and 3. Smoothed power spectral and bispectral estimates were made by windowing (using a Hanning window) and averaging the 16 256-point ensembles for each record. Resulting estimates have 30 degrees of freedom (dof). The values contoured in Figure IV.3 are the observed bicoherences at the triad of frequencies (f_1, f_2, f_1+f_2) (denoted $b(f_1,f_2)$) which are significant at a $(1-\alpha) = 0.90$ level ($b_{90\%} = (4.6/\text{dof})^{1/2}$ [Elgar and Guza, 1988]). Owing to the symmetry properties of the bispectrum, it necessary only to calculate the bispectrum within a triangular region defined by $0 \le f_1 \le f_N, f_2 \le f_1$, and $f_1+f_2 \le f_N$, where f_N is the Nyquist frequency [Kim and Powers, 1979]. It is important to note that the direction of the nonlinear interaction is not given by the bispectrum, that is, sum interactions (interactions at f_1 and f_2 that produce $f_3 = f_1+f_2$) are not distinguished from difference interactions (interactions at f_3 and f_2 that

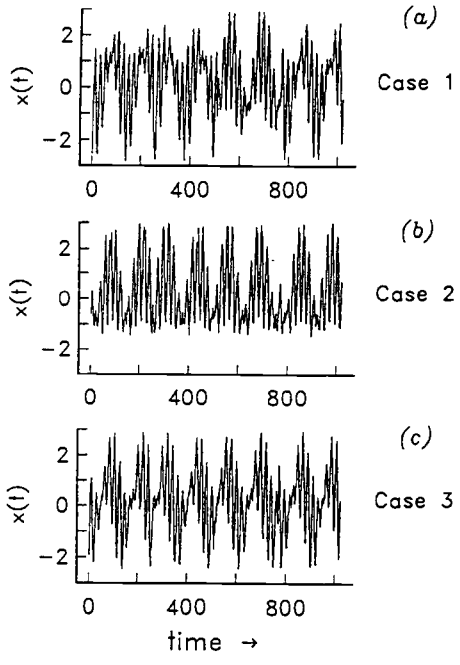

Figure IV.1. Portions of each time series for cases 1-3 (see text): (a) case 1 ($f_1+f_2=f_3$; ϕ_1, ϕ_2, ϕ_3 are random), (b) case 2 ($f_1+f_2=f_3$; $\phi_1+\phi_2=\phi_3$), and (c) case 3 ($f_1+f_2=f_3$; $\phi_1+\phi_2=\phi_3-\pi/2$). The units are arbitrary.

produce $f_1 = f_3 - f_2$, for example). This information comes instead from other aspects of the physical system under examination, including the biphase [Kim et al., 1980; Elgar and Guza, 1985].

In case 1, the linear case in which no phase coupling is present, bicoherences near the triad (0.059, 0.051, 0.110) = 0.370 are significant at a 90% level (Figure IV.3a). Although all bicoherences in this case should be zero, any finite length time series will yield some nonzero values of bicoherence. This value of bicoherence represents the high values that can be expected to occur by random chance for a linear process with 30 dof. On the other hand, bicoherence at (0.01, 0.043, 0.053) (the (f_1, f_2, f_3) triad) is 0.167, which is below the 90% significance level.

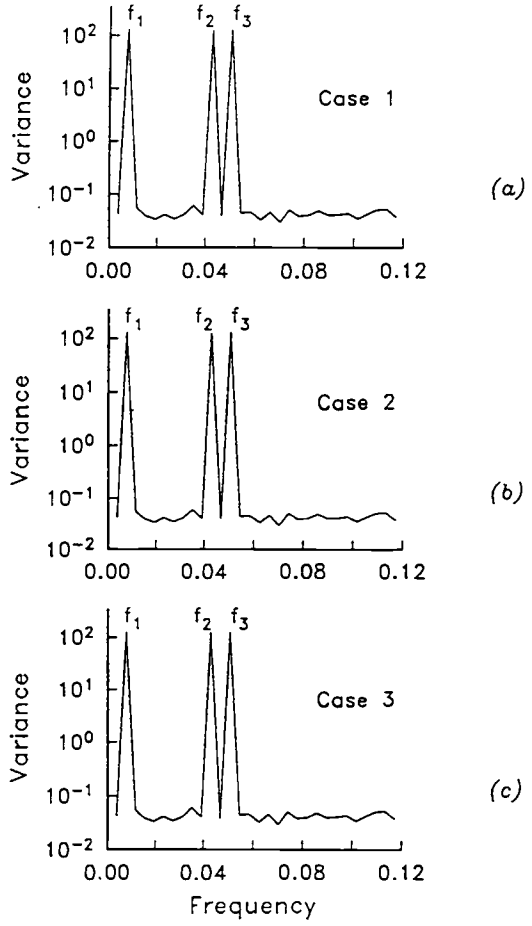

Figure IV.2. Power spectra for cases 1-3. Smoothed power spectral estimates having 30 degrees of freedom were obtained using a Hanning window and by averaging 16 256-point ensembles for each record: (a) case 1, (b) case 2, and (c) case 3. The units are arbitrary.

In cases 2 and 3, where phases are coupled, $b(0.01, 0.043) = 0.917$ and $b(0.01, 0.043) = 0.912$, respectively, indicating high bicoherence at the (0.01, 0.043, 0.053) triad (Figures IV.3b and IV.3c). In case 2, the value of bicoherence indicates that at frequency 0.053, approximately 84% of the variance is quadratically coupled to the other two components of the triad. The value is less than 1.0 owing to the addition of noise.

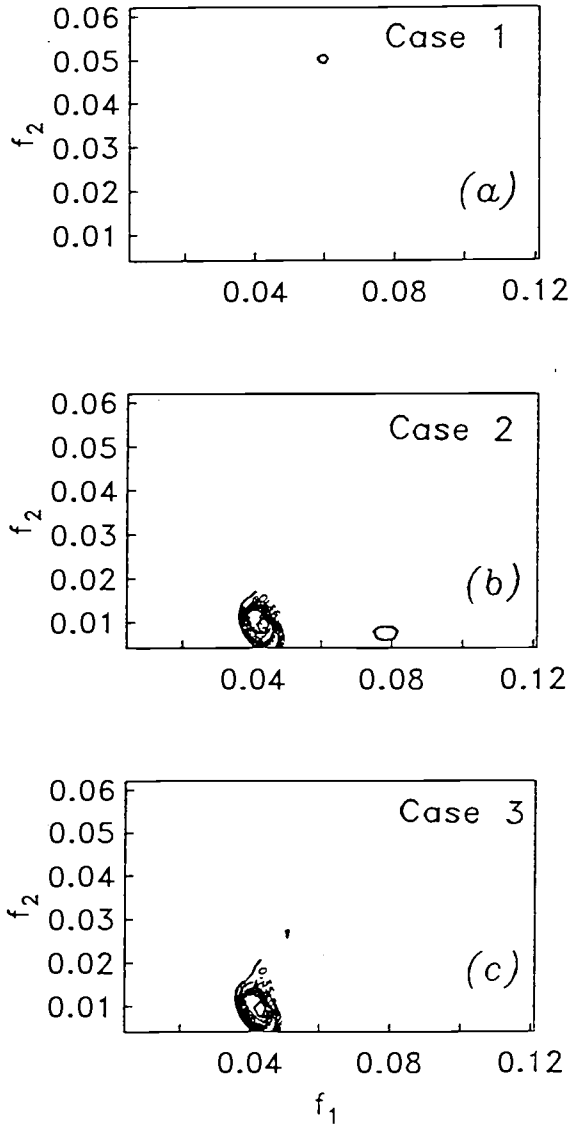

Figure IV.3. Contours of bicoherence for cases 1-3. Smoothed bispectral estimates were obtained in the same manner as power spectral estimates and have 30 degrees of freedom. The minimum bicoherence value contoured (significant at a 0.90 level) is b=0.39 with additional contours every 0.05: (a) case 1, (b) case 2, and (c) case 3. The units of frequency are arbitrary.

Biphase estimates are related to the shape of the waveform (time series) [Masuda and Kuo, 1981; Elgar, 1987]. The waveform shape is often described by two normalized third moments, skewness and asymmetry. Skewness is the normalized third moment of the time series and indicates asymmetry with respect to a horizontal axis, or top-bottom asymmetry. Asymmetry is the normalized third moment of the Hilbert transform of the time series [Elgar, 1987] and indicates asymmetry with respect to a vertical axis, or fore-aft asymmetry. For a time series which is purely Gaussian, having only random phase relationships, the biphase is also random for every triad of frequencies.

In case 1 of the above example, the shape of the waveform is symmetrical, and skewness and asymmetry are zero. In Figure IV.1a, skewness = -0.12 and asymmetry = -0.16. The small nonzero third-moment estimates are caused by statistical fluctuations. In case 2, the biphase for the (0.01, 0.043, 0.053) interaction is zero, and the waveform is positively skewed (in Figure IV.1b, skewness = 0.80, asymmetry = 0). In case 3, the same triad has biphase of $\pi/2$, and the waveform is asymmetric or "sawtooth" shaped (in Figure IV.1c, skewness = 0, asymmetry = -0.79).

The asymmetric record of case 3 is qualitatively similar in shape to the SPECMAP stack (Figure IV.4), a smoothed composite record of five late Pleistocene ice volume ($\delta^{18}O$) records [Imbrie et al., 1984]. The SPECMAP record displays steep terminations representing the end of glacial stages, followed by a slow, gradual ice buildup. With minor adjustments to the record of case 3 (reduction of the amplitudes of f_2 and f_3) the resemblance to the SPECMAP stack is striking (Figure IV.4). The implications of this similarity are that quadratic phase couplings are of importance in the paleoclimatic record and that through the use of higher order statistics, these couplings can be quantified.

NONLINEAR COUPLINGS AMONG ORBITAL PARAMETERS

The bispectrum of the normalized time series of radiative (insolation) forcing (as calculated by Berger [1978b] is now examined. (Note that in this paper the 1978 solution of Berger is used. A more recent solution [Berger and Loutre, 1988] has been found to yield essentially the same results in the bispectrum as the older [Berger, 1978b] solution, although the orbital values in the new solution differ from the older solution in the time domain prior to 1 Ma. Because the values of the newer solution from 1.0 to 0 Ma are less well reproduced at present than those of the older solution, the 1978 values are used here.) Long-term (of the order of 100 kyr) variations in the Earth's insolation are produced through interacting motions of the Sun and planets relative to the Earth. At a given latitude on the Earth in a given season, the solar energy available is a function of the solar constant, the eccentricity of the Earth's orbit, the obliquity of the Earth's axis, and the longitude of perihelion as measured from the vernal equinox [Berger, 1978c].

Many studies have examined the paleoceanographic response to changes in these orbital parameters. Studying each orbital parameter separately has been considered reasonable as obliquity variations affect the latitudinal distribution of insolation, preces-

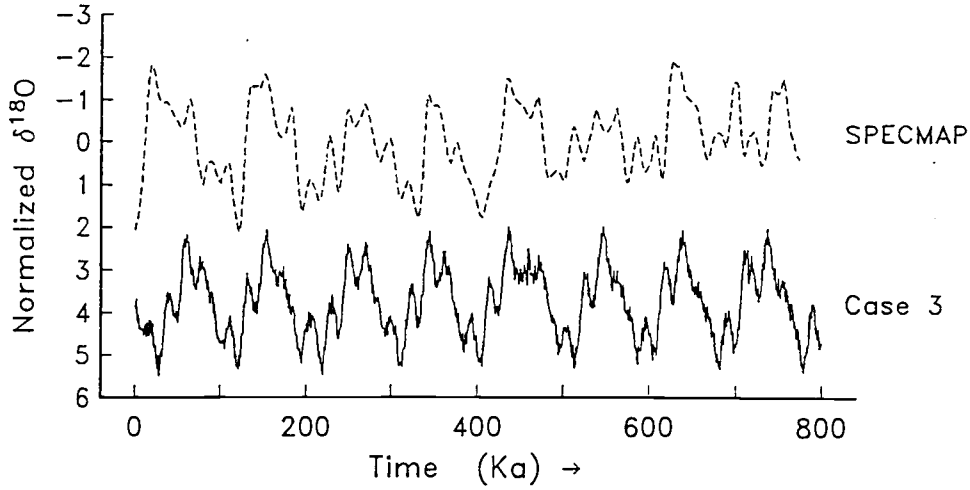

Figure IV.4. SPECMAP composite $\delta^{18}O$ stack (dashed line) [Imbrie et al., 1984] compared to part of a modified version of case 3 (solid line) (see Figure IV.1c). The amplitude of f_1 is the same as in case 3, but the amplitudes of f_2 and f_3 have been reduced 60% and 70%, respectively.

sional changes affect the seasonal distribution, and eccentricity variations affect the total insolation received over time. Examination of the terms that are used to derive long-term Earth orbital variations [e.g., Berger, 1978c] indicates that eccentricity, tilt, and precession [e, ε, and $e\sin\omega$] are indeed coupled to one another. However, no quantitative estimates of the strength of these couplings has been made. Bispectral analysis of the insolation record allows phase-coupled oscillations to be isolated.

A 4.096 m.y. record of July 65°N radiation sampled at 2000 year intervals is shown in Figure IV.5a. The power spectrum of this record (Figure IV.5b) shows concentrations of energy at periods of 41, 23, and 19 kyr (0.024, 0.043, and 0.053 cycles/kyr, respectively).

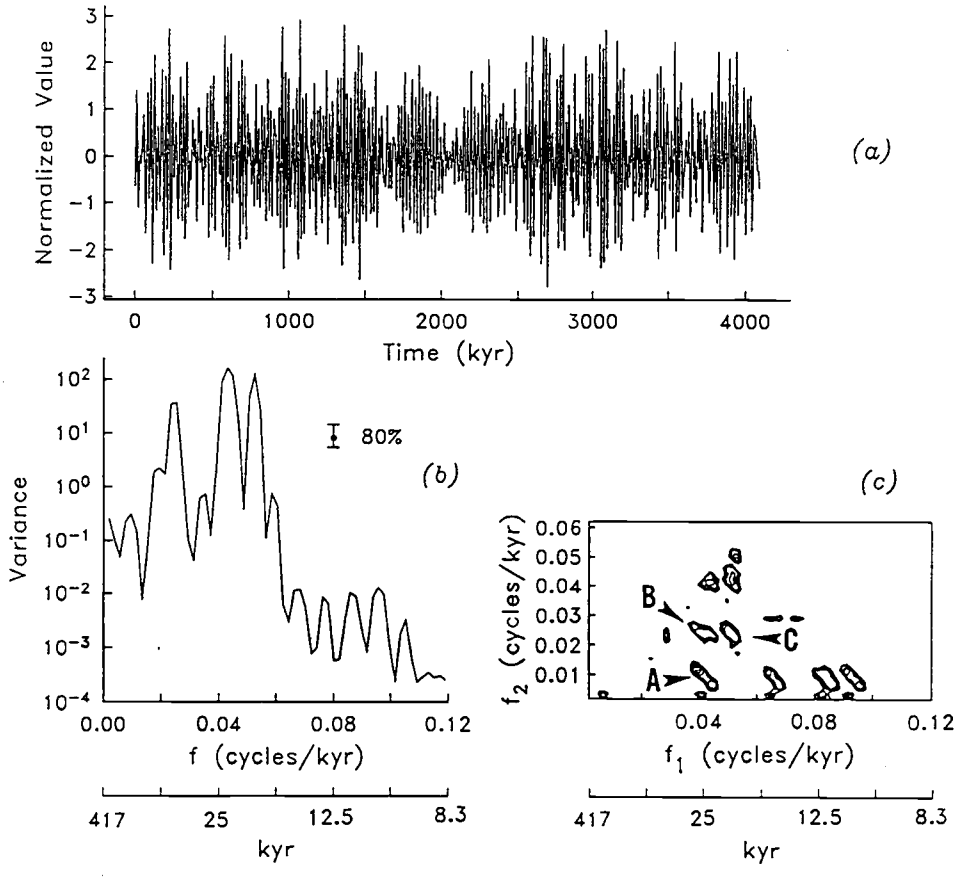

Figure IV.5. July 65°N insolation, for the interval from 4.096 to 0 Ma (from Berger, [1978b] solution]: (a) time series, (b) power spectra, and (c) significant ($1-\alpha = 0.90$) contours of bicoherence. The minimum value contoured is 0.57, and contour interval is 0.10. To obtain power spectral and bispectral estimates having 14 degrees of freedom, data were Hanning windowed, and eight ensembles of 0.512 m.y. length were averaged. Regions A, B, and C are referred to in the text.

Less energetic, but significant, peaks are also present near 100, 28, and 15 kyr (0.01, 0.036, 0.067 cycles/kyr, respectively). The bicoherence spectrum for this record (Figure IV.5c), shows that many modes in the radiative forcing are strongly coupled. Significant (1- α =0.90) phase coupling between eccentricity and precession is indicated by $b(0.041, 0.012)$ = 0.978 (region A in Figure IV.5c). The bicoherence spectrum also indicates significant coupling between orbital tilt and precession. For example, $b(0.041, 0.025) = 0.960$ (region B in Figure IV.5c) and $b(0.055, 0.023) = 0.969$ (region C in Figure IV.5c). The third components in these interacting triads have frequencies 0.066 (15 kyr) and 0.078 (12.8 kyr), respectively, and appear as less energetic peaks in the radiation power spectrum (Figure IV.5b).

The most notable interaction is at the triad (0.041, 0.012, 0.053), (region A in Figure IV.5c), which has a bicoherence of 0.978. This high value of bicoherence indicates that precession components of 19 and 23 kyr are nonlinearly coupled to 100 kyr eccentricity terms (although 0.012 cycles/kyr is a 83 kyr period, this frequency represents the 100 kyr band after averaging has been completed). This result is confirmed by examining the terms in the series expansion of eccentricity and precession given by Berger [1977, Tables 1 and 3]. Difference interactions between the individual precession terms listed in this reference can produce virtually all of the listed eccentricity terms [Berger, 1989]. This difference interaction indicates that at frequency f_2= 0.012 cycles/kyr (100 kyr band), greater than 95% of the variance is quadratically coupled to oscillations at f_1=0.41 cycles/kyr (23 kyr) and f_3=0.53 cycles/kyr (19 kyr). The energy at 100 kyr is small in comparison with that at 41, 23, and 19 kyr (Figure IV.5b). However, almost all of the variance at 100 kyr is quadratically coupled through nonlinear interactions with the precessional terms. The biphase of the (0.041, 0.012, 0.053) triad is zero, indicating that the phase of f_2 is equal to the difference of the phases of f_3 and f_1. This is also confirmed by Berger [1977], as differences between the phases of the individual precession terms listed are exactly equal to the corresponding phases of the eccentricity terms.

In addition to significant bicoherence values, other analyses suggest that the observed phase couplings do not result from random fluctuations. Time series generated by replacing the phases in the July 65°N radiation time series (Figure IV.5a) with random phases uniformly distributed over (0, 2π) are shown in Figure IV.6a. The power spectrum of this random phase time series (Figure IV.6b) is identical to that of the radiation record (Figure IV.5b) because phase information is not retained by the power spectrum. The bicoherence spectrum (Figure IV.6c) of this random phase record clearly indicates an absence of phase coupling, as is expected for a purely linear system. Similar to case 1 above, the two values above the 0.90 significance level, (0.039, 0.037, 0.076) = 0.509 and (0.105, 0.008, 0.113) = 0.589), represent high bicoherence values that can be expected to occur

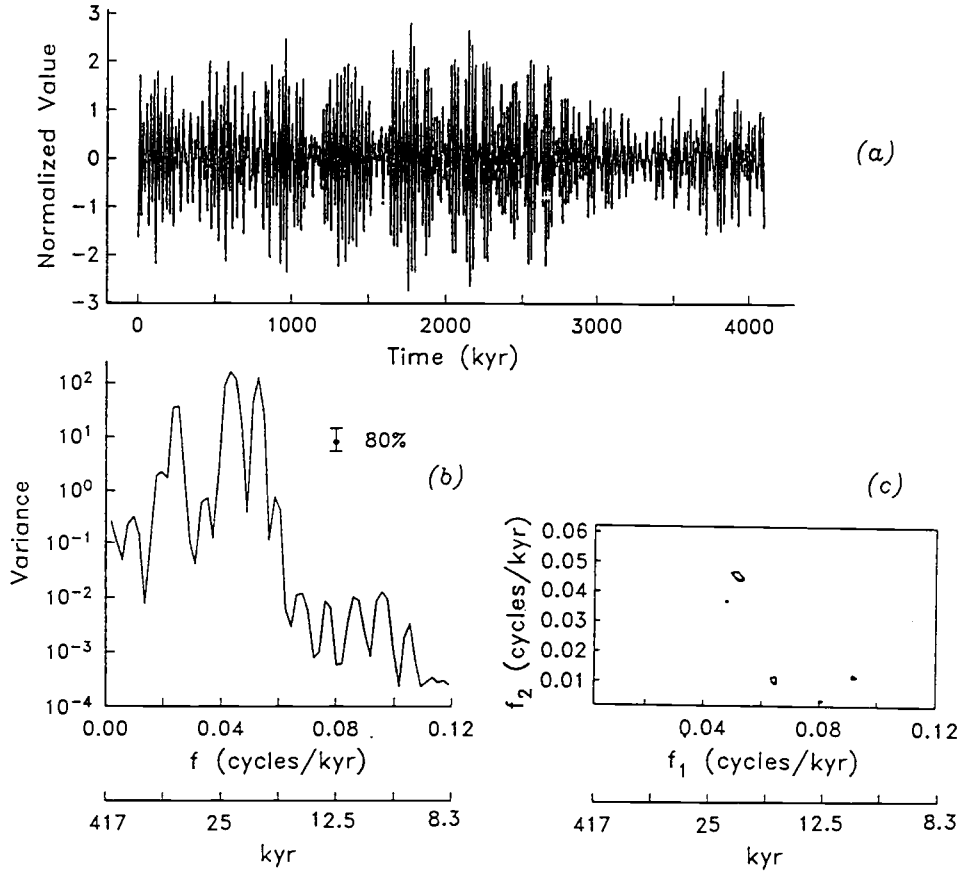

Figure IV.6. Simulated time series generated by replacing the phases in the July 65°N insolation record (Figure IV.5a) with random phases. Power spectral and bispectral estimates were obtained as described in Figure IV.5: (a) time series, (b) power spectra, and (c) significant (1-α =0.90) contours of bicoherence.

through random chance. The result of the random phase simulation shown in Figure IV.6 is consistent with the conclusion that the high bicoherences observed in the radiation record are not a result of random fluctuations, but result from phase couplings within the orbital record. Similar low values of bicoherence were observed in several other random phase simulations (not shown).

These results illustrate the use of bispectral analyses for detecting quadratically nonlinear interactions. Strong nonlinear coupling is detected between oscillations in the precession and eccentricity bands in the estimated record of radiative forcing of Berger [1978b]. Using the terms given by Berger [1977], a difference interaction of precession terms is equivalent to eccentricity [Berger, 1989]. This interaction was not observable through examination of the time series and power spectra. The bicoherence spectrum also indicates significant nonlinear interactions between precession and obliquity. In the present solution of Berger [1978b], the strength of these nonlinear interactions does not vary through time, and thus analysis of a 4 m.y. record yields the same results as analysis of shorter (1 m.y.) records.

A purely linear response of climate to this nonlinear forcing will produce a paleoclimatic record that contains the same nonlinear interactions as the forcing. The response will also be linearly coherent with the forcing at the forcing frequencies. On the other hand, a nonlinear response of climate to this nonlinear forcing will produce responses that are not necessarily coherent with oscillations at the same frequencies as the forcing. In the next section, three records of paleoclimate are examined to determine the extent of linear and nonlinear responses to orbital forcing.

ANALYSIS OF $\delta^{18}O$ RECORDS

The relatively short record lengths (typically 400-800 kyr) of most paleoclimatic time series has precluded application of bispectral analysis in the past. Variance of bispectral estimates are higher than power spectral estimates, and short records do not have enough degrees of freedom to yield statistically stable results. Recent efforts, however, have produced a number of long (>1 m.y.) records of paleoclimatic change [Shackleton and Hall, 1989; Ruddiman et al., 1989; Raymo et al., 1989]. The bispectrum of three relatively long $\delta^{18}O$ records from the North Atlantic and eastern equatorial Pacific are now examined.

The records examined here were taken from Ocean Drilling Project site 677 (eastern equatorial Pacific, 1°12'N, 83°44'W) and Deep Sea Drilling Project site 607 (North Atlantic, 41°00'N, 32°58'W). At site 677, time series of planktic and benthic $\delta^{18}O$ were examined, and at site 607, benthic $\delta^{18}O$ time series were examined. The site 677 record was generated and initially studied by Shackleton and Hall [1989] and Shackleton et al. [1990]. The site 607 record was generated and studied by Ruddiman et al. [1989] and Raymo et al. [1989]. For each of these studies the authors have developed a chronology for these records by making use of orbital tuning procedures. Differences between the time scale used by

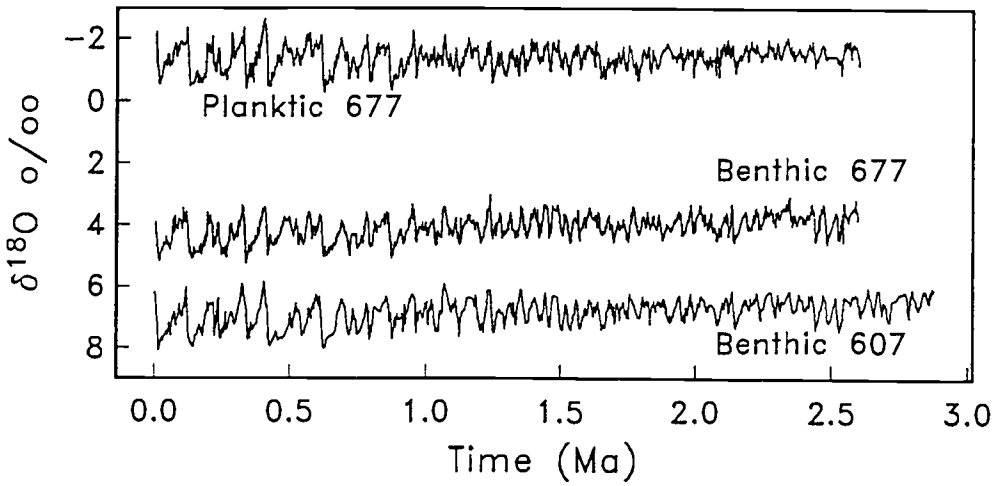

Figure IV.7. Time series of planktic (*G. ruber*) and benthic (primarily *Uvigerina*) $\delta^{18}O$ from site 677 [Shackleton and Hall, 1989] and benthic (*Cibicidoides*) $\delta^{18}O$ from site 607 [Ruddiman et al., 1989; Raymo et al., 1989]. The 607 data are offset from actual values to allow visual comparison.

Shackleton et al. [1990] and Ruddiman et al. [1989] and Raymo et al. [1989] are substantial. The issue of chronologies and approaches to orbital tuning is complicated, and for consistency, only the most recent time scale of Shackleton et al. [1990] is used here. This time scale has been applied to both the 677 and 607 records [Shackleton et al., 1990]. Although it appears that the site 677 and site 607 bispectra presented here are robust to slight time scale changes, the potentially critical effects of time scale variability on bispectrum estimates will be treated in a later paper.

The time series of planktic (*Globeriginoides ruber*) and benthic (primarily *Uvigerina senticosa*) $\delta^{18}O$ from site 677, and benthic (*Cibicidoides*) $\delta^{18}O$ from site 607 are shown in Figure IV.7. The records from site 677 are approximately 2.6 m.y. in length, while the site 607 record is approximately 2.8 m.y. long. The average sampling interval for the 677 data is 2000 years, and the average for the 607 data is 3500 years.

It is well known that a change in the character of the Neogene global ice volume record occurred near 1 Ma [Pisias and Moore, 1981; Ruddiman and Raymo, 1988]. Oscillations at around 100 kyr, which are generally not prevalent previous to 1 Ma, become very strong in the late Pleistocene. This is clearly seen by comparing the power spectra of these records before (Figure IV.8a) and after (Figure IV.8b) 1 Ma. Because of this apparent nonstationarity in the record, all records are analyzed in two parts, from 1.0 to 0 Ma and from 2.6 to 1.0 Ma (2.8 to 1.0 Ma at site 607). The records are divided at 1.0 Ma to obtain the longest late Pleistocene record possible. The precise location (within +/- 100 kyr) where the records are divided does not change the results significantly.

So that each $\delta^{18}O$ time series could be processed identically, the time series from site 607 was overinterpolated to match the sampling resolution of the site 677 data. While the Nyquist frequency of the 607 time series is at 7 kyr (as opposed to 4 kyr in the case of the site 677 records), this oversampling allows for direct comparison of the three data sets after processing. For the interval from 1.0 to 0 Ma, all smoothed spectral estimates were obtained by averaging four 128 point (256 kyr) ensembles for 6 degrees of freedom. For

the interval from 2.6 to 1.0 Ma, smoothed estimates were obtained by averaging six 128-point ensembles for 10 degrees of freedom. In each case the frequency resolution is 0.0039 cycles/kyr, and a Hanning window was used to reduce leakage. (Results using this method of spectral analysis were not significantly different than results obtained using the Blackman-Tukey truncated lag (autocovariance) method.)

For the interval from 1.0 to 0 Ma, the power spectrum of each $\delta^{18}O$ record has variance concentrated at the Milankovitch frequencies of 0.012, 0.023, 0.043, and 0.053 cycles/kyr, corresponding to the 100, 41, and 23, and 19 kyr bands, respectively (Figure

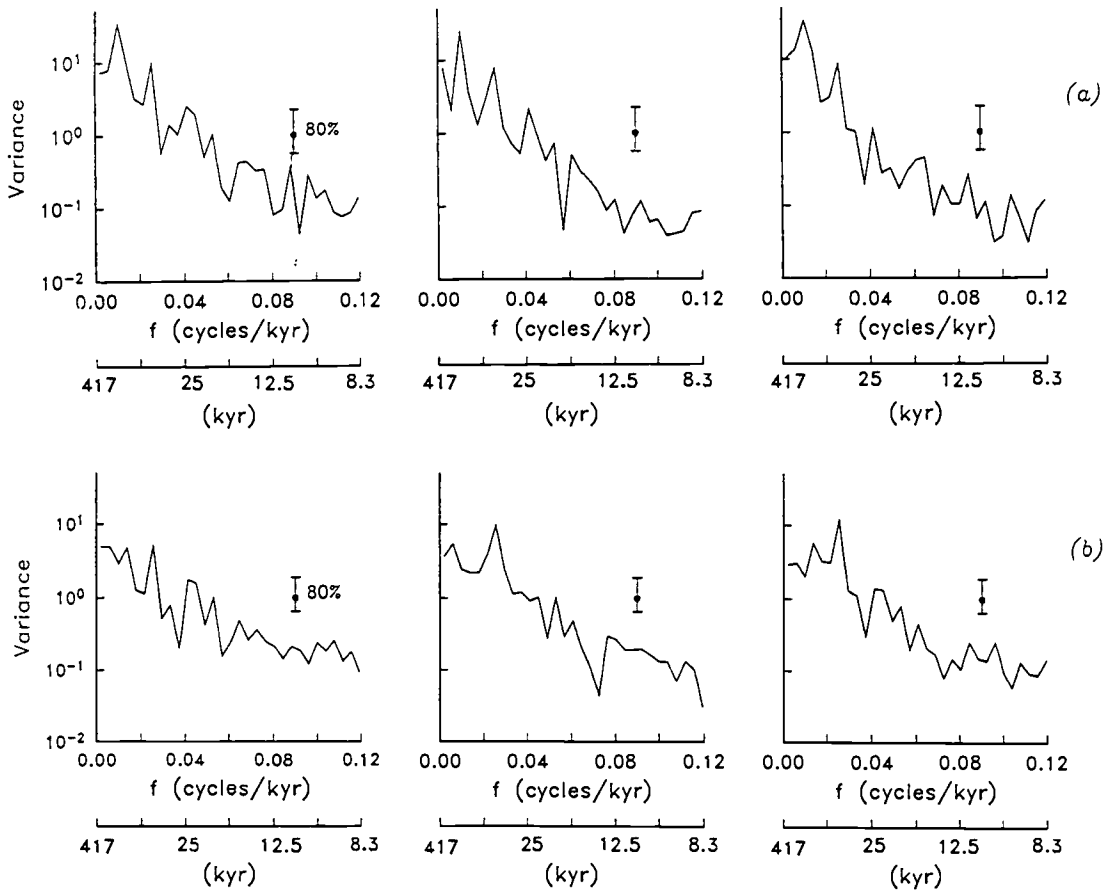

Figure IV.8. (a): Power spectra of isotopic records for the interval 1.0 to 0 Ma: site 677 planktic $\delta^{18}O$ (left), site 677 benthic $\delta^{18}O$ (middle), and site 607 benthic $\delta^{18}O$ (right). Estimates having 6 degrees of freedom were obtained by using a Hanning window and averaging four 256 kyr subrecords. (b): Power spectra for the interval 2.6 to 1.0 Ma: site 677 planktic $\delta^{18}O$ (left), site 677 benthic $\delta^{18}O$ (middle), and site 607 benthic $\delta^{18}O$ (right). Estimates having 10 degrees of freedom were obtained using a Hanning window and averaging six 256 kyr subrecords.

IV.8a). While the site 677 records show significant variance concentrated at the precessional frequency of 19 kyr, this peak is not prominent in the site 607 data. The planktic $\delta^{18}O$ time series for site 677 contains additional variance at periods of 15 kyr and 12 kyr, which correspond to sum frequencies of orbital precession and obliquity, and the site 607 time series contains significant variance near 15 kyr as well.

For the interval from 2.6 to 1.0 Ma, the total variance contained in each time series is lower than in the interval from 1.0 to 0 Ma. Each time series shows variance concentrated primarily at 41 kyr (0.023 cycles/kyr) (Figure IV.8b). Low-frequency power, dominant from 1.0 to 0 Ma, is diminished relative to 41 kyr power. In each time series, low-frequency variance is distributed between 400 kyr and 71 kyr, rather than concentrated at 100 kyr. In this older interval, the site 677 planktic $\delta^{18}O$ record also shows power at 23 kyr. This 23 kyr peak is also present in the benthic records, although to a lesser extent than in the site 677 planktic $\delta^{18}O$.

Coherence and phase spectra between July 65°N insolation and each $\delta^{18}O$ time series for 1.0 to 0 Ma and from 2.6 to 1.0 Ma are displayed in Figures IV.9 and IV.10 and are summarized in Table IV.1. In the interval from 1.0 to 0 Ma, significant ($1-\alpha = 0.90$) coherence occurs at the four primary Milankovitch frequencies for each time series. The coherence spectrum at site 607 is similar to that of both site 677 records, although coherence with insolation at 23 kyr is weaker, and coherency at 100 kyr occurs over a wider band. With the exception of the 41 kyr band in the insolation/site 607 phase spectrum, the phase spectrum for each record is similar. As noted in the Introduction, this overall high coherence between insolation and $\delta^{18}O$ provides evidence for a strong linear relationship between insolation forcing and the paleoclimatic response.

Coherence with insolation is weaker in the interval from 2.6 to 1.0 Ma. Significant coherence with insolation occurs in the 41 kyr and 23 kyr bands with each isotopic time series, and in the 19 kyr band in the site 677 time series (Figure IV.10 and Table IV.1). The coherence is not as strong as in the interval from 1.0 to 0 Ma, however. In each time series,

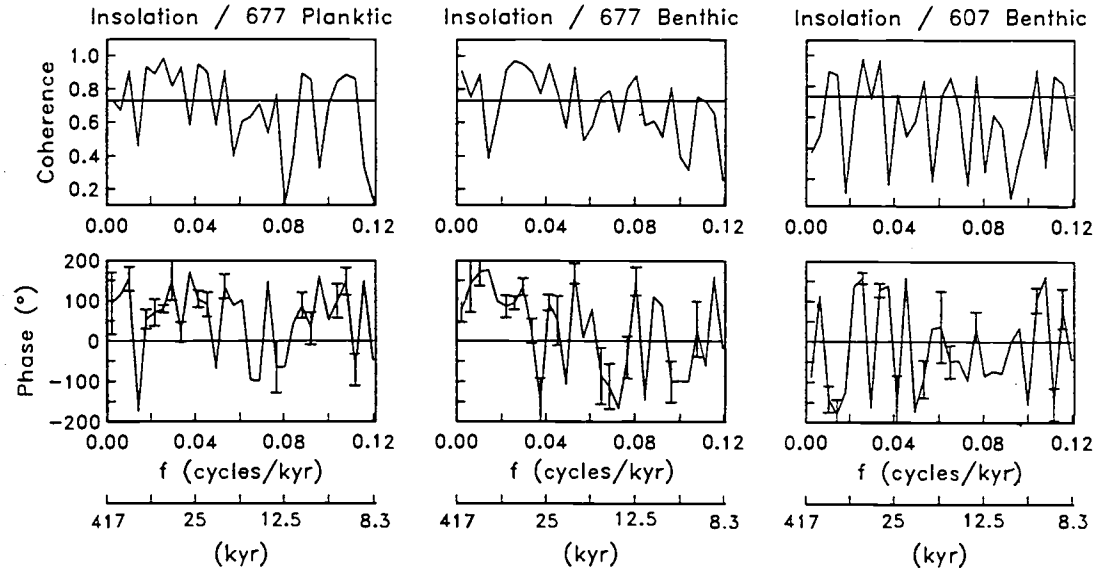

Figure IV.9. Coherence (top) and phase (bottom) between 65°N insolation and $\delta^{18}O$, for the interval from 1.0 to 0 Ma: site 677 planktic $\delta^{18}O$ (left), 677 benthic $\delta^{18}O$ (middle), and site 607 benthic $\delta^{18}O$ (right). The 90% significance level for coherence (horizontal line) is 0.73. The 90% confidence interval for phase estimates is indicated by vertical bars. Positive phase indicates insolation leads $\delta^{18}O$. The data were processed as described in the caption to Figure IV.8a.

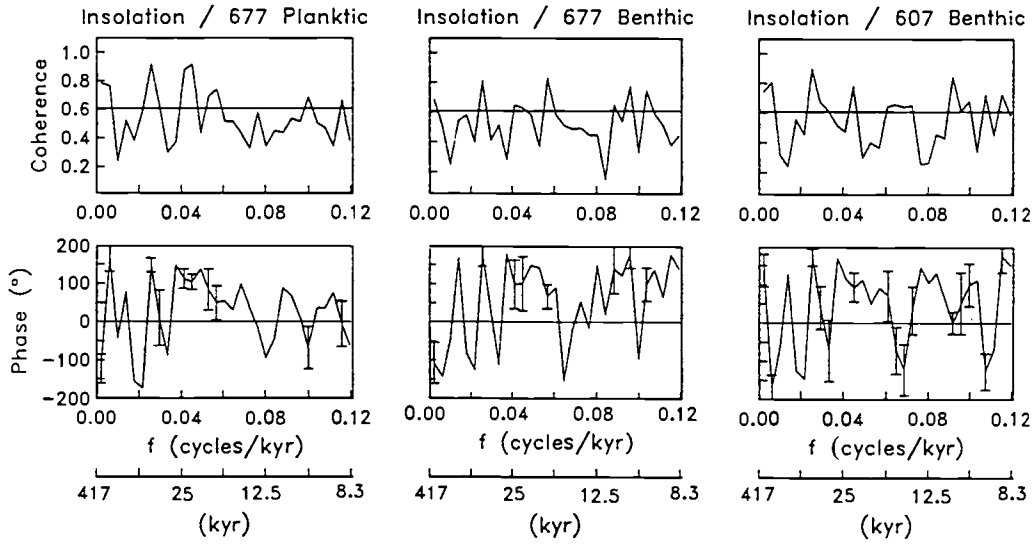

Figure IV.10. Coherence (top) and phase (bottom) between 65°N insolation and $\delta^{18}O$, for the interval from 2.6 to 1.0 Ma: site 677 planktic $\delta^{18}O$ (left), 677 benthic $\delta^{18}O$ (middle), and site 607 benthic $\delta^{18}O$ (right). The 90% significance level for coherence (horizontal line) is 0.61. The 90% confidence interval for phase estimates is indicated by vertical bars. Positive phase indicates insolation leads $\delta^{18}O$. The data were processed as described in the caption to Figure IV.8b.

there is significant coherence with insolation at frequencies lower than 100 kyr. In addition, the site 607 time series shows high coherence with insolation near 30 kyr. In this time interval, each of the insolation/$\delta^{18}O$ phase spectra are similar.

Table IV.1. Coherence, Gain, and Phase Shift Between Insolation and $\delta^{18}O$ Response Near 100, 41, 23, and 19 kyr Periods for the Intervals from 1.0 to 0 and from 2.6 to 1.0 Ma

Record	Frequency, cycles/kyr	Period, kyr	Coherency	Gain	Phase, deg
		0-1 Ma			
677 planktic	0.012	~100	0.9076	9.220	154
	0.023	~ 41	0.9877	0.488	79
	0.043	~ 23	0.9504	0.134	105
	0.053	~ 19	0.9077	0.087	136
677 benthic	0.012	~100	0.7903	7.739	170
	0.023	~ 41	0.9677	0.429	95
	0.043	~ 23	0.9529	0.124	96
	0.053	~ 19	0.9301	0.074	167
607 benthic	0.012	~100	0.8948	9.096	-142
	0.023	~ 41	0.9755	0.448	158
	0.043	~ 23	0.7437	0.070	75
	0.053	~ 19	0.8320	0.032	-92
		1-2.6 Ma			
677 planktic	0.0101	~100	0.2409	1.221	-40
	0.0257	~ 41	0.9181	0.342	148
	0.0452	~ 23	0.9141	0.096	103
	0.0570	~ 19	0.7407	0.055	5
677 benthic	0.0101	~100	0.2493	1.154	-48
	0.0257	~ 41	0.8065	0.415	179
	0.0452	~ 23	0.6275	0.053	101
	0.0570	~ 19	0.8283	0.859	67
607 benthic	0.0101	~100	0.3197	1.334	-63
	0.0257	~ 41	0.8949	0.508	171
	0.0452	~ 23	0.7807	0.074	93
	0.0570	~ 19	0.3658	0.309	-93

Returning to the 1.0 to 0 Ma records, coherence between insolation and $\delta^{18}O$ near 100 cycles/kyr is estimated as 0.91, 0.79, and 0.89 for the 677 planktic, 677 benthic, and 607 benthic records, respectively. If these estimates represent the true value of coherence (these estimates are not corrected for a small bias), then between 62% and 82% of the variance in the $\delta^{18}O$ record is linearly related to variations in direct eccentricity forcing. For 677 planktic and benthic data, the phase of the response changes by close to 90° near 100 kyr, and for each record the gain at 100 kyr is relatively high (Table IV.1). These results are consistent with a response at 100 kyr which is linear and resonant. This is discussed below.

The bicoherence spectra for each $\delta^{18}O$ record over the 1.0 to 0 Ma interval are shown in Figures IV.11a-c. Smoothed bispectral estimates were calculated in the same manner as the corresponding power spectral and cross-spectral estimates. Bispectra calculated from short records have coarser frequency resolution, as is clearly illustrated in Figure IV.11d, where the bicoherence spectrum of 65°N insolation for a 1 m.y. record is shown (compare to Figure IV.5c, the bicoherence spectrum for a 4.096 m.y. record). The estimates for the 4 m.y. record shown in Figure IV.5c have 14 dof, and the 0.90 significance level is 0.58. The 1 m.y. record (Figure IV.11d), on the other hand, has 6 dof, and the 0.90 significance level is 0.88 (bicoherences reported below are significant at a 0.80 level). Owing to the low degrees of freedom for these time series, the bias of the observed bicoherences is not negligible [Elgar and Sebert, 1989]. Although the bicoherence values reported in this section have not been corrected for bias, such a correction would not significantly change the overall results presented here.

For the interval from 1.0 to 0 Ma at site 677, statistically significant ($1-\alpha = 0.80$) bicoherences indicate phase coupling among components which are also coupled in the insolation record, as well as among components which are not coupled in the insolation record. In both the planktic and benthic $\delta^{18}O$ records, phase coupling occurs between oscillations at 0.012 cycles/kyr (100 kyr band), 0.043 cycles/kyr (23 kyr band), and 0.053

cycles/kyr (19 kyr band). For the planktic record, $b(0.043, 0.012) = 0.794$, and for the benthic record, $b(0.043, 0.012) = 0.792$. The phase relationship between these modes has changed, however, from a biphase of 0° in the insolation forcing to a biphase of -90° in the benthic data and -114° in the planktic data (these biphase values of -90° and -114° are within an 80% confidence interval of one other and thus are not statistically different). There are also statistically significant couplings in the site 677 records between 23 kyr band variations and 41 kyr ($b(0.043, 0.023)$=0.840 in the planktic record and $b(0.043, 0.023) = 0.741$ in the

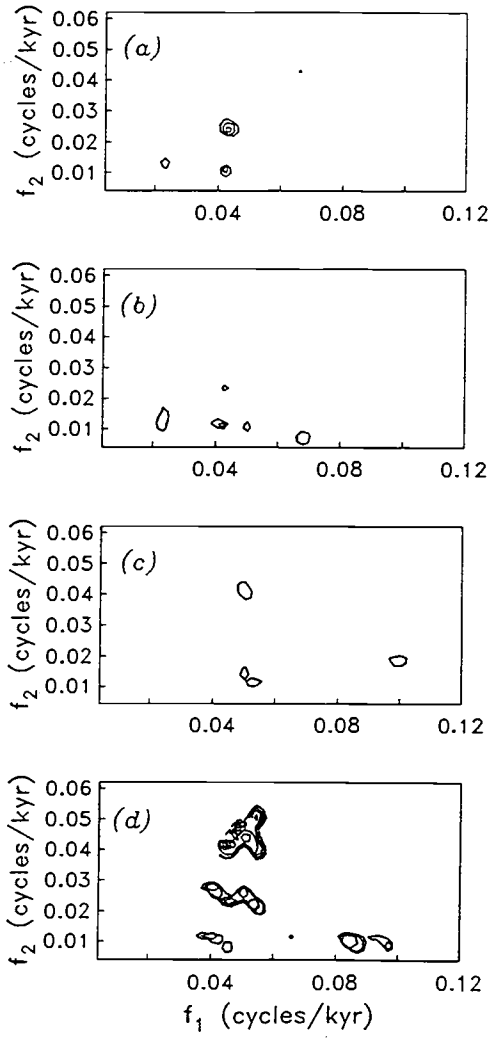

Figure IV.11. Contours of bicoherence, for the interval from 1.0 to 0 Ma. The data were processed as described in the caption to Figure IV.8a. The minimum bicoherence value contoured (significant at a 80% level) is 0.73 with a contour interval of 0.05: (a) site 677 planktic $\delta^{18}O$, (b) site 677 benthic $\delta^{18}O$, (c) site 607 benthic $\delta^{18}O$, and (d) 65°N insolation.

benthic record). This phase coupling, also present in the insolation forcing, indicates that oscillations at periods of 23 kyr and 41 kyr are coupled to oscillations at 15 kyr. Finally, statistically significant phase coupling is present between 41, 100, and 30 kyr oscillations ($b(0.023, 0.012) = 0.723$ in the planktic record and $b(0.023, 0.012) = 0.772$ in the benthic record). This last interaction is not present in the insolation forcing and could represent part of a nonlinear response in the climate system.

The bispectrum for site 607 is different than that for site 677 from 1.0 to 0 Ma. Statistically significant phase coupling occurs among two triads of frequencies, (0.051, 0.016, 0.067) and (0.051, 0.043, 0.094), with bicoherences of 0.520 and 0.766, respectively. While the latter triad is also present in the insolation bispectrum, this phase coupling involves higher frequencies that are close to the Nyquist frequency for this time series. With this time series, it is particularly notable that no significant phase coupling occurs with oscillations at 41 kyr or 100 kyr, as in the site 677 records. For instance, while power spectral peaks are present at 100, 41, and 15 kyr in the site 607 data, the bicoherence for this triad is not significant at a 0.80 level. In the site 677 data, on the other hand, the bicoherence for this triad is statistically significant. While the cause of this discrepancy between Atlantic and Pacific $\delta^{18}O$ data sets warrants further study, the low bicoherences in the site 607 data may be an artifact of the low degrees of freedom.

At site 677, evidence for a nonlinear response of the climate system to orbital forcing is given by high bicoherence in the (0.023, 0.012, 0.035) triad. However, the results at site 677 are also noteworthy because of the similarity of the phase couplings in the climate response to those in the orbital forcing. The phase coupled oscillations present in $\delta^{18}O$ time series from this site includes several of the same modes that are coupled in the forcing. This is consistent with a linear response of the climate system to insolation forcing. Changes in the phase relationships between each mode occur, however, because the biphases for every coupled triad in the data are close to -90°, whereas in the insolation record the corresponding biphases are near 0°.

As with the radiation time series above, simulations with synthetic time series can be used to reinforce these results. Synthetic time series were generated for the site 677 and site 607 $\delta^{18}O$ data over the 1.0 to 0 Ma time interval. The amplitude spectrum of each time series was preserved, but the observed phases were replaced with random phases. For each record, 10 simulations were made, and the bispectrum calculated for each. At site 677, although some significant bicoherences occurred in the planktic data (through random chance, expected at an 80% level), no simulation showed significant bicoherence at the same sets of triads that are coupled in the insolation forcing. For the site 677 benthic data, bicoherences from only one in 10 simulations resemble those in the insolation data. At site 607, significant bicoherences similar to the data occur in two simulations, consistent with an 80% significance level. These results add strength to the argument that despite the low degrees of freedom of these records, the couplings observed in the data are indeed significant and are not likely to be caused by random fluctuations.

Bicoherences for the site 677 and 607 $\delta^{18}O$ time series for the interval from 2.6 to 1.0 Ma are shown in Figure IV.12. Bicoherences from the site 677 planktic $\delta^{18}O$ data show one region of statistically significant ($1-\alpha = 0.80$) phase coupling that is similar to the insolation forcing (the triad consisting of oscillations at 19, 41, and 12 kyr has b=0.662). This same phase coupling is present in the site 677 benthic $\delta^{18}O$, where b=0.603. In the benthic 677 data, two other triads have significant bicoherences that are not similar to coupled modes in the insolation forcing, $b(0.047, 0.016) = 0.620$ and $b(0.078, 0.027) = 0.606$. At site 607, the only significant phase coupling occurs among high-frequency components ($b(0.055, 0.051) = 0.599$).

Unlike the interval from 1.0 to 0 Ma, the results from the lower Pleistocene and upper Pliocene $\delta^{18}O$ time series do not strongly support a linear response of the paleoclimate record to insolation forcing. Only one coupled triad that is present in the insolation record has high bicoherence in the site 677 records. Orbital frequencies that contain most of the variance in the $\delta^{18}O$ power spectrum for 2.6 to 1.0 Ma do not appear to be as strongly

coupled to insolation as in the 1.0 to 0 Ma interval. Oscillations having a 62-70 kyr period, present in the $\delta^{18}O$ power spectra for 2.6 to 1.0 Ma, are phase coupled to 19 kyr oscillations in the site 677 benthic $\delta^{18}O$ data. As there is no coherence between insolation and $\delta^{18}O$ at this frequency (Figure IV.10), the 62-70 kyr peak may represent a nonlinear (difference interaction) between 15 kyr and 19 kyr. Together, these observations indicate a change in the nature of the climate response between 1.0 to 0 Ma and 2.6 to 1.0 Ma.

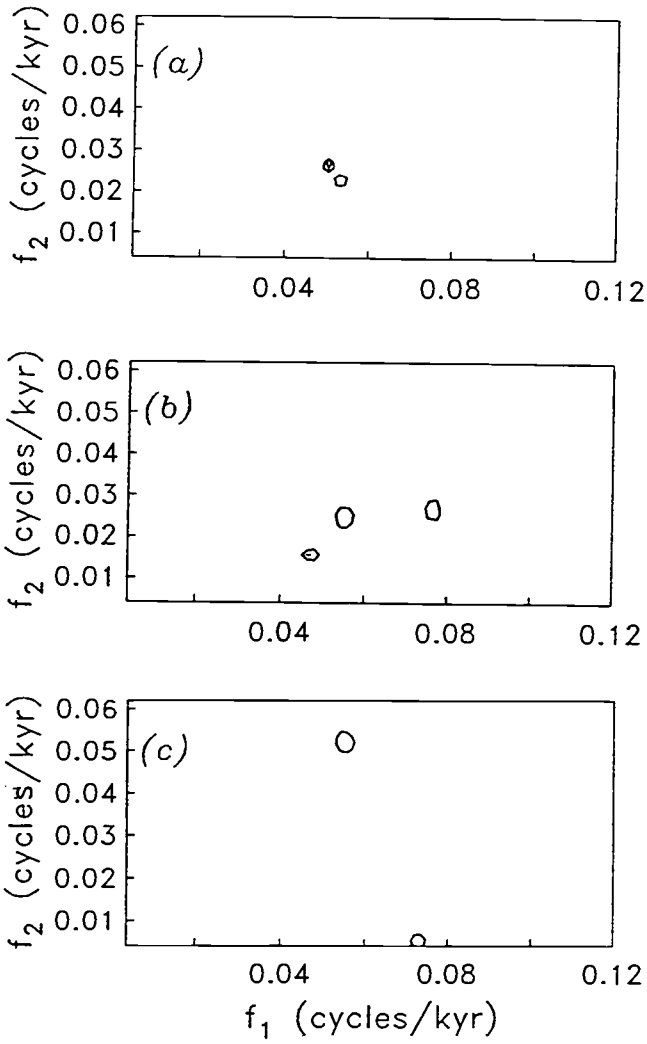

Figure IV.12. Contours of bicoherence, for the interval from 2.6 to 1.0 Ma. The data were processed as described in the caption to Figure IV.8b. The minimum bicoherence value contoured (significant at a 80% level) is 0.57 with a contour interval of 0.05: (a) site 677 planktic $\delta^{18}O$, (b) site 677 benthic $\delta^{18}O$, and (c) site 607 benthic $\delta^{18}O$.

Similar to the results for the 1.0 to 0 Ma interval, numerical simulations with synthetic time series having random phases suggest that the observed bicoherences (Figure IV.12) were not caused by random fluctuations. At site 677 for both planktic and benthic $\delta^{18}O$ data, bicoherences of the simulated, random phase records were similar to bicoherences of the data in only 2 of 10 simulations. At site 607, only one simulation had phase coupling similar to that observed in the data. In no case did the significant bicoherences resemble those of the insolation data. Thus, as in the 1.0 to 0 Ma interval, these simulations add supporting evidence that the phase couplings suggested by bispectral analysis are not due to random fluctuations.

In summary, bispectral estimates for site 677 $\delta^{18}O$ data indicate that from 1.0 to 0 Ma, phase couplings similar to those present in the insolation time series occur. This is consistent with a linear response to insolation forcing. This result is not seen in the 1.0 to 0 Ma benthic $\delta^{18}O$ time series from site 607, however. From 2.6 to 1.0 Ma, evidence for a linear response of the $\delta^{18}O$ record is not as strong at either location. Although all of the time series have very low numbers of degrees of freedom, and correspondingly high nonzero significance levels, Monte Carlo simulations suggest that the significant bicoherences observed are not caused by random fluctuations.

EVOLUTION OF THIRD MOMENTS

As noted above, the "mid-Pleistocene transition" of global $\delta^{18}O$ records from a mainly 41 kyr oscillation in the early Pleistocene to a 100 kyr "sawtooth" shape oscillation in the late Pleistocene is well known. Subsequent models of paleoclimate have sought to reproduce this asymmetric response [Saltzman and Maasch, 1988]. The evolution of skewness and asymmetry (normalized third moments, as defined above) of the site 677 and site 607 $\delta^{18}O$ time series are now examined. These third-moment quantities are related to the shape of the time series (as shown in the example above) and are given by the integrated real and imaginary parts of the bispectrum, respectively [Elgar and Guza, 1985; Elgar, 1987]. The third moments allow the observed long-term evolution of the $\delta^{18}O$ record to be quantified.

The evolution of the skewness and asymmetry of the site 607 and site 677 $\delta^{18}O$ records is shown in Figure IV.13. Skewness and asymmetry are calculated for overlapping 512-point records, that is, from 1.0 to 0 Ma, from 1.5 to 0.5 Ma, from 2.0 to 1.0 Ma, and from 2.5 to 1.5 Ma (because it is 2.8 m.y. long, for site 607 estimates from 2.8 to 1.8 Ma

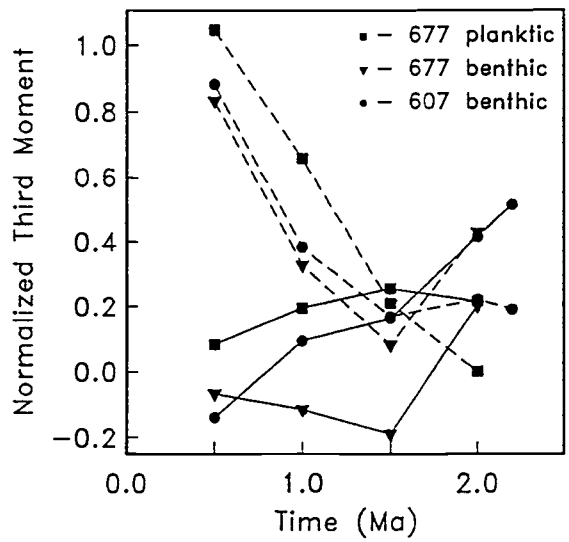

Figure IV.13. Skewness (solid line) and asymmetry (dashed line) of $\delta^{18}O$ records versus time. Each symbol represents a 1 m.y. average and is plotted at the midpoint of the time interval. Squares indicate 677 planktic $\delta^{18}O$; triangles, 677 benthic $\delta^{18}O$; and circles, 607 benthic $\delta^{18}O$.

are included). There is an increase in the asymmetry (sawtoothness) of the time series from 2.5 Ma to present and a simultaneous decrease in the skewness (peakedness) of the record. In the oldest part of the records, there is relatively high skewness which decreases to near zero in the late Pleistocene. Monte Carlo simulations suggest that these third-moment estimates are significantly different from zero. (Recall that for no coupling (a Gaussian time series) the third moments are zero.)

There are large differences between the skewness and asymmetry of the $\delta^{18}O$ records and that of the insolation record (Figure IV.14). The asymmetry of the insolation record is close to zero throughout the past 2.5 m.y., and skewness is only slightly greater than zero. Thus, although the climate system is responding linearly to insolation forcing (at least over the last million years), the nature of the phase coupling within the system is evolving. This observation is consistent with the results of Pisias et al. [1990], who showed evidence for a nonconstant phase between orbital forcing and ice volume over the past 700,000 years.

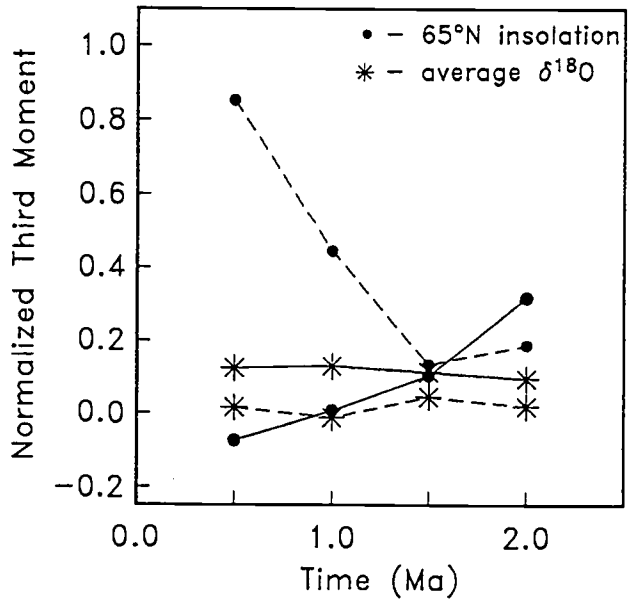

Figure IV.14. Skewness (solid line) and asymmetry (dashed line) of the average of the three $\delta^{18}O$ records presented in Figure IV.13 (circles), and skewness and asymmetry of 65°N insolation (asterisks) versus time.

DISCUSSION

The analyses above demonstrate that the orbital parameters which combine to cause long-term changes in solar insolation are nonlinearly coupled to one another. In particular, the coupling between precession terms of 23 kyr and 19 kyr and the 100 kyr eccentricity parameter is very strong. With respect to this coupling, it is important to note that the strength of the precession-eccentricity coupling in the insolation forcing is related to the presence of the $1/(1-e^2)$ term in the insolation formula used in this study. Only the solution of Berger [1978b] includes this term. Previous insolation solutions have not included it [see Berger, 1978a] because it does not contribute significantly to the overall insolation change (around 0.1%). When this term is removed from the insolation formulae of Berger [1978b], the phase coupling between precession and eccentricity is weaker. Recalling that the only orbital element that can modify the total solar energy received by the Earth is eccentricity (although forcing at 100 kyr is small in comparison with precessional or obliquity forcing), this term is very important, as emphasized by Berger [1978a] and Berger [1989].

The dilemma of whether the 100 kyr peak present in the $\delta^{18}O$ spectrum during the late Pleistocene is a linear response to eccentricity forcing, or a nonlinear response to precession band interactions is now addressed. The insolation data indicate that eccentricity and precession bands are highly coupled in the insolation record. The linear coherence between insolation and $\delta^{18}O$ in the eccentricity band is greater than 0.90, and the same phase couplings are present in the isotopic record. These results suggest that a nonlinear response is not required to explain the observed response. A simple linear resonance model may help to explain the processes leading to the dominance of 100 kyr oscillations in the late Pleistocene ice volume record.

A brief review of resonance demonstrates that the results reported here are consistent with a resonant response to insolation forcing in the 100 kyr band. The simple physical system of a forced oscillator with damping is

$$x = \frac{F}{m(\omega_o^2 - \omega^2 + i\gamma\omega)} \tag{4}$$

where x is the displacement (i.e., response), F is the force driving the oscillator, m is the mass of the oscillator, ω_o is the natural (resonant) frequency of the system, ω is the frequency of the forcing, and γ is the damping force. For the case of zero damping, the magnitude of x is related to the size of the force by the factor $1/(\omega_o^2 - \omega^2)$, and as ω approaches ω_o, this magnitude approaches infinity. In this context, the gain of the system response is

$$\rho^2 = \frac{1}{m^2[(\omega^2 - \omega_o^2)^2 + \gamma^2\omega^2]} \tag{5}$$

The corresponding phase shift of the system response is given by

$$\theta = \arctan\left(-\frac{\gamma\omega}{\omega_o^2 - \omega^2}\right) \tag{6}$$

The gain and phase change of the system response for different values of ω are shown in Figure IV.15.

For any amount of damping (γ), maximum gain occurs where ω equals ω_o. In addition, a phase change of up to 180° occurs as ω changes from $\omega > \omega_o$ to $\omega < \omega_o$. If solar insolation is the forcing, and the climate system response is being measured, then as a small amount of insolation is applied to this system at $\omega = 0.01$, the climate system response becomes greatly amplified because of the proximity of ω to ω_o, the natural resonant frequency of the climate system.

The gain of the 100 kyr band in the insolation - $\delta^{18}O$ cross spectra is about an order of magnitude higher than the gain in the 41 kyr band, and about 2 orders of magnitude higher than the gain in the 23, or 19 kyr bands (Figure IV.15 and Table IV.1). In addition, the phase

spectra (Figures IV.9a and IV.16) show evidence for a shift which corresponds to that predicted by linear resonance. Note, however, that in this study July 65°N insolation values are used, and the phase of the response in the precession band depends on the particular month chosen. The small amount of eccentricity forcing at 100 kyr (approximately 0.1% of the total variance in the insolation and approximately 3 orders of magnitude less than the variance of precessional forcing) may occur at or near a resonant frequency in the climatic

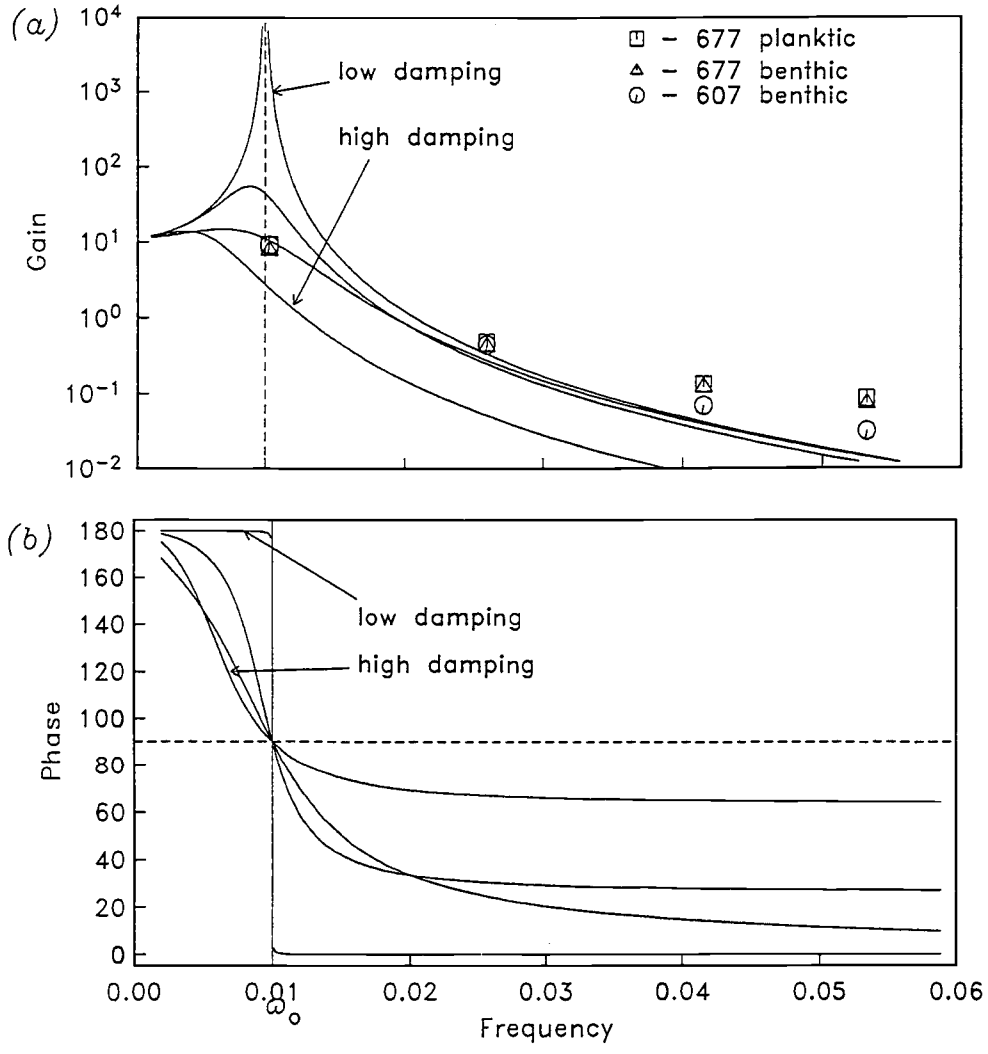

Figure IV.15. (a): Gain versus frequency for the resonance model described in the text (equation (4)). Solid curves indicate the gain of the system response for different values of damping, γ. The vertical dashed line at ω_o represents the resonant frequency of the system. Symbols plotted are the estimated gain of $\delta^{18}O$ from Table IV.1. Squares indicate 677 planktic $\delta^{18}O$; triangles, 677 benthic $\delta^{18}O$; and circles, 607 benthic $\delta^{18}O$. (b): Phase versus frequency for the resonance model described in the text (equation (4)).

system, and the large amplitude response observed in the $\delta^{18}O$ record results from this resonance. The absence of such a resonant response in the late Pliocene and lower Pleistocene may signify a changing resonant frequency as the climate system evolves.

Linear resonance is a straightforward method of accounting for the observed climate response of the past 1 m.y. As noted in the Introduction, paleoclimate models have explored a variety of mechanisms accounting for this climatic response. The observations presented here support the results of Saltzman and Sutera [1984] and Saltzman et al. [1984] that imply an inherently sensitive climate system at the 100 kyr period during the late Pleistocene. The observations also supports Berger's [1989] statement that the influence of eccentricity forcing alone is very important. While it is likely that a range of mechanisms, both linear and nonlinear, are acting to produce the observed climate response, the data presented here are consistent with a resonant response. Models which simulate climatic changes must be consistent with these observations.

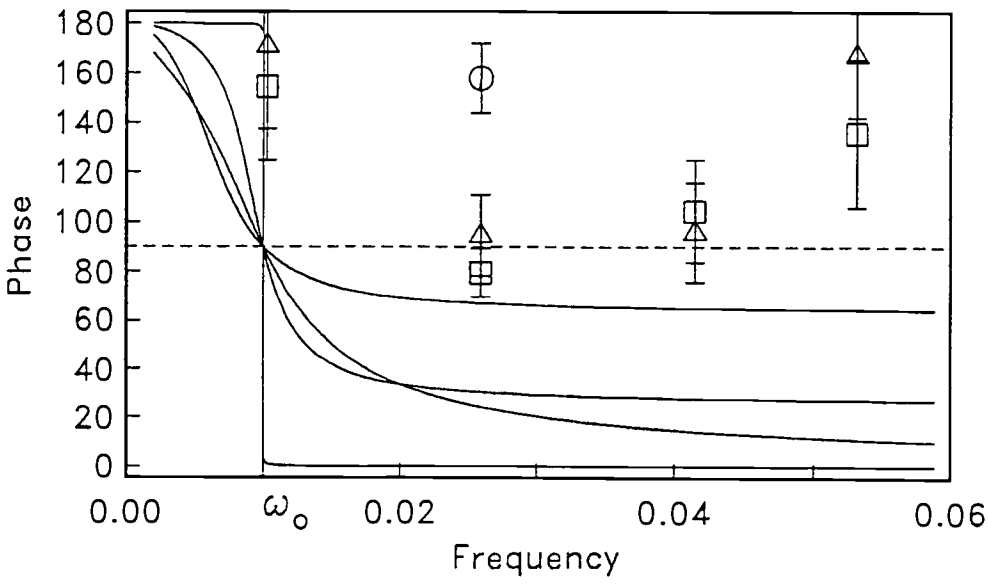

Figure IV.16. Phase shift versus frequency for the resonance model described in the text (equation (4) and Figure IV.15b), compared to $\delta^{18}O$ phase from Table IV.1. The model phases have been shifted by 65° to allow comparison of the model to the data. Symbols plotted are the estimated phase of $\delta^{18}O$ from Table IV.1. Squares indicate 677 planktic $\delta^{18}O$; triangles, 677 benthic $\delta^{18}O$; and circles, 607 benthic $\delta^{18}O$. Vertical bars indicate 90% confidence intervals for the phase estimates.

This analysis has also demonstrated differences between the climatic response in the late Pleistocene, which may be primarily a linear response to insolation forcing, and the early Pleistocene/Pliocene, which may include a nonlinear response. The observations, including the evolution of third moments, suggest there is an evolution in the climatic response.

Finally, it is necessary to consider these results in light of some important assumptions that have been made to carry out the above analysis. It has been assumed that a correct time scale has been used. While it is known that different time scales will produce different results, it is unknown how sensitive bispectral estimates are to errors in the time scale. It has also been assumed that the above results are not an artifact of the particular orbital tuning strategy used by Shackleton et al. [1990]. This important issue is left to a separate study.

CONCLUSIONS

Bispectral analysis was used to detect nonlinear phase couplings in the time series of long-term solar insolation. Orbital eccentricity and precession are highly nonlinearly coupled, as are precession and obliquity. The quadratic phase couplings present in the insolation forcing have been compared to phase couplings in the climatic time series of $\delta^{18}O$, a global ice volume proxy. Power spectra, cross spectra, and third moments (skewness and asymmetry) of the data suggest an evolution in the climate system response from late Pliocene to late Pleistocene. Quantitative estimates of this evolution are seen in increasing asymmetry (sawtoothness) and decreasing skewness (peakedness) from 2.6 to 0 Ma at site 677 and site 607. From 2.6 to 1.0 Ma, the same phase couplings that are observed in the insolation record are not observed in the oxygen isotope records. From 1 to 0 Ma, benthic and planktic $\delta^{18}O$ from ODP site 677 contain the same significant bicoherences as the orbital time series. The observed bicoherences, combined with high linear coherence between orbital forcing and climatic response at orbital frequencies during this time period, indicate that most of the climatic ($\delta^{18}O$) response to insolation forcing is linear, including the response at 100 kyr. The 100 kyr peak in the $\delta^{18}O$ spectra shown here is consistent with a linear, resonant response of the climate system to direct eccentricity forcing.

CHAPTER FIVE

IMPLICATIONS OF VARIABILITY IN SAMPLING AND TIME SCALE FOR HIGH RESOLUTION PALEOCEANOGRAPHIC STUDIES

ABSTRACT

The choice of time scale is possibly the most important aspect of any high resolution paleoceanographic time series study. This makes the issue of timescale variability and its implications for paleoceanographic studies a fundamental concern. However, the effects of time scale error have only rarely been rigorously approached. In addition, the effects of time scale and data errors on cross spectral estimates have not been considered in a marine geological context. In this study the effects of small scale and large scale age model variability and amplitude variability in the time series on coherence and bicoherence estimates is explored using a Monte-Carlo approach. In addition, the applicability of a proposed test for time scale "jitter" or variability that makes use of the statistical properties of the bispectrum is investigated.

INTRODUCTION AND BACKGROUND

The study of Hays et al. (1976) was the first successful use of spectral analyses to provide confirmation of the Milankovitch hypothesis. Three different paleoclimatic records (ice volume proxy, sea surface temperature proxy, and upwelling proxy) were demonstrated to have variance concentrated at 19,000 23,000 41,000 and 100,000 years. In making this demonstration the authors also tested the robustness of different chronologies. The three chronologies had increasing orders of complexity, the simplest having only 2 age control points with linear interpolation between, the most complex having age adjustments made based on the phase relationship between data and orbital obliquity. Monte Carlo tests by the authors suggested that achieving the constant phase relationship by chance was unlikely (Hays, et al., 1976). Kominz and Pisias (1979) and Kominz et al. (1979) applied cross-spectral analyses to a Pacific $\delta^{18}O$ record using an extension of the "TUNE-UP" chronology of Hays, et al. (1976). Their study confirmed that orbital changes are coherent with ice volume changes at 19,000 years, 23,000 years and 41,000 years.

The age model used by Kominz et al. (1979) was developed by assuming that the phase between orbital obliquity, having an approximately 41,000 year period, and ice volume ($\delta^{18}O$) has remained constant over that last 800,000 years. A bandpass filtered record of the geological record was compared to orbital obliquity, and adjustments were made to achieve a constant phase. Complex demodulation was also used to confirm the phase constancy. This is known as "orbital tuning". Since any two bandpass filtered records will obviously contain the same frequency components, the circularity of this approach was questioned. This and the assumptions used in orbital tuning were tested by Pisias (1983). Using a Monte-Carlo approach, it was demonstrated that the concentration of variance observed in the $\delta^{18}O$ record at 41,000 years that is coherent with obliquity was not likely to be artificially induced from a random time series having similar statistical properties. The validity of the orbital tuning approach was also confirmed in the observation that oscillations in the $\delta^{18}O$ data matching the orbital precessional periods of 23,000 and

19,000 years were not used in timescale calibration, yet these oscillations are highly coherent after tuning to 41,000 years. The simulations indicated that this is also unlikely to occur through random chance. The numerical experiments suggested that the strong linear relationship observed between ice volume and orbits could be used to improve late Pleistocene chronologies.

From this point on, few if any numerical tests of orbital tuning sensitivity were made, yet orbital tuning assumed a major role in paleoceanography. The SPECMAP group adopted the strategy of using the time series of astronomical changes (Berger, 1978, Berger and Loutre, 1988) as a timescale calibration tool in order to document phase relationships between several geological variables over all of the oceans (e.g. Martinson, et al., 1987). The concept of a metronome was introduced to suggest high coherence and constant phase between ice volume ($\delta^{18}O$) and insolation as an indicator of time scale fit. After calibrating in this manner, the phase relationships of oceanographic variables can be measured. Pisias et al. (1990) used complex demodulation to reexamine the assumption of constant phase between ice volume and orbital variations during the late Pleistocene, and determined that a time varying phase is actually present. A similar phase evolution was documented using higher order statistics by Hagelberg et al. (1991).

Regardless, the calibration of geological timescales through orbital tuning has revolutionized chronostratigraphy during the past decade. Examples of applications to late Pleistocene studies have become too numerous to list. Although only tested in the late Pleistocene, orbital tuning and the assumptions of a linear climate-orbit relationship have been extended into the Pliocene (Pisias and Moore, 1981; Raymo et al., 1989, Hagelberg and Pisias, 1990; Shackleton et al., 1990; Shackleton et al., 1993) and Miocene (Hilgen et al., 1992; Shackleton et al., 1993). Orbital tuning has also been used as a calibration tool for Cretaceous and older geological sections (e.g. Herbert and Fischer, 1987; Herbert and D'Hondt, 1990; Park and D'Hondt, 1992). This time scale calibration approach has been extended so far as to have become the basis for adjustment of radiometrically-dated datums,

and has even become a basis for adjustments in radiometric decay constants (Shackleton, et al., 1990). Further adjustments to geochronology based on agreement of tuned paleoclimatic records with reversals is likely as evidenced by a 1992 AGU session dedicated to reconciling paleomagnetic and orbitally calibrated chronologies.

Despite the widespread use of orbital tuning approaches, it is still not well understood how robust coherence between orbital changes and paleoclimatic records is to errors in time scale. Since coherence and phase are a basis for evaluating chronologic adjustments, this is an important issue which has bearing on the validity of the approach. Martinson et al. (1987) addressed the use of several different approaches to orbital tuning, and in doing so they examined the validity of assumptions involved in orbital tuning. The issue of robustness to age model error was not addressed, however. This study seeks to understand the impact of age model error on coherence estimates as well as higher order coherence estimates.

Noise in the observations of a time series is another issue which has not been rigorously addressed in a paleoceanographic context. There is considerable interest in this issue because of recent advances in using proxy tools to estimate geological and geochemical variables. An example is the use of wet bulk density measurements as a predictor for sedimentary calcite in equatorial oceans (e.g. Mayer, 1991, Herbert and Mayer, 1992, Hagelberg et al., 1993). Another example is the use of sedimentary magnetic susceptibility as an indicator of terrigenous flux in the Arabian Sea (deMenocal et al., 1991). The advantage to having predictive tools is that rapid, high resolution estimates of geochemical processes are available, which might not be feasible to produce in a laboratory with a reasonable amount of time or money. Concern over the accuracy of prediction has led some to discount this approach. However, this may be premature given that the effects of analytic noise in spectral and cross-spectral investigations of the paleoclimatic processes are not well defined. Short record length and age model variability may be much more limiting than amplitude error in the time series.

The concern regarding errors in proxy estimates also applies to the precision of isotopic measurements of $\delta^{18}O$. Considerable attention is given to the influence of vital effects of some foraminifer species on isotopic measurements, which is important for paleoenvironmental interpretations, but the extent to which this source of isotopic variability affects frequency domain results has not been addressed. Thus, it is useful to examine the sensitivity of coherence and higher order spectral estimates to amplitude noise in a sampled paleoceanographic time series.

Higher order spectral estimates, notably bispectral estimates, a third moment estimate, are a means of resolving quadratically nonlinear couplings in time series data. These methods were applied to geologic time series to investigate the extent of nonlinear interactions in the paleoclimatic record (Hagelberg et al., 1991). Using the age model of Shackleton et al. (1990), which has been orbitally tuned to insolation, significant quadratic phase couplings were detected in 1 myr records of benthic and planktic $\delta^{18}O$ from ODP Site 677 in the equatorial Pacific. With the exception of one statistically significant phase coupling between oscillations at 100 kyr, 41 kyr, and 30 kyr, the significant phase couplings present in the ice volume proxy record are also present in the insolation record. This result suggested that the phase couplings in the 677 $\delta^{18}O$ records do not necessarily result from nonlinear interactions in climate, but rather could be consistent with a linear response to the nonlinear insolation forcing. Similar phase couplings were not observed in the benthic $\delta^{18}O$ record from DSDP Site 607 in the North Atlantic. This raised the question whether the differences between 677 and 607 are related to true changes in the response of the isotopic records, indicating oceanic differences, or only to sensitivity of bispectral estimates to different levels of noise.

The strength of quadratic phase couplings is measured by bicoherence, a quantity analogous to coherence (Kim and Powers, 1979). Like coherence, squared bicoherence indicates the fraction of power at frequency $f_j + f_k = f_{j+k}$ which is due to quadratically nonlinear interactions between three oscillations at f_j, f_k, and f_{j+k}. Little is known about the

robustness of bicoherence estimates to variability in both the amplitudes of the observed time series and the age model, particularly given the short record lengths of paleoceanographic time series. If the observation of significant bicoherence is robust to age model noise, then it is likely that phase couplings are detectable under a variety of age model distortions. On the other hand, if bicoherence estimates are highly sensitive to time scale variability, then detection of any statistically significant bicoherences in geologic time series is likely to indicate not only nonlinear interactions, but also low age model noise.

Variance of bispectral estimates are higher than the variance of cross-spectral estimates. In theory, variance of coherence and bicoherence estimates are similar. Hinich and Clay (1968) and Kim and Powers (1979) determined that variance of bicoherence estimates have the same form as variance of coherence estimates, being linearly proportional to $(1-b^2)^2$, where b is the true bicoherence. However, Elgar and Sebert (1989) determined empirically that variance of squared bicoherence estimates are proportional to $b^2(1-b^2)^3$ as compared to variance of squared coherence estimates which are proportional to $\text{coh}^2(1-\text{coh}^2)^2$, and thus, bicoherence estimates have higher variance. This has led some to discount its applicability altogether, especially for short records. Thomson (1989) noted that "these problems are more serious when only a short data record is available and is exacerbated if the spectrum has a large dynamic range or has a complicated frequency dependence....these effects, combined with a dearth of robust estimators for bispectra, may be responsible for the poor reputation of bispectra". This prompted Thomson (1989) to propose alternative approaches to bispectral analysis which may provide more consistent estimates. Thus it is likely that bicoherence estimates are much more sensitive to age model noise and amplitude noise than coherence estimates. It is necessary to understand this sensitivity if bispectra are to be a reliable tool for discriminating quadratically nonlinear interactions from paleoclimatic time series. This has bearing not only on the study of Hagelberg et al. (1991), but for paleoclimatic studies on the millennial scale (e.g. G. Bond et al, in prep) and in Cretaceous records (e.g., Park and d'Hondt, 1992).

The first phase of this study examines the issues of time scale error and measurement errors in amplitudes using both observed data and synthetic time series. A Monte-Carlo approach is taken. Two paleoclimatic time series are used as the basis for the simulations. The first is the time series of planktic $\delta^{18}O$ from ODP Site 677 (Shackleton et al., 1990), a well studied record which is broadly taken to indicate global ice volume variability. As described above, the upper 1 myr of this time series has significant phase couplings, and also high coherence with orbital insolation (Hagelberg, et al., 1991; Figure 1). The second time series represents the bulk of variability in eastern equatorial Pacific carbonate sedimentation (the first EOF of $\%CaCO_3$ from Hagelberg et al., 1993). The upper 1 myr of this time series is studied. Like the Site 677 $\delta^{18}O$, this record has high coherence with insolation in the Milankovitch band (Figure V.1). Statistically significant phase couplings in the EOF-1 time series are at two of the same triads as the $\delta^{18}O$ time series, (100, 41, 30) kyr and (41, 23, 15) kyr, and at (62, 19, 14) kyr (Figure V.1). Only the (41, 23, 15) kyr triad is also present in the insolation forcing.

The second phase of the present study involves the examination of a proposed application of the bispectrum, a test for time series jitter. It has been proposed in statistical (Hinich and Wolinsky, 1988) and signal processing literature (Sharfer and Messer, in press) that the mathematical properties of the bispectrum can be used to test a time series for aliasing or for time scale jitter. In the signal processing context, "jitter" refers to variability in the sampling clock of measurements of a process. If a bandlimited (unaliased) time series has variability in the "sampling clock" or jitter, and if that time series has a nonzero bispectrum, then a subset of the principal domain of the bispectrum (described below) will have nonzero values. On the other hand, if the time series does not have clock jitter, the bispectrum the same region will be zero. The proposed test has not yet been applied to any geophysical time series to detect jitter. If this test is applicable to the problem of age model and time scale variability in geologic time series, it may provide a powerful and objective means of evaluating and possibly constraining age models. If applicable, such a test has

applications outside of the "Milankovitch band" of paleoclimate research. It may prove to be more important in time intervals where less is known about the forcing mechanism (eg century-millennial scale climate variability). The records described above are used to examine the applicability of the test to paleoclimatic records. In addition, synthetic records having prescribed bicoherences and age model jitter are used to evaluate the usefulness of the test under the constraint of short record length encountered in paleoceanographic time series.

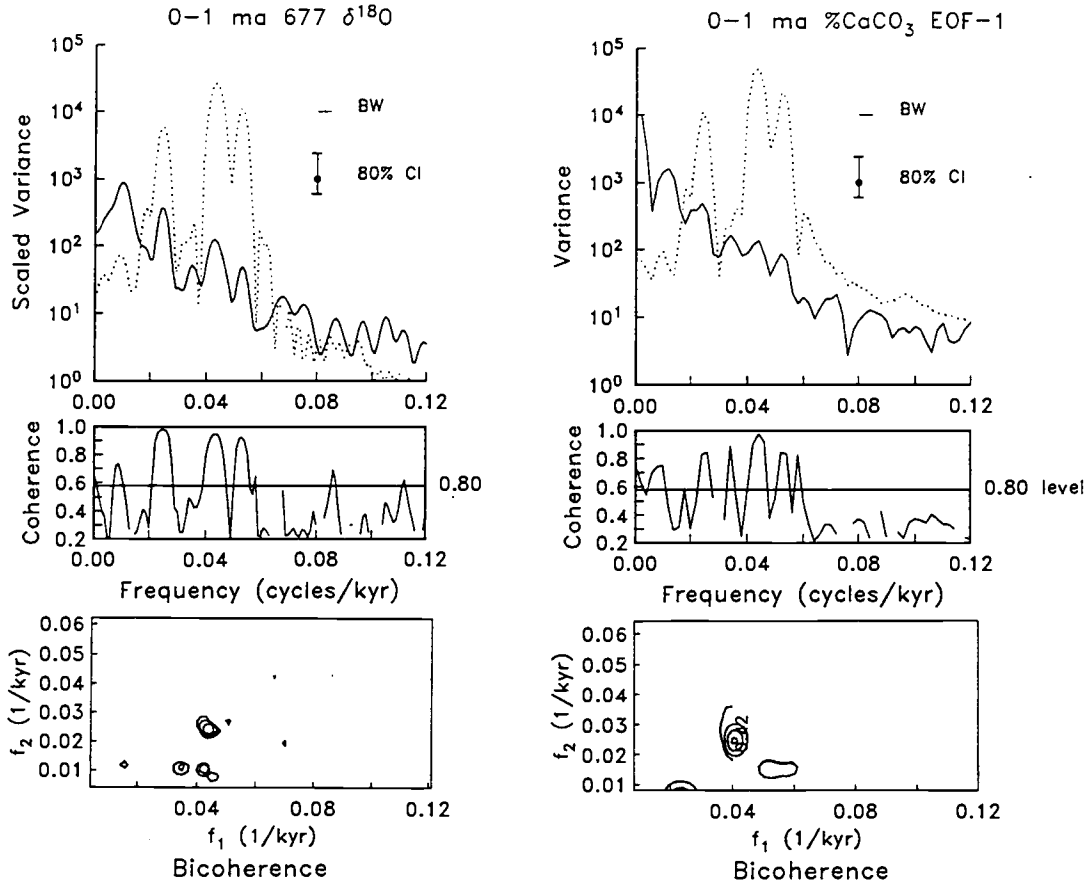

Figure V.1. Left: Power spectra (top), coherence spectra (middle), and bicoherence (bottom) for the site 677 planktic $\delta^{18}O$ time series. Right: power spectra, coherence spectra, and bicoherence for $\%CaCO_3$ EOF-1 time series. Power and cross spectral estimates were made using the Blackman-Tukey truncated lag auto (or cross) covariance method, using 137 lags of the 512 point record for 10 degrees of freedom in the $\delta^{18}O$ data and 268 lags of the 1000 point record for 10 degrees of freedom in the EOF-1 record. The horizontal line in the middle panel indicates the .80 level for significant coherence. Contours of bicoherence significant at a .80 level are given in the lower panel.

The Bispectrum as a Test for Time Scale Jitter

Where the power spectrum of a real valued time series has two-fold symmetry, the bispectrum, a higher order spectral estimate, has 8 fold symmetry. The lines of symmetry, given in Figure V.2 (A) are: $f = 0$, $g = 0$, $f = g$, $f = -2g$, $f = -g/2$, and $f = -g$ (Hinich and Wolinsky, 1988). For a signal sampled at the rate $1/\Delta t$, for example, an infinite set of parallel symmetry lines are introduced at intervals of $1/2\Delta t$ (the Nyquist frequency), at $2f + g = 2/\Delta t$ and $f + 2g = 2/\Delta t$. Thus the principal domain of the sampled bispectrum becomes the triangle $\{f,g: 0 \leq f \leq 1/2\Delta t, g \leq f, f + g/2 = 1/2\Delta t\}$ (Figure V.1). If the time series under study is stationary, bandlimited, and unjittered, the principal domain reduces to $\{f,g: 0 \leq f \leq 1/2\Delta t, g \leq f, 0 \leq f + g \leq 1/2\Delta t\}$. In most applications of bispectral analysis to detect quadratically phase coupled interactions in time series data, it is only necessary to calculate the bispectrum over this subset of the principal domain, which is referred to as the "Inner Triangle" (IT). Although only a subset of the principle domain of the bispectrum, this region is commonly mistaken to be the principal domain (Hinich and Wolinsky, 1988).

A second subset of the principal domain is known as the "Odd Triangle" (OT; Figure V.2) which consists of $\{f,g: g \leq f, 1/2\Delta t \leq f + g \leq 1/\Delta t - f\}$. This region is typically not considered because for a band limited signal the sum frequency in this region is greater

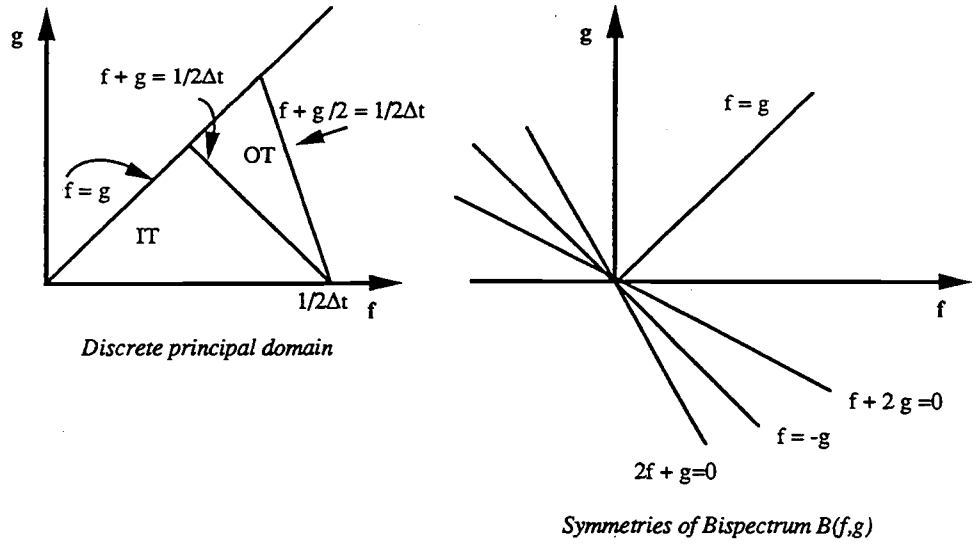

Figure V.2. The principal domain of the bispectrum

than the Nyquist frequency. If the time series being observed is bandlimited (i.e. has no aliasing) and is sampled at constant time steps (i.e. no time scale jitter), then in theory the Odd Triangle region of the bispectrum is zero even if the IT region contains significant phase couplings. However, Hinich and Wolinsky (1988) showed that if an aliased time series having a nonzero bispectrum is examined, the bispectrum in OT contains statistically significant phase couplings. This is because of the folding frequencies of the aliased energy. With power spectral estimates, variance in a sampled time series generated at frequencies higher than the Nyquist fold into the spectrum, and cannot be distinguished from lower frequencies. In the bispectrum, however, the folding is more complex, and involves phase coupling among a triad of frequencies. Sharfer and Messer (in press) extended this property to note that if a time series is not aliased, then a nonzero bispectrum in OT indicates that the sampled process has a non constant sampling interval, and thus time scale jitter.

Both of the above studies proposed a test statistic to determine if an observed sampled time series has been alternatively jittered OR aliased. Like the coherence spectrum in second order spectral analysis, any finite length time series will have a nonzero bispectrum. Thus a means of discriminating statistically significant phase coupling in OT from random, nonzero phase couplings in OT is necessary. The tests proposed by Hinich and Wolinsky (1988) and Sharfer and Messer (in press) are essentially identical. The hypothesis test is as follows:

$$H_o: 2|b(f,g)|^2 = 0 \quad (f,g) \in OT \Rightarrow \text{ no jitter} \qquad (1)$$
$$H_1: 2|b(f,g)|^2 \neq 0 \quad (f,g) \in OT \Rightarrow \text{ jitter}$$

where b*(f,g)* is the smoothed bicoherence (the normalized magnitude of the bispectrum) using the Haubrich normalization (Haubrich, 1965). Under the null hypothesis that there is no time scale jitter, the large sample distribution of $2|\,b(f,g)\,|^2$ is central χ^2 with 2 degrees of freedom. Hinich and Wolinsky (1988) and Sharfer and Messer (in press) sum the χ^2 statistics over all bifrequencies in OT for a test statistic T_c which is central χ^2_{2K} under the

null hypothesis, where K is the number of bifrequencies in the smoothed OT. If the sampled time series does not follow the null hypothesis, T_c has a distribution that is approximately noncentral χ^2_{2K} with a positive noncentrality parameter. For a significance level α, if the test statistic calculated over OT exceeds $\chi^2(\alpha, 2K)$, then the null hypothesis can be rejected.

The performance of this test is unclear. Hinich and Wolinsky (1988) only report that their test is robust for records having as few as 256 observations, and thus is applicable to stock records which may be aliased. Sharfer and Messer (in press) analyze the probability of jitter detection for a flat nonzero bispectrum as a function of signal skewness (3rd moment) and record length, and suggest that even for high signal skewness, very long record lengths are required. These authors also summarized the probability of jitter detection (again, for a flat bispectrum) as a function of jitter variance and signal skewness. For a record length of 10,000, performance was determined to depend linearly on signal skewness and on the square of the jitter variance. Sharfer and Messer (in press) develop a condition for high detection probability which is

$$\rho = \frac{T_c}{2\sqrt{2K + T_c}} > 2 \qquad (2)$$

Despite the theoretical development, there are no examples of the performance of this test with respect to time jitter, not even with synthetic time series. Furthermore, all of the theoretical development for the time jitter test was based on the existence of a flat, (e.g. white) bispectrum, as opposed to a bispectrum having a more complex shape. Thus, it is necessary to determine if this test is applicable to paleoceanographic data sets.

METHODS

In the first phase of this study, two paleoceanographic time series are used as models for the simulated records. As described above, the two time series are the planktic $\delta^{18}O$ record from ODP Site 677 (hereafter referred to simply as $\delta^{18}O$) and the first EOF of carbonate concentration in the eastern equatorial Pacific over the past 1 ma (hereafter referred to simply as EOF-1). The $\delta^{18}O$ record is 1.024 million years long and has a 2000 year sampling interval, for a 512 point record. EOF-1 is a 1.0 million year sampled at 1000 year intervals.

For each time series, three experiments were performed: The first experiment for each record involved addition of noise to the amplitudes of the observations in order to understand the effects of amplitude noise on coherence and bicoherence estimates. The second and third experiments involved the addition of noise to the age models rather than the time series observations. Noise was added to the relatively tightly constrained age models for δ18O and for EOF-1 in the second experiment. In the third experiment, noise was added to "relaxed" age models having fewer age control points. In all three experiements the effects of noise addition on coherence and bicoherence estimates were evaluated. 100 realizations were generated at incremental noise levels. "Noise" in this context and through the remainder of the paper refers to uniformly distributed (-1,1) random variables which are by definition equally distributed over frequency ("white" noise). Coherence estimates indicate coherence between orbital insolation time series (given by Berger and Loutre, 1988) and the simulations.

The noise added in the first experiment is expressed as a percentage of the original time series variance. For example, addition of 10% noise means that variance of the simulated time series has variance equal to the original variance + 10%; likewise, 100% variance means that the variance of the simulated time series has variance equal to twice the original variance. Realizations were generated for the amplitude experiment simply by adding to each single observation a random variable chosen from a uniform distribution

which was scaled to the appropriate level of variance. Results from adding the noise in this manner are no different than adding the noise in the frequency domain. Note that this experiment does not seek to address the "true" noise which may already be present in the time series; this is not necessary for the purpose of this study which is to determine robustness to increasing levels of noise.

Uniformly distributed noise was added to the $\delta^{18}O$ and EOF-1 time series in increments of 10%, 20%, 50%, 100%, 200%, and 500% of the original time series variance. 100 realizations were calculated at each variance increment. Example realizations of 10% - 500% noise as scaled to the variance of the Site 677 planktic $\delta^{18}O$ time series (variance = 0.216) are given in Figure V.3 with the corresponding power spectrum. The spectra demonstrate that variance is equally distributed over frequency. Figure V.4 shows one realization at each variance increment of the $\delta^{18}O$ + noise time series and the corresponding power spectrum. Power spectral and cross spectral estimates were made using the same

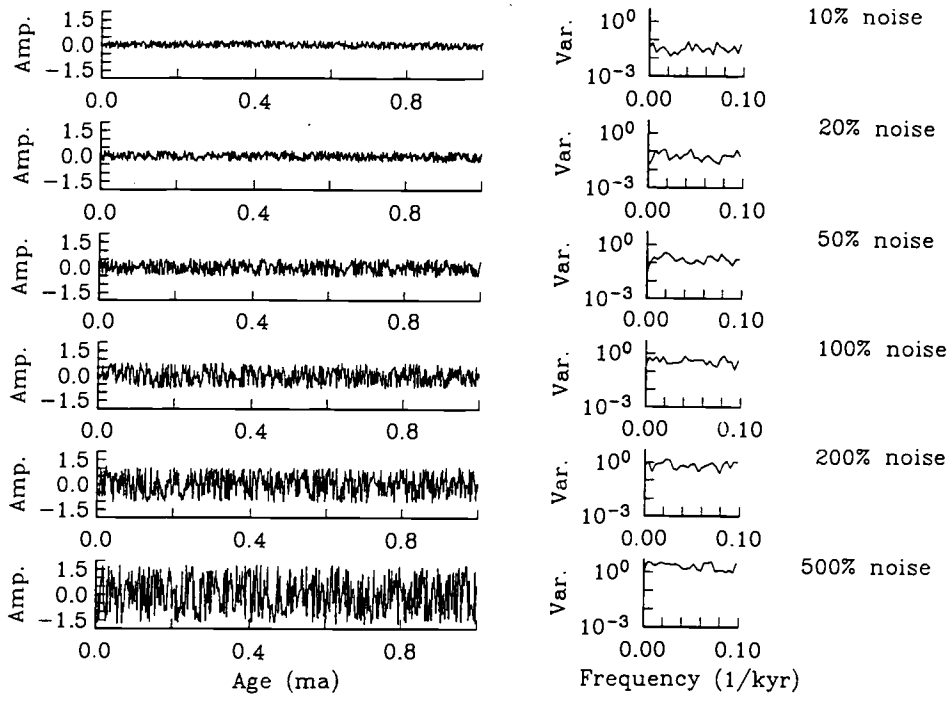

Figure V.3. Individual realizations of the incremental steps of uniformly distributed noise added to the Site 677 planktic $\delta^{18}O$ time series. Left: Time series; Right: power spectra. Power spectral estimates are as described in the caption to Figure V.1.

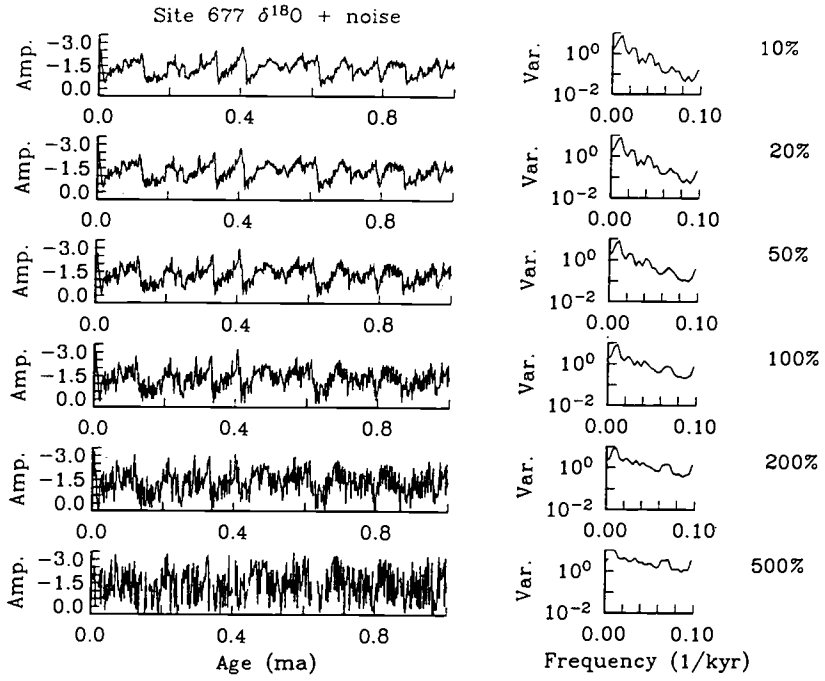

Figure V.4. Individual realizations of Site 677 planktic $\delta^{18}O$ plus incremental noise. Left: Time series; Right: power spectra. Power spectral estimates are as described in Figure V.1.

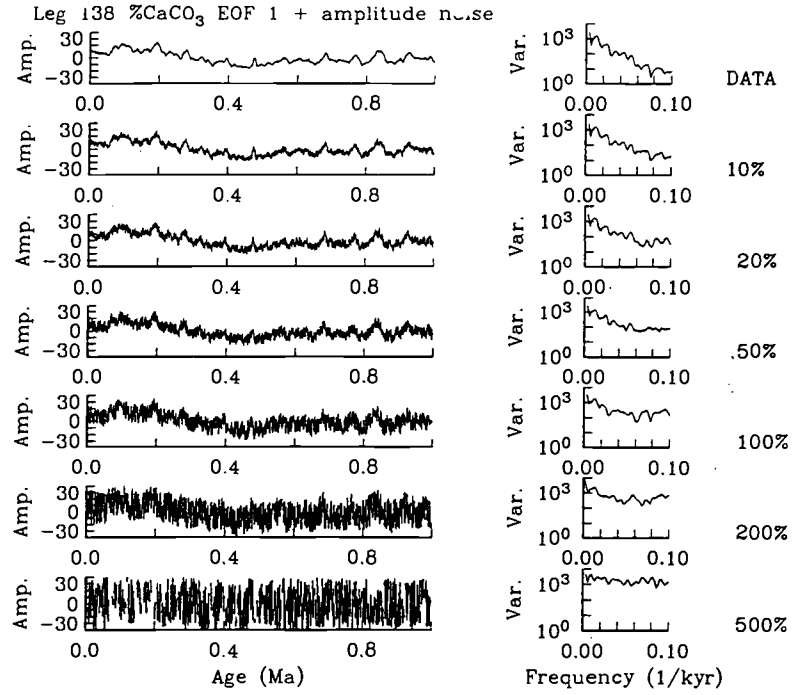

Figure V.5. Individual realizations of Leg 138 $\%CaCO_3$ EOF-1 plus incremental noise. Left: Time series; Right: power spectra. Power spectral estimates were made as described in the caption to Figure V.1.

steps as the original data (Figure V.1) for 10 degrees of freedom. Bicoherence estimates were made by averaging four 128 point ensembles and using a Hanning window for 8 degrees of freedom. Figure V.5 shows one realization at each variance increment of the EOF-1 + noise time series and the corresponding power spectrum for that realization. Power spectral and cross spectral estimates having 10 degrees of freedom were calculated. Bicoherence estimates were made by averaging 8 125 point ensembles for 16 degrees of freedom.

In the second experiment noise was added to the age models rather than the observations. There are several different methods by which to add incremental variance to time observations. It is most useful to paleoceanographers to add noise that will be consistent with the manner in which time scales are developed. That is, conversion of a record sampled in the depth domain to the time domain involves interpolation between "fixed" age-depth calibration points. Note that if noise were simply added to the time series in the frequency domain, as the level of noise went up, observations which were originally monotonically increasing in depth could become transposed, depending on the level of noise and the sampling interval. Thus it is most useful to jitter, or add variance to, the age-depth model which defines the time scale.

The reference age model for the Site 677 $\delta^{18}O$ record is the orbitally tuned age model presented by Shackleton et al. (1990). The age model contains 35 control points, for an average of one control point every 31,000 years. For EOF-1, it is difficult to arrive at a single age-depth model since the EOF incorporates 8 records having 8 different age-depth relationships. The sedimentation rate patterns between Leg 138 sites, however, are very similar though differing in amplitude (Pisias et al., 1993). In addition, the same age control points are used at different sites. A composite "age model" was constructed as a means of constraining the points between which the time scale is jittered. This age model has 52 control points (approximately one every 20,000 years). Both age models are given in Table V.1A.

Table V.1. Age models used in age model noise experiments.

A. 1ST EXPERIMENT

677 $\delta^{18}O$	$\%CaCO_3$	EOF-1
Depth	**Age**	**Age**
0.00	0.0	0.0
0.40	0.006	0.033
3.80	0.061	0.056
4.90	0.085	0.070
6.10	0.122	0.082
8.17	0.194	0.103
9.05	0.214	0.114
10.20	0.238	0.126
12.02	0.286	0.148
12.30	0.295	0.173
13.54	0.329	0.196
14.04	0.339	0.218
16.34	0.405	0.241
17.40	0.428	0.262
18.65	0.459	0.277
19.25	0.481	0.290
19.85	0.501	0.311
20.25	0.509	0.333
21.25	0.534	0.354
22.50	0.573	0.372
22.70	0.582	0.386
23.25	0.595	0.397
23.50	0.602	0.408
23.85	0.616	0.425
24.40	0.626	0.462
26.74	0.688	0.504
27.50	0.709	0.515
30.43	0.784	0.528
32.40	0.821	0.565
33.75	0.860	0.577
37.49	0.953	0.598
38.39	0.976	0.609
39.09	0.996	0.620
39.49	1.005	0.631
40.09	1.027	0.648
		0.692
		0.712
		0.749
		0.787
		0.805
		0.824
		0.863
		0.884
		0.908
		0.925
		0.936
		0.957
		0.978
		1.000

B. 2ND EXPERIMENT ("RELAXED" AGE MODEL)

677 $\delta^{18}O$	$\%CaCO_3$	EOF-1
Depth	**Age**	**Age**
0.00	0.0	0.0
0.40	0.006	0.033
3.80	0.122	0.056
6.10	0.122	0.126
8.17	0.194	0.148
10.20	0.238	0.173
14.04	.339	0.218
16.34	.405	0.241
18.65	0.459	0.262
20.25	0.509	0.290
22.50	0.573	0.311
24.40	0.626	0.333
30.43	0.784	0.354
33.75	0.860	0.386
37.49	0.953	0.408
39.09	0.996	0.462
40.09	1.027	0.473
		0.484
		0.504
		0.515
		0.528
		0.577
		0.598
		0.620
		0.648
		0.692
		0.712
		0.787
		0.863
		0.908
		0.936
		0.978
		1.000

Uniformly distributed noise was added to the age models at levels of 10%, 20%, 50%, 100%, and 200%. Variance was added to the differences between successive ages, analogous to adding errors to sedimentation rates. A constraint that the age model must increase monotonically between age control points was imposed. The age-depth model presented by Shackleton et al. (1990) and example individual realizations of age-depth models with noise added are given in Figure V.6. 100 realizations at each variance increment were generated. The jittered age models were then applied to the original data records, and re-interpolated to a constant sampling interval. Individual realizations and the corresponding power spectra for the $\delta^{18}O$ are in Figure V.7. Example realizations of the same for EOF-1 are given in Figure V.8.

The third experiment consisted of repeating the second experiment, but with a relaxed age model having fewer age control points than the previous experiment. This was done in order to allow more variability to enter into the sedimentation rate model, as the above experiment only allowed maximum variations on the order of 20,000 years. This

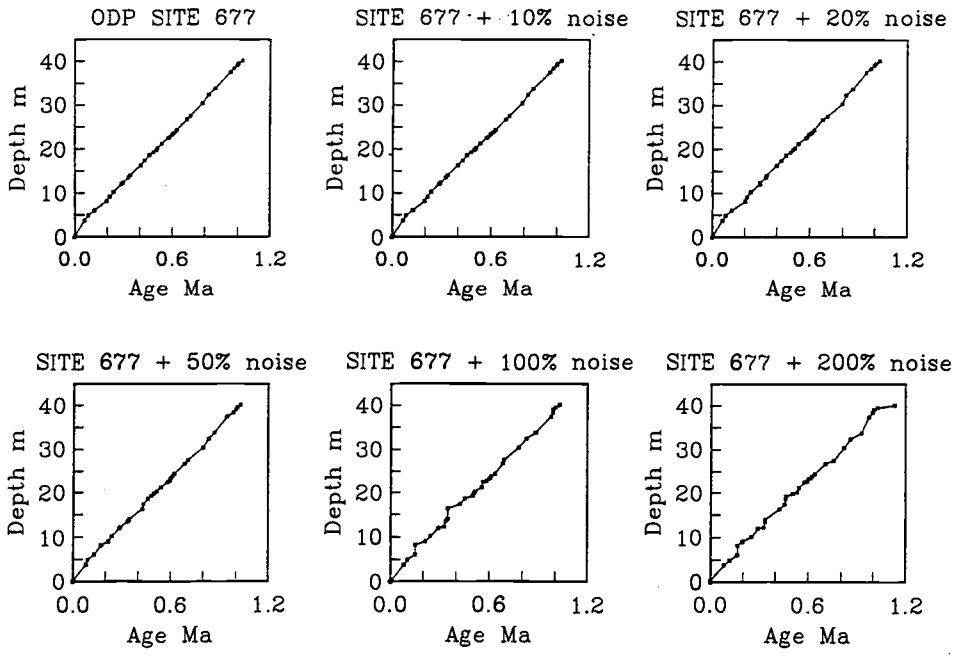

Figure V.6. Age vs depth for the orbitally tuned age model for Site 677 (Shackleton et al., 1990), and for individual realizations of this age model + incremental noise added to the sedimentation rates. This age model has 35 control points.

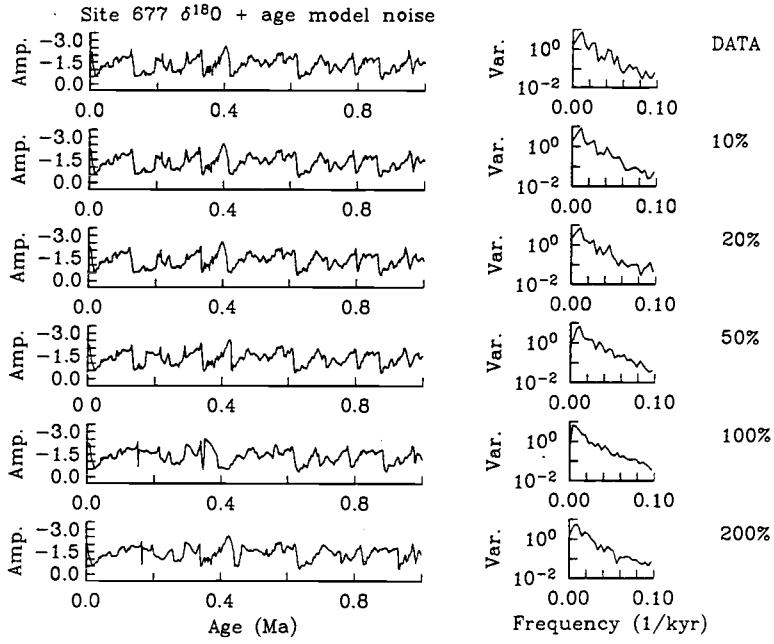

Figure V.7. Individual realizations of the Site 677 $\delta^{18}O$ data on age models containing incremental amounts of variability in the sedimentation rates. Power spectra are averaged as described in Figure V.1.

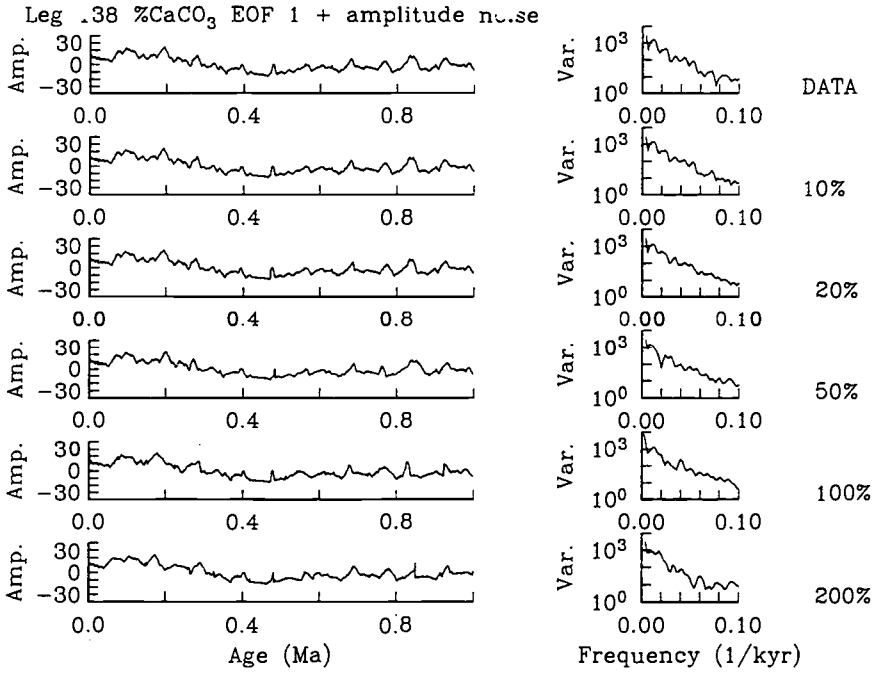

Figure V.8. Individual realizations of the Leg 138 $\%CaCO_3$ EOF-1 on age models containing incremental amounts of variability in the sedimentation rates, and corresponding power spectra. The age models used are based on the orbitally tuned chronologies for Leg 138 Sites 846-852 (Shackleton, et al., in prep), and contains 52 control points.

experiment allows variation on the order of 30,000 years up to 100,000 years to be introduced. For the site 677 $\delta^{18}O$ record, an age model having 17 age control points for an average of 60 kyr intervals between control points was used. Example age-depth plots having incremental levels of noise are given in Figure V.9, and Figure V.10 shows individual realizations and the corresponding power spectra. For the EOF-1 record, an age model having approximately half the resolution of the first age model was used, with an average of 30 kyr between age control points. Individual realizations of the interpolated time series at each incremental jitter step and the corresponding power spectra is given in Figure V.11. The control age models for each record are in Table V.1B.

In each case in the above experiments, uncorrelated noise was added. Correlated noise or noise having different statistical distributions and frequency dependencies could be used. However, for the case of correlated noise, Balakrishnan (1962) examined the effect of uncorrelated jitter relative to correlated jitter on signals, and concluded that correlation in jitter decreases the effect on the spectral estimates. Thus, the "worst case" scenario is examined here.

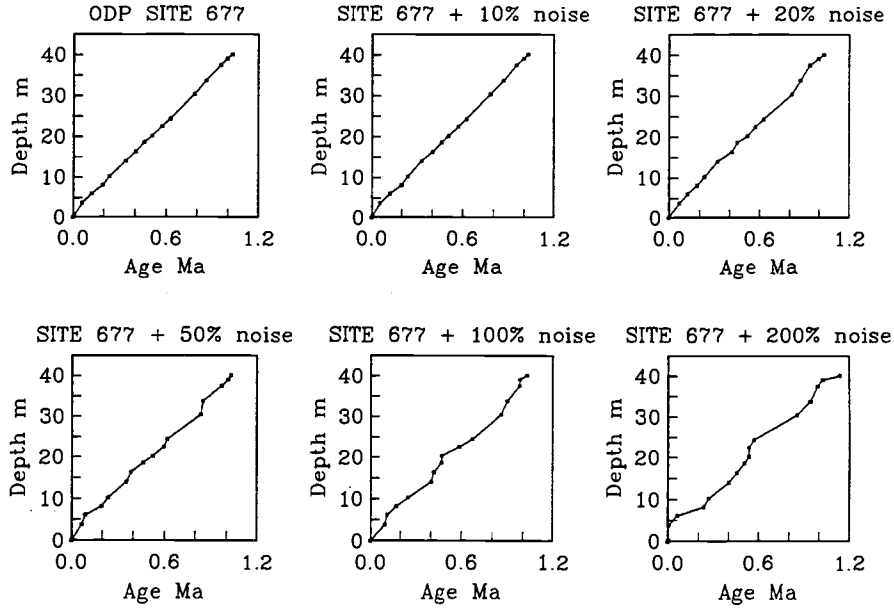

Figure V.9. Age vs depth for a Site 677 age model having less control points than the orbitally tuned model. Individual realizations of this age model + incremental noise added to the sedimentation rates are given. This age model has 17 control points.

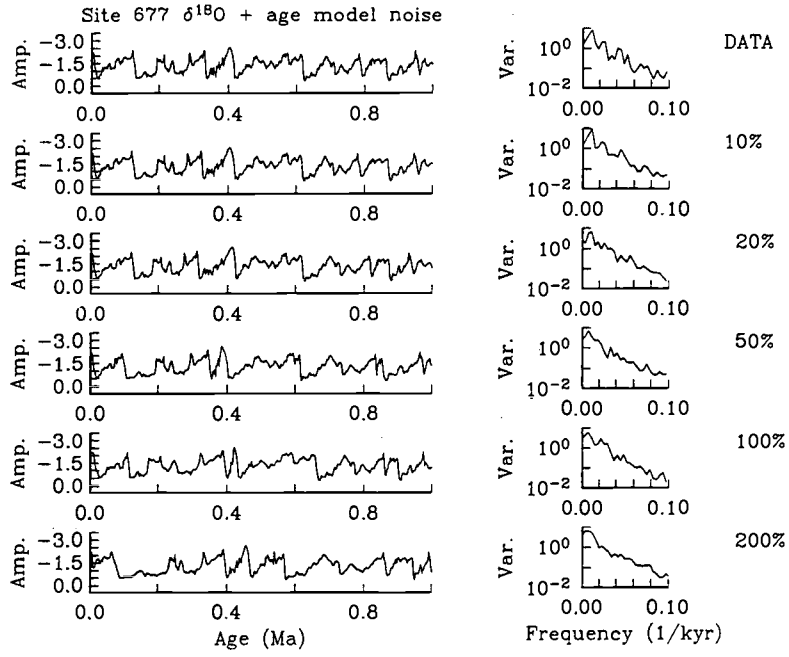

Figure V.10. Individual realizations of the Site 677 $\delta^{18}O$ data on age models containing incremental amounts of variability in the sedimentation rates, and corresponding power spectra. The age models are the "relaxed" age models illustrated in Figure V.9.

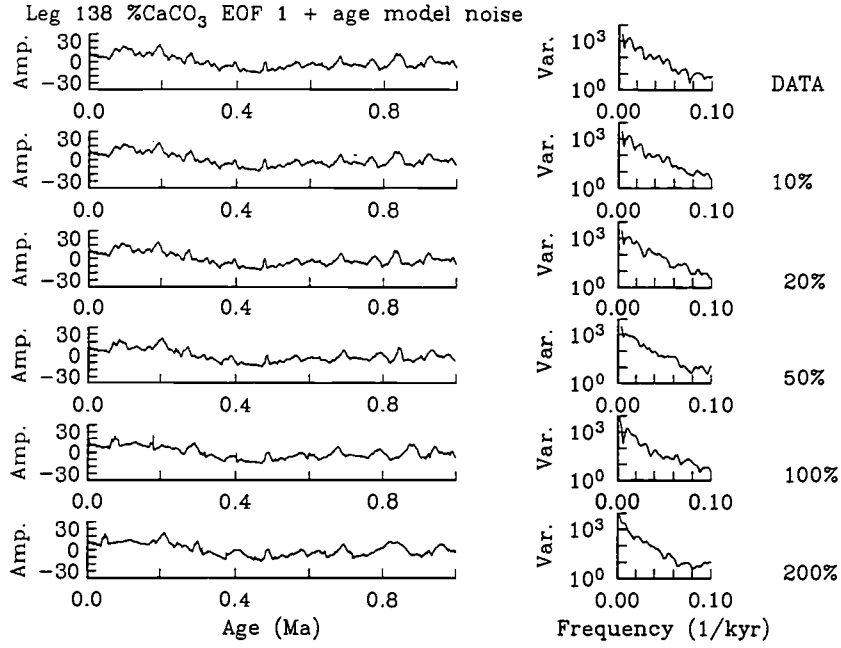

Figure V.11. Individual realizations of the Leg 138 $\%CaCO_3$ EOF-1 on age models containing incremental amounts of variability in the sedimentation rates and corresponding power spectra. The age models used are "relaxed" age models as described in text, containing 33 control points.

The final phase of this study was to examine the test statistic for time scale jitter from the realizations of the second and third experiments described above. These statistics were used to evaluate the feasibility of the jitter test. Additionally, synthetic time series having prescribed bicoherences and prescribed time scale jitter, but relatively short record lengths (comparable to the test records in this study) were used to study the utility of the proposed time jitter test under more controlled conditions.

RESULTS AND DISCUSSION

Experiment 1

The effects of amplitude noise on estimates of coherence and bicoherence are summarized in Figure V.12 for $\delta^{18}O$ and Figure V.13 for EOF-1. Coherence for the $\delta^{18}O$ records are summarized for the four frequency bands having high coherence in the insolation-Site 677 $\delta^{18}O$ cross spectra, 100 kyr, 41 kyr, 23 kyr, and 19 kyr (Figure V.1). Coherence for the EOF-1 records are summarized for five highly coherent frequency bands (Figure V.1): 100 kyr, 41 kyr, 30 kyr, 23 kyr, and 19 kyr. Bicoherence results are summarized for the 4 significant triads of frequencies resolved in the $\delta^{18}O$ data corresponding to approximately (100,23,19) kyr, (41,23,15) kyr, (30,41,100) kyr, and (35,65,100) kyr (Figure V.1). For the EOF-1 records bicoherences are summarized at the 3 statistically significant triads corresponding to approximately (100,41,30) kyr, (41,23,15) kyr, and (62,19,14) kyr (Figure V.1).

Note from the individual realizations in Figures V.4 and V.5 that the power spectral peaks resolved with the data at these frequencies are visible even after addition of 50% uniform noise. The results with the coherence spectrum are analogous: Almost no change in coherence is detected at the 10% and 20% level, and even when the noise added has a variance equal to the variance of the original time series (i.e., 100%), statistically significant (0.80 level) coherence between insolation and the data is resolved. In the case of the $\delta^{18}O$ record, significant coherence between insolation and the noisy data persists even to the highest noise level used (500%, or 5 times the original data variance; Figure V.12).

These results indicate very high robustness of coherence estimates to large additions of noise to the amplitudes of measured data. In every primary Milankovitch band, significant coherence between insolation and the record is present even in the presence of large amounts of noise. A decrease with frequency and spectral energy also appears to be evident: while coherence at the higher frequencies of precession are higher initially than in the 100 kyr band, the drop off in coherence as noise is added is much steeper in the

precession band, whereas the drop off is much more gradual at lower frequencies. This is true for both $\delta^{18}O$ and EOF-1 (Figures V.12 and V.13). This is proportional to the amount of spectral energy within each frequency band. Thus, higher frequencies which contain lower total variance than the lower frequencies in the $\delta^{18}O$ and EOF-1 time series are more sensitive to the addition of noise when noise is added equally to each frequency.

In both the $\delta^{18}O$ and the EOF-1 simulations, bicoherences drop below the 0.80 significance level very quickly as amplitude noise is added, much faster relative to the coherence estimates. The variance of the bicoherence estimates as noise is added is also much higher than for coherence estimates. A dependence on initial energy level also seems to be present among higher order moments, as the drop off in bicoherence is much steeper when one frequency is higher than ~ 19 kyr, and changes in bicoherence are much more

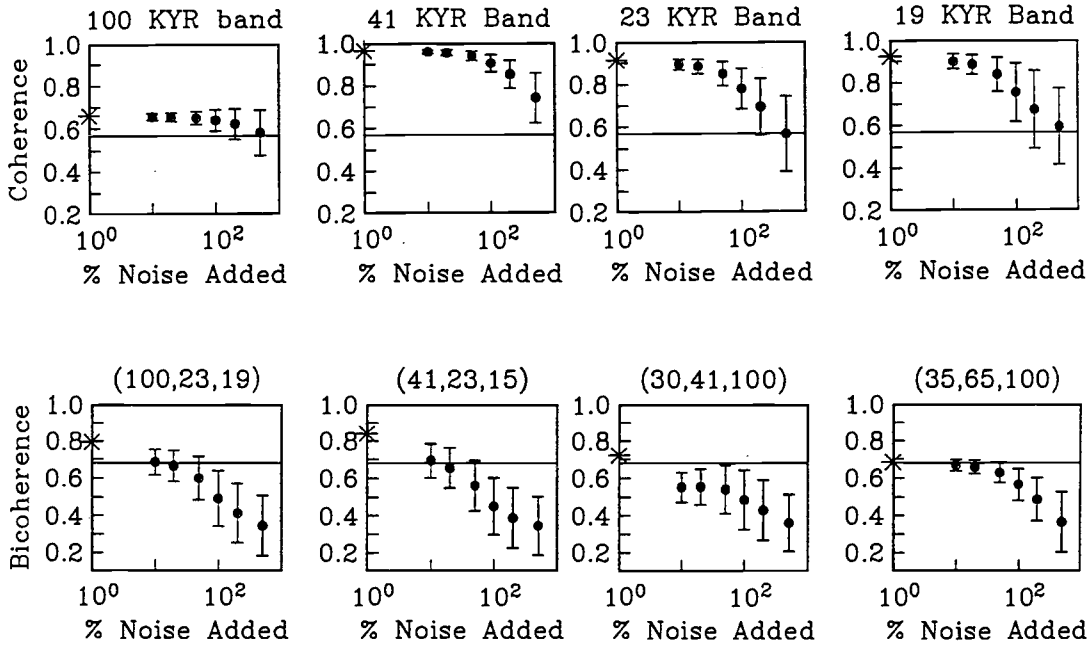

Figure V.12. (Top): Summary of changes in coherence between solar insolation and Site 677 $\delta^{18}O$ as noise is added to the $\delta^{18}O$ amplitudes. The asterisk indicates the coherence estimated from the original record. The horizontal line (coherence = 0.57) indicates the .80 level for significant coherence. (Bottom): Summary of changes in bicoherence for the Site 677 planktic $\delta^{18}O$ record. The bicoherence value plotted is the bicoherence for the triad incidated at the top of each panel. The horizontal line (bicoherence = 0.68) incicates the .80 level for significant bicoherence. The asterisk is the bicoherence estimated from the data.

stable when all frequencies in the triad are lower than ~ 30 kyr. These results suggest that bicoherence estimates are much more sensitive to amplitude noise in a time series than cross-spectral estimates.

The above results with noisy data suggest that given a time scale which is not jittered, the detection of any significant bicoherences may indicate a record with relatively little random noise. This may have implications for the lack of significant bicoherence in

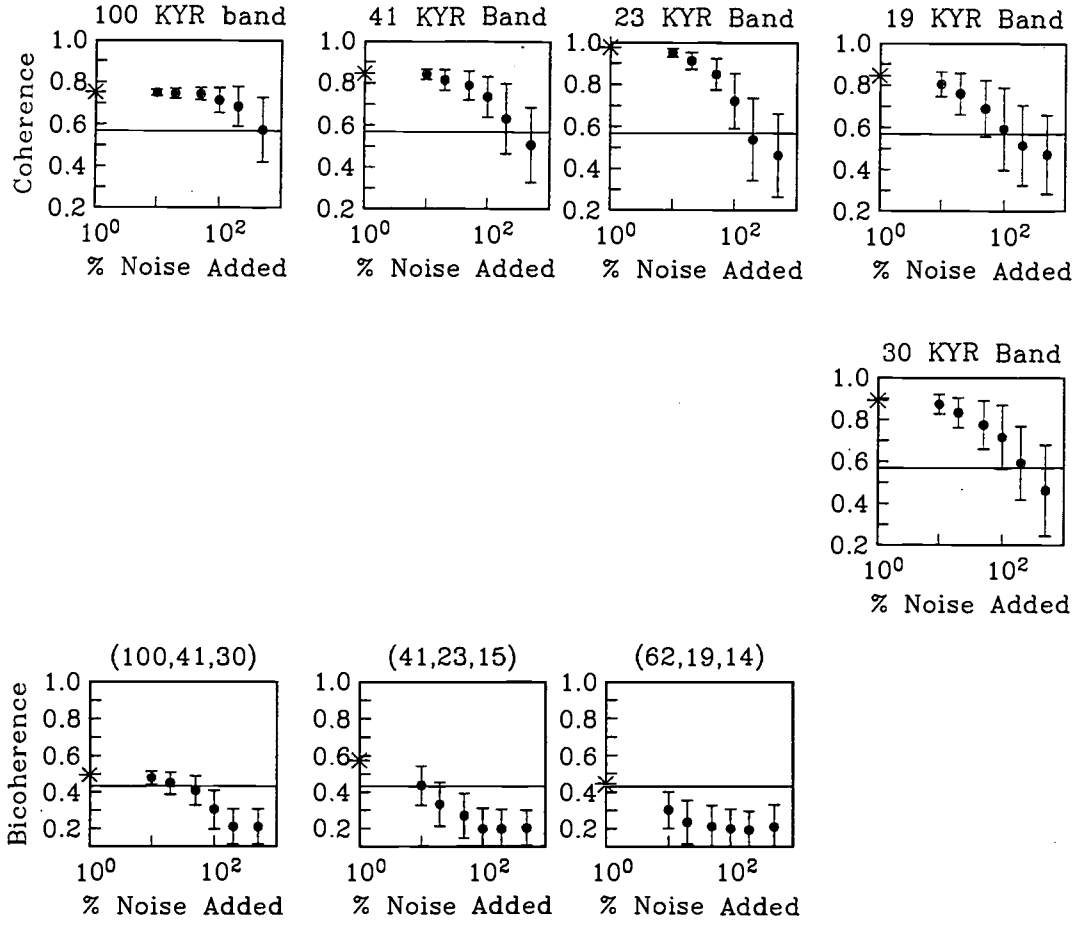

Figure V.13. (Top): Summary of changes in coherence between solar insolation and $\%CaCO_3$ EOF-1 as noise is added to the EOF amplitudes. The asterisk indicates the coherence estimated from the original record. The horizontal line (coherence = 0.57) indicates the .80 level for significant coherence. (Bottom): Summary of changes in bicoherence for the $\%CaCO_3$ EOF-1 record. The bicoherence value plotted is the bicoherence for the triad incidated at the top of each panel. The horizontal line (bicoherence = 0.43) incicates the .80 level for significant bicoherence (bicoherence estimates for these records have 14 degrees of freedom). The asterisk is the bicoherence estimated from the data.

he benthic $\delta^{18}O$ record from DSDP Site 607 examined in Hagelberg et al (1991). Increased variability in the amplitudes that is due to random noise could be greater than in the 677 records. This possibility was considered by Hagelberg et al., and given the demonstrated sensitivity of bicoherence estimates to small amounts of introduced noise, it may be one potential factor.

Experiment 2

Results of changes in coherence and bicoherence from the addition of incremental amounts of uniformly distributed noise to the reference age models are summarized in Figure V.14 for $\delta^{18}O$ and Figure V.15 for EOF-1. Unlike the addition of noise to the amplitudes, the power spectral peaks of the jittered age models quickly lose resolution (Figures V.7 and V.8). Likewise, coherence results drop off faster than in the amplitude experiment. Significant coherence between insolation and the jittered data is lost after 50% addition of noise to the age model. With the coherence results, a plateau effect seems to occur: whereas the decrease in coherence with additional noise added was fairly uniform in the amplitude experiment, the decrease in coherence in the age model experiment drops off steeply after 50% noise. This is true of both the $\delta^{18}O$ data and EOF-1.

A frequency dependent attenuation is also evident. The variance in the levels of coherence and the decrease as age model noise increases are correlated with the frequency band rather than the initial level of coherence (Figures V.14 and V.15). Balakrishnan (1962) demonstrated that the effect of time jitter was to introduce a frequency distortion which increases according to the factor

$$-10\log_{10}\left|\left(\frac{\sin 2\pi f}{2\pi f}\right)\right|^2 \qquad (3)$$

for uniformly distributed jitter. Although adding jitter to the age model and reinterpolating the time series is not the same as directly adding uniformly distributed time scale jitter, a

frequency attenuation is still present. This frequency attenuation may also be related to the intial energy level withing the individual frequency bands, as variance in $\delta^{18}O$ and EOF-1 also decreases with frequency.

Results for bicoherence estimates as a function of increasing age model noise are similar. However, if results of Experiments 1 and 2 are compared, the bicoherence estimates appear slightly more robust to age model noise than to amplitude noise. As with the amplitude noise experiment, bicoherence estimates are more sensitive to additional age model noise than coherence estimates. Also, the decrease in bicoherence as a function of increasing age model noise is faster than in the amplitude experiment. A frequency attenuation occurs between bifrequencies. Implications of the results of this experiment for bicoherence and coherence estimates are discussed following the next section.

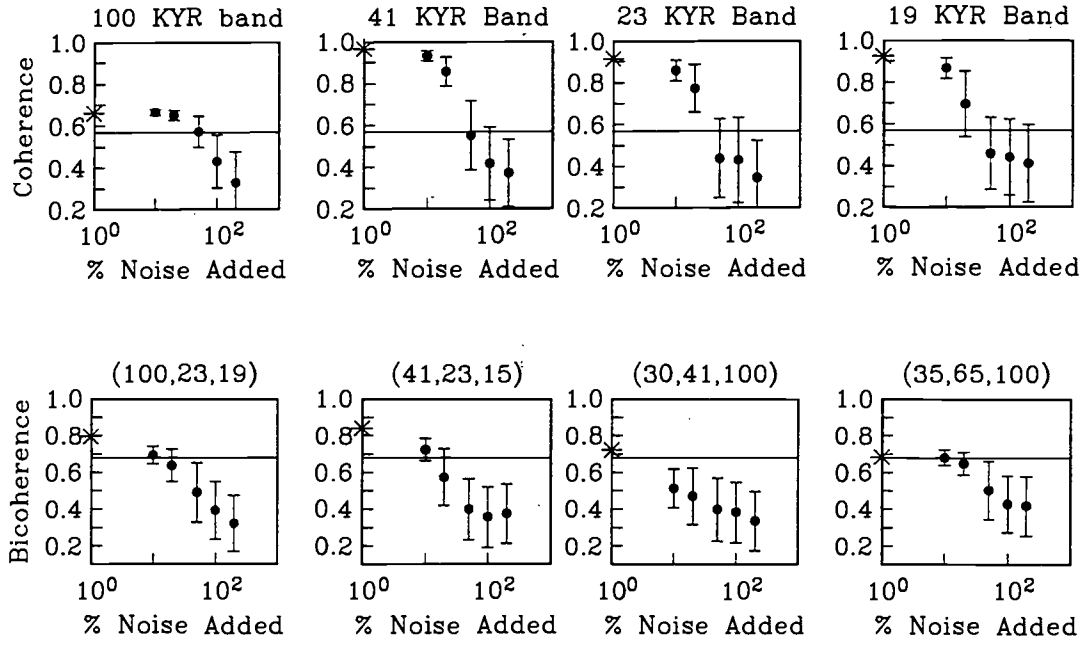

Figure V.14. (Top): Summary of changes in coherence between solar insolation and Site 677 $\delta^{18}O$ as noise is added to the age model. (Bottom): Summary of corresponding changes in bicoherence for the Site 677 planktic $\delta^{18}O$ record. Notation is the same as described in the caption to Figure V.12.

Experiment 3

Individual realizations of power spectra of time series having incremental noise added to the "relaxed" age models of the third experiment suggest that the failure to resolve the spectral peaks present in the data occurs at about the same variance level as the previous experiment (Figures V.10 and V.11). The results of changes in coherence and bicoherence from the addition of incremental amounts of uniformly distributed noise to the relaxed (fewer control points) age models are summarized in Figure V.16 for $\delta^{18}O$ and Figure V.17 for EOF-1. In this experiment, one would expect results to show even greater decreases in coherence and bicoherence with increasing noise added to the age model, because age

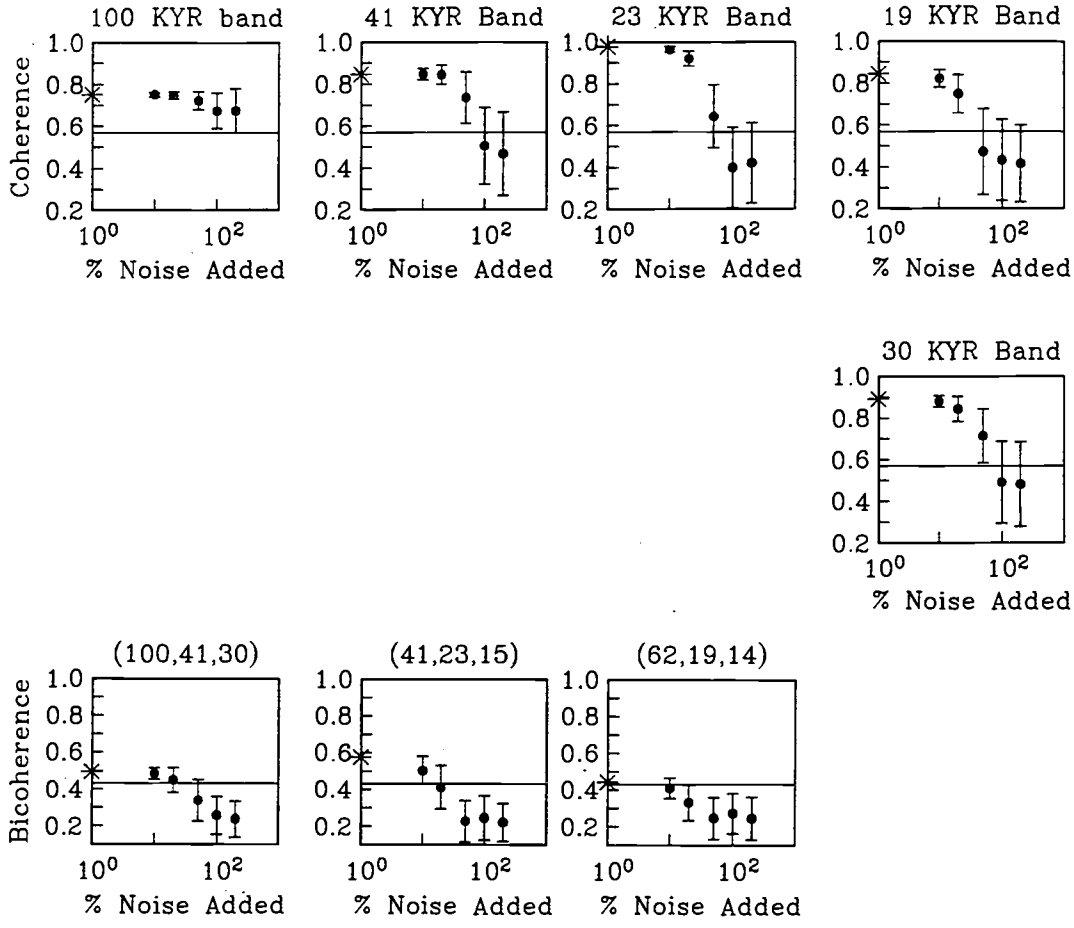

Figure V.15. (Top): Summary of changes in coherence between solar insolation and %CaCO3 EOF-1 as noise is added to the age models illustrated in Figure V.8. (Bottom): Summary of changes in bicoherence for the $\%CaCO_3$ EOF-1 record. Notation is the same as described in the caption to Figure V.12.

model variability is allowed to expand over a greater range, over 30,000 -50,000 years rather than 20,000 - 30,000 years. The results are consistent with this expectation. While coherence dropped sharply by the addition of 50-100% age model noise in the previous experiment, it drops to nonsignificant levels by 10-20% in this experiment (Figures V.16 and V.17). The decrease in bicoherence with increasing age model noise shows a similar result, falling to levels below the .80 significance level by the addition of even 10% age model noise. In this age model experiment the bicoherence estimates are more sensitive to noise than in the amplitude experiment.

Implications

The high sensitivity of bicoherence estimates to both amplitude noise and even more so to age model noise raises two points, one pessimistic and one optimistic. The pessimistic point is that bicoherence estimates from relatively short records having few

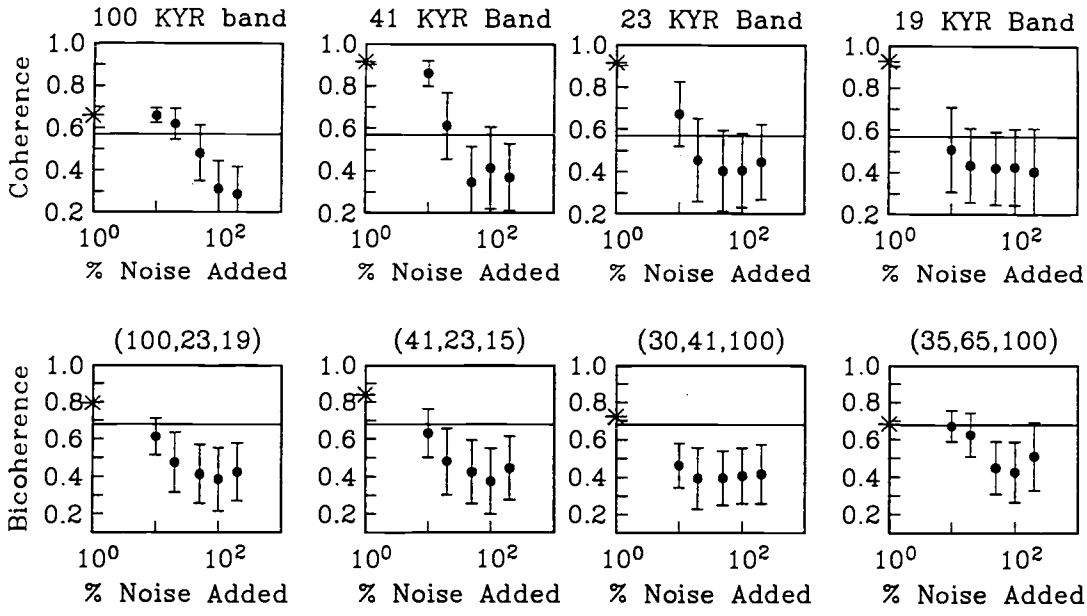

Figure V.16. (Top): Summary of changes in coherence between solar insolation and Site 677 $\delta^{18}O$ as noise is added to the "relaxed" age models illustrated in Figure V.10. (Bottom): Summary of corresponding changes in bicoherence for the Site 677 planktic $\delta^{18}O$ record. Notation is the same as described in the caption to Figure V.12.

degrees of freedom cannot be reliable indicators of nonlinear interactions in time series data because any addition of noise will degrade the estimates. McComas and Briscoe (1980) support this point, and regard bispectra as having low utility for studying oceanic internal waves because of the fact that many triads, not just a few, are contributing to each component, and a large number of dof required to gain marginally significant results. In addition, when the level of nonlinearities in the process under study is low, as was believed to be the case for internal waves, the problem of gaining significant results becomes even more confounded.

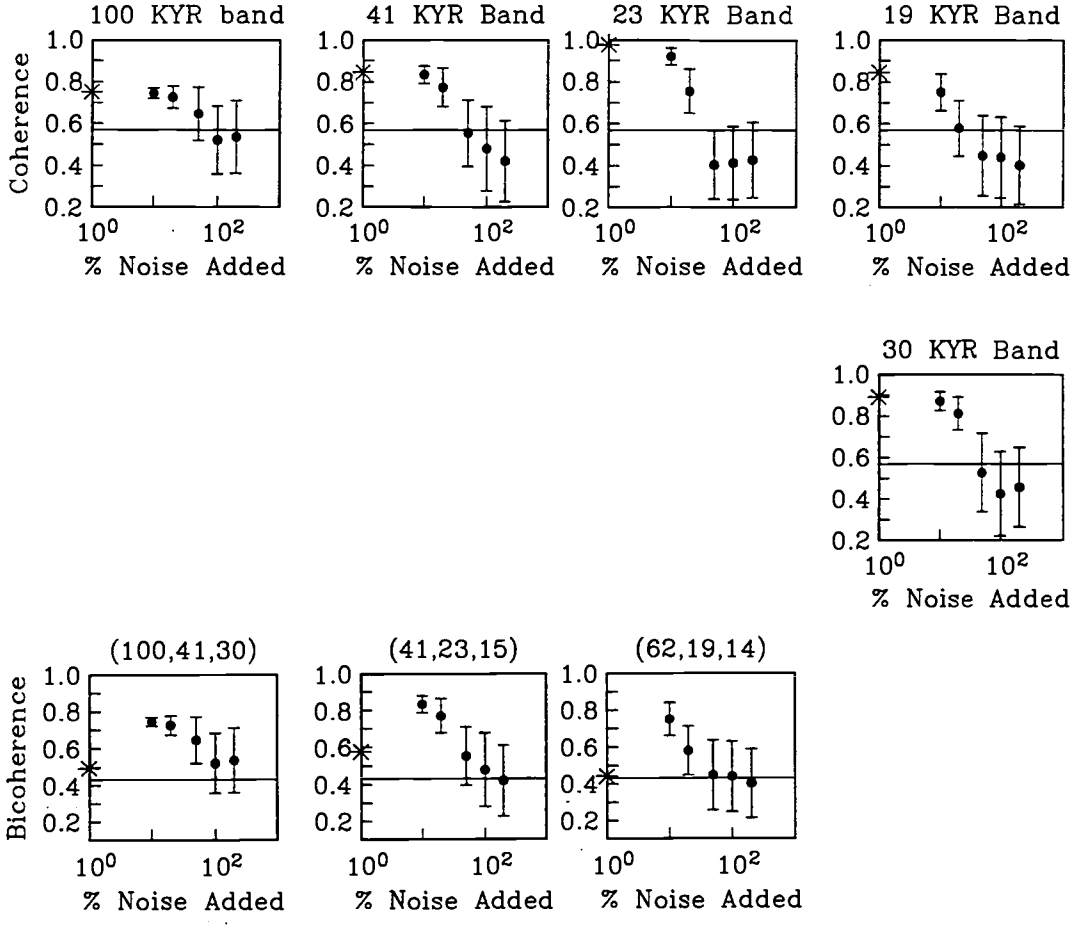

Figure V.17. (Top): Summary of changes in coherence between solar insolation and $\%CaCO_3$ EOF-1 as noise is added to the "relaxed" age models illustrated in Figure V.15. (Bottom): Summary of changes in bicoherence for the $\%CaCO_3$ EOF-1 record. Notation is the same as described in the caption to Figure V. 12.

The second, more optimistic viewpoint is that this study and the previous study by Hagelberg et al (1991) has demonstrated that when statistically significant bicoherences are detected in paleoclimatic records having few degrees of freedom, it can be demonstrated by Monte Carlo simulations that these phase couplings are unlikely to be the result of random variability in the bicoherence estimates. Given a record which does not contain high levels of amplitude noise, the detection of statistically significant bicoherences is likely to indicate that the age model is good, and the underlying process has quadratically nonlinear interactions. Similarly, given a record which has a fairly accurate and well constrained age model, the detection of significant bicoherences can indicate that the data set has low levels of amplitude noise. Finally, given that in reality paleoclimatic time series are noisy in both the observations and in the age model, detection of significant bicoherences at a low level of degrees of freedom indicates that the level of nonlinear interaction contributing must be very strong. Future work involves using Monte-Carlo modeling to approximate what the true level of phase coupling of the climatic signal might be, given that the short record length and noise lowers the observed level. Since phase couplings have been determined to be present in two proxy records of global ice volume (Hagelberg et al., 1991), it should be possible to resolve these phase couplings in any global ice volume proxy record. Because this measure has a much higher sensitivity than coherence, it may provide a finer constraint on time scale evaluation.

Table V.2. Summary of time jitter test statistics for data and for simulations from the first age model experiment.

	$\delta^{18}O$	EOF-1
DATA	113	25
10%	105	26
20%	108	24
50%	109	24
100%	116	33
200%	120	39

A Test for Time Scale Jitter

The test for time scale jitter using the OT region of the principal domain of the bispectrum is now examined. Test statistics for the two data sets and for the simulations from the first age model experiment are given in Table V.2. For the $\delta^{18}O$ data, T_c is 105, and for EOF-1, T_c is 25. Both of these records fulfill the conditions for high probability of detection as given by Sharfer and Messer (Eq. 2). Figure V.18 shows the change in the OT test statistic as a function of increasing amounts of age model noise. For both $\delta^{18}O$ and EOF-1, there are 341 bifrequency pairs in the smoothed OT bispectrum. At a .80 level of significance, the normal approximation to a χ^2 distribution gives a test statistic of 363. In order to reject the null hypothesis and accept the hypothesis that the time scale is jittered, the sample test statistic needs to exceed this value. Obviously, the test statistic is much higher than sample test statistics from the data and from the age model jittered time series. At no noise level can the null hypothesis be rejected. The level of OT bicoherence required to reject the null hypothesis provides a useful comparison: if every single triad in OT were significant at the .80 level (bicoherence of 0.68), the sample test statistic would be 464, and the null hypothesis would be rejected.

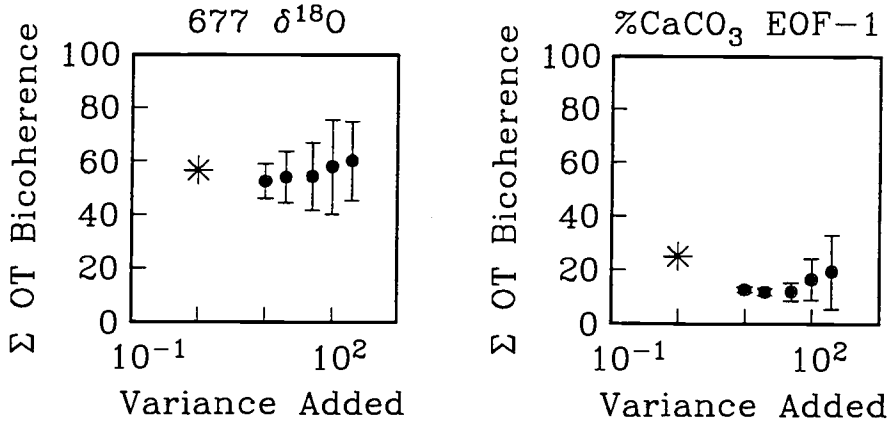

Figure V.18. The sum of bicoherences over OT as age model variance increases for the $\delta^{18}O$ and EOF-1 time series from the first age model experiment.

This result leads to several issues regarding the proposed test of Sharfer and Messer (in press). First, Sharfer and Messer developed the test based on the existence of a flat bispectrum in the principal domain. Its unlikely that the records studied here have a flat true bispectrum, it is more likely that the bispectrum consists of a few phase coupled triads. The same sum of bicoherences in OT can be achieved by having many grid points with medium bicoherence, or alternatively, by fewer grid points having high bicoherence. It is unknown whether both of these sums obtained two different ways indicate the same levels of time scale jitter. This point is difficult to address using records in which the true level of bicoherence and the true level of timescale jitter are unknown, so it is necessary to do some simulations. Second, it is unknown at what level of time jitter the test is no longer applicable. Recall that the time series must have a nonzero bispectrum in the IT in order for the OT test to be applicable. With increasing age model jitter, bispectral values in the principal domain decrease.

Even if the time scale jitter observed using the above records is low, it is useful to know if the proposed time scale jitter test has any potential usefulness for paleoclimatic time series. Sharfer and Messer discuss the performance of the jitter test, but left simulations to evaluate the test performance to future work. In addition, their performance criteria are based on records having many more degrees of freedom than are encountered in geological records. However, Hinich and Wolinsky (1988) suggest that the test (for aliasing) is powerful even for records having very few degrees of freedom. The utility of the test can easily be investigated with synthetic time series having prescribed phase couplings and prescribed time series jitter of different variances.

All simulations are made using time series with a record length of 1024, and estimates with 16 degrees of freedom are made. Although a range of record lengths and frequency resolutions need to be examined, this short record length and associated low degrees of freedom are typical of paleoclimatic records. In the Milankovitch band, the ability to obtain longer records is complicated by nonstationarity.

Seventeen synthetic time series having varying numbers of phase coupled triads and varying prescribed phase coupling are generated. The sum of bicoherences over OT were calculated from time series having no prescribed phase coupling, partial prescribed phase coupling, and high prescribed phase coupling (true bicoherence = 1.0). In each case, records having 1, 2, 4, 6, and 10 triads were generated. The sum of bicoherences over OT as a function of number of triads and amount of prescribed phase coupling are given in Figure V.19. The result is not encouraging in that the differences between the sum over OT for high and low prescribed phase coupling are not great for short records. The sum over OT for the 1 triad case is highest. For 2 triads to 6 triads, the sum increases, until 10 triads where overall bicoherence in the principal domain decreases because of phase mixing and leakage. Thus it appears that for short data records, the test will only have potential if less than 10 triads are interacting nonlinearly.

Realizations were made of the 1,2,4 and 6 triad time series with incremental amounts of time scale jitter to examine the effect on OT. As in the experiments above, time jitter was added as a function of an "age model". Five "age models" with varying

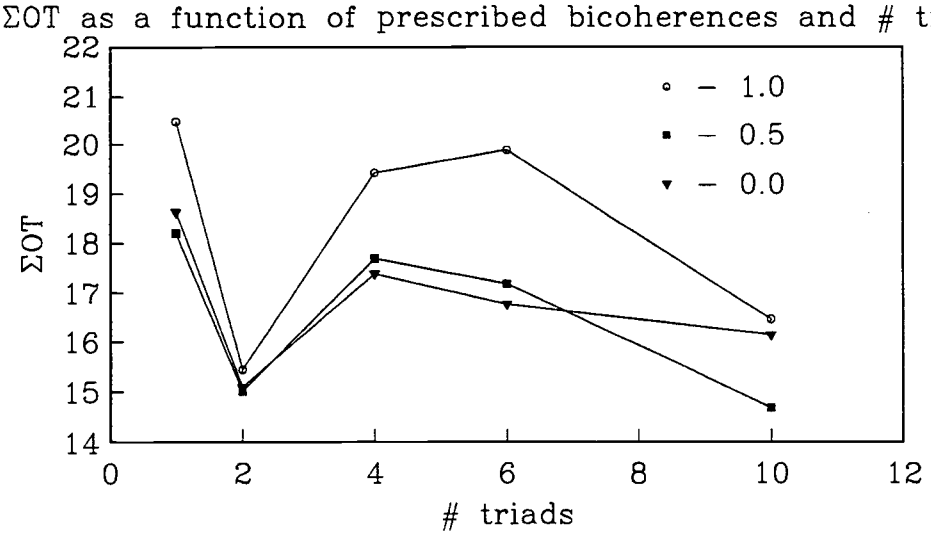

Figure V.19. The sum of bicoherences over OT as a function of the number of triads in the prescribed synthetic time series and the prescribed level of phase coupling among the triads.

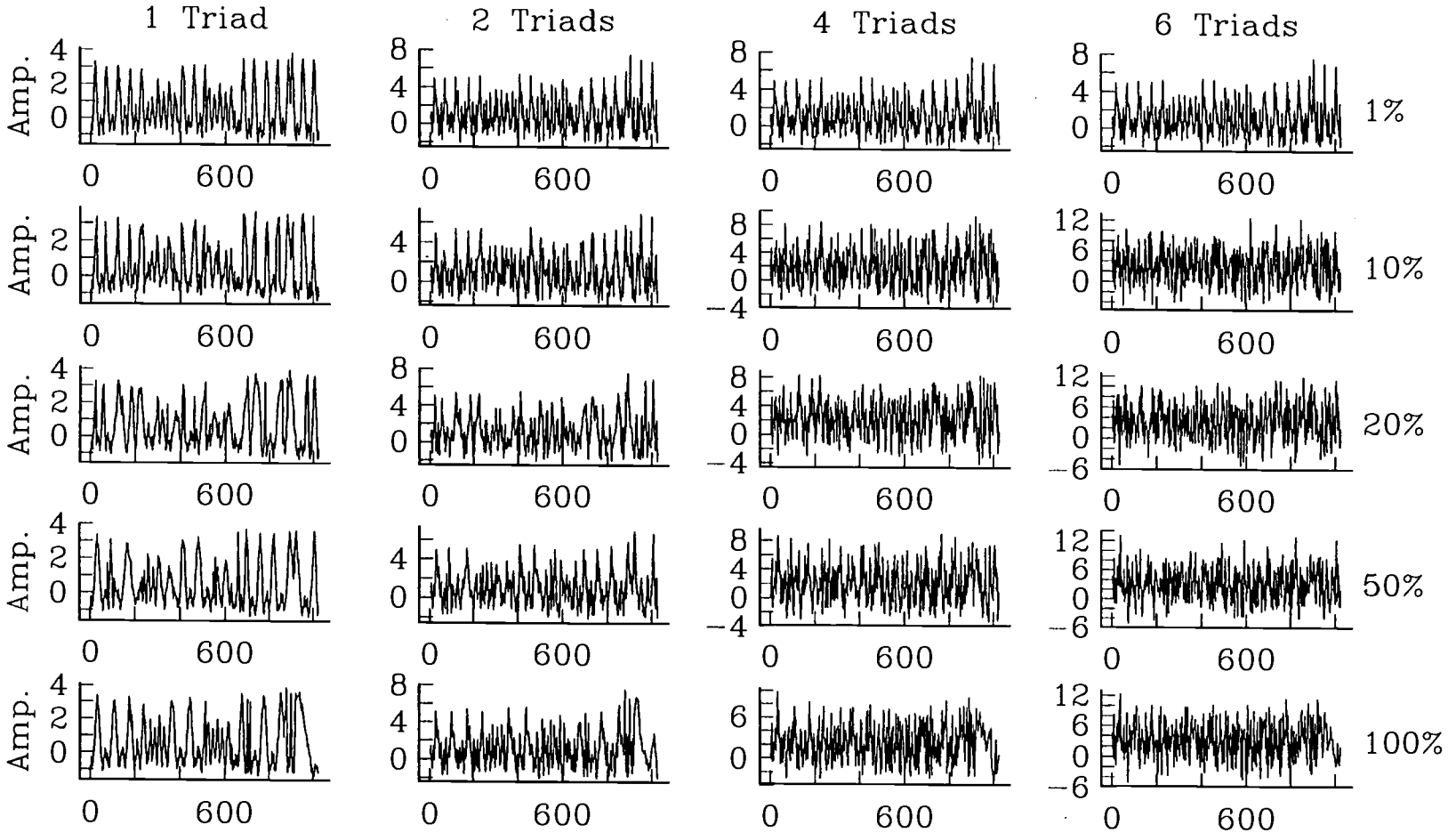

Figure V.20. Example realizations of synthetic time series having 1, 2, 4, and 6 phase coupled triads with increasing levels of "age model" noise as described in text.

resolutions were used: the first consisted of 1024 points for the 1024 point record. That is, jitter was confined to the increments between the successive evenly spaced points. The second "age model" consisted of 102 points, spaced every 10 steps, thus allowing greater variability. The third age model consisted of 51 points, every 20 steps, the fourth consisted of 21 points, every 50 steps, and the last age model consisted of 11 points every 100 steps. At each increment for each of the 4 time series, 10 realizations were calculated. Example realizations for each time series at each increment are given in Figure V.20.

The sum of bicoherences over OT as a function of increasing noise is summarized in Figure V.21. For the 1 triad and 2 triad case, the OT sum increases for increased age model jitter, but large differences between the unjittered case and the jittered case are not seen until at least the third noise increment. For the 4 triad and 6 triad case, no significant increase in the OT sum is seen. This is most likely due to leakage among the contributing frequencies. Experiments with longer time series can address this.

Since the general (within an order of magnitude) record lengths and frequency resolution of the data for which this test is of interest is limited, it is unlikely that the test proposed by Sharfer and Messer can be directly applied to the problem of paleoclimatic age models. However, knowledge of the properties of the OT of the bispectrum may prove useful in that empirical tests for time jitter may be developed after examining many more records. Also, it is unknown whether the test is more applicable to and possibly more appropriate to the issue of aliased time series.

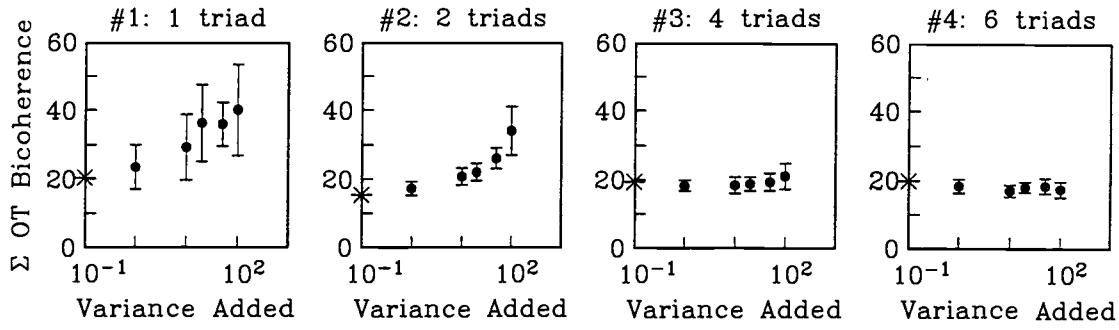

Figure V.21. The sum of bicoherences over OT for the time series illustrated in Figure V.20.

CONCLUSIONS

The above experiments address the sensitivity of coherence and bicoherence estimates to incremental amounts of random noise in the amplitudes of a time series as well as in the age models from which the time series is constructed. Although the above cases measure coherence between a noisy record and a time series (insolation) which contains no noise, if two noisy time series are considered the sensitivity of coherence estimates can be expected to be much higher. The results indicate that for addition of noise (uniformly distributed and uncorrelated) to amplitudes of time series, coherence estimates are fairly robust. Bicoherence estimates are more sensitive. Bicoherence estimates are also more sensitive to additional age model noise than coherence estimates. In each experiment with $\delta^{18}O$ and EOF-1, a decrease in coherence and bicoherence with increasing frequency was observed, regardless of the initial level of coherence or bicoherence. This relationship probably results from the decrease in initial spectral energy with frequency observed in the $\delta^{18}O$ and EOF–1 time series. The first three sets of experiments given above suggest that given data that is not noisy, detection of significant bicoherence is likely to indicate good age model control if underlying process has quadratically nonlinear interactions. Given data from short records which have both amplitude noise and age model noise, the detection of significant bicoherence most likely indicates very strong nonlinear interactions, as sensitivity is so high. This result suggests that documentation of significant phase couplings, particularly in $\delta^{18}O$ records, can provide a better indication of time scale fit than coherence estimates.

The test for time scale jitter proposed by Sharfer and Messer (in press) does not appear to be directly applicable to paleoclimatic time series. However, it may be possible to develop an empirical test for time jitter in records having few degrees of freedom. It is unknown whether similar results holds for the aliasing test proposed by Hinich and Wolinsky (1988).

Finally, Monte-Carlo simulations are very important for paleoceanography because record lengths are short, degrees of freedom are typically low, and data and age models typically contain nontrivial amounts of noise. Given these factors, the application of higher order spectral methods and other advanced statistical applications to these data is possible provided that simulations such as those shown above can be done to reinforce the results.

BIBLIOGRAPHY

Adelseck, C.G., Jr., and T.F. Anderson, 1978. The late Pleistocene record of productivity fluctuations in the eastern equatorial Pacific Ocean. *Geology*, 6, 388-391.

Alexandrovitch, J.M. and J.D. Hays, 1989. High-resolution stratigraphic correlation of ODP Leg 111 holes 677A and 677B and DSDP Leg 69 Hole 504, in Becker, K., Sakai, H., et al., *Proc. ODP, Sci. Results, 111*: College Station, TX (Ocean Drilling Program), 263-276.

Archer, D.E., 1991a. Equatorial Pacific calcite preservation cycles: production or dissolution? *Paleoceanography*, 6(5), 561-571.

Archer, D.E., 1991b. Modeling the calcite lysocline, *J. Geophys. Res.*, 96, 17,037-17,050.

Arrhenius, G.O., 1952. Sediment cores from the East Pacific: *Swedish Deep-Sea Expedition Report. 1947-1948*, V. 5, pt. 3, 189-201.

Balakrishnan, A.V., 1962. On the problem of time jitter in sampling, *IRE Trans. Inform. Theory*, 8, 226-236.

Berger, A., 1977. Support for the astronomical theory of climatic change, *Nature*, *268*, 44-45.

Berger, A., 1978a. Long-term variations of caloric insolation resulting from the earth's orbital elements, *Quat. Res.*, *9*, 139-167.

Berger, A., 1978b. A simple algorithm to compute long term variations of daily or monthly insolation, *Contrib. 18*, Inst. d' Astron. et de Geophys. G. Lemaitre, Univ. Cath. de Louvain, Louvain-la-Neuve, Belgium.

Berger, A., 1978c. Long-term variations of daily insolation and Quaternary climatic changes, *J. Atmos. Sci.*, *35*, 2362-2367.

Berger, A., 1988. Milankovitch Theory and Climate. *Reviews of Geophysics, 26* (4), 624-657.

Berger, A., 1989. The spectral characteristics of pre-Quaternary climatic records, and example of the relationship between the astronomical theory and geosciences, in *Climate and Geosciences*, edited by A. Berger et al., Kluwer Academic, Boston, Mass., 47-76.

Berger, A. and M.F. Loutre, 1988. New insolation values for the climate of the last 10 million years, *Sci. Rep. 1988/13*, Inst. d'Astron. et de Geophys. G. Lemaitre, Univ. Cath. de Louvain, Louvain-la-Neuve, Belgium, 1988.

Berger, W.H., 1973. Deep-sea carbonates: Pleistocene dissolution cycles. *J. Foraminiferal Res.*, 3, 187-195.

Birchfield, G.E., and R.W. Grumbine, 1985. "Slow" physics of large continental ice sheets and underlying bedrock and its relation to the Pleistocene Ice Ages, *J. Geophys. Res.*, *90*, 11,294-11,302.

Birchfield, G.E., and J. Weertman, 1978. A note on the spectral response of a model continental ice sheet, *J. Geophys. Res.*, *83*, 4123-4125.

Bond, G., in prep, Evidence of an ~11,000 year climate cycle and implications for Heinrich deposits, the Younger Dryas event and Neoglaciation.

Boyce, R.E., 1976, Definitions and laboratory techniques of compressional sound velocity parameters and wet-water content, wet-bulk density, and porosity parameters by gravimetric and gamma ray attenuation techniques, *In* Schlanger, S.O., E.D. Jackson, et al., *Init. Repts., DSDP, 33*: Washington, DC: (US Govt Printing Office), 931-958.

Boyle, E.A., 1988. The role of vertical chemical fractionation in controlling late Quaternary atmospheric carbon dioxide. *J. Geophys. Res.*, 93: 15,701 - 15,714.

Bretagnon, P., 1984. Accuracy of long term planetary theory, in *Milankovitch and Climate*, edited by A. Berger et al., D. Riedel, Norwell, Mass. 41-53.

Broecker, W.S. and T.-H. Peng, 1982. *Tracers in the Sea.* Palisades, N.Y.: LDGO Press, 690p.

Broecker, W.S., D.L. THurber, J. Goddard, T. Ku, R.K. Matthews, and K.J. Mesolella, 1968. Milankovitch hypothesis supported by precise dating of coral reefs and deep sea sediments. *Science*, *159*, 297-300.

Cox, A. and D. Engebretson, 1985. Change in motion of Pacific plate at 5 Myr BP. *Nature*, *313* (7), 472-474.

Croll, J., 1875. Climate and Time in Their Geological Relations. New York: Appleton.

deMenocal, P., J. Bloemendal, and J. King, 1991. A rock-magnetic record of monsoonal dust deposition to the Arabian Sea: Evidence for a shift in the mode of deposition at 2.4 Ma, *In* Prell, W.L., Niitsuma, N., et al., *Proc. ODP, Sci. Results, 111*: College Station, TX (Ocean Drilling Program), 389-407.

Doose, H., K. Emeis, A. Mix, and D. Schulz-Bijll, (submitted). Alkenone sea surface temperature estimates at site 846. *In* Mayer, L., Pisias, N., et.al., *Proc. ODP, Sci. Results*, 138: College Station Tx (Ocean Drilling Program).

Elgar, S., 1987. Relationships involving third moments and bispectra of a harmonic process, *IEEE Trans. Acoust. Speech Signal Process.*, *35*(12), 1725-1726,.

Elgar, S., and R.T. Guza, 1985. Observations of bispectra of shoaling surface gravity waves, *J. Fluid Mech.*, *161*, 425-448.

Elgar, S., and R.T. Guza, 1988. Statistics of bicoherence, *IEEE Trans. Acoust. Speech Signal Process.*, *36*(10), 1667-1668,

Elgar, S., and G. Sebert, 1989. Statistics of bicoherence and biphase, *J. Geophys. Res.*, *94*, 10,993-10,998.

Farrell, J.W. and T.R. Janecek, 1991. Late Neogene paleoceanography and paleoclimatology of the northeast Indian Ocean (Site 758), *In* Weissel, J., Peirce, J., Taylor, E., Alt, J., et al., *Proc. ODP, Sci. Results, 121:* College Station, TX (Ocean Drilling Program), 297-315.

Farrell, J.W. and W.L Prell, 1989. Climatic change and $CaCO_3$ preservation: An 800,000 year bathymetric reconstruction from the central equatorial Pacific Ocean, *Paleoceanography*, 4(4), 447 -466.

Farrell, J.W., and W.L. Prell, 1991. Pacific $CaCO_3$ preservation and $\delta^{18}O$ since 4 Ma: Paleoceanic and paleoclimatic implications. *Paleoceanography*, 6(4), 485-498.

Finney, B.P., M.W. Lyle, and G.R. Heath, 1988. Sedimentation at MANOP Site H (eastern equatorial Pacific) over the past 400,000 years: climatically induced redox variations and their effects on transition metal cycling. *Paleoceanography*, 3(2), 169-189.

Froelich, P.N., P.N. Malone, D.A. Hodell, P.F. Ciesielski, D.A. Warnke, F. Westall, E.A. Hailwood, D.C. Nobes, J. Fenner, J. Mienert, C.J. Mwenifumbo, and D.W. Muller, 1991, Biogenic opal and carbonate accumulation rates in the subantarctic South Atlantic: The late Neogene of Meteor Rise Site 704, *In* Ciesielski, P.F., Kristoffersen, Y., et. al., *Proc. ODP, Sci. Results, 114:* College Station, TX (Ocean Drilling Program), 515-550.

Gardner, J., 1982. High-resolution carbonate and organic-carbon stratigraphies for the late Neogene and Quaternary from the western Caribbean and eastern equatorial Pacific, *In* Prell, W.L., Gardner, J., et al., *Init. Rpts. DSDP 68:* Washington DC (US Govt Printing Office), 347-364.

Hagelberg, T.K., S. Harris, A. Mix, N. Pisias, and N. Shackleton, (submitted). Refinement of a high resolution continuous sedimentary sequence for the study of equatorial Pacific paleoceanography. *In* Mayer, L., Pisias, N., et.al., *Proc. ODP, Sci. Results*, 138: College Station TX (Ocean Drilling Program).

Hagelberg, T.K., L.A. Mayer, N.G. Pisias, N.J. Shackleton, (submitted). Spatial and temporal variability of late Neogene equatorial Pacific carbonate: ODP Leg 138. *In*, Mayer, L.A., N. Pisias, et al., *Proc. ODP, Sci. Results*, 138: College Station, TX (Ocean Drilling Program).

Hagelberg, T.K. and N.G. Pisias, 1990. Nonlinear response of Pliocene climate to orbital forcing: evidence from the eastern equatorial Pacific. *Paleoceanography,* 5(4), 595-617.

Hagelberg, T.K., N.G. Pisias, and S.L. Elgar, 1991. Linear and nonlinear couplings between orbital forcing and the marine $\delta^{18}O$ record during the late Neogene. *Paleoceanography*, 6 (6), 729-746.

Hagelberg, T.K, Shackleton, N.J, N. Pisias, and Shipboard Scientific Party, 1992. Development of composite depth sections for Sites 844 through 854, *In* Mayer, L., Pisias, N., Janecek, T., et al., *Proc. ODP, Sci. Results, 138*: College Station, TX (Ocean Drilling Program), 79-85.

Harris, S., T. Hagelberg, A. Mix, N Pisias, and N. Shackleton, (submitted). Core-log comparisons between GRAPE and Log density data, *In* Mayer, L., N. Pisias, et. al., *Proc. ODP, Sci. Results, 138:* College Station, TX (Ocean Drilling Program).

Hasselman, K., 1976. Stochastic climate models, Part 1: Theory, *Tellus*, *28*, 473-486.

Hasselman, K., W. Munk, and G. MacDonald, 1963. Bispectra of ocean waves, in *Time Series Analysis*, edited by M. Rosenblatt, John Wiley, New York, 125-139.

Haubrich, R., Earth noises, 5 to 500 millicycles per second, 1, 1965.*J. Geophys. Res.*, *70*, 1415-1427.

Hays, J.D., J. Imbrie, and N.J. Shackleton, 1976. Variations in the Earths orbit: Pacemaker of the Ice Ages. *Science*, 194, 1121-1132.

Hays, J.D., T. Saito, N.D. Opdyke, and L.H. Burckle, 1969. Pliocene-Pleistocene sediments of the equatorial Pacific: their paleomagnetic, biostratigraphic, and climatic record. *Geological Soc. Amer. Bull.*, 80, 1481-1514.

Hays, P.E., N.G. Pisias, and A.K Roelofs, 1987. Paleoceanography of the eastern equatorial Pacific during the Pliocene: A high-resolution radiolarian study, *Paleoceanography*, 4(1), 57-74.

Heath, G.R. and C. Culberson, 1970. Calcite: degree of saturation, rate of dissolution, and the compensation depth in the deep oceans, *Geol. Soc. Amer. Bulletin*, 81, 3157-3160.

Heath, G.R., Rea, D.H., and Levi, S., 1984. Paleomagnetism and accumulation rates of sediments at sites 576 and 578, Deep Sea Drilling Project Leg 86, western North Pacific, *In* Heath, G.R., Burckle, L.H., et al., *Init. Rpts. DSDP, 86:* Washington (U.S. Govt. Printing Office), 459-502.

Heinze, C., E. Maier-Reimer, and K. Winn, 1991. Glacial pCO_2 reduction by the world ocean: experiments with the Hamburg carbon cycle model, *Paleoceanography*, 6(4), 395-430.

Herbert, T.D., and A.G. Fischer, 1986. Milankovitch climatic origin of mid-Cretaceous black shale rhythms in central Italy, *Nature* 321, 739-743.

Herbert, T.D., and S.L. D'Hondt, 1990. Precessional climate cyclicity in Late Cretaceous -Early Tertiary marine sediments: a high resolution chronometer of Cretactous-Tertiary boundary events. *Earth and Planetary Sci. Lett.*, 99, 263-275.

Herbert, T.D. and L.A. Mayer, 1991. Long climatic time series from sediment physical property measurements. *Journ. Sed. Pet.*, 61(7), 1089-1108.

Hilgen, F.J., 1991. Extension of the astronomically calibrated (polarity) time scale to the Miocene/Pliocene boundary. *Earth Planet. Sci. Lett.*, 107, 349-368.

Hinich, M. and C.S. Clay, 1968. The application of the discrete Fourier transform in the estimation of power spectra, coherence, and bispectra of geophysical data. *Rev. Geophysics*, 6 (3), 347-363.

Hinich, M.J. and Wolinsky, M.A., 1988. A test for aliasing using bispectral analysis. *Journ. Amer. Statistical Assoc.*, 83, 402, 499-502.

Imbrie, J., E.A. Boyle, S.C. Clemens, A. Duffy, W.R. Howard, G. Kukla, J. Kutzbach, D.G. Martinson, A. McIntyre, A.C. Mix, B. Molfino, J.J. Morley, L.C. Peterson, N.G. Pisias, W.L. Prell, M.E. Raymo. N.J. Shackleton, and J.R. Toggweiler, in press. On the structure and origin of major glaciation cycles 1. Linear responses to Milankovitch forcing. *Paleoceanography.*

Imbrie, J., J.D. Hays, D.G. Martinson, A. McIntyre, A.C. Mix, J.J. Morley, N.G. Pisias, W.L. Prell, and N. Shackleton, 1984. The orbital theory of Pleistocene climate: Support from a revised chronology of the marine $\delta^{18}O$ record, in *Milankovitch and Climate*, edited by A. Berger et al., D. Riedel, Norwell, Mass., 269-305.

Imbrie, J., and J.Z. Imbrie, 1980. Modeling the climatic response to orbital variations, *Science, 207*, 943-953.

Imbrie, J., and K.P. Imbrie, 1979. *Ice Ages: Solving the Mystery.* Short Hills, New Jersey: Enslow Publishers, 224 pgs.

Imbrie, J., A. McIntyre, and A. Mix, 1989.Oceanic response to orbital forcing in the late Quaternary: observational and experimental strategies, in *Climate and Geosciences*, edited by A. Berger et al., Kluwer Academic, Boston, Mass., 121-163.

Jenkins, G.M. and D.G. Watts, 1968. *Spectral Analysis and its applications*. San Francisco: Holden-Day, 525 pgs.

Karlin, K., W.F. Ruddiman, and A. McIntyre, 1989, Comparison of late Plieocene and late Pleistocene sea-surface temperatures of the equatorial Atlantic divergence, *In* Ruddiman, W., Sarnthein M., et al., *Proc. ODP, Sci. Results, 108:* College Station, TX (Ocean Drilling Program).

Kemp, A.E.S. and J. Baldauf, (submitted). Origins and paleoceanographic significance of laminated diatom ooze from the eastern equatorial Pacific. *In* Mayer, L., Pisias, N., et.al., *Proc. ODP, Sci. Results*, 138: College Station TX (Ocean Drilling Program).

Kent, D.V., and Spariosu, D.J., 1982. Magnetostratigraphy of Caribbean Site 502 hydraulic piston cores, in, Prell, W.L., Gardner, J., et al., Init. Rpts. DSDP 68: Washington DC (US Govt Printing Office), 419-433.

Kim, Y.C., and E.J. Powers, 1979. Digital bispectral analysis and its applications to nonlinear wave interactions, *IEEE Trans. Plasma Sci., PS-7*(2), 120-131.

Kim Y.C., J.M. Beall, and E.J. Powers, 1980. Bispectrum and nonlinear wave coupling. *Phys. Fluids, 23*(2), 258-263.

Kominz, M.A., G.R. Heath, T.-L. Ku, and N.G. Pisias, 1979. Bruhnes time scales and the interpretation of climatic change. *Earth Planet. Sci. Lett.*, 45, 394-410.

Kominz, M.A., and N.G. Pisias, 1979. Pleistocene climate: deterministic or stochastic? *Science*, 204, 171-173.

Le, J., A. Mix, and N.J. Shackleton, (submitted). Pleistocene paleoceanography in the eastern equatorial Pacific from planktonic foraminifera: a high-resolution record from ODP Site 846. *In* Mayer, L., Pisias, N., et.al., *Proc. ODP, Sci. Results*, 138: College Station TX (Ocean Drilling Program).

Le Treut, H., and M. Ghil, 1983. Orbital forcing, climatic interactions, and glaciation cycles, *J. Geophys. Res.*, *88*, 5167-5190.

Luz, B. and N.J. Shackleton, 1975. $CaCO_3$ solution in the tropical east Pacific druing the past 130,000 years. *In* W.V. Sliter, A.W. Be, and W.H. Berger,eds. *Dissolution of Deep-Sea Carbonates*, Foraminiferal Res. Ser., Washington D.C.: Cushman Foundation, 142-150.

Lyle, M.W., D.W. Murray, B.P. Finney, J. Dymond, J.M. Robbins, and K. Brooksforce, 1988. The record of late Pleistocene biogenic sedimentation in the eastern tropical Pacific Ocean. *Paleoceanography*, 3(1), 39-59.

Maasch, K.A., and B. Saltzman, 1990. A low-order dynamical model of global climatic variability over the full Pleistocene, *J. Geophys. Res.*, *95*, 1955-1963.

MacKillop, K., J. Farrell, Jarret, and K. Moran, 1993 (submitted). Consolidation behavior of eastern equatorial Pacific sediments (Eastern Transect), *In* Mayer, L., N. Pisias, et. al., *Proc. ODP, Sci.Results, 138:* College Station, TX (Ocean Drilling Program).

Maier-Reimer, E., U. Mikolajewicz, and T.Crowley, 1990. Ocean general circulation model sensitivity experiment with an open Central American Isthmus. *Paleoceanography*, 5(3), 349-366.

Martinson, D.G., W. Menke, and P. Stoffa, 1982. An inverse approach to signal correlation, *Journ. Geophys. Res.*, 87, B6, 4807-4818.

Martinson, D.G., N.G. Pisias, J.D. Hays, J. Imbrie, T.C. Moore, Jr. and N.J. Shackleton, 1987. Age dating and the orbital theory of the Ice Ages: Development of a high-resolution 0 to 300,000 year chronostratigraphy. *Quat. Res.* 27, 1-29.

Masuda, A., and Y-Y Kuo, 1981. A note on the imaginary part of bispectra, *Deep Sea Res.*, *28A*(3), 213-222.

Matteucci, G., 1989. Orbital forcing in a stochastic resonance model of the Late Pleistocene climatic variations, *Clim. Dyn.*, *3*, 179-190.

Mayer, L.A., 1978. Deep sea carbonates: acoustic, physical, and stratigraphic properties. *Journ. Sed. Pet.*, 49(3), 819-836.

Mayer, L.A., 1980, Deep-sea carbonates: physical property relationships and the origin of high-frequency acoustic reflectors, *Marine Geology* 38, 165-183.

Mayer, L.A., 1991, Extraction of high-resolution carbonate data for palaeoclimate reconstruction, *Nature* 352, 148-150.

Mayer, L.A., N. Pisias, T. Janecek, et al., 1992. *Proc. Ocean Drilling Program, Initial Reports*, 138: College Station, TX (Ocean Drilling Program).

Mayer, L.A., N.J. Shackleton, T. Hagelberg, N. Pisias, C. Ware, K. Marinelli, and the Shipboard Scientific Party, 1992, 3-D visualization of evolutionary spectra of Leg 138 carbonate records. *Proc., Fourth Intl. Conf. on Paleoceanography*, Kiel, Germany, 21-25 September, 1992, 192.

Mayer, L.A., T.H. Shipley, and E.L. Winterer, 1986, Equatorial Pacific seismic reflectors as indicators of global oceanographic events, *Science,* 233, 761-764.

McComas, C.H., and M.G. Briscoe, 1980. Bispectra of internal waves. *J. Fluid Mech.*, 97, 1, 205-213.

Milankovitch, M.M., 1941. Kanon der Erdbestrahlung, Royal Serbian Academy Special Publication 132, Section of Mathematical and Natural Sciences, 33. (Canon of insolation and the ice-age problem, English translation by Israel Program for Scientific Translations, Jerusalem, 1969.)

Mix, A.C., T. Hagelberg, A. Morey, N. Pisias, B. Rugh, N. Shackleton, and J. Wilson, (submitted). Benthic foraminiferal $\delta^{18}O$ and $\delta^{13}C$ from ODP Site 849: Implications for paleoproductivity and global ocean circulation. *In* Mayer, L., Pisias, N., et.al., *Proc. ODP, Sci. Results*, 138: College Station TX (Ocean Drilling Program).

Moore, T.C., Jr., N.G. Pisias, and D.A. Dunn, 1982. Carbonate time series of the Quaternary and late Miocene sediments in the Pacific Ocean: A spectral comparison. *Marine Geology*, 46, 217-233.

Moore, T.C., Jr., N.G. Pisias, and G.R. Heath, 1977. Climate changes and lags in Pacific carbonate preservation, sea surface temperature, and global ice volume. *In* N.R. Andersen and A. Malahoff, eds.,*The Fate of Fossil Fuel CO_2 in the Oceans*, New York: Plenum Publishing, 145-165.

Murray, D.W., 1987. Spatial and temporal variations in sediment accumulation in the central tropical Pacific. Ph.D. dissertation, Oregon State University, Corvallis, 220 pages.

Murray, D.W., J. Farrell, and V. McKenna, (submitted). Biogenic sedimentation at ODP Site 847, eastern equatorial Pacific during the past three million years. *In* Mayer, L., Pisias, N., et.al., *Proc. ODP, Sci. Results*, 138: College Station TX (Ocean Drilling Program).

Murray, D.W. and W.L. Prell, 1991. Pliocene to Pleistocene variations in calcium carbonate, organic carbon, and opal on the Owen Ridge, Northern Arabian Sea, *In* Prell, W.L., Niitsuma, N., et al., *Proc. ODP, Sci. Results, 111*: College Station, TX (Ocean Drilling Program), 343-363.

Nikias, C.L., and M.R. Raghuveer, 1987. Bispectrum estimation: A digital signal processing framework, *Proc. IEEE, 75*, 869-891.

Oerlemans, J., 1982. Glacial cycles and ice sheet modelling, *Clim. Change, 4*, 353-374.

Park, J., and S. D'Hondt, 1992. Late Cretaceous precessional cycles in double time: evidence from South Atlantic DSDP Site 516F. *EOS, Trans. AGU*, Fall 1992 meeting, 99.

Parker, F.L., and W.H. Berger, 1971. Faunal and solution patterns of planktonic Foraminifera in surface sediments of the South Pacific. *Deep Sea Research*, 18, 73-107.

Pedersen, T.F., Increased productivity in the eastern equatorial Pacific during the last glacial maximum (19,000 to 14,000 yr B.P.), *Geology*, 11, 16-19.

Peltier, R., 1982. Dynamics of the ice age earth, *Adv. Geophys., 24*, 1-146.

Pisias, N.G., 1983. Geologic time series from deep-sea sediments: time scales and distortion by bioturbation. *Marine Geology*, 51, 99-113.

Pisias, N.G., L. Mayer, T. Hagelberg, and N. Shackleton, (submitted). Response to equatorial Pacific sedimentation to orbital forcing during the past XX million years: the movie. *In*, Mayer, L.A., N. Pisias, et al., *Proc. ODP, Sci. Results*, 138: College Station, TX (Ocean Drilling Program).

Pisias, N.G. and A.C. Mix, 1988. Aliasing of the geologic record and the search for long-period Milankovitch cycles. *Paleoceanography*, 3 (5), 613-619.

Pisias, N.G., A.C. Mix, and R. Zahn, 1990. Nonlinear response in the global climate system: evidence from benthic oxygen isotopic record in core RC13-110, *Paleoceanography*, *5*(2), 147-160.

Pisias, N.G., and T.C. Moore, Jr., 1981. The evolution of Pleistocene climate: A time series approach, *Earth Planet. Science Letters*, 52, 450-458.

Pisias, N.G., T.C. Moore, Jr., and A. Roelofs (submitted). Spatial reconstructions of radiolarian assemblages. *In* Mayer, L., Pisias, N., et.al., *Proc. ODP, Sci. Results*, 138: College Station TX (Ocean Drilling Program).

Pisias, N.G., and W.L. Prell, 1985. Changes in calcium carbonate accumulation in the equatorial Pacific during the last Cenozoic: Evidence from HPC Site 572, *In The Carbon Cycle and Atmospheric CO_2: Natural Variations Archean to Present*, Geophysical Monograph 32, American Geophysical Union, 443 - 454.

Pisias, N.G. and D.K Rea, 1988. Late Pleistocene paleoclimatology of the central equatorial Pacific: sea surface response to the southeast trade winds. *Paleoceanography* 3(1), 21-38.

Pisias, N.G., L.A. Mayer, N. Shackleton, T. Hagelberg, A. Mix, and ODP Leg 138 Shipboard Scientific Party, 1992. Temporal response of the east Pacific carbonate system to orbital forcing: evidence form site 849 leg 138. *Proc., Fourth Intl. Conf. on Paleoceanography*, Kiel, Germany, 21-25 September, 1992, 228.

Pollard, D., 1983. A coupled climate-ice sheet model applied to the Quaternary ice ages, *J. Geophys. Res.*, *88*, 7705-7718.

Prahl, F.G., L.A. Muehlhausen, and M. Lyle, 1989. An organic geochemical assessment of oceanographic conditions at MANOP site C over the past 26,000 years. *Paleoceanography*, 4(5), 495-510.

Prell, W.L., Gardner, J. et al., 1982, *Init. Rpts. DSDP 68:* Washington DC (US Govt Printing Office).

Ravelo, A.C., R. Pacanowski, and S.G.H. Philander, 1992. Changes in the east tropical Pacific seasonal thermocline over the past 2.5 ma: observation and model comparison. *Trans., AGU*, 73(43), 249.

Raymo, M.E., W.F. Ruddiman, J. Backman, B.M. Clement, and D.G. Martinson, 1989. Late Pliocene variation in Northern Hemisphere ice sheets and North Atlantic deep water circulation. *Paleoceanography,* 4(4), 413-446.

Raymo. M.E., W.F. Ruddiman, and P.N. Froelich, 1988. Influence of late Cenozoic mountain building on ocean geochemical cycles. *Geology*, 16, 649-653.

Raymo, M.E., W.F. Ruddiman, J. Backman, B.M. Clement, and D.G. Martinson, 1989. Late Pliocene variation in Northern Hemisphere ice sheets and North Atlantic deep water circulation. *Paleoceanography*, 4(4), 413-446.

Raymo, M.E., W.F. Ruddiman, N.J. Shackleton, and D.W. Oppo, 1990. Evolution of Atlantic-Pacific $\delta^{13}C$ gradients over the last 2.5 my. *Earth and Planetary Science Letters*, 97, 353-368.

Rea, D.K., N.G. Pisias, and T. Newberry, 1991. Late Pleistocene paleoclimatology of the central equatorial Pacific: flux patterns of biogenic sediments. *Paleoceanography*, 6(2), 227-244.

Rice, J.A., 1988. *Mathematical Statistics and Data Analysis.* Pacific Grove, CA: Wadsworth and Brooks/Cole, 595 pgs.

Robinson, S.G., 1990. Applications for whole-core magnetic susceptibility measurements of deep-sea sediments: Leg 115 results, *In* Duncan, R.A., Backman, J., Peterson, L.C., et al., *Proc. ODP, Sci. Results, 115:* College Station TX (Ocean Drilling Program), 737-771.

Ruddiman, W.F., D. Cameron, and B.M. Clement, 1987, Sediment disturbance and correlation of offset holes drilled with the hydraulic piston corer: Leg 94, *In* Ruddiman, W.F., Kidd, R.B., Thomas, E. et al., *Init. Repts. DSDP, 94:* Washington (US Govt. Printing Office), 615-634.

Ruddiman, W.F., and M.E. Raymo, 1988. Northern Hemisphere climate regimes during the past 3 Ma: possible tectonic connections, *Philos. Trans. R. Soc. London, Ser. B, B318*, 411-430.

Ruddiman, W.F., M.E. Raymo, D.G. Martinson, B.M. Clement, and D.G. Martinson, 1989. Pleistocene Evolution: Northern Hemisphere ice sheets and North Atlantic Ocean. *Paleoceanography*, 4(4), 353-412.

Ruddiman, W., Sarnthein, M., et al., 1988, *Proc. Ocean Drilling Program, Init. Rpts 108:* College Station, TX (Ocean Drilling Program).

Saltzman, B., 1985. Paleoclimatic modeling, in *Paleoclimatic Analysis and Modeling*, edited by A.D. Hecht, John Wiley, New York, 341-396.

Saltzman, B., and K.A. Maasch, 1988. Carbon cycle instability as a cause of the late Pleistocene Ice Age oscillations: Modeling the asymmetric response, *Global Biogeochem. Cycles*, *2*(2), 177-185.

Saltzman, B., and A. Sutera, 1984. A model of the internal feedback system involved in late Quaternary climatic variations, *J. Atmos. Sci.*, *41*(5), 736-745.

Saltzman, B., A.R. Hansen, and K.A. Maasch, 1984. The late Quaternary glaciations as the response of a three-component feedback system to earth-orbital forcing, *J. Atmos. Sci.*, *41*(23), 3380-3389.

Schlanger, S.O., E.D. Jackson, et al., 1976, *Proc. DSDP, Init. Rpts. 33:* Washington D.C. (US Govt. Printing Office).

Shackleton, N.J., A. Berger, and W.R. Peltier, 1990, An alternative astronomical calibration of the lower Pleistocene timescale based of ODP Site 677., *Trans., Royal Soc. of Edinburgh: Earth Sciences,* 81, 251-261.

Shackleton, N.J., S. Crowhurst, T. Hagelberg, and N. Pisias (submitted) Astronomical calibration of the late Neogene timescale. *In* Mayer, L., Pisias, N., et.al., *Proc. ODP, Sci. Results*, 138: College Station TX (Ocean Drilling Program).

Shackleton, N.J., S.J. Crowhurst, N. Pisias, T. Hagelberg, D. Schneider, A. Mix, and ODP Leg 138 Shipboard Party, 1992. An astronomically calibrated Pliocene time scale based on Leg 138 GRAPE density records, (abs), *Proc., Fourth Intl. Conf. on Paleoceanography,* Kiel, Germany, 21-25 September 1992, 240.

Shackleton, N. J., and M.A. Hall, (submitted). Pliocene stable isotope stratigraphy of site 846. *In* Mayer, L., Pisias, N., et.al., *Proc. ODP, Sci. Results*, 138: College Station TX (Ocean Drilling Program).

Shackleton, N.J., and M.A. Hall, 1989. Stable isotope history of the Pleistocene at ODP Site 677, *In,* Becker, K. et al., *Proc. Ocean Drill. Program Sci. Results, 111*, 295-316.

Shackleton, N.J., and Hall, M.A., 1983. Stable isotope record of hole 504 sediments: high resolution record of the Pleistocene, *In* Cann, J.R., Langseth, M.G., Honnorez, J., Von Herzen, R.P., White, S.M., et al., *Init. Rpts. DSDP, 69:* Washington (U.S. Govt. Printing Office), 431-441.

Shackleton, N.J., Hall, M.A., and U. Bleil, 1984. Carbon-isotope stratigraphy, Site 577 leg 86, *In* Heath, G.R., Burckle, L.H., et al., *Init. Rpts. DSDP, 86:* Washington (U.S. Govt. Printing Office), 503-511.

Shackleton, N.J. and N.G. Pisias, 1985. *Atmospheric carbon dioxide, orbital forcing, and climate, in The Carbon Cycle and Atmospheric CO_2: Natural Variations Archean to Present*, Geophysical Monograph 32, American Geophysical Union, 303-317.

Shackleton, N.J. and Shipboard Scientific Party, 1992, Sedimentation rates: toward a GRAPE density stratigraphy for Leg 138 carbonate sections. *In* Mayer, L., Pisias, N., Janecek, T., et al., *Proc. ODP, Init. Rpts. 138:* College Station, TX (Ocean Drilling Program), 87-92.

Sharfer, I. and H. Messer, in press, The bispectrum of sampled data: Part I - Detection of the sampling jitter. *IEEE, Acoustics, Speech, Signal Processing.*

Sneider, R.K., 1985, The origin of the 100,000 year cycle in a simple ice age model, *J. Geophys. Res., 90*, 5661-5664.

Thomson, D.J, 1989. Multi-Window bispectrum estimates. *Proceedings of the workshop on higher order spectral analysis*, J.M. Mendel and C.L. Nikias, eds., Vail Colorado, USA, 19-23.

van Andel, Tj.H., G.R. Heath, and T.C. Moore, 1975. Cenozoic tectonics, sedimentation and paleoceanography of the central equatorial Pacific, *Mem. Geol. Soc. Am.*, 143, 134 pgs.

Wigley, T.M.L., 1976. Spectral analysis and the astronomical theory of climatic change, *Nature, 264*, 629-631.

Winograd, I.J., T.B. Coplen, J.M. Landwehr, A.C. Riggs, K.R. Ludwig, B. J. Szabo, P.T. Kolesar, and K.M. Revesz, 1992. Continuous 500,000-year climate record from vein calcite in Devils Hole, Nevada, *Science*, 258, 255-260.

APPENDIX

APPENDIX I. INTERVALS OF CORED SECTION NOT INCLUDED IN COMPOSITE DEPTH SECTION FORMATION OWING TO CORING DISTURBANCE OR ABSENCE OF GRAPE MEASUREMENTS. WITH THE EXCEPTION OF DISCRETE GRAPE MEASUREMENTS THAT ARE OUTLIERS, THE REMAINDER OF MEASUREMENTS IN THESE CORES WERE USED IN REVISING COMPOSITE DEPTHS AND COMPILING STACKED GRAPE RECORDS FOR EACH SITE.

SITE	HOLE	CORE	SECTION	SECTION DEPTH	ODP DEPTH	MCD DEPTH
846	B	3H	1	0-6 cm	16.50 - 16.56	18.58 - 18.64
846	B	3H	1	78-142 cm	17.28 - 17.92	19.36 - 20.00
846	B	3H	7	35-42 cm	25.85 - 25.92	27.93 - 28.00
846	B	4H	7	51-105 cm	35.51 - 36.06	38.66 - 39.21
846	B	5H	1	0-18 cm	35.50 - 35.68	40.70 - 40.88
846	B	5H	7	76-101 cm	45.26 - 45.51	50.49 - 50.74
846	B	6H	1	0-5 cm	45.00 - 45.05	51.50 - 51.55
846	B	6H	3	0-150 cm	47.94 - 49.53	54.44 - 56.03
846	B	6H	6	115-144	53.65 - 53.94	60.15 - 60.44
846	B	7H	1	0-11 cm	54.50 - 54.61	62.80 - 62.91
846	B	7H	7	45-73 cm	63.95 - 64.23	72.28 - 72.56
846	B	8H	1	0-76 cm	64.00 - 65.76	73.70 - 74.46
846	B	9H	1	27-124 cm	73.77 - 74.74	83.92 - 84.89
846	B	9H	7	22-54 cm	82.72 - 83.04	92.90 - 93.22
846	B	10H	1	0-58 cm	83.00 - 83.58	95.55 - 96.13
846	B	10H	5	145-150 cm	90.45 - 90.50	103.00 -103.05
846	B	10H	6	0-38 cm	90.50 - 90.88	103.05 - 103.43
846	B	10H	7	92-123 cm	92.92 - 93.23	105.47 - 105.78
846	B	11H	1	0-9 cm	92.50 - 92.59	106.03 - 106.12
846	B	11H	7	66-83 cm	102.06 - 102.23	115.59 - 115.76
846	B	12H	1	0-37 cm	102.00 - 102.37	116.80 - 117.17
846	B	12H	2	0-155 cm	103.45 - 105.00	118.25 - 119.80
846	B	12H	3	0-7 cm	105.00 - 105.07	119.80 - 119.87
846	B	12H	7	35-80 cm	111.35 - 111.80	126.15 - 126.60
846	B	13H	1	0-42 cm	111.50 - 111.92	127.95 - 128.37
846	B	13H	7	52-112 cm	121.02 - 121.62	137.50 - 138.10
846	B	14H	1	0-45 cm	121.00 - 121.45	138.15 - 138.60
846	B	14H	6	139-150 cm	129.89 - 130.00	147.04 - 147.15
846	B	14H	7	0-50 cm	130.00 - 130.50	147.15 - 147.65
846	B	15H	1	0-33 cm	130.50 - 130.83	150.20 - 150.53
846	B	16H	1	0-150 cm	140.00 - 141.50	160.20 - 161.70
846	B	16H	2	0-30 cm	141.50 - 141.80	161.70 - 162.00
846	B	16H	7	54-82 cm	149.54 - 149.82	169.74 - 170.02
846	B	17H	1	0-24 cm	149.50 - 149.74	170.75 - 170.99
846	B	17H	7	82-112 cm	159.32 - 159.62	180.60 - 180.90
846	B	18H	1	0-12 cm	159.00 - 159.12	180.85 - 180.97
846	B	18H	7	50-117 cm	168.50 - 169.17	190.35 - 191.02
846	B	19H	1	0-28 cm	168.50 - 168.78	192.30 - 192.58
846	B	19H	7	87-112 cm	178.37 - 178.62	202.20 - 202.45
846	B	20H	1	0-16 cm	178.00 - 178.16	203.60 - 203.76
846	B	20H	5	115-150 cm	185.15 - 185.50	210.75 - 211.10
846	B	20H	6	0-68 cm	185.50 - 186.18	211.10 - 211.78
846	B	20H	7	0-50 cm	187.00 - 187.50	212.60 - 213.10

APPENDIX 1, CTD.

SITE	HOLE	CORE	SECTION	SECTION DEPTH	ODP DEPTH	MCD DEPTH
846	B	21H	1	0-86 cm	187.50 - 188.36	214.48 - 215.34
846	B	21H	7	72-115 cm	197.22 - 197.65	224.20 - 224.63
846	B	22H	1	0-11 cm	197.00 - 197.11	227.45 - 227.56
846	B	22H	1	60-146 cm	197.60 - 198.46	228.05 - 228.91
846	B	22H	7	34-110 cm	206.34 - 207.10	236.79 - 237.55
846	B	23X	1	0-5 cm	206.50 - 206.55	240.50 - 240.55
846	B	23X	7	49-70 cm	215.99 - 216.20	249.99 - 250.20
846	B	24X	1	0-8 cm	216.20 - 216.28	251.60 - 251.68
846	B	25X	4	144-150 cm	231.64 - 231.70	266.74 - 266.80
846	C	1H	1	0-23 cm	2.50 - 2.73	2.85 - 3.08
846	C	2H	7	57-85 cm	21.56 - 21.84	21.09 - 21.37
846	C	3H	1	0-14 cm	21.50 - 21.64	24.50 - 24.64
846	C	4H	7	80-109 cm	40.80 - 41.09	44.00 - 44.29
846	C	5H	1	0-92 cm	40.50 - 41.42	44.55 - 45.50
846	C	5H	7	80-116 cm	50.30 - 50.66	54.38 - 54.74
846	C	6H	1	0-25 cm	50.00 - 50.25	56.95 - 57.20
846	C	6H	6	89-92 cm	58.39 - 58.42	65.34 - 65.37
846	C	7H	1	0-50 cm	59.50 - 60.00	66.40 - 66.90
846	C	7H	3	104-146 cm	63.54 - 63.96	70.47 - 70.89
846	C	7H	7	56-88 cm	69.06 - 69.28	75.99 - 76.61
846	C	8H	1	0-150 cm	69.00 - 70.50	76.60 - 78.10
846	C	8H	2	0-82 cm	70.50 - 71.32	78.10 - 78.92
846	C	9H	1	0-6 cm	78.50 - 78.56	89.75 - 89.81
846	C	9H	6	126-134cm	87.26 - 87.34	98.54 - 98.62
846	C	10H	1	0-37 cm	88.00 - 88.37	101.65 - 102.02
846	C	10H	1	135-150 cm	89.35 - 89.50	103.00 - 103.15
846	C	10H	2	0-43 cm	89.50 - 89.93	103.15 - 103.58
846	C	10H	7	67-105 cm	97.67 - 97.95	111.32 - 111.60
846	C	11H	1	0-18 cm	97.50 - 97.68	111.60 - 111.78
846	C	11H	6	133-151 cm	106.33 - 106.51	120.47 - 120.65
846	C	12H	1	0-14 cm	107.00 - 107.14	122.55 - 122.69
846	C	12H	1	71-96 cm	107.71 - 107.96	123.26 - 123.51
846	C	12H	6	83-150 cm	115.33 - 116.00	130.88 - 131.55
846	C	12H	7	0-48 cm	116.00 - 116.48	131.55 - 132.07
846	C	13H	1	0-64 cm	116.50 - 117.14	133.00 - 133.64
846	C	13H	7	36-52 cm	125.86 - 126.02	142.36 - 142.52
846	C	14H	1	0-31 cm	126.00 - 126.31	144.40 - 144.71
846	C	14H	6	113-150 cm	134.63 - 135.00	153.03 - 153.40
846	C	15H	1	0-48 cm	135.50 - 135.98	154.00 - 154.48
846	C	15H	2	141-150 cm	138.41 - 138.50	156.91 - 157.00
846	C	15H	3	0-20 cm	138.50 - 138.70	157.00 - 157.20
846	C	15H	5	136-143 cm	142.86 - 143.34	161.36 - 161.84
846	C	15H	7	27-51 cm	144.77 - 145.01	163.27 - 163.51
846	C	16H	1	0-150 cm	145.00 - 146.50	165.70 - 167.20
846	C	16H	2	0-20 cm	146.50 - 146.70	167.20 - 167.40
846	C	16H	2	69-78 cm	147.19 - 147.28	167.89 - 167.98
846	C	16H	2	113-122 cm	147.63 - 147.72	168.33 - 168.42
846	C	16H	6	110-150 cm	153.60 - 154.00	174.30 - 174.70
846	C	16H	7	50-55 cm	154.50 - 154.55	175.20 - 175.25
846	C	17H	7	34-53 cm	163.84 - 164.03	185.34 - 185.53

APPENDIX 1, CTD.

SITE	HOLE	CORE	SECTION	SECTION DEPTH	ODP DEPTH	MCD DEPTH
846	C	18H	1	0-20 cm	164.00 - 164.20	187.20 - 187.40
846	C	18H	5	141-150 cm	171.41 - 171.50	194.61 - 194.70
846	C	18H	6	0-150 cm	171.50 - 173.00	194.70 - 196.20
846	C	18H	7	0-30 cm	173.00 - 173.30	196.20 - 196.50
846	C	19H	1	0-34 cm	173.50 - 173.84	197.20 - 197.54
846	C	19H	7	36-51 cm	182.86 - 183.01	206.56 - 206.71
846	C	20H	1	0-6 cm	183.00 - 183.06	208.30 - 208.36
846	D	1H	1	0-8 cm	4.00 - 4.08	3.00 - 3.08
846	D	1H	1	50-120 cm	4.50 - 5.20	3.50 - 4.20
846	D	1H	6	129-150 cm	12.79 - 13.00	11.79 - 12.00
846	D	1H	7	0-12 cm	13.00 - 13.12	12.00 - 12.12
846	D	2H	1	0-14 cm	13.50 - 13.64	15.40 - 15.54
846	D	2H	5	130-150 cm	19.78 - 19.98	21.68 - 21.88
846	D	2H	6	120-145cm	21.18 - 21.43	23.08 - 23.33
846	D	3H	1	0-52 cm	23.00 - 23.52	24.70 - 25.22
846	D	3H	7	58-73 cm	32.58 - 32.63	34.28 - 34.43
846	D	4H	1	0-120 cm	32.50 - 33.70	36.10 - 37.30
846	D	4H	7	75-91 cm	42.45 - 42.61	45.85 - 46.01
846	D	5H	1	0-11 cm	42.00 - 42.11	47.60 - 47.71
846	D	6H	6	24-150 cm	59.24 - 60.50	64.64 - 65.90
846	D	6H	7	0-69 cm	60.50 - 61.19	65.90 - 66.59
846	D	7H	1	0-38 cm	58.80 - 59.18	67.20 - 67.58
846	D	7H	7	57-65 cm	68.37 - 68.45	76.77 - 77.85
846	D	8H	1	0-76 cm	68.30 - 69.06	77.70 - 78.46
846	D	9H	1	0-53 cm	77.80 - 78.33	88.20 - 88.73
846	D	9H	6	0-150 cm	85.25 - 86.75	95.65 - 97.15
846	D	9H	7	78-93 cm	87.58 - 87.73	97.98 - 98.13
846	D	10H	1	0-13 cm	87.30 - 87.43	98.60 - 98.73
846	D	10H	7	82-87 cm	97.12 - 97.17	108.42 - 108.47
846	D	11H	1	0-24 cm	96.80 - 97.04	109.20 - 109.44
846	D	11H	2	71-94 cm	99.01 - 99.24	111.41 - 111.64
846	D	11H	7	136-150 cm	105.66 - 105.80	118.06 - 118.20
846	D	11H	7	0-23 cm	105.80 - 106.03	118.20 - 118.43
846	D	12H	1	0-12 cm	106.30 - 106.42	119.80 - 119.92
846	D	12H	2	119-138 cm	108.99 - 109.18	122.49 - 122.68
846	D	12H	7	10-40 cm	115.40 - 115.70	128.90 - 129.30
846	D	13H	1	0-5 cm	115.80 - 115.85	130.40 - 130.45
846	D	13H	7	67-81 cm	125.47 - 125.61	140.07 - 140.21
846	D	14H	1	0-26 cm	125.30 - 125.56	142.10 - 142.36
846	D	14H	2	129-150 cm	128.09 - 128.30	144.89 - 145.10
846	D	14H	6	111-123cm	133.91 - 132.03	150.71 - 150.83
846	D	15H	1	0-30 cm	134.80 - 135.10	152.80 - 153.10
846	D	15H	7	80-87 cm	144.60 - 144.67	162.60 - 162.67
846	D	16H	1	0-15 cm	144.30 - 144.45	164.30 - 164.45
846	D	16H	7	53-73 cm	153.83 - 154.03	173.83 - 174.03
846	D	17H	1	0-12 cm	153.80 - 153.92	174.60 - 174.72
846	D	17H	7	59-69 cm	163.39 - 163.49	184.19 - 184.29
846	D	18X	1	0-54 cm	163.30 - 163.84	185.40 - 185.94
846	D	19X	1	0-47 cm	172.80 - 173.27	195.70 - 196.17
846	D	19X	7	23-45 cm	182.03 - 182.25	204.93 - 205.15

APPENDIX 1, CTD.

SITE	HOLE	CORE	SECTION	SECTION DEPTH	ODP DEPTH	MCD DEPTH
846	D	20X	1	0-34 cm	181.80 - 182.14	207.10 - 207.44
846	D	20X	6	83-150 cm	190.13 - 190.80	215.43 - 216.10
846	D	20X	7	0-52 cm	190.80 - 191.32	216.10 - 216.62
846	D	21X	1	0-99 cm	191.40 - 192.39	221.95 - 222.94
846	D	21X	7	26-55 cm	200.66 - 200.95	231.21 - 231.50
846	D	22X	1	0-14 cm	201.10 - 201.24	231.45 - 231.59
846	D	22X	7	40-43 cm	210.50 - 210.53	240.85 - 240.88
846	D	23X	1	0-150 cm	210.70 - 212.50	244.55 - 246.05
846	D	23X	2	0-63 cm	212.50 - 213.13	246.05 - 246.68
846	D	24X	7	45-50 cm	229.85 - 229.90	263.20 - 263.41
847	A	1H	1	0-23 cm	0.00 - 0.23	1.80 - 2.03
847	B	1H	1	0-10 cm	0.00 - 0.11	0.00 - 0.11
847	B	1H	5	36-38 cm	6.36 - 6.38	6.36 - 6.38
847	B	2H	1	0-30 cm	6.50 - 6.80	6.63 - 6.93
847	B	2H	7	19-32 cm	15.69 - 16.82	15.82 - 16.95
847	B	3H	1	0-25 cm	16.00 - 16.25	16.35 - 16.60
847	B	3H	7	75-80 cm	25.75 - 25.80	26.10 - 26.15
847	B	4H	1	0-7 cm	25.50 - 25.57	28.33 - 28.40
847	B	4H	7	68-80 cm	35.18 - 35.30	37.89 - 38.01
847	B	5H	1	0-34 cm	35.00 - 35.34	37.80 - 38.14
847	B	5H	7	69-83 cm	44.68 - 44.82	47.48 - 47.62
847	B	6H	1	0-8 cm	44.50 - 44.58	49.58 - 49.66
847	B	6H	7	75-82 cm	54.25 - 54.32	59.33 - 59.40
847	B	7H	1	0-8 cm	54.00 - 54.08	60.75 - 60.83
847	B	7H	7	67-82 cm	63.67 - 63.82	70.42 - 70.57
847	B	8H	1	0-17 cm	63.50 - 63.67	71.68 - 71.85
847	B	8H	6	139-150 cm	72.39 - 72.50	80.57 - 80.68
847	B	9H	1	0-26 cm	73.00 - 73.26	82.48 - 82.74
847	B	9H	7	72-83 cm	82.72 - 82.83	92.20 - 92.31
847	B	10H	1	0-150 cm	82.50 - 84.00	92.73 - 94.23
847	B	10H	2	0-28 cm	84.00 - 84.28	94.23 - 94.51
847	B	10H	4	119-150 cm	88.19 - 89.00	98.42 - 98.73
847	B	10H	5	0-44 cm	89.00 - 89.44	98.73 - 99.17
847	B	10H	7	76-88 cm	92.26 - 92.38	102.49 - 102.61
847	B	11H	1	0-26 cm	92.00 - 92.26	104.90 - 105.16
847	B	11H	1	113-129 cm	93.13 - 93.29	106.03 - 106.19
847	B	11H	7	0-52 cm	100.84 - 101.36	113.74 - 114.26
847	B	12H	1	0-20 cm	101.50 - 101.70	114.53 - 114.73
847	B	12H	7	69-80 cm	111.19 - 111.30	124.22 - 124.33
847	B	13H	1	0-56 cm	111.00 - 111.56	125.00 - 125.56
847	B	13H	7	65-77 cm	120.65 - 120.77	134.65 - 134.77
847	B	14H	1	0-7 cm	120.50 - 120.57	135.98 - 136.05
847	B	14H	7	49-62 cm	129.99 - 130.22	145.47 - 145.60
847	C	1H	1	0-27 cm	2.00 - 2.27	2.40 - 2.6
847	C	1H	7	62-74 cm	11.62 - 11.74	12.02 - 12.14
847	C	2H	1	0-7 cm	11.50 - 11.57	13.18 - 13.25
847	C	3H	7	81-85 cm	30.81 - 30.85	33.21 - 33.25
847	C	4H	1	0-30 cm	30.50 - 30.80	33.80 - 34.10
847	C	4H	7	66-69 cm	40.16 - 40.19	43.46 - 43.49
847	C	5H	7	68-82 cm	49.68 - 49.82	54.18 - 54.32

APPENDIX 1, CTD.

SITE	HOLE	CORE	SECTION	SECTION DEPTH	ODP DEPTH	MCD DEPTH
847	C	6H	1	0-8 cm	49.50 - 49.58	55.20 - 55.28
847	C	7H	1	0-8 cm	59.00 - 59.08	66.80 - 66.88
847	C	7H	7	77-82 cm	68.77 - 68.82	76.57 - 76.62
847	C	8H	1	0-23 cm	68.50 - 68.73	76.70 - 76.93
847	C	8H	6	102-150 cm	77.02 - 77.50	85.22 - 85.70
847	C	9H	7	75-81 cm	87.75 - 87.81	97.65 - 97.71
847	C	10H	1	0-5 cm	87.50 - 87.55	98.20 - 98.25
847	C	10H	7	79-83 cm	97.29 - 97.33	107.99 - 108.03
847	C	11H	1	0-11 cm	97.00 - 97.11	108.90 - 109.01
847	C	11H	7	73-78 cm	106.73 - 106.78	118.63 - 118.88
847	C	12H	1	0-30 cm	106.50 - 106.80	118.80 - 119.10
847	C	12H	7	58-65 cm	116.08 - 116.15	128.38 - 128.45
847	C	13H	1	0-5 cm	116.00 - 116.05	129.85 - 129.90
847	C	13H	7	64-83 cm	125.64 - 125.83	139.49 - 139.68
847	C	14X	1	0-150 cm	125.50 - 127.00	139.30 - 140.80
847	C	14X	2	0-52 cm	127.00 - 127.52	140.80 - 141.32
847	C	14X	7	15-27 cm	134.65 - 134.77	148.45 - 148.57
847	D	1H	1	0-150 cm	0.00 - 1.50	
847	D	1H	2	0-150 cm	1.50 - 3.00	
847	D	1H	3	0-150 cm	3.00 - 4.50	
847	D	1H	4	0-150 cm	4.50 - 6.00	
847	D	1H	5	0-39 cm	6.00 - 6.39	
847	D	2H	1	0-93 cm	6.60 - 7.53	8.40 - 9.33
847	D	2H	7	60-71 cm	16.20 - 16.31	18.00 - 18.11
847	D	3H	1	0-54 cm	16.10 - 16.64	19.10 - 19.64
847	D	3H	5	0-150 cm	22.10 - 23.60	25.00 - 26.60
847	D	3H	6	0-17 cm	23.60 - 23.77	26.60 - 26.77
847	D	3H	7	51-57 cm	25.61 - 25.67	28.61 - 28.67
847	D	4H	1	0-11 cm	25.60 - 25.71	29.60 - 29.71
847	D	5H	1	0-82 cm	35.10 - 35.92	39.30 - 40.12
847	D	5H	2	0-26 cm	36.60 - 36.86	40.80 - 41.06
847	D	5H	7	47-55 cm	44.57 - 44.65	48.77 - 48.85
847	D	6H	1	0-5 cm	44.60 - 44.65	50.80 - 50.85
847	D	6H	6	130-137 cm	53.40 - 53.47	59.60 - 59.67
847	D	7H	1	0-8 cm	54.10 - 54.18	61.30 - 61.38
847	D	7H	7	22-32 cm	63.32 - 63.42	70.52 - 70.62
847	D	8H	1	0-8 cm	63.60 - 63.68	71.90 - 71.98
847	D	8H	7	22-32 cm	72.82 - 72.92	81.12 - 81.22
847	D	9H	1	0-90 cm	73.10 - 74.00	81.80 - 82.70
847	D	9H	7	71-82 cm	82.81 - 82.92	91.51 - 91.62
847	D	10H	1	0-33 cm	82.60 - 82.93	94.30 - 94.63
847	D	10H	2	144-150 cm	85.54 - 85.60	97.24 - 97.30
847	D	10H	3	0-150 cm	85.60 - 87.10	97.30 - 98.80
847	D	11H	1	0-11 cm	92.10 - 92.21	104.80 - 104.91
847	D	11H	7	73-81 cm	101.83 - 101.91	114.53 - 113.61
847	D	12H	1	0-8 cm	101.60 - 101.68	115.20 - 115.28
847	D	12H	6	115-150 cm	110.25 - 110.60	123.85 - 124.20
847	D	12H	7	0-91 cm	110.60 - 111.51	124.20 - 125.11
847	D	13H	1	0-8 cm	111.10 - 111.18	124.90 - 124.98
847	D	13H	7	71-74 cm	120.87 - 120.90	134.67 - 134.70

APPENDIX 1, CTD.

SITE	HOLE	CORE	SECTION	SECTION DEPTH	ODP DEPTH	MCD DEPTH
847	D	14H	1	0-11 cm	120.60 - 120.71	135.60 - 135.71
847	D	14H	6	127-150 cm	129.37 - 129.60	144.37 - 144.60
847	D	14H	7	0-36 cm	129.60 - 129.36	144.60 - 144.96
848	A	1H	6	142-150 cm	9.00 - 9.08	9.22 - 9.30
848	A	1H	7	0-22 cm	9.08 - 9.30	9.30 - 9.52
848	B	1H	1	0-8 cm	0.00 - 0.08	0.20 - 0.28
848	B	1H	1	131-150 cm	1.31 - 1.50	1.51 - 1.70
848	B	1H	2	0-21 cm	1.50 - 1.71	1.70 - 1.91
848	B	1H	2	49-58 cm	1.99 - 2.08	2.19 - 2.28
848	B	2H	1	0-38 cm	2.20 - 2.58	5.03 - 5.41
848	B	2H	7	80-84 cm	11.99 - 12.03	14.82 - 14.86
848	B	3H	1	0-9 cm	11.69 - 11.78	15.68 - 15.77
848	B	3H	7	75-81 cm	21.45 - 21.51	25.44 - 25.50
848	B	4H	1	0-40 cm	21.20 - 21.60	25.58 - 25.98
848	B	4H	7	74-77 cm	30.94 - 30.97	35.32 - 35.35
848	B	5H	1	0-34 cm	30.70 - 31.04	36.35 - 36.39
848	C	1H	1	0-21 cm	0.00 - 0.21	0.00 - 0.21
848	C	1H	4	57-70 cm	5.07 - 5.20	5.07 - 5.20
848	C	2H	1	0-11 cm	5.50 - 5.61	7.77 - 7.88
848	C	3H	1	0-53 cm	15.00 - 15.53	18.52 - 18.55
848	C	3H	7	75-81 cm	24.75 - 24.81	27.77 - 27.83
848	C	4H	1	0-21 cm	24.50 - 24.71	28.69 - 29.00
848	C	4H	7	74-83 cm	34.24 - 34.33	38.53 - 38.62
848	C	5H	1	0-17 cm	34.00 - 34.17	38.59 - 38.76
848	C	5H	7	6-12 cm	43.06 - 43.12	47.65 - 47.71
848	D	1H	2	142-150 cm	2.92 - 3.00	3.12 - 3.20
848	D	1H	6	63-71 cm	8.13 - 8.21	8.33 - 8.41
848	D	2H	1	0-34 cm	8.40 - 8.74	10.35 - 10.69
848	D	2H	7	52-64 cm	17.92 - 18.00	19.87 - 19.95
848	D	3H	1	0-7 cm	17.90 - 17.97	20.60 - 20.67
848	D	4H	1	0-20 cm	27.40 - 27.60	30.00 - 30.20
848	D	5H	7	55-65 cm	46.45 - 46.55	50.45 - 50.55
849	B	1H	5	57-65 cm	6.57 - 6.65	6.57 - 6.65
849	B	2H	1	0-46 cm	6.70 - 7.16	9.69 - 9.15
849	B	2H	6	114-128 cm	15.34 - 15.48	17.33 - 17.47
849	B	3H	1	0-34 cm	16.20 - 16.34	20.26 - 20.60
849	B	3H	6	121-150 cm	24.91 - 25.20	28.97 - 29.26
849	B	4H	1	0-13 cm	25.70 - 25.83	30.79 - 30.92
849	B	4H	2	72-83 cm	27.92 - 28.03	33.01 - 32.12
849	B	4H	7	53-58 cm	35.23 - 35.28	40.32 - 40.37
849	B	5H	7	71-81 cm	44.91 - 45.01	51.37 - 51.47
849	B	6H	1	0-11 cm	44.71 - 44.81	52.25 - 52.35
849	B	6H	7	50-60 cm	54.20 - 54.30	61.74 - 61.84
849	B	7H	1	0-7 cm	54.20 - 54.27	63.67 - 63.73
849	B	7H	7	69-80 cm	63.88 - 63.99	73.34 - 73.45
849	B	8H	1	0-17 cm	63.70 - 63.87	74.44 - 74.61
849	B	8H	7	59-65 cm	73.29 - 73.35	84.03 - 84.09
849	B	9H	1	0-56 cm	73.20 - 73.76	84.86 - 85.42
849	B	9H	7	75-85 cm	82.86 - 82.96	94.52 - 94.62
849	B	10H	1	0-53 cm	82.70 - 83.23	94.54 - 95.07

APPENDIX 1, CTD.

SITE	HOLE	CORE	SECTION	SECTION DEPTH	ODP DEPTH	MCD DEPTH
849	B	10H	7	43-52 cm	92.13 - 92.22	103.97 - 104.06
849	B	11H	1	0-8 cm	92.20 - 92.28	105.81 - 105.89
849	B	11H	7	68-80 cm	101.88 - 102.00	115.49 - 115.61
849	C	1H	1	0-101 cm	1.00 - 2.01	1.75 - 2.76
849	C	1H	7	49-59 cm	10.35 - 10.45	11.10 - 11.20
849	C	2H	1	0-14 cm	10.50 - 10.64	13.50 - 13.64
849	C	2H	7	72-82 cm	20.22 - 20.32	23.22 - 23.32
849	C	3H	1	0-38 cm	20.00 - 20.38	26.40 - 26.78
849	C	3H	6	134-150 cm	28.84 - 29.00	35.24 - 35.40
849	C	4H	1	0-5 cm	29.50 - 29.55	36.68 - 36.73
849	C	4H	6	133-146 cm	37.51 - 37.64	44.69 - 44.82
849	C	5H	1	0-8 cm	39.00 - 39.08	47.15 - 47.23
849	C	5H	7	75-80 cm	48.75 - 48.80	56.90 - 56.95
849	C	6H	6	137-150 cm	57.11 - 57.24	66.71 - 66.84
849	C	7H	1	0-8 cm	58.00 - 58.08	68.95 - 69.03
849	C	7H	7	75-84 cm	67.75 - 67.84	78.70 - 78.79
849	C	8H	1	0-22 cm	67.50 - 67.72	79.30 - 79.52
849	C	8H	7	33-72 cm	76.83 - 77.22	88.63 - 89.02
849	C	9H	7	29-41 cm	86.29 - 86.41	98.89 - 99.01
849	C	10H	7	85-88 cm	96.35 - 96.38	110.80 - 110.83
849	C	11H	1	0-34 cm	96.00 - 96.34	111.20 - 111.54
849	C	11H	4	144-150 cm	101.94 - 102.00	117.14 - 117.20
849	C	11H	5	0-150 cm	102.00 - 103.50	117.20 - 118.70
849	C	11H	7	68-80 cm	101.88 - 102.00	115.49 - 115.61
849	D	1H	1	0-15 cm	4.00 - 4.15	7.30 - 7.45
849	D	1H	3	129-134 cm	8.08 - 8.13	11.38 - 11.43
849	D	2H	1	0-150 cm	13.50 - 15.00	17.40 - 18.90
849	D	2H	3	66-90 cm	17.16 - 17.40	21.06 - 21.30
849	D	2H	6	37-150 cm	21.37 - 22.50	25.27 - 26.40
849	D	2H	7	0-27 cm	22.50 - 22.77	26.40 - 26.67
849	D	3H	1	0-150 cm	23.00 - 24.50	26.85 - 28.35
849	D	3H	2	0-124 cm	24.50 - 25.74	28.35 - 29.59
849	D	3H	3	0-7 cm	25.74 - 25.81	29.59 - 29.66
849	D	3H	7	78-84 cm	32.52 - 32.58	36.37 - 36.43
849	D	4H	1	0-22 cm	32.50 - 32.72	39.05 - 39.27
849	D	4H	2	86-100 cm	34.86 - 35.00	41.41 - 41.55
849	D	4H	6	100-135 cm	41.00 - 41.35	47.55 - 47.90
849	D	5H	1	0-13 cm	42.00 - 42.13	50.45 - 50.58
849	D	5H	7	62-71 cm	51.63 - 51.72	60.08 - 60.17
849	D	6H	1	0-34 cm	51.50 - 51.84	59.75 - 61.09
849	D	6H	7	8-24 cm	60.58 - 60.76	69.83 - 69.99
849	D	7H	7	61-69 cm	70.61 - 70.69	80.06 - 80.14
849	D	8H	1	0-27 cm	70.50 - 70.77	81.60 - 81.87
849	D	8H	6	86-98 cm	78.86 - 78.98	89.96 - 90.08
849	D	9H	1	0-8 cm	80.00 - 80.08	92.90 - 92.98
849	D	9H	3	130-150 cm	84.30 - 84.50	97.20 - 97.40
849	D	9H	4	0-24 cm	84.50 - 84.74	97.40 - 97.64
849	D	10H	1	0-15 cm	86.50 - 86.65	103.75 - 103.90
849	D	10H	6	139-150 cm	98.39 - 98.50	112.64 - 112.75
849	D	10H	7	0-50 cm	98.50 - 99.00	112.75 - 113.25

APPENDIX 1, CTD.

SITE	HOLE	CORE	SECTION	SECTION DEPTH	ODP DEPTH	MCD DEPTH
849	D	11H	1	0-23 cm	99.00 - 99.23	113.85 - 114.08
850	A	1H	5	134-145 cm	7.34 - 7.45	7.34 - 7.45
850	A	2H	1	0-15 cm	7.50 - 7.85	9.29 - 9.44
850	A	2H	6	121-134 cm	16.33 - 16.47	17.92 - 18.05
850	A	3H	1	0-9 cm	17.20 - 17.29	18.86 - 18.95
850	A	3H	7	57-78 cm	26.77 - 26.98	28.43 - 28.64
850	A	4H	1	0-15 cm	26.70 - 26.85	29.74 - 29.89
850	A	4H	7	70-85 cm	36.40 - 36.55	39.44 - 39.59
850	A	5H	1	0-9 cm	36.20 - 36.28	40.00 - 40.09
850	A	5H	7	58-77 cm	45.78 - 45.97	49.59 - 49.78
850	A	6H	1	0-8 cm	45.70 - 45.78	51.49 - 51.57
850	A	6H	7	75-81 cm	55.45 - 55.51	61.24 - 61.30
850	A	7H	1	0-8 cm	55.20 - 55.28	62.56 - 62.64
850	A	7H	7	69-80 cm	64.89 - 65.00	72.25 - 72.36
850	A	8H	7	77-81 cm	74.47 - 74.51	83.51 - 83.55
850	B	1H	1	0-8 cm	4.50 - 4.58	4.50 - 4.58
850	B	1H	6	130-150 cm	11.80 - 12.00	11.80 - 12.00
850	B	1H	7	0-60 cm	12.00 - 12.60	12.00 - 12.60
850	B	2H	1	0-150 cm	12.80 - 14.40	14.40 - 15.90
850	B	2H	2	0-38 cm	14.30 - 14.38	15.90 - 16.28
850	B	2H	6	140-150 cm	21.40 - 21.50	23.30 - 23.40
850	B	2H	7	0-55 cm	21.50 - 22.05	23.40 - 23.95
850	B	3H	1	0-150 cm	22.00 - 23.50	23.65 - 25.15
850	B	3H	2	0-9 cm	23.50 - 23.59	25.15 - 25.24
850	B	3H	7	49-58 cm	31.49 - 31.58	33.14 - 33.23
850	B	4H	1	0-14 cm	31.50 - 31.64	35.85 - 35.99
850	B	4H	7	72-83 cm	41.22 - 41.33	45.57 - 45.68
850	B	5H	1	0-33 cm	41.00 - 41.33	45.42 - 45.75
850	B	5H	7	79-83 cm	50.79 - 50.83	55.21 - 55.25
850	B	6H	1	0-13 cm	50.50 - 50.63	56.00 - 56.13
850	B	6H	7	77-86 cm	60.27 - 60.38	65.77 - 65.86
850	B	7H	1	0-7 cm	60.00 - 60.07	66.57 - 66.64
850	B	7H	1	104-124 cm	61.04 - 61.24	67.61 - 67.81
850	B	7H	7	70-84 cm	69.70 - 69.84	76.27 - 76.41
850	B	8H	7	81-86 cm	79.31 - 79.36	87.06 - 87.11
851	A	1H	4	88-150 cm	5.34 - 6.00	5.34 - 6.00
851	A	1H	5	0-25 cm	6.00 - 6.25	6.00 - 6.25
851	B	1H	1	0-7 cm	0.00 - 0.07	0.00 - 0.07
851	B	1H	5	128-137 cm	7.28 - 7.35	7.28 - 7.35
851	B	2H	1	0-15 cm	7.50 - 7.65	9.88 - 10.03
851	B	2H	6	143-150 cm	16.43 - 16.50	18.81 - 18.88
851	B	2H	7	0-48 cm	16.50 - 16.98	18.88 - 19.36
851	B	3H	1	0-7 cm	17.00 - 17.07	21.15 - 21.22
851	B	3H	7	79-84 cm	26.79 - 26.84	30.94 - 30.99
851	B	4H	1	0-7 cm	26.50 - 26.57	31.93 - 32.00
851	B	4H	7	58-64 cm	36.08 - 36.14	41.51 - 41.57
851	B	5H	1	0-7 cm	36.00 - 36.07	42.30 - 42.37
851	B	5H	6	50-98 cm	44.00 - 44.48	50.30 - 50.78
851	B	5H	7	63-69 cm	45.63 - 45.69	51.93 - 51.99
851	B	6H	1	0-11 cm	45.50 - 45.61	53.38 - 53.49

APPENDIX 1, CTD.

SITE	HOLE	CORE	SECTION	SECTION DEPTH	ODP DEPTH	MCD DEPTH
851	B	6H	7	69-81 cm	55.18 - 55.30	63.06 - 63.18
851	B	7H	1	0-11 cm	55.00 - 55.11	63.00 - 63.11
851	B	7H	7	72-78 cm	64.72 - 64.78	73.17 - 73.23
851	B	8H	1	0-13 cm	64.50 - 64.63	74.43 - 74.63
851	B	8H	7	75-82 cm	74.25 - 74.32	84.18 - 84.25
851	C	1H	6	139-150 cm	11.39 - 11.50	14.92 - 15.03
851	C	2H	6	142-150 cm	20.92 - 21.00	24.92 - 25.00
851	C	2H	7	0-63 cm	21.00 - 21.63	25.00 - 25.63
851	C	3H	6	143-150 cm	30.43 - 30.50	36.50 - 36.57
851	C	3H	7	0-71 cm	30.50 - 31.21	36.57 - 37.28
851	C	4H	7	66-80 cm	40.66 - 40.80	47.52 - 47.66
851	C	6H	1	0-18 cm	50.00 - 50.18	58.70 - 58.88
851	C	6H	7	67-70 cm	59.67 - 59.70	68.37 - 68.40
851	C	7H	1	0-150 cm	59.50 - 61.00	69.10 - 70.60
851	C	7H	7	43-52 cm	68.93 - 69.02	78.53 - 78.62
851	D	1H	7	49-85 cm	9.49 - 9.85	9.49 - 9.85
851	D	2H	1	0-62 cm	9.50 - 10.12	11.50 - 12.12
851	E	1H	1	121-150 cm	1.21 - 1.50	1.21 - 1.50
851	E	1H	2	0-150 cm	1.50 - 3.00	1.50 - 3.00
851	E	1H	7	72-85 cm	9.48 - 9.61	9.48 - 9.61
851	E	2H	1	0-13 cm	9.50 - 9.63	13.00 - 13.13
851	E	2H	7	30-59 cm	18.68 - 18.97	22.18 - 22.47
851	E	3H	1	0-19 cm	19.00 - 19.19	23.20 - 23.39
851	E	4H	1	0-33 cm	28.50 - 28.83	34.70 - 35.03
851	E	4H	7	50-74 cm	38.00 - 38.24	44.20 - 44.44
851	E	5H	1	0-14 cm	38.00 - 38.14	44.80 - 44.94
851	E	5H	7	79-84 cm	47.79 - 49.84	54.59 - 54.64
851	E	6H	7	77-82 cm	57.27 - 57.32	64.87 - 64.92
851	E	7H	7	77-83 cm	66.77 - 66.83	75.37 - 75.43
851	E	8H	1	0-18 cm	66.50 - 66.68	76.10 - 76.28
851	E	8H	7	53-59 cm	76.03 - 76.09	85.63 - 85.69
852	B	1H	6	103-137 cm	8.53 - 8.87	8.73 - 9.07
852	B	2H	1	0-20 cm	8.90 - 9.10	9.15 - 9.35
852	B	2H	7	67-79 cm	18.57 - 18.69	18.82 - 18.94
852	B	3H	1	0-68 cm	18.40 - 19.08	19.22 - 19.90
852	B	3H	7	74-83 cm	28.14 - 28.23	28.96 - 29.05
852	B	4H	1	0-6 cm	27.90 - 27.96	30.30 - 30.36
852	B	5H	1	0-12 cm	37.40 - 37.52	40.27 - 40.39
852	B	5H	7	71-84 cm	47.11 - 47.24	49.98 - 50.03
852	B	6H	1	0-8 cm	46.90 - 46.98	51.85 - 51.93
852	B	6H	7	47-79 cm	56.37 - 56.69	61.32 - 61.64
852	B	7H	1	0-17 cm	56.40 - 56.57	62.27 - 62.44
852	B	7H	7	88-91 cm	66.07 - 66.10	71.94 - 71.97
852	B	8H	1	0-6 cm	65.90 - 65.96	72.65 - 72.71
852	B	9H	1	0-12 cm	75.40 - 75.52	83.92 - 84.04
852	B	9H	7	63-80 cm	85.03 - 85.20	93.55 - 93.72
852	B	10H	1	0-11 cm	84.90 - 85.01	94.90 - 95.01
852	B	10H	7	79-86 cm	94.69 - 94.76	104.69 - 104.76
852	B	11H	1	0-11 cm	94.40 - 94.51	105.40 - 105.51
852	B	11H	7	75-84 cm	104.15 - 104.24	115.15 - 115.24

APPENDIX 1, CTD.

SITE	HOLE	CORE	SECTION	SECTION DEPTH	ODP DEPTH	MCD DEPTH
852	B	12H	1	0-37 cm	103.90 - 104.27	116.10 - 116.47
852	B	12H	7	60-76 cm	113.50 - 113.66	125.70 - 125.86
852	C	1H	4	119-124 cm	5.69 - 5.74	5.69 - 5.74
852	C	2H	1	0-8 cm	6.00 - 6.08	6.80 - 6.88
852	C	2H	7	55-78 cm	15.55 - 15.78	16.35 - 16.58
852	C	3H	1	0-33 cm	15.50 - 15.83	16.90 - 17.23
852	C	3H	7	10-27 cm	24.60 - 24.77	26.00 - 26.17
852	C	4H	7	67-83 cm	34.67 - 34.83	35.87 - 36.03
852	C	5H	1	0-9 cm	34.50 - 34.59	38.00 - 38.09
852	C	5H	7	69-79 cm	44.19 - 44.29	47.69 - 47.89
852	C	6H	1	0-13 cm	44.00 - 44.13	49.00 - 49.13
852	C	6H	7	78-83 cm	53.78 - 53.83	58.78 - 58.83
852	C	7H	1	0-44 cm	53.50 - 53.94	58.60 - 59.04
852	C	7H	7	71-82 cm	63.21 - 63.32	68.31 - 68.42
852	C	8H	1	0-7 cm	63.00 - 63.07	69.70 - 69.77
852	C	8H	7	73-83 cm	72.00 - 72.73	79.43 - 79.53
852	C	9H	1	0-14 cm	72.50 - 72.64	80.70 - 80.84
852	C	9H	7	62-78 cm	82.12 - 82.28	90.32 - 90.48
852	C	10H	1	0-8 cm	82.00 - 82.08	91.95 - 92.03
852	C	10H	7	59-82 cm	91.59 - 91.82	101.54 - 101.78
852	C	11H	1	0-13 cm	91.50 - 91.63	102.05 - 102.18
852	C	11H	7	69-79 cm	101.19 - 101.29	111.74 - 111.84
852	C	12H	1	0-13 cm	101.00 - 101.13	112.00 - 112.13
852	C	12H	7	71-79 cm	110.71 - 110.79	121.71 - 121.79
852	C	13X	1	0-150 cm	111.50 - 112.00	120.90 - 122.40
852	C	13X	2	0-150 cm	112.00 - 113.50	122.40 - 123.90
852	C	13X	3	0-7 cm	113.50 - 113.57	123.90 - 123.97
852	C	13X	4	60-150 cm	115.60 - 116.50	126.00 - 126.90
852	D	1H	1	0-20 cm	2.00 - 2.20	0.90 - 1.10
852	D	1H	7	79-83 cm	11.79 - 11.83	10.69 - 10.73
852	D	2H	1	0-15 cm	11.50 - 11.65	11.75 - 11.90
852	D	2H	7	77-82 cm	21.27 - 21.32	21.52 - 21.57
852	D	3H	1	0-4 cm	21.00 - 21.04	21.05 - 21.09
852	D	3H	7	75-79 cm	30.75 - 30.79	30.80 - 30.84
852	D	4H	1	0-8 cm	30.50 - 30.58	32.40 - 32.48
852	D	4H	7	73-79 cm	40.23 - 40.29	42.13 - 42.19
852	D	5H	1	0-7 cm	40.00 - 40.07	43.30 - 43.37
852	D	5H	7	55-62 cm	49.35 - 49.42	52.65 - 52.72
852	D	6H	1	0-7 cm	49.50 - 49.57	54.00 - 54.07
852	D	6H	7	73-83 cm	59.23 - 59.33	63.73 - 63.83
852	D	7H	1	0-23 cm	59.00 - 59.23	65.40 - 65.63
852	D	7H	7	80-85 cm	68.80 - 68.85	75.20 - 75.25
852	D	8H	1	0-7 cm	68.50 - 68.57	75.80 - 75.87
852	D	8H	7	47-84 cm	77.97 - 78.34	85.27 - 85.64
852	D	9H	1	0-7 cm	78.00 - 78.07	87.05 - 87.12
852	D	9H	7	71-82 cm	87.71 - 87.82	96.76 - 96.87
852	D	10H	1	0-13 cm	87.50 - 87.63	97.45 - 97.58
852	D	10H	7	46-67 cm	96.96 - 97.17	106.91 - 107.02
852	D	11H	1	0-13 cm	97.00 - 97.13	108.00 - 108.13
852	D	11H	7	74-89 cm	106.74 - 106.89	117.74 - 117.89

APPENDIX 1, CTD.

SITE	HOLE	CORE	SECTION	SECTION DEPTH	ODP DEPTH	MCD DEPTH
852	D	12H	1	0-5 cm	106.50 - 106.55	118.25 - 118.30
852	D	12H	7	65-68 cm	116.15 - 116.18	127.90 - 127.93